Thermal Safety of a Retinal Prosthesis

Nicholas Lachlan Opie

Submitted in total fulfilment of the requirements of the degree of Doctor of Philosophy

January, 2011

Department of Electrical and Electronic Engineering
The University of Melbourne

Nicholas Opie

ABSTRACT

For over 27 million patients worldwide suffering from visual loss and impairment caused by retinitis pigmentosa and age related macular degeneration, a retinal implant with the ability to restore their sight at even a rudimentary level is highly desired. Current clinical trials, performed with between 16 and 60 electrodes, have had some success of eliciting perceptions of the visual field through electrical stimulation of the remaining retinal neurons. These studies, as well as computational simulations, suggest that in excess of 1000 electrodes may be required to provide mobility, facial recognition, and the ability to read at a normal speed. As the desire for enhanced visual acuity and resolution increases, the potential for hazardous amounts of thermal energy to be released into the delicate retinal neurons through the implanted circuitry is a large concern.

Previous studies that investigated the effects of thermal damage on retinal tissue were predominantly performed using lasers and electromagnetic irradiation. Not only do these studies exclude the possibility of mechanical trauma caused by prosthesis implantation to exacerbate thermally induced damage, but are performed using powers greater than those dissipated by implant circuitry and durations shorter than a potential eighteen hour daily use. Thus, the primary aim of this thesis is to investigate the effects of thermal heating by an implant on retinal tissue, to ensure that energy dissipated by an implanted visual prosthesis does not induce cellular damage or death. Determination of temperatures that cause thermal damage in an acute and chronic setting can be used to assist in the design of implant circuitry and stimulation protocols to maximize the performance of visual prostheses while ensuring patient safety is not compromised.

To assist with answering the question of whether the thermal safety of retinal implants can be ensured, temperature measurement and delivery devices were designed. These implants, temperature measurement systems and power sources were shown in cadaver, *in vitro* and *in vivo* experiments to be able to be implanted epiretinally in rat eye-cups and both suprachoroidally and epiretinally in cat eyes. These implants, designed to be of comparable size to current retinal prosthesis microchips, were also shown to be capable of inducing, measuring and recording the localised retinal tissue temperature increases in multiple positions simultaneously.

A finite element thermal model has been specifically designed as a component of this research to model devices implanted in both an epiretinal and suprachoroidal location. The model has the versatility to investigate the many factors that contribute to the temperature of neighbouring retinal tissue such as heat dissipated by the implant circuitry, room and body temperature, choroidal and retinal blood perfusion volumes and flow rates, thermal conductivity changes related to cellular reorganization and death of retinal neurons, and metabolically generated heat. This model can be employed to greatly reduce the number of animals that would otherwise be required to perform such a large number of thermal experiments and has been shown through cadaver tests to accurately represent temperatures within the eye. There was a negligible contribution to retinal tissue temperature increase caused by alterations in room temperature, body temperature and metabolically generated heat; however, the power dissipated by the implants, the thermal conductivity of the tissue and the rate of blood perfusion were observed to play a significant role in the distribution of the implant-induced power dissipation. Comparisons between the thermal models, cadaver trials, and *in vivo* trials performed on cats indicated a very consistent and replicable behaviour between the finite element simulations and the experiments. Thus, the use of these models could significantly reduce the number of animals sacrificed in order to more thoroughly assess the thermal impact of retinal implants.

In vivo cat experiments and *in vitro* rat experiments were also conducted and have assisted in the optimisation of surgical strategies and protocols for suprachoroidal prosthesis implantation. Preliminary results from the *in vivo* work indicated that thermoregulatory mechanisms will assist in maintaining a homeostatic retinal temperature when subjected to an implant-induced thermal elevation greater than 2°C. Analysis of *in vitro* microglial morphological changes, observed through retraction of microglial processes and an increase in microglia soma areas, indicated that any thermal or mechanical insult will instigate changes within the retinal tissue. Mechanical trauma, caused by insertion of a foreign object into the retina, induced a response that was greatly exacerbated in the presence of thermal stress, and it is recommended that prior to operation of an implanted prosthesis (where power will be dissipated by the implanted circuitry), the induced mechanical trauma be allowed as much time as is required to stabilise, to reduce the potential for irreversible cellular damage to occur.

To ensure an implanted retinal prosthesis will not cause extensive damage to neighbouring neurons, careful monitoring of an implant is recommended. Thermal increases of 2.54°C were observed to cause activation of microglia in *in vitro* rat preparations, and we recommend that retinal implants restrict power dissipation to below 31.91 mW (equivalent to a power density of 23.46 mW/mm^2) to reduce the potentially deleterious effects caused by thermal heating.

DECLARATION

This is to certify that

i.   the thesis comprises only my original work towards the PhD,

ii.   due acknowledgement has been made in the text to all materials used,

iii.   the thesis is less than 100,000 words in length, exclusive of tables, maps, bibliographies and appendices

_____

Nicholas Lachlan Opie

ACKNOWLEDGEMENTS

First and foremost I would like to thank my ever supporting wife Rachelle, for without her encouragement and patience this thesis would not have been possible.

To my supervisors Anthony Burkitt, Hamish Meffin and David Grayden I thank you for your ideas and input; your commitment to this project was inspirational and I can only hope your enthusiasm and professionalism carries forward to all your future students. To all those working in the Fletcher Lab, Erica Fletcher, Una Greferath, Michelle Ward and Kirsten Vessey, I express my sincere gratitude. Your generosity with your time and knowledge was humbling and the experimental success achieved was only made possible through your extensive help. I would like to thank Elisa Borg for her expert animal training and never-ending assistance and patience, Chris Williams, Rob Shepherd, James Fallon, Meera Ulaganathan and Alexia Freemantle for all your help prior to and during the acute experiments. To Penny Allen and Mark McCoombe, I am still in awe of your surgical skill and wish to thank you for all your time and ingenuity both during the equipment design phases and throughout the tests. Your suggestions and recommendations were invaluable to the success of the project.

To the engineers who assisted in the design, construction and calibration of the high resolution temperature measurement system and current sources, I give thanks, particularly Gavin Pearce, Peter Farrell and Michael Yarrow. I would like to thank Stan Skafidas and NICTA for their contributions and opportunities that to the project that were made available through your generosity.

I would also like to thank my colleagues and friends whom have made the journey enjoyable and can only wish the best for them, whatever their futures may bring.

CONTENTS

1

BACKGROUND   1

2

EQUIPMENT DESIGN AND CALIBRATION 69

3

FINITE ELEMENT THERMAL MODELS 121

4

CAT RETINA CADAVER TRIALS 149

5

THERMAL HEATING OF CAT RETINAL TISSUE *IN VIVO* 167

6

IN VITRO RAT RETINAL TISSUE STUDIES   199

7

THESIS CONCLUSIONS 251

1

BACKGROUND

The highly complex human visual system enables the conversion of wavelengths of light into electrical signals that give the perception of a three dimensional image. This process, however ingenious, is not immune to disease or damage. Estimates in 2002 of the worldwide vision impaired community indicated in excess of 161 million people suffer from visual loss, with 3.9% of those congenitally blind (Resnikoff, Pascolini et al. 2002). Not only does this emphasise the importance of research being conducted on alternate visual means but also on the extreme fragility of the system as a whole.

In order for sight to be regained by a blind person through a visual prosthesis, the method and ability of a prosthesis device to translate individual photons over a wide range of wavelengths into patterns that can be perceived in the cortex to give an accurate representation of the visual field is fundamental. Thus, an understanding of how the visual pathway operates and how certain diseases can affect this method of sensory input is crucial in the design of a bionic replacement.

Electrical stimulation of retinal and cortical neurons used to elicit perceptions of vision to those suffering from profound vision loss is a method which has received much attention, particularly in the last few decades. Many groups around the globe are investing large amounts of time and money into researching a beneficial and feasible way of providing electrically induced vision, with placement of the electrical stimulators both within the eye and within the optic nerve and cortex. While each of the investigated locations provides distinct advantages and disadvantages, a global requirement for retinal prosthesis to provide patients with the ability to read, distinguish faces and be independently mobile will require the resolution of current devices to be improved. In order to enhance the resolution of visual field perceptions by users of a

visual prosthesis, electrode numbers will have to increase. This will result in an increase in the required amount of power being delivered to the electrode array and, consequently, the thermal energy dissipated within the prosthesis circuitry may induce damaging temperature increases in neighbouring tissue.

Research performed to investigate the effects of thermal heating have been analysed, with the primary modes of thermal damage caused by laser irradiation, whole body incubation and direct conductive heat transfer related to temperature increases that may be observed through visual prosthesis use. These studies will be used to assist in determination of a power budget, a threshold temperature increase for the implanted circuitry, although many different animal models and tissues have been involved in threshold analysis. Further, there is a large difference in the endpoints (at what stage retinal damage is determined) and measurement methods used to evaluate damage in many of these publications, resulting in a large range of potentially damaging thermal stimuli. A comparison between the animal models and the experimental design is important to ensure that these studies can be accurately compared to thermal damage caused by the heating of a retinal prosthesis and will assist in ensuring implanted visual aids function efficiently and are safe for patient use.

1.1 VISUAL PATHWAY

To understand how photons are transformed into information relating to where and what things are, it is important to be aware of the components involved and the diseases and conditions which can affect their function. The visual pathway is essentially a sequence of events that occurs throughout the different orbital and cortical structures, with each structure having a unique and important task in the process of converting light energy into useful perceptions.

Initially, photons of light are reflected off objects and are presented to the most external of the visual system components, the cornea. The cornea, a 500 µm thick, multilayered structure, provides approximately two thirds of the eye's focusing ability (Roberts 2002) with the central layer, the stroma, being comprised of parallel collagen fibrils that utilise glycoproteins for the absorption of harmful wavelengths of light within the ultraviolet spectrum (Scott 1988; L'Esperence 1989; LaManna, McCracken et al. 1989). Light that is able to pass through the corneal layers is then transmitted through the anterior chamber, filled with aqueous humor, to the iris and lens, and it is through the relaxation and constriction of the muscles controlling the lens that subsequently controls its convexity and ensures that light is focused on the retinal surface (Sauerland 1999; Moore and Agur 2002; Drake, Vogl et al. 2005).

Light that has been focused by the lens will traverse through the posterior chamber of the eye which accounts for almost 80% of the eye's volume (Roberts 2002). The vitreous fluid within this chamber is almost perfectly transparent and has a viscosity of two to four times that of pure water. As a person ages, the vitreous humor can change from a gel to a liquid. This shrinking and collapsing of the vitreous mass may separate and fall away from the retina resulting in a posterior vitreous detachment, which can also result in the much more severe condition of retinal detachment in places where the vitreous and retina are still firmly attached. Apart from maintaining the intraocular pressure, the large fluid filled cavity also acts to absorb photons of light in the far infrared spectrum, thus allowing only photons within the visible spectrum and the near infrared spectrum to pass through to the retinal layer, where they in turn are absorbed by retinal and choroidal pigments (Birngruber, Puliafito et al. 1987; Carroll and Humphreys 2006). It is thought that the vitreous fluid could be used as a heat sink to remove thermal energy dissipated by implanted prosthesis, and is being investigated by many groups around the world as a location for implanting heat generating prosthesis components.

The ability of the visual system to transform photons into neural signals occurs in the photoreceptor layer. Photoreceptors line the retina which forms the interior surface of the eye from the fovea frontalis (corresponding to the axis of the eye) to the ora serrata near the ciliary body. There are four main types of photoreceptors characterised by their dispersion, design and their ability to absorb light of different wavelengths, and it is within the folds and disks of these photoreceptors that the photo-isomerisation of amino acid chains occurs, resulting in the transduction of voltage-gated ionic signals to be generated and transmitted.

The three types of cone photoreceptors, specialised for daylight vision, are predominantly located in the 2 mm diameter fovea (Roberts 2002), 15° from the blind spot on the temporal side in the macula lutea. This area is specialized by being free of any blood vessels that could potentially absorb and scatter passing photons, which would reduce the information passed to the photoreceptors. Although the macula lutea comprises only 4% of the retinal area (6 mm diameter), it is responsible for majority of useful vision and accounts for almost 10% of the visual field. This is due to the significantly increased cone photoreceptor density within this region (around 150,000 cells/mm^2), with comparatively few cone cells in the peripheral retina. This is opposite to the relative numbers of rod photoreceptors which are very dense (greater than 150,000 cells/mm^2) at a 20° eccentricity from the fovea, tapering down to a cell density of 40,000 cells/mm^2 at the limbus at the edge of the retinal layer (Vander, Sherman et al. 2001; Roberts 2002; Gehrs, Anderson et al. 2006). Between 15° to 20° on the nasal side, both rod and cone photoreceptors are absent, and it is within this blind spot that axons pass from the eye through the optic nerve to the cortex.

In order to ensure that the large and constant amount of metabolic work done in the photoreceptor layer does not cause a temperature increase capable of damaging the delicate cellular components, a layer of blood vessels, the choroid, lies posterior to the retinal pigment epithelial layer. This layer has average total arterial and venous volumetric flow rates of 33 µL/min and 34 µL/min respectively (Riva, Grunwald et al. 1985), and is one of the most perfused areas in the body, with a perfusion rate of 2000 ml/min/100g (Sailer, Shinoda et al. 2007).

Signals generated by the photoreceptors undergo a large amount of processing prior to extraction from the eye to the cortex through the optic nerve, interconnecting with horizontal, bipolar and amacrine neurons. Projections from these cells connect to ganglion cells located in the ganglion cell layer, with bundles of ganglion cell axons forming the optic nerve. This highly connected network of cells plays a large and important role in the processing of the visual information, reducing the coded information from hundreds of millions of photoreceptors to only one million ganglion

cell axons. The ability to utilize this rich inter-retinal connectivity is one of the major advantages of retinally implanted prosthesis over optic nerve and cortical designs.

Once the ganglion cell axons from each eye leave the globe via the optic disk (blind spot), they cross over at the optic chiasm where cells providing information on the controlateral and ipsilateral hemispheres are differentiated. The retinal projections travel to the lateral geniculate nucleus (LGN) of the thalamus (first synaptic connection) before projecting into the primary visual cortex (V1). The axonal connections from the ganglion cells are organised in such a way that the adjacent retinal cells project to adjacent cells in the LGN, which in turn project to adjacent cells in V1. This visuotopic representation thus forms a retinotopic map of the visual field within the cortex, with the connections between V1 and extrastriate areas (and among extrastriate areas) also topographically organized (Rosa and Tweedale 2003). Differences within the axonal terminations of the fibres from the LGN are commonly due to having specified stimuli for vision processing. A schematic diagram of the visual pathway is shown in Figure 1.1, showing a magnification of the retinal tissue layer and the primary components of the eye, as well as the lateral geniculate nucleus and the primary visual cortex, two of the proposed locations for extraorbital visual prosthesis implantation.

With individual areas of the visual cortex being responsible for different parameters of vision, it is thought that while cortical prosthesis will not be able to harness the processing power of the retinal neurons, the well-defined and highly organised cortical layer will allow selective stimulation for a cortically implanted visual aid to provide beneficial vision restoration across many modalities and for diseases and traumas that render the optic nerve and tract useless.
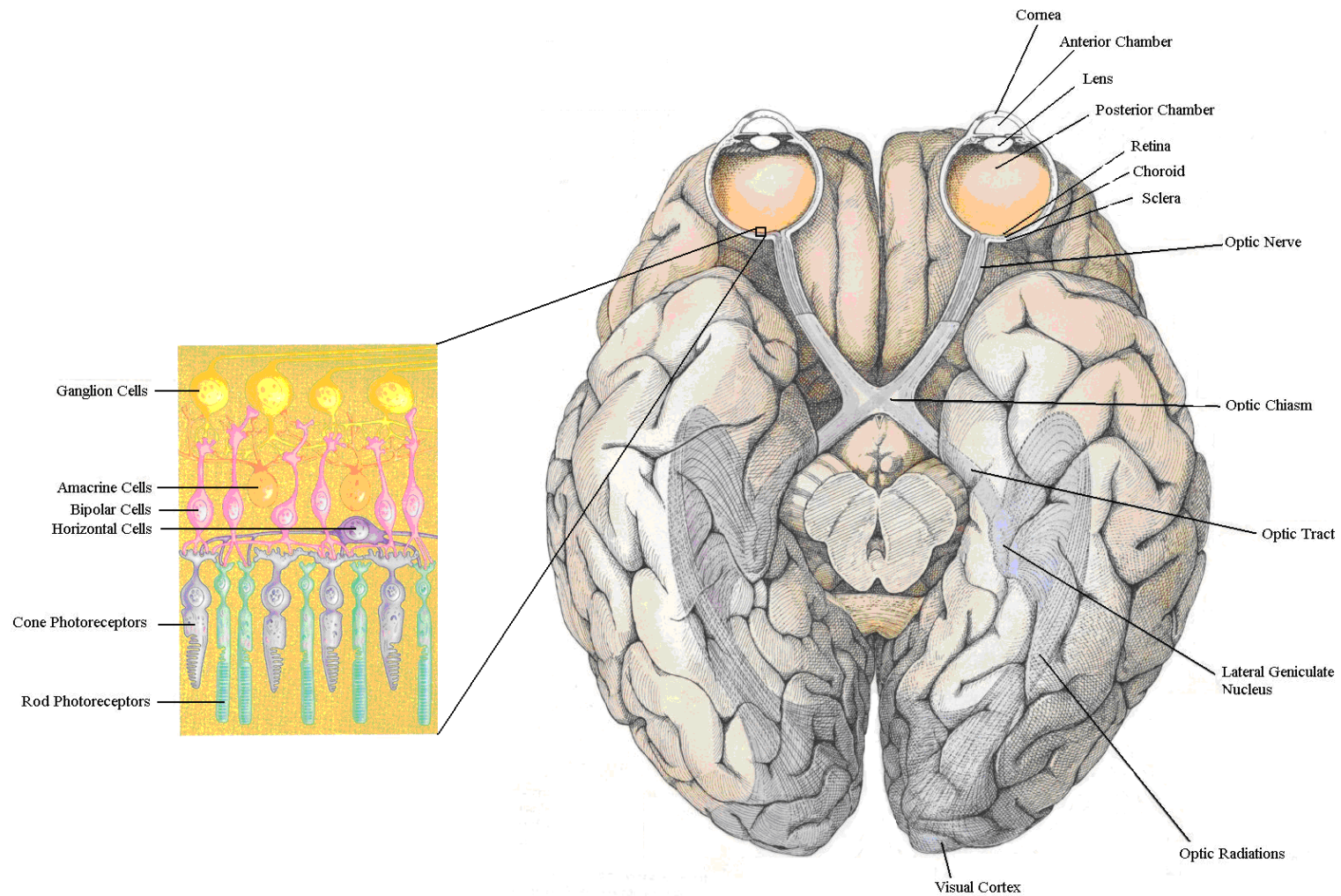
Figure 1.1. Visual pathway from rod and cone photoreceptors to the visual cortex indicating visual processing within the interneurons (amacrine, bipolar and horizontal cells), connection from the ganglion cells (and their axons which for the optic nerve) through the optic chiasm and optic tract to the lateral geniculate nucleus and the optic radiations from the lateral geniculate nucleus to the visual cortex. Major components of the eye are also indicated. Images are adapted from Hubel (1988) and Vander et al. (2001)

1.2   RETINAL DISEASES

With such a large number of components required by the visual system to symbiotically function to transmit and represent the perception of sight, it is surprising to note that two dystrophies account for over 60% of blind persons over the age of 60, totalling over 50 million people worldwide (Foran, Wang et al. 2003; Tasman and Rover 2004). Retinitis pigmentosa (RP) and age-related macular degeneration (AMD) are both progressive degenerative diseases that are the largest contributors to vision impairment in developed countries. These two conditions that currently have no cure and no method of prevention, specifically target the photoreceptor cells and will become increasingly prevalent as the global population increases from 600 million people over 60 in the year 2000 to over 2000 million people over 60 by 2050 (Hymen 1987; Resnikoff, Pascolini et al. 2002; WHO 2004).

Studies have indicated that the financial burden of AMD in Australia alone will increase from $2.6 billion per year to $6.5 billion per year, with a total expenditure of greater than $59 billion over the next twenty years (Gehrs, Anderson et al. 2006; Taylor, Guymer et al. 2006). The economic impact in America is similarly high, with an expected annual cost of vision loss estimated at nearly $68 billion (Weiland and Humayun 2008).

Even through these dystrophies are almost opposite, initially affecting either peripheral vision or central vision, the ultimate fate of these conditions is total blindness. Figure 1.2 depicts the differences in vision and vision loss that occur in RP and AMD compared to normal vision. A mid to late stage of RP is shown to have a severe effect on peripheral vision while in AMD, this involves a predominantly central visual loss.

One of the major causes of blindness worldwide is the formation of cataracts (opacities in the crystalline lens). This condition, however, is not a neural disease and vision improvement though implantation of a retinal prosthesis is not expected to be beneficial. As such, cataracts will not be investigated as a potential disease requiring a retinal implant. Other common diseases such as diabetic retinopathy and glaucoma affect the optic nerve and neurons in the ganglion cell layer. Damage to these structures is caused by abnormal blood vessel retardation of neural retinal nutrients in diabetic retinopathy and by increased intraocular pressure in patients with glaucoma (Weiland and Humayun 2008). While current optic nerve implants will be discussed, the potential of persons

with these diseases to benefit from retinal implants is limited, and the diseases will not be discussed in detail.
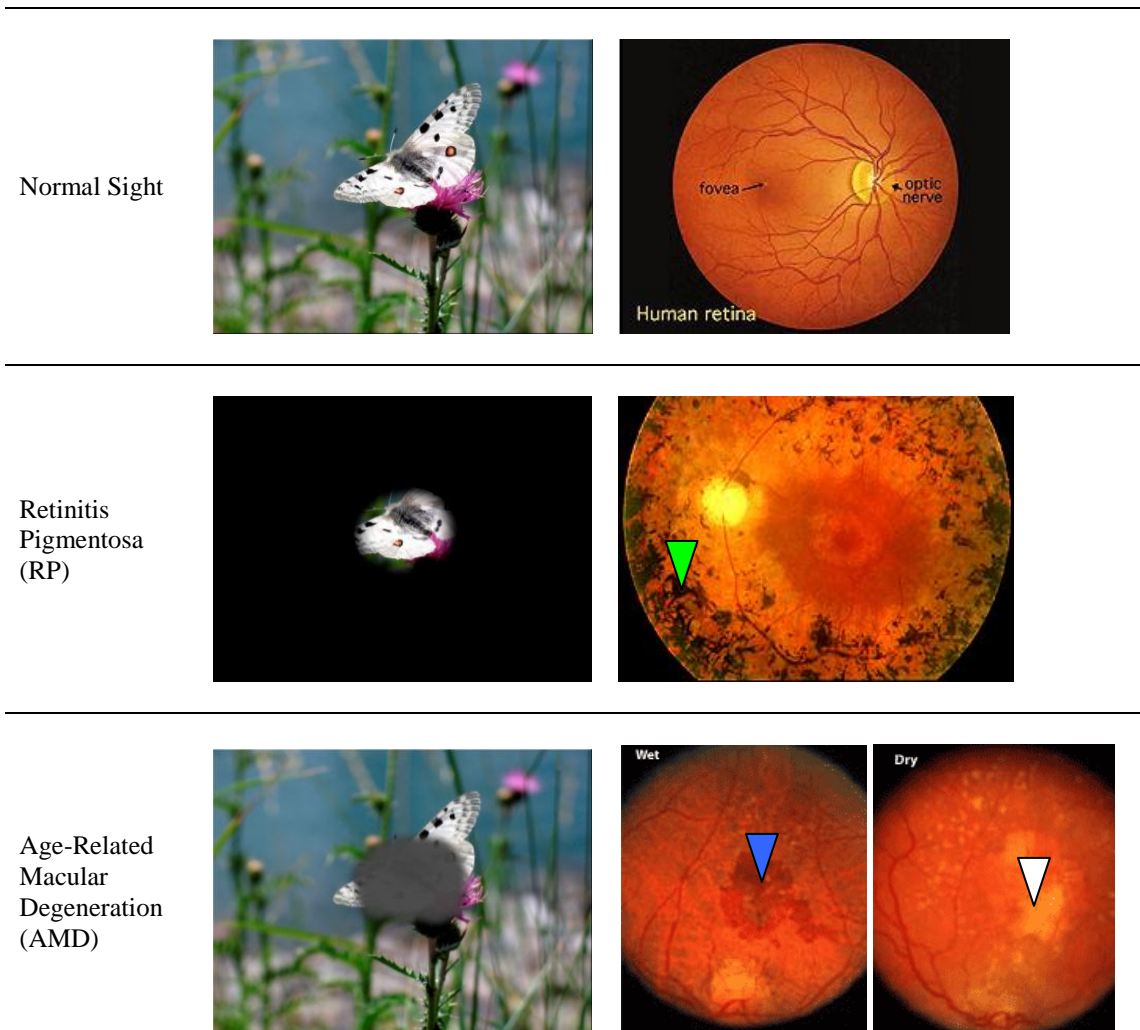
Figure 1.2. Field of view and fundus photograph of normal sighted and people with retinitis pigmentosa and age related macular degeneration prior to complete visual loss. Fundus photographs indicate peripheral vision loss in RP patients (green arrow) and central vision loss in people with wet AMD (blue arrow) and dry AMD (white arrow). Image courtesy of the National Eye Institute, National Institutes of Health.

1.2.1   Retinitis Pigmentosa

Affecting approximately one person in 4000, the progressive and degenerative condition of retinitis pigmentosa is regarded by medical practitioners as several related, yet distinct, dystrophies of the rod photoreceptors and pigment epithelium. This condition is a combination of more than 70 genetic defects, and while it can affect people at any age,

is predominantly seen in persons over 65 (Hazzard, Bierman et al. 1994; Fauci, Martin et al. 1998; Humayun 2001; Tallis and Fillit 2003; Weiland and Humayun 2008).

The initial stages of the disease typically begin with cell loss in the mid-periphery which leads to the formation of a ring scotoma, spreading both centrally and peripherally. While early stages of both RP and AMD cause smaller visual fields and slower temporal processing of letters than age matched trials (Cheong, Legge et al. 2008), progression of the disease will eventually lead to a severely contracted central visual field, leaving the patient with a loss of peripheral and night vision, reduced spatial and temporal contrast sensitivity and reduced visual acuity (Turano, Herdman et al. 1993). Cone cells located in the foveal region of the retina, although not specifically targeted, will also become indirectly damaged as the disease progresses, due to the reduction in blood flow caused by the accumulation of necrotic tissue.

Although almost all of the photoreceptors will be damaged in late stages of the disease, bipolar, amacrine and horizontal interneurons as well as ganglion cells remain functional, with histological studies indicating over 80% of cells in the inner nuclear layer and between 30 and 90% of cells in the ganglion cell layer remain intact (Humayun, Prince et al. 1999). With such a large number of ganglion cells still responsive, electrical activation of these neurons is expected to allow those with visual impairments to regain some vision. Activation of the ganglion cells will also utilise the retinotopic organisation, and, although some reorganization of the retina will occur, this is not expected to prevent the ability of a retinal prosthesis to deliver functional vision to sufferers of this condition.

1.2.2 Age-Related Macular Degeneration

As the name suggests, this disease primarily effects the aged community, with an incidence of one person in every 2000 over the age of 65 (Hazzard, Bierman et al. 1994; Tallis and Fillit 2003), with almost 700,000 new AMD patients (70,000 becoming legally blind) each year in the United States (Weiland and Humayun 2008). This current, leading cause of gradual, painless, bilateral visual loss has an average onset at an age of 65 and comes in two distinct forms, exudative (wet) and non-exudative (dry). Australian studies have indicated that this condition is the cause of over 50% of the

blind community, with their definition of blindness being a vision less than 20/200 (Newland, Hiller et al. 1996; Foran, Wang et al. 2003).

Dry AMD, accounting for almost 90% of affected persons, is characterized by the accumulation of extracellular deposits beneath the retinal pigment epithelium, appearing as small yellow lesions clustered in the macula. These deposits of drusen can be hard (nodular with well-defined borders) or soft (more irregular in shape without clear borders) and contain complex fatty lipids and calcium (Johnson, Lewis et al. 2003; Gehrs, Anderson et al. 2006). The build-up of these molecules is caused by oxidative stress, one of the bi-products of aging, and as a result there is no current cure. The initial symptoms of dry AMD will be minor blurring of vision. As the disease progresses and the drusen becomes larger and more confluent, large dark spots (blind spots) will appear in the field of vision, continually growing to eventually result in total blindness. This is expected to be caused by accumulation of drusen deposits, impairing the normal exchange of ions and metabolites between the choroidal blood supply and the photoreceptors through establishment of a physical barrier, compromising the function of retinal pigment epithelium cells, damage to photoreceptor structural integrity and the containment of cytotoxic molecules (Johnson, Lewis et al. 2003). Choroidal blood flow in non-exudative age related macular degeneration is reduced by 37%, expected to be due to a 33% decrease in the choroidal blood volume (Grunwald, Hariprasad et al. 1998). This reduction in blood flow could have detrimental effects on the eye's ability to remove thermal energy, exacerbating damage caused by the heating of an implanted prosthesis.

Wet AMD (or choroidal neovascularisation) occurs when neovascular vessels from the choroid grow through holes in Bruch's membrane caused by haemorrhage and atrophy in the space beneath the retinal pigment epithelium (Grunwald, Hariprasad et al. 1998). Venous congestion of these vessels can result in rupture and bleeding, causing blurring and distorting of vision as the pigment epithelial layer is subsequently elevated. The onset of these symptoms is gradual, with acute vision loss caused by bleeding from the subretinal choroidal neovascular membranes followed by fibrosis of the damaged cells, developing into rounded atrophic scar tissue that can cause permanent visual loss.

While both the diseases of RP and AMD have risk factors associated with a family history of hypertension, cardiovascular disease, smoking, genetic predispositions, hyperopia, light skin, eye colour and cataracts, these contributing factors are all secondary to aging (Hazzard, Bierman et al. 1994; Tallis and Fillit 2003). Current therapies and treatments such as gene therapy (Silverman and Hughes 1989; Ali, Sarra et al. 2000; Acland, Aguirre et al. 2001), retinal stem cell transplantation (Seiler and Aramant 1998; Humayun, Juan et al. 2000; Schraermeyer, Thumann et al. 2001;

Radtke, Aramant et al. 2004; Qiu, Seiler et al. 2005), hyperbaric oxygen therapy (Vingolo, Rocco et al. 2008) and pharmaceutical and nutritional therapies (Johnson, Lewis et al. 2003) are aimed at reducing the degenerative process caused by these conditions, with results indicating clinical trials are still a long way off.

Both these degenerative retinal conditions, however, affect only the cellular elements responsible for phototransduction and, as a result, leave a large majority of the cellular elements used in the initial stages of processing (bipolar, amacrine and horizontal cells) and in transmission of the visual scene (ganglion cells and axons) intact. By doing so, the detrimental effects of the diseases can be counteracted, bypassing the damaged photoreceptors responsible for the transformation of photons into electrochemical signals by implanting electrodes that directly stimulate subsequent neural layers.

While persons with either of these conditions will ultimately be suitable candidates for a retinal prosthesis, currently only patients who have no light perception are being considered. For this reason, patients with retinitis pigmentosa will for the majority of initial implantees. Persons suffering from AMD, who have a visual acuity often above counting fingers, will be more strongly considered once an increased certification is given that the implants will be of greater benefit to their current visual acuity.

1.3   ELECTRICAL STIMULATION

The phenomenon of electrical phosphene induction, the perception of light brought on by electrical stimulation, dates back to the 18th century when LeRoy (1755), using electrical stimulation to 'heal various illnesses', noted that an electrical pulse delivered to the eye produced the sensation of light. This was further investigated by Foerester (1929) by directly applying stimulation to the occipital cortex, with the first retinal stimulator patented in 1953 by the Australian inventor Graham Tassicker. In the late 1960's, Brindley and Lewin (1968) designed a cortical cap containing 80 transmitters connected to 80 receivers that was capable of eliciting up to 40 perceived phosphenes in a subject with glaucoma, subsequently allowing her to read Braille characters using the device alone.

An example of how phosphenes can be used to create recognisable perceptions is shown in Figure 1.3, comparing a normal black and white image (Figure 1.3A) with phosphene visions produced by altering the phosphene brightness (Figure 1.3B) and the phosphene sizes (Figure 1.3C). Current trials have reported large variations in the appearance of phosphenes, with colours ranging from white to yellow and blue and shapes reported by patients to look like hooks, threads and spots (Weiland, Humayun et al. 1999; Weiland, Humayun et al. 1999; Humayun 2001; Weiland 2010). Brightness of the phosphenes has been reported to depend on the stimulation protocol (pulse lengths, widths and frequency), the magnitude of the currents used in stimulation and the degree of cellular degeneration (Balthhasar, Patel et al. 2008).

There has been much debate over the optimal method that should be employed to elicit phosphene vision, both in terms of the location and implantation of the electrode array and the protocols used to drive the stimulating circuitry. The three primary strategies employed to induce a visual perception in a blind patient include direct stimulation of the visual cortices of the brain, stimulation of the pathway connecting the brain to the eye (optic nerve stimulation) and direct stimulation of the retinal tissue. Epiretinal, suprachoroidal and subretinal implantations all directly stimulate retinal tissue and will be discussed in detail individually, with each stimulation method having a unique set of advantages and disadvantages.
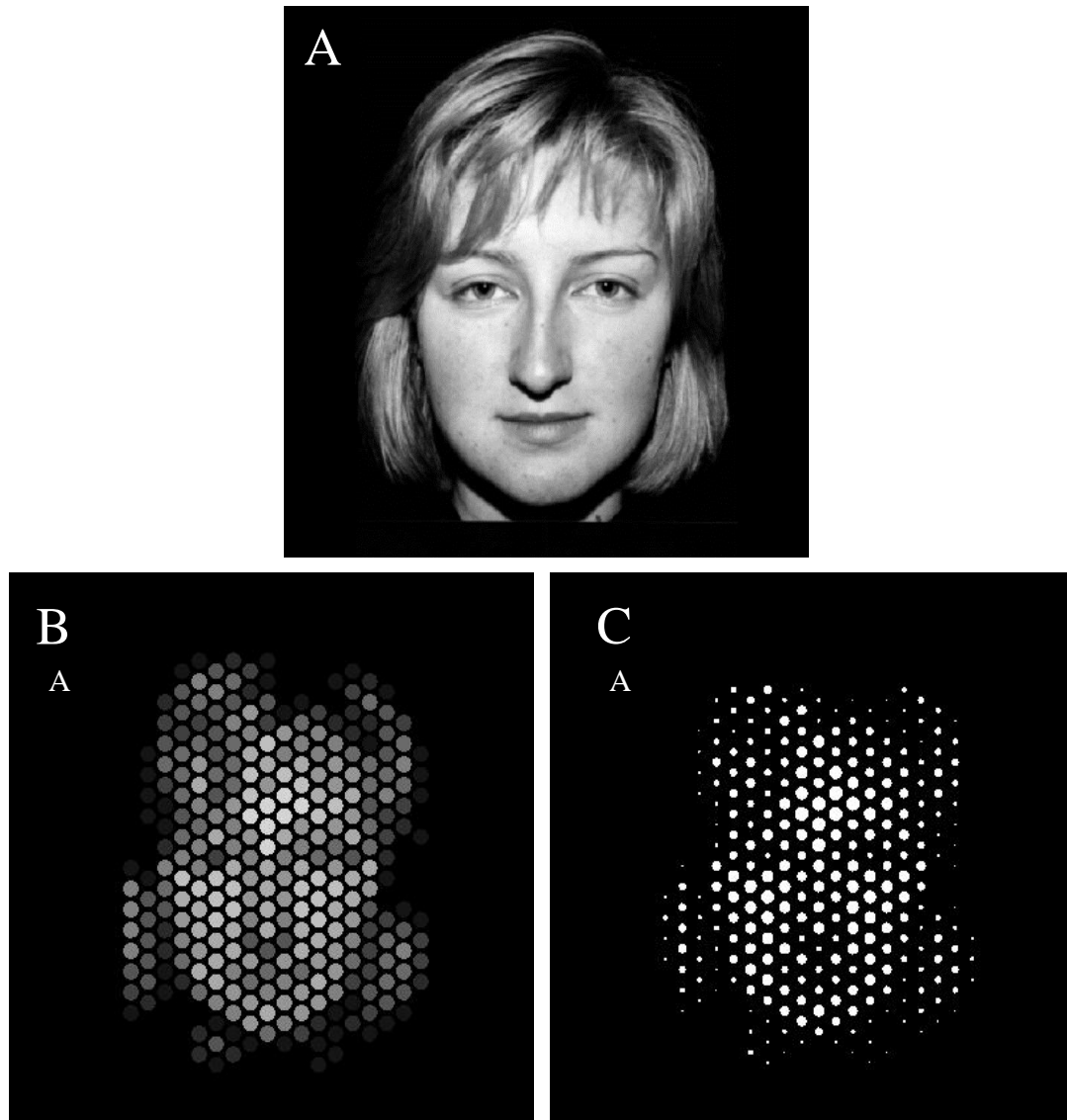
Figure 1.3. Possible phosphene vision indicating **(A)** normal vision of a ladies face, the same face produced by **(B)** phosphenes of varying brightness and **(C)** produced by phosphenes varying in size. (Image courtesy of Bionic Vision Australia)

1.3.1　　Cortical Stimulation

One of the earliest attempts to restore vision through cortical stimulation was performed by Brindley (1968), who implanted an 80-electrode device on the visual cortex of a 52 year old blind woman. Each of the 80 electrodes was connected by wires to a radio receiver, firmly attached to the patients' outer bony surface. To activate the electrodes and illicit phosphene perceptions, an oscillator coil was placed above a given receiver, activating the receiver via radio frequency and hence stimulating the cortex with the induced electrical current. While not all 80 electrodes could induce phosphene

perception, the 40 electrodes that could showed not only that electrical stimulation was possible, but that phosphenes could be discriminated according to relative positions within the visual field. Due to the large, surface attached electrodes, the visual acuity in these initial trials was poor and the potential for overstimulation to cause seizures was large.

By using smaller intracortical electrodes, currents of 10-100 times less than surface electrodes were achieved by Schmidt et al. (1996), who elicited phosphenes by inserting the microelectrodes directly into the visual cortex. Further studies by this group involved a four month implantation of a 38 electrode prosthesis into a ten year glaucoma-blind patient. Results indicated that the subject was able to perceive phosphenes predictably and reproducibly and could perceive patterns when the electrodes were concurrently stimulated.

The Dobelle Institute in Zurich, Switzerland, has been implanting patients with cortical prosthesis since the 1970's, with one subject who was implanted in 1978 due to trauma induced blindness still reported to have been using the prosthesis twenty years after the initial implantation (Dobelle, Mladejovsky et al. 1974; Dobelle, Mladejovsky et al. 1976; Dobelle 2000). This patient had a hexagonal array of 1 mm platinum electrodes (5 mm centre to centre spacing) implanted on the mesial surface of the right occipital lobe. When an individual electrode was stimulated with a biphasic pulse, numerous (one to four) closely spaced phosphenes were reported, suggestive that smaller electrodes would be beneficial to increase visual resolution. With scanning, the patient was able to routinely recognise a six-inch square tumbling E at five feet, Snellen letters, HOTV test letters, Landolt rings and Lea figures of a similar size, corresponding to a visual acuity of 20/1200. The percentage of his correct answers in these tests decreased rapidly as the letter size became smaller (or as the distance was increased), with a less than 60% correct and less than 20% correct answer rate for tumbling E tests performed at visual acuities of 20/1000 and 20/800 respectively.

One of the largest difficulties facing cortical prosthesis is the location, with much of the visual field buried in the calcacrine fissure. Further, the cortical crenulations create an uneven accessibility to parts of the visual field that is represented on the gyral and sulcal surfaces, and implants that are designed to stimulate tissue on only the exposed gyral tissue will miss a large fraction of the underlying visual field. While this can (to some extent) be controlled using stimulating electrodes of non-uniform length, a slow degradation has been shown to occur to electrodes implanted in the cortical surfaces, hypothesised to be due to micro-movements. This type of prosthesis is also expected to involve a large amount of complex neural encoding and would require gaze information when conveying images from a head mounted camera to the stimulating circuitry.

Stimulation of the 250 mm^3 lateral geniculate nucleus would remove some of the problems of attempting to provide accurate visual field representations on the uneven cortical surfaces, while still possessing the advantage of being feasible for persons suffering from glaucoma and optic nerve dystrophies. The surgical procedure for a thalamic visual prosthesis, similar those used for deep brain stimulation, involves the insertion of microelectrodes through a cortical burr hole and penetration through the cortex down to the level of the thalamus. A subcutaneous lead would be routed to a subclavicular or cranial stimulator to reduce the likelihood of infection through transcutaneous lead wires. Current animal experiments on monkeys have shown that brush microwires with eight stimulating electrodes have been successful in creating multiple individual phosphenes when stimulated sequentially (Pezaris and Eskandar 2009; Pezaris and Reid 2009; Pezaris 2010).

1.3.2   Optic Nerve Stimulation

As cortical stimulation requires implantation of electrodes directly in the visual cortex, the ability to harness the retinotopic map traversing from the retina to the cortex is lost. Further, any image processing occurring before or immediately after the electrode implantation sites are not utilised. Optic nerve stimulation is one method taking advantage of cortical processing, with electrodes implanted in the optic nerve directly stimulating ganglion cell axons prior to any cortical processing. This method, while not expected to be of advantage to persons with optic nerve damage (such as glaucoma), has indicated that spatial mapping of ganglion cell stimulation is well correlated with phosphene perceptions.

Electrical stimulation of the optic nerve in the pre-chiasmatic region posterior to the eye has been performed by Veraart (1998, 1999, 2003) and Brelen et al. (2010) using disk electrodes located on the inside surface of a cylindrical cuff implanted around the optic nerve. In 1998, a 57 year old patient, blinded by retinitis pigmentosa had a four contact, self-spiralling optic nerve cuff electrode implanted intercranially around the right optic nerve, with the neurostimulator implanted later in August 2000. The charge density used to stimulate the ganglion cell axons was always below 150 μC/(cm^2/phase) up to 50 Hz, corresponding to a charge per phase of 300 nC/phase with a contact area of 0.2 mm^2. Phosphenes produced by optic nerve stimulation was reported to consist of sets of 2 to 30 dots, arranged in rows, arrays or lumps of various colours with diameters ranging from 10 to 40 arc-minutes. The patient was able to distinguish between and locate a set of common objects (large and small bottle, cup, knife, CD case and a

toothpaste container) well above guess rate (Duret, Brelen et al. 2006). A three, 0.05 mm electrode optic nerve prosthesis has also been reported to produce yellow, round oval and linear phosphenes in a patient blinded by retinitis pigmentosa by Sakaguchi et al. (2009).

This approach, like the cortical stimulation regimen will not be able to make use of the processing ability of the retinal interneurons and is expected to require implantation techniques that are more invasive, increasing the surgical risk. The retinotopic organisation of the optic nerve is more difficult to utilise as the axons are bundled and the ability to insert enough electrodes to provide useful vision has yet to be shown. This type of stimulation will also require processing to allow for movement of the eyes (for a camera mounted on or connected to the head), and is limited to diseases that affect the eyes or photoreceptors only. Optic nerve stimulation, however, is expected to be very helpful in eliciting perceptions of visual space in those whom have suffered retinopathies and other diseases requiring the enucleation of one or both eyes.

1.3.3 Epiretinal Stimulation

An epiretinal prosthesis is aimed at generating phosphene vision by direct electrical stimulation of the ganglion cell layer, and although this strategy bypasses many of the retinal interneurons responsible for high performance vision, it is the visuotopic mapping of the retina onto the cortex that makes this method appealing. To enable a visual perception of the outside world, epiretinal prostheses will probably comprise of both an extraocular unit (including a camera for image acquisition, an image processor and a telemetry system) and a hermetically sealed intraocular unit. Telemetrically encoded power and data sent by radio frequency links to the intraocular components will be used to power the telemetry decoder and the stimulating chip that will inject currents of varying magnitudes through electrodes located adjacent to retinal cells (Suaning, Gill et al. 2003; Suaning, Hallum et al. 2004). The close proximity of the electrodes and stimulating circuitry to the delicate retinal neurons will require careful analysis of thermal energy dissipation from the implanted components to ensure cell damage is not magnified in the already diseased tissue. An image of an implanted, 60 electrode epiretinal visual prosthesis, used in current clinical trials, is shown in Figure 1.4.
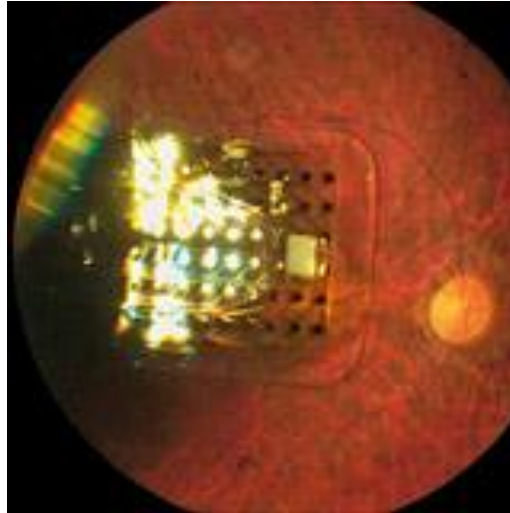
Figure 1.4. Photograph of implanted 60 electrode epiretinal prosthesis over the macular region in a patient with age-related macular degeneration. Image courtesy of Second Sight ® Medical Products, Inc.

The primary disadvantage of this method involves the mechanical anchorage of the implant and the long term stability of the interface at the inner retinal surface. The fragility of the retinal tissue makes the weight and inertial forces of the implant particularly detrimental and may lead to bleeding, retinal detachment and cellular overgrowth which would compromise the retinal-electrode interface (Normann, Maynard et al. 1996; Wyatt 1996; Rizzo and Wyatt 1997; Singh, Cela et al. 2007; Balthhasar, Patel et al. 2008). Anchorage of the implant has been trialled by different methods including retinal tacks (DeJuan, McCuen et al. 1986; DeJuan and Crittenden 1994), biocompatible glues (Hartnett and Hirose 1998; Lowenstein, Rizzo et al. 1999) and hydrogels (Rizzo, Socha et al. 1994), with much investigation still required to ensure a firm and lasting retinal-electrode contact.

Due to the positioning of the epiretinal implant, stimulation of ganglion cell somas are expected to coincide with activation of ganglion cell axons from peripheral retinal regions. This would be expected to lead to more diffuse perceptions, with microelectrode arrays being hindered by the co-stimulation of superficial passing axons. *In vivo* human trials, however, have indicated that this may not be the case (Humayun, Juan et al. 1996; Sekirnjak, Hottowy et al. 2008). Rattay (2004) has demonstrated through cellular modelling that threshold current requirements for perceptions to be elicited is lowest at the ganglion cell soma, (267 µA cathodic first pulse, -196 µA anodic first pulse) increasing in required magnitude along the cell axon (434 µA cathodic first pulse, -280 µA anodic first pulse, at a distance of about 300 µm). These results suggest that although there will be some level of axonal excitation, the ganglion cell somas will be excited by lower thresholds, and thus, it is possible to reduce the number of excited axons (and thus maximize the induced visual resolution) by using currents of lower magnitudes.

The initial clinical trial conducted by Second Sight using an epiretinal visual prosthesis began in 2002 and implanted six patients blinded by retinitis pigmentosa with a sixteen electrode device. The subjects have been able to detect motion and locate and discriminate between objects (cup, knife and a plate). Subjects have also been able to follow a white line painted on the floor and locate an open door (with a white frame) by scanning. The ability to discern the motion of a bar passed in front of a camera, correctly determine the orientation of a black and white grating pattern and discriminate between spatiotemporal pulse train patterns based on phase differences across electrodes has also been reported (Weiland and Humayun 2008; Horsager, Greenberg et al. 2010). More recently, Second Sight implanted 32 patients with a 60 electrode wireless device and reported that perceptions could be perceived from all patients. Patients were able to determine the location of a square (top left, top right, bottom left, or bottom right) with a 97% accuracy and could determine grating motion direction correctly in 57% of trials (Greenberg and Mech 2010; Weiland 2010).

Researchers at the Boston Retinal Implant Project have reported that elicited perceptions have some degree of controllability, with trials indicating that phosphenes could be induced by single electrode stimulations or multiple concurrent stimulations. By using 100 μm and 400 μm electrodes and charge injections ranging from 196 μA to 350 μA, they were able to produce perceptions at various positions within the visual field. Their findings, however, concluded that all injection thresholds required to induce phosphene perception in blind patients were over the safety limits (0.252 mC/cm^2), with ranges from 0.28 to 2.8 mC/cm^2 required (Shannon 1992). They also observed that larger pulse durations per phase required larger threshold charge densities, which could increase the thermal energy dissipated into the neighbouring retinal neurons (Wyatt 1996; Rizzo et al. 2003a; Rizzo et al. 2003b; Fried 2010; Rizzo 2010).

Epiretinal stimulation is one of the most advanced (in terms of clinical trials and commercialisation) and the ability to provide some useful vision with only sixteen to sixty electrodes is very encouraging for high resolution devices that aim at utilising 100's or 1000's of electrodes to provide facial recognition, the ability to read and to allow patients the ability to walk unassisted and unaided. 13 of the 22 groups worldwide are investigating epiretinal implantation as a means of visual restoration, with many of the groups expected to begin clinical trials within the next decade (Gerding 2008). Epiretinal implants could use vitreous fluid and choroidal perfusion as heat sinks to remove thermal energy generated by implanted chips. How effective the vitreous fluid is, and whether thermal damage thresholds are reduced when combined with mechanical stress (from implantation) and reduced choroidal blood flow (inherent in retinal diseases) is still unknown and may become a greater problem when electrode numbers (and hence power generated by the implanted chip) increase.

1.3.4 Subretinal Stimulation

Subretinal implants seek to stimulate the retina at its outer surface between the retinal pigment epithelium and the retinal photoreceptor layer, with current devices using both micro-photodiode arrays and electrodes (Chow and Chow 1998; Peyman, Chow et al. 1998; Gekeler, Schwahn et al. 2001; Sachs, Schanze et al. 2005; Schanze, Sachs et al. 2006; Gekeler, Szurman et al. 2007; Lovell, Morley et al. 2010; Rizzo 2010). Like the epiretinal prosthesis, the subretinal device will take advantage of the retinal, thalamic and cortical signal processing with direct preservation of the retinotopic organisation if the cells can be stimulated directly. It also has the added advantage that the prosthesis could be coupled to the eye movements controlled by the recti and oblique muscles, being of marked advantage if the recipients' eye motility functions normally.

A subretinal implant, located anterior to the choroid (still posterior to the retinal pigment epithelium) has the disadvantage that it may act to block nutrients from the choroid to the retinal tissue which could result in atrophy and necrosis of tissue in areas surrounding the implant (Rizzo and Wyatt 1997; Peyman, Chow et al. 1998; Gekler, Szurman et al. 2007). Whether this risk surpasses the benefit of not having to pass current through the choroidal blood supply (as is the case for suprachoroidal implants) is still in debate. Placing the electrodes closer to the bipolar cells (compared to an epiretinal approach) is expected to permit lower bipolar cell stimulus thresholds, reducing the total amount of charge (and hence power dissipation from the electronics) required for stimulation (Chow and Chow 1998; Chow and Peachey 1998; Zrenner, Stett et al. 1999).

The first clinical trial of a permanently implanted prosthesis was initiated by Optobionics, Inc., in 2000. Their subretinal prosthesis trials indicated that six people blinded by RP could pick out shapes and recognise faces after the implant of the micro-photodiode array, each containing 3500 micro-photodiodes per chip (Peyman, Chow et al. 1998; Gekeler, Schwahn et al. 2001; Rizzo 2010). The initial problem facing the subretinal prosthesis group was the lack of apparent power that could be transmitted through to the micro-photodiode electrode array, as the amount of light reaching the device is limited and was shown to generate insufficient current to stimulate adjacent cells, although this issue has since been revoked (Palanker, Vankov et al. 2005; Palanker 2010). The photodiodes, coupled to bipolar electrodes have proven to be electrically functional over the course of long term implantation in the subretinal space, although there was some degree of electrode corrosion and photoreceptor loss (10-15%) which consequently reduced the electrical functionality of the device five months after

implantation (Gekeler, Schwahn et al. 2001). It has been hypothesised that increasing the ratio of the photodiode area will overcome the devices sub-threshold charge injection and by manufacturing the micro-photodiode chip to allow fluid communication between the choroid and the retina, damage caused by nutrient blocking will be avoided. This will also allow the choroidal perfusion to remove any additional thermal energy dissipated by the chip, reducing the potential for tissue damage caused by thermal insult.

A subretinal prosthesis, implanted in twelve patients for four weeks developed by Retina Implant GmbH (Reutlingen, Germany), has shown some convincing results since their clinical trials began in 2006. Their patients were implanted with a 1500 photocell implant with 38×40 μm (72 μm separated) photodiodes coupled to an electrode array of 50×50 μm titanium-nitride (TiN) micro-electrodes on a polyimide substrate. The implant covers an area of 3×3 mm, with a visual field of approximately $11° \times 11°$. Perceptions of light in particular shapes and patterns, localisation and recognition of letters, objects and light sources (such as a lamp or window) and bright objects against a dark background have been reported. Horizontal lines, vertical lines and positions have been recognised by patients with selective brightness amplification, with Landolt rings of 0.9 cm observed at a distance of 62 cm, equivalent to a visual acuity of 20/1108 (Zrenner, Wilke et al. 2008; Zrenner 2010).

Advantages of the subretinal approach over epiretinal approaches include the ability to anchor the implant between the inner and outer retinal layers without requiring retinal tacks. This advantage, however, has the trade-off that stimulation strengths are likely to be higher due to the increased distance between the electrodes and the ganglion cells. The advantage of not blocking any incoming light to photoreceptors (as would be the case with an epiretinal implant) is also avoided, although initial patients are not expected to have any residual vision prior to implantation. Disadvantages of the implantation site do not exclude the danger of damaging cells when a foreign material is implanted behind the eye, both as a risk of infection and due to the additional volume of the implanted electronics although this has not been reported to be an issue.

1.3.5 Suprachoroidal Stimulation

A suprachoroidal implant technique, used to implant the electrode array between the sclera and the choroid is currently being developed by Bionic Vision Australia among other international groups (including the Vision Institute of Nidek). Due to the fragility

of the retinal tissue and the ease at which retinal detachment can occur through subretinal implantation, this method implants the electrode array beneath the choroid (as opposed to directly beneath the retinal pigment epithelium, as is the case with subretinal implants).

While surgical procedures are far simpler than both the epiretinal and subretinal methods mentioned (requiring only a small 5 mm incision 7 mm from limbus in which to slide the electrode implant into position) this location is expected to require larger currents to be passed through the choroidal vessels to stimulate remaining neurons (Yamauchi, Franco et al. 2005). This method of visual restoration will require biodegradable masks if penetrating electrodes are to be used to project through the choroid, with flat disk electrodes currently being trialled. The confines of the suprachoroidal space will limit the size of the electrode array stimulator, although as our device aims at combining the electrodes, stimulation and telemetry circuitry on a single chip, this may not be an issue.

Only one group (Vision Institute of Nidek) has implanted patients using suprachoroidal stimulation at the time of writing. They acutely implanted two patients using a suprachoroidal-transcranial stimulation technique and reported that while individual phosphenes could be elicited (having the appearance of a small bar or circle), the stability of the phosphene properties such as the brightness and threshold charge remained unclear (Terasawa 2010).

The anchorage of the suprachoroidal implant between the sclera and the choroid is advantageous over both the epiretinal and suprachoroidal methods, with the implant blocking neither incoming light to remaining photoreceptors or nutrients from the choroid to the retina. The surgical implantation has been shown to be very stable in acute and chronic *in vivo* cat experiments (Chapters 4 and 5). This is not only beneficial in reducing trauma caused by retinal tacks or inertial implant movement, but will also act to ensure that the implant will not move during stimulation which could blur the perceived image.

1.3.6 Comparison of Visual Prostheses

Each of the visual prostheses discussed have individual advantages and disadvantages, and it would not do any method justice to attempt to choose the best prosthesis. It is, however, important to extract the features of each design that are advantageous over other methods, with the choice of which prosthesis to be used dependant on the type and degree of disease and individual patient requirements.

For conditions or diseases that have interrupted the normal function of photoreceptors, each method can be used to restore lost vision. For conditions affecting the ganglion cells, an optic nerve or cortical prosthesis would be advantageous, with a cortical prosthesis optimal for conditions affecting the retina or optic pathway. Disadvantages of prosthesis that are closer to the visual cortex are predominantly surrounding the higher potential for serious damage to occur if the prosthesis or implanted components become sources of infection. Similarly, prostheses which have transcutaneous connections have a higher associated infection risk, although this has not been a problem reported by any of the groups so far.

The ability to utilise and harness the intrinsic retinal organisation and processing that occurs in the retinal neurons and along the optic pathway to the visual cortex is one advantage that retinal (and to some degree optic nerve) prostheses have over cortical designs, with the ability to provide spatiotemporal patterns that are replicated in the cortex suggested to be easier. The method of implantation is also a parameter which is advantageous to suprachoroidal prostheses, although the distance from the electrodes to the excitable tissue is greater. While subretinal and suprachoroidal implants may block nutrient supply to the retinal tissue, the stability of these implants is superior to epiretinal placement where saccadic movements and inertial forces have a greater potential to dislodge the device.

Advantages and disadvantages of each prosthesis type are listed in Table 1.1, listing the number of patients chronically or acutely implanted as of the end of 2010. Electrode numbers, diameters and implant abilities are also reported and relate directly to the devices used in clinical trials, not necessarily related to the most recent designs and ideas in each respective area. To date, the total number of implanted patients has been 62, with the majority of patients (38) having been implanted epiretinally by Second Sight and subretinally (18 patients) by the German group at the University of Tubingen.

While there is much debate over whether there should be standardised tests to evaluate the visual prosthesis performance between each group, the ability to construct tests that are also beneficial to patients' vision is yet to be achieved. Current measurements such as Landolt rings and Snellen letters provide a good inter-method comparison, although the potential for this to be useful to persons with a visual implant has been argued to be a poor use of clinical testing time with minimal benefit to prosthesis users.

As the requirement for enhanced resolution increases, the power generated by the implanted chips to steer currents or to supply more electrodes will also increase, and this may increase the neural tissue temperature beyond a safe level, regardless of the implant location. Knowledge of the thermal damage thresholds of retinal and neuronal tissue can be used in combination with simulations investigating the effects of disease induced reductions in blood perfusion, alterations in thermal conductivities and the ability to remove thermal energy as well as increases in power consumption and dissipation by implanted chips and electrodes to ensure visual implants do not cause or exacerbate implant safety or functionality.

Table 1.1. Comparison between cortical, optic nerve, epiretinal, subretinal and suprachoroidal implants designed to restore vision, indicating current visual restoration abilities, implant designs, advantages and disadvantages of each implant type.

	Cortical (Dobelle 2000)	Optic Nerve (Brelen et al. 2010)	Epiretinal (Weiland 2010)	Subretinal (Zrenner 2010)	Suprachoroidal (Terasawa 2010)
Current Stage	Chronic Human (n=2)	Chronic Human (n=2)	Chronic Human (n=38)	Acute Human (n=12), Chronic Human (n=6)	Acute Human (n=2)
Abilities	Snellen letters, (20/1200), finger count, Braille	Object localisation and discrimination	Object localisation and discrimination, grating orientation, motion direction, unaided navigation, letters and short words, basic colour, track following	Shapes and object localisation and discrimination, Snellen letters (20/1108), facial and pattern recognition and orientation, motion direction	Basic two choice discrimination
Power / Data Link	Subcutaneous	Wireless	Subcutaneous (n=6), Wireless (n=32)	Wireless (photodiode)	Subcutaneous
Electrode Number	64	4	16 (n=6), 60 (n=30)	1500 (n=18)	84
Electrode Diameter	1 mm	3 mm	260 μm and 580 μm	50 x 50 μm	125 μm, 160 μm and 395 μm
Electrode Spacing (Centre-Centre)	Hexagonal, 5 mm	Varied	600 μm	50 μm	Varied
Electrode Type	Disk	Cuff, Penetrating	Disk	Disk	Disk
Disease Coverage	All global, retinal and optic tract	All global and retinal	Photoreceptor	Photoreceptor	Photoreceptor
Implant Obstructions	None	None	Light	Blood / Nutrients	None
Comparative Surgical Difficulty	Difficult	Medium	Difficult	Difficult	Easy
Serious Infection Risk	High	Medium	Low	Low	Low
Utilises Retinotopic Map	No	No	Yes	Yes	Yes
Utilises Retinal Processing	No	No	Yes	Yes	Yes
Device Processing Ability	Poor	Poor	Good	Good	Good
Electrode Array Anchorage	None required	Self sizing cuff	Retinal tacks, and glues, implant holes	None required	None required
Device Stability	Good	Good	Poor	Good	Good
Thermal Heating Risk Areas	Visual cortex	Optic nerve	Retinal neurons	Retinal neurons	Retinal neurons
Possible Heat Removal Methods and Heat Sinks	Cortical perfusion	Extra-orbital fat	Choroidal perfusion, vitreous humor	Choroidal perfusion	Choroidal perfusion, extra-orbital fat

1.4 ELECTRODES

One of the only features of a visual prosthesis that is uniformly accepted is the requirement that a large number of phosphenes will be required for vision suitable for reading, walking unaided and facial recognition. This will require a large number of electrodes in combination with advanced stimulation techniques. Normal 20/20 vision corresponds to an angular separation of lines by 1 minute of arc, or a spatial separation on the retina of about 10 μm which would require 5 μm electrodes (Smith and Atchison 1997; Butterwick, Vankov et al. 2007). These electrodes, expected to induce phosphene perception similar to the method in which a computer screen portrays an image using individual pixels, have been suggested to be required in numbers of at least 300 to 625 for resolving images in the visual field (Margalit, Maia et al. 2002; Eckhorn, Wilms et al. 2006). These results are similar to numerical calculations indicating the need for between 600 and 1000 electrodes to restore visual function to a level that will allow the blind to read, navigate a room unaided and recognize faces (Cha, Horch et al. 1992; Cha, Horch et al. 1992; Hayes, Yin et al. 2003; Sivaprakasam, Liu et al. 2005), with 625 electrodes implanted in a 1 cm^2 area near the fovea, expected to be able to produce a phosphene vision acuity of 20/30 (Margalit, Maia et al. 2002).

To produce perceptions that do not flicker, stimulation rates of 40-60 Hz are required (Humayun, DeJuan et al. 1999; Humayun 2001; Chen, Lovell et al. 2004; Hallum, Lovell et al. 2005; Sivaprakasam, Liu et al. 2005), decreasing with increasing age at a rate of approximately 0.059 Hz/year (Eisenbarth, MacKeben et al. 2008). Due to the majority of persons that would require a visual prosthesis being elderly, this may allow slightly slower stimulation rates (~5 Hz). Powers required by implanted electronics will be highly dependent on the stimulation strategies employed, the location of the chip and circuitry in relation to the retinal tissue and the amount of electrodes to be stimulated, with the type of electrode used (size and material) and their proximity to the cells to be stimulated also imposing limits on prosthesis design (Weiland, Humayun et al. 1999; Merrill, Bikson et al. 2005; Palanker, Vankov et al. 2005; Sachs, Schanze et al. 2005; Schanze, Sachs et al. 2006; Loudin, Simanovskii et al. 2007; Balthhasar, Patel et al. 2008).

When these stimulation rates are coupled with the large number of pixels (or electrodes) requiring simultaneous stimulation (and thus a large power requirement) and a daily usage of between 12 and 18 hours, the effect that dissipated thermal energy will have on retinal tissue is of great concern. A calculation performed by Weiland and Humayun

(1999) indicated that for a tissue impedance of 30 kΩ and a 100 µA stimulation current, a power of 300 mW would be present on the 1000 electrode surface (if all used simultaneously). Even with pulses at 60 Hz/second with a 1 ms biphasic pulse phase, the power requirement for stimulation would be 36 mW. The potential for powers of this magnitude to thermally damage the neural tissue or exacerbate mechanical trauma caused by implantation is a serious concern and may alter the ability of patients to achieve high resolution vision. Calculations performed by Butterwick et al. (2007) indicated that the temperature increase on at the surface of a 0.5 mm^2 electrode after a single 1 ms pulse with a 1 A/cm^2 current density would be 0.017°C. For chronic stimulation (25 Hz repetitive pulses) the temperature increase was 0.22°C. They further suggested that charge will not be conserved along the strength duration curve and that the ratio of damage thresholds to stimulation thresholds will depend on the pulse duration.

Figure 1.5, produced by Palanker at al. (2005), indicates the relationship between electrode size and visual acuity, ensuring that the induced retinal tissue temperature increase remains below 1°C. This shows the potential of large electrodes in close proximity to retinal neurons, aimed at producing high levels of perception to cause thermal damage (Palanker, Vankov et al. 2005; Loudin, Simanovskii et al. 2007).
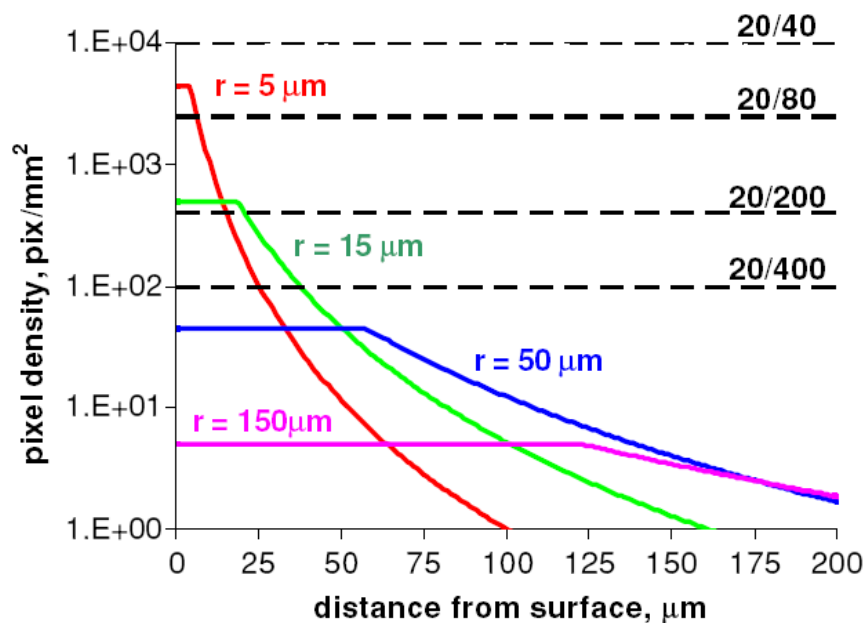
Figure 1.5. Maximal pixel density in a 3 mm implant to keep heating below 1°C with 1 ms pulses applied at repetition rate of 50 Hz via IrO$_x$ electrodes. The horizontal segments on each curve represent packing density limit, corresponding to the electrodes separation by a radius. Image used with permission from Palanker et al. (2005)

A 20/20 vision, which can resolve differences of 1/60 of one degree of visual angle, translates to 5 µm on the retinal surface, and thus vision of this acuity could require electrodes of this size or smaller. Smaller electrodes are advantageous in allowing higher resolution when in close proximity to the retinal neurons, but larger electrodes would be advantageous as the distance increases as the thermal energy would be more widely distributed. It has been reported however, that in order to stimulate neural tissue 40 nC was required, irrespective of electrode size (using 520 µm and 260 µm diameter electrodes), suggesting that as the electrodes get smaller, if the charge required doesn't change, the electrode will be damaged with the charge per unit area exceeding the safe limit thresholds (Weiland 2010).

Current electrode arrays fabricated by The University of New South Wales for suprachoroidal implantation have thicknesses ranging from 50 µm to 200 µm, with thinner implants (<100 µm) requiring an introducer to avoid implant buckling. These electrode arrays are designed to accommodate 98×250 µm diameter platinum electrodes with a centre to centre spacing of about 582 µm. The total width of the array is approximately 7.4 mm, with a total active area (area covered by electrodes) approximately 4.8 mm^2. To investigate the ability of retinal tissue to tolerate thermal insult, a heating element similar to this design will be constructed (Chapter 3) and used in cadaver tissue experiments (Chapter 4) and *in vivo* cat experiments (Chapter 5).

1.5 THERMAL HEATING

As the number of patients receiving visual prosthesis increases and the insight into the resolution required to produce useful vision is better understood, it is becoming increasingly clear that a small number of electrodes will not be sufficient to provide patients with the ability to read, recognise faces and walk unassisted and unaided.

Glial scars that form around tissue in contact with foreign materials such as electrodes and retinal tacks are expected to elevate the charge required to induce neural stimulation (Ohira et al. 1991; Seese et al. 1998; Seo et al. 2006; Colodetti et al. 2007; Ray et al. 2009). While a reduction in the currents required to excite cells to threshold will be reduced by reducing the distance between the electrodes and the cells, a larger number of electrodes will still require greater amounts of power to be generated by the implanted stimulating circuitry. The downside to this is the potential for large power dissipations in close proximity to delicate neural tissue to cause thermal damage. When this increase in power is coupled with a flicker frequency of around 50 Hz and an expected daily operation potentially greater than 18 hours per day, the ability to ensure thermally induced heating is below the threshold for damage is a real challenge.

Although most current retinal implants used by the blind community require a transcutaneous data and power link, future generations of the design are aimed at being entirely wireless. Not only will this increase the ability of the prosthesis to use natural eye tracking mechanisms without potentially causing damage to either the lead wires or the tissue surrounding the wire insertion point, but will also reduce the likelihood of intraocular infection. The performance of the inductive link is related to the power transfer efficiency (a measure of how well the primary and secondary coils are coupled), the driving efficiency and the carrier-modulated bandwidth, with the amount of power dissipated by the prosthesis highly dependent on a number of inductive parameters including the coil geometry (Zierhofer and Hochmair 1997; Kendir, Liu et al. 2004; Kendir, Liu et al. 2005), carrier frequency (Ko, Liang et al. 1977; Suaning and Lovell 2002), coil separation distance (Flack, James et al. 1971; Ko, Liang et al. 1977), number of coil turns (Donaldson and Perkins 1983; Kim, Zoschke et al. 2006) and the angular alignment and the amplifier choice of the wireless inductive link (Wang, Liu et al. 2004).

Many groups have been designing wireless devices for retinal prosthesis with small differences in their designs having large deviations in the amount of power that can be

transmitted as well as the expected amount of power dissipated in the tissue (Wang and Fujiwara 1999; Kendir, Liu et al. 2004; Wang, Liu et al. 2004; Kendir, Liu et al. 2005; Kim, Zoschke et al. 2006; Zhou, Liu et al. 2006; Zimmerman, Chaimanonart et al. 2006; Soora, Gosalia et al. 2008). Kendir et al. (2004, 2005) has reported that the link used by his group can deliver smart bi-directional telemetry powers of 250 mW over 7 mm with a 67% efficiency. Liu et al. (2005) calculated that for a 100 electrode device receiving 100 frames/sec with a data rate of 40 kbps, a total dissipation would be 5 mW, and suggested that an increase in power caused by the primary coil moving closer to the secondary coil will result in the dissipation of additional power in the tissue as heat, which should be avoided. Their colleagues have computationally demonstrated that a 0.25 mm gauge gold coil imitating a wireless receiver located in place of the lens carrying 150 mA, would dissipate 984 µW and would increase the neighbouring tissue in excess of 0.4°C. While this may not be low enough to ensure retinal damage is avoided, the placement of the current carrying coils in the lens and away from the delicate neural tissue was reported to reduce the temperature increase of the retina to 0.025°C (Bashirullah, Liu et al. 2003; Lazzi 2005).

Although the ability to ensure a retinal implant does not cause apoptosis or necrosis is one of the main priorities in ensuring permanently implanted retinal prostheses are safe, it should be mentioned that the effectiveness of a prosthesis that causes large thermal increases (short of the threshold for cell death) will also be reduced. Studies performed on the effects of temperature increases on brain tissue have indicated that changes in cell excitability are evident at an increase of 0.5°C and that changes in network function and blood brain barrier function can occur at increases of 1°C (Hoffman and Dionne 1983; Moser, Mathieson et al. 1993; Elwassif, Kong et al. 2006). Low temperature increases over a sustained period (up to 3°C) have also been observed to cause profound deleterious effects on brain function, causing mild localized hyperthermia and myelin degradation (Sharma and Hoopes 2003; Elwassif, Kong et al. 2006). Studies have shown that even hyperthermia's too mild to produce heat stroke can produce long lasting neurological deficits (Chia and Teo 2003) and pathological changes in the brain (Sharma and Hoopes 2003) with even mild thermal elevations, which by themselves are not sufficient to produce neuronal death, are able to exacerbate the delayed neuronal death following an ischemic insult. White et al. (2007) has indicated that the five major effects heat can have on tissue, including damage to proteins, mitochondrion, DNA, cytoskeletal molecules and cation channels. This indicates the requirement of a stain or damage analysis method to be able to detect damage occurring over a range of cellular components and pathways.

Temperature changes affecting cell membranes and pump kinetics (Klee, Pierau et al. 1974; Fujii and Ibata 1982; Rodrigues, Sigg et al. 1998; Fujii, Sasaki et al. 2002;

Kiyatkin 2007) can reduce the synaptic efficacy, affecting firing thresholds, peak firing rates (Hirsch, Appleton et al. 1977; Wasowicz, Morice et al. 2002; Elwassif, Kong et al. 2006) and may cause reductions in the amplitudes and durations of elicited action potentials (Sykes, Robison et al. 1981; Lint, Norren et al. 1992; Moser, Mathieson et al. 1993; Caprioli, Kitano et al. 1996; Vizi 1998; Stiles, Kovyanzina et al. 1999; Kim, Park et al. 2006) This not only reiterates the importance of conducting temperature measurements for the safety of the patient, but also to ensure the efficacy of the implanted device.

Studies performed to investigate the tolerance of tissue to thermal increases can be divided into four groups, lasers and electromagnetic irradiation, conductive thermal transfer, incubation and other heating mechanisms such as ultrasound and drug administration. While the studies relating thermal damage to direct, conductive heat transfer are the most appropriate and similar to a retinal prosthesis, this type of induced damage also has the least amount of publications and literature, especially for retinal tissue. For this reason, other studies have been investigated, with comparisons made between the temperatures that have been reported to be safe and those which result in permanent damage.

1.5.1   Conductive Thermal Damage

Visual prostheses which implant the stimulating circuitry directly into the orbital cavity in close proximity to the retinal neurons have the greatest potential to cause thermal damage. The epiretinal implant considered by Bionic Vision Australia aims at attaching the stimulating circuitry directly to the penetrating electrode array, and must be carefully designed to ensure neither power from wireless transmission or from conduction of dissipated heat from the implanted electronics can adversely affect retinal tissue.

Australian and international guidelines impose a temperature increase threshold of 1-2°C for the body core, similar to the European Standard (BS EN 45502-1:1998), which imposes a 2°C limit above the surrounding body temperature on any outer implant surface (AS-EN 2002; AS-ISO 2003; Singh, Cela et al. 2007). Determination of the amount of power a retinal prosthesis requires and will dissipate into neighbouring tissue will assist in optimising implanted circuitry to ensure these limits are not breached and thermal damage is avoided.

Sivaprakasam et al. (2005) have reported that their variable range biphasic stimulator would require an energy consumption of 500 µW in order to produce a 600 µA biphasic pulse train with 8×1 ms anodic and cathodic pulses. Power calculations have been performed by DeMarco and Lazzi (2003) indicated that a 60 electrode stimulator chip (5.5×5.35 mm) occupying the central position in the eye, would have thermal losses equivalent to 9.1862 mW for a 400 µA current supplied by 1 ms biphasic pulses at 50 Hz, and 46.4672 mW for a 600 µA current supplied by 3 ms biphasic pulses at 60 Hz. Scribner et al. (2007) indicated that a retinal prosthesis device based on CMOS technology would dissipate between 30 and 72 mW, with a 5V DC input and 32 Hz frame rate, increasing the temperature of a 300 ml saline bath by 1.2°C and 0.6°C for 3200 pixels with 1 µA stimulation, 0.8°C and 0.5°C for 0.5 µA stimulation currents and by 0.6°C and 0.3°C for 0 µA stimulation currents measured at the front and back of the implants respectively.

One of the earliest publications relating to direct, internal, conductive thermal heating was performed by Rawson et al. (1967, 1969) who implanted plate heaters in the abdominal muscles of sheep. After 60 days (without heating), the heaters were encapsulated in a tough, pale yellow, fibrous avascular tissue. After 18 days with the plate heaters set to 42°C and 45°C, enlarged venous channels were observed and the heaters were encapsulated in deep red, highly vascularised connective tissue. From these observations, it is expected that the implantation of a visual prosthesis into the retina will induce a cellular response and that the combination of thermal and mechanical traumas will exacerbate the damage caused. Rawson at al. (1973) also observed that abdominal heating of monkeys and sheep using an implanted 44°C thermode would rapidly induce changes in metabolic heat production. If thermal energy dissipation from implanted circuitry also increases the amount of metabolic heat generated, the potential to breach a thermal damage threshold will increase.

Using an etched foil conductive heating element (1 mm diameter encapsulated in polyimide), Goldblatt et al (1989) heated the retinal tissue of 38 rabbits. He observed that a heating element temperature of 45°C could be tolerated for 45 minutes by the eye with no histological or electron microscopically visible damage (observed after one week). No damage was observed one day after 15 minutes of heating at 45°C, with the first observable change (45°C for 15 minutes) being slight stromal oedema. With temperatures of 52°C, immediate collagen changes and disorganisation were observed (after 15 minutes) with 45 minutes at 52°C enough to induce stromal destruction. Necrosis was observed after 15 minutes of heating at 59°C, observed after one day. While these temperatures are greater than would be reasonable for a retinal implant, the duration of the heating is much shorter than for a permanently implanted prosthesis. Whether the duration of stimulation is a large factor limiting the magnitude of the

induced thermal elevation needs to be investigated, and experiments designed to assess the safety of retinal implants should be conducted over a similar time scale (at least 18 hours).

Using disk heaters implanted in the latissimus dorsi muscles of Holstein calves, Seese et al. (1998) observed that a 43°C heater would induce a 2.4 mm necrotic region surrounding the implant after 2 – 4 weeks. After 6 weeks, however, the necrotic region had decreased to 1.1 mm and the temperature of the heating element (supplied by a constant power source delivering a uni-directional 0.08 W/cm^2 heat) was measured to have reduced to 42.1°C. This was attributed to increased vascularisation surrounding the implant. Whether increased vascularisation will also be present in implanted retinas has yet to be investigated, although this may greatly increase the amount of power that can be dissipated by the visual prosthesis circuitry. Damage was also observed by Colodetti et al. (2007, 2009) to be associated with mechanical trauma caused by implantation, with damage observed only when an implant was in contact with the retinal tissue.

One of the few retinal thermal safety experiments that has been conducted *in vivo* was performed by Piyathaisere et al. (2003), who observed that a 1.4 × 1.4 × 1.0 mm, 240 Ω resistor measured at a temperature of 77°C when dissipating 500 mW, could be tolerated in the mid-vitreous region for 2 hours with no histological sign of tissue damage. This caused a retinal temperature increase 2°C to 3°C above normal, again without causing tissue damage. When direct contact with the retinal tissue was made however, even a one second touch of a 50 mW probe (25.5 mW/cm^2) would immediately whiten the retina (indicating severe damage), with 100 mW touches still visible after a month. While a retinal implant that can operate for less than one second prior to causing damage is highly impractical, this study is one of the only published works that investigates the effect of direct contact to retinal tissue by an implanted heating element. Their group have since theoretically calculated that the maximum temperature increase due to a 60 electrode array in contact with the retina driven by biphasic pulses of 60 µA was found to be less than 0.01°C, with a secondary coil carrying 150 mA and dissipating about 1 mW. Their 50 mW dissipating integrated circuit caused a retinal temperature rise of 0.45°C and a temperature increase to the surrounding tissue of 3.5°C (Singh, Cela et al. 2007). Numerical, iterative, thermal simulations suggest that an intraocular temperature increase of 0.4°C to 0.6°C in a chip positioned at mid-vitreous and approximately 0.2°C at the retinal surface would result from power dissipation from a 60 channel stimulator implanted in an anatomically derived 0.25 mm head and eye model (DeMarco, Lazzi et al. 2003).

To ensure thermal damage studies are as accurate as possible, experiments need to be performed *in vivo.* A study performed by Kim et al. (2007a, 2007b) and Harrison et al.

(2007) implanted a 5×6 mm microheater dissipating between 0 and 40 mW directly on the cortical surface of a cat. Temperature increases of 0.067°C/mW and 0.050°C/mW were measured for *in vitro* and *in vivo* conditions, respectively. They attributed the 22% lower temperature increase observed during *in vivo* measurements to the effect of blood circulation removing heat away from the cortical tissue. As they used an infra-red camera, they were unable to measure the effect of the implant with the scalp attached and heat is expected to have convectively escaped.

Inconsistencies when using different damage measurement techniques have been observed by Nakauchi et al. (2007). Using ophthalmoscopy, a conductive damage threshold of -0.614 mA/ms was observed, compared to a -0.517 mA/ms threshold observed using fluorescein angiography. This research indicates the importance of damage assessment selection, and the potential for damage to be obscured and missed if the method of analysis is inappropriate.

Much of the research conducted to investigate thermal elevations in tissue, have used models to determine the effects of heating. Many models use the Pennes bioheat equation

$$\underbrace{C\rho\frac{\partial T}{\partial t}}_{\substack{\textit{Thermal}\\\textit{Elevation}}} = \underbrace{\nabla.(K\nabla T)}_{\substack{\textit{Thermal}\\\textit{Spatial}\\\textit{Diffusion}}} + \underbrace{A_0}_{\substack{\textit{Tissue}\\\textit{Metabolism}}} - \underbrace{B_0(T-T_0)}_{\substack{\textit{Blood}\\\textit{Perfusion}\\\textit{Coefficient}}} + \underbrace{\rho SAR + P_{electronics}}_{\substack{\textit{External}\\\textit{Heat}\\\textit{Sources}}}$$

(1.1)

where the thermal elevation of the tissue (related to the specific heat of the tissue, C [J/(kg °C)], the density of the tissue, ρ (kg/m^3), temperature, T (°C), and the time, t) is determined as the sum of the thermal spatial diffusion (which involves the thermal conductivity of the medium, K [W/(m °C)], the heat generated by tissue metabolism, A_0 (W/m^3), the electromagnetically generated and absorbed power, ρSAR (W/m^3), and the power dissipation from the electronics, $P_{electronics}$ (W/m^3), minus the heat removed by blood perfusion (where B_0 is the blood perfusion rate [W/(m^3 °C)], and T_0 is the arterial blood temperature(°C)). While Eq. (1.1) has been used by many groups to investigate thermal damage thresholds, almost none of these studies have performed *in vivo* or even *in vitro* testing of their models, and assume that the retina is homogenous (both neglecting various cellular components and spatial differences), and perfect without degenerative diseases or other conditions which may interfere with the ability of the eye to remove excess heat (Scott 1988; Okuno 1991; Hirata, Ushio et al. 1999; Wang and Fujiwara 1999; Hirata, Matsuyama et al. 2000; DeMarco, Lazzi et al. 2003; Gosalia, Weiland et al. 2004; Hirata 2005; Hirata, Fujimoto et al. 2006; Flyckt, Raamakers et al. 2007; Ng and Ooi 2007; Ng and Ooi 2007). The ability to verify the model findings with experimental results is of great importance, especially in the case of a visual

prosthesis where small differences may result in diminished prosthesis function and increased cellular death.

Acute and chronic thermal damage research that investigated induced temperature elevations directly through conductive heat transfer or mechanical damage associated implantation are listed in Table 1.2.

1.5.2   Thermal Damage from Lasers and Electromagnetic Irradiation

Many measurements and studies have looked at the effect of thermally induced damage to retinal tissue using lasers and electromagnetic irradiation over a range of intensities and wavelengths. The three principle components thought to be responsible for laser induced reactions include thermal, mechanical and electromagnetic effects. The most relevant mechanism of thermal damage is that of photo-oxidative (photochemical) damage (Marshall 1969). This results when an incident light reacts with endogenous chromophores in the ocular tissue (photoreceptor visual pigments, heme proteins, flavoproteins and melanin and lipofuscin in the retinal pigment epithelium) causing a chemical change un-related to a thermal increase in the irradiated tissue (Glickman 2002).

Thermal damage caused by laser irradiation has been documented to occur at temperature elevations of 10-20°C, with effects including alterations in the genetic apparatus of cells, inactivation of enzymes and denaturation of proteins and nucleic acids which leads to necrosis, homeostasis and coagulation (Krauss, Puliafito et al. 1986; L'Esperence 1989; Glickman 2002; Carroll and Humphreys 2006; Chen, Thomsen et al. 2006; Lund 2006).

Table 1.2. Published data on thermal damage caused by conductive heating devices

Author	Model		Measurement Device		Test				Endpoint
	Animal	Tissue	Temperature	Analysis	Heater	Temperature (°C)	Power	Time	
(Rawson, Hardy et al. 1967)	Sheep (n=2)	Abdominal	Electronic temperature sensor	Histology (H&E)	Plate Heater, 5.1 x 15.1 x 0.64 cm	Control	-	60 d	Encapsulation of heaters in tough, pale yellow, fibrous, avascular tissue
						42	-	18 d	Enlarged venous channels, heaters encapsulated in deep red highly vascularised connective tissue envelopes
						45	-	18 d	
(Rawson, Quick et al. 1969)	Sheep (n=1)	Abdominal	-	-	Plate Heater 150 cm^2	+1.5	22 W	30 min	Increase in respiratory evaporative heat loss and respiratory frequency
(Adair and Rawson 1973)	Sheep (n=3), Squirrel Monkey (n=3)	Abdominal	Thermocouple	-	Thermode	44	20 W	220 min	Changes in metabolic heat production
(Goldblatt, Finger et al. 1989)	Rabbit (n=38)	Eye, retina	Thermocouple	Histology, electron microscopy (time 0, 24h and 1 week)	Etched foil conductive heating element (75Ω), 1 cm diameter, >1 mm thick encased in polyimide	38	-	5 min	No damage measured 1 week post
								15 min	
								45 min	
						45	-	5 min	
								15 min	
								45 min	Stromal oedema measured 1 day post
						52	-	5 min	Immediate collagen change and disorganisation 1 day post
								15 min	Immediate superficial stromal changes and disorganised stroma 1 day post
								45 min	Stromal destruction and vacuolisation 1 day post
						59	-	5 min	Stromal destruction 1 day post
								15 min	Damage characterised by necrosis 1 day post
								45 min	
(Seese, Harasaki et al. 1998)	Holstein Calves (n=15)	Latissimus Dorsi Muscle	Thermistors (0, 1, 3 and 7 mm from heater)	Histology (H&E, Trichrome, PCNA, Elastic Van Giesen)	Disk Heater	43.0 ± 2.2 (initial), 42.1 ± 0.2 (final)	0.08 W/cm^2	2 -4 wks	2.4 ± 0.8 mm necrotic tissue adjacent to implant
								6 wks	1.1 ± 0.5 mm necrotic tissue adjacent to implant

Table 1.2 (cont'd). Published data on thermal damage caused by conductive heating devices

Author	Model		Measurement Device		Test				Endpoint
	Animal	**Tissue**	**Temperature**	**Analysis**	**Heater**	**Temperature (°C)**	**Power**	**Time**	
(Piyathaisere, Margalit et al. 2003)	Canine (n=15)	Retina, Mid-Vitreous	Type-T thermocouple (0 and 6 mm from heater)	Fundus Photography, Electroretinography, Histology	240Ω Resistor, 1.4 x 1.4 x 1.0 mm	-	50 mW (retina)	1 s	Immediate subtle retinal whitening and mild changes in retinal pigment epithelium, no histological damage at 4 weeks post
						-	500 mW (mid-vitreous)	1 s	Full thickness retinal disorganization and disruption of the retinal pigment epithelium with mild pigment migration
						+2 retina, +5 vitreous	100 mW (mid-vitreous)	2 h	No damage. Slight reduction in ERG a and b waves at 1 week, returning to normal thereafter, no histological damage
(Kim, Tathireddy et al. 2007)	Cat	Cortex	IR Thermal Imaging Camera	-	5 x 6 mm microheater	+1 to +2	0 to 40 mW	-	Temperature increased by 0.067°C/mW for *in vitro* and 0.050°C/mW for *in vivo* measurements
(Nakauchi, Fujikado et al. 2007)	Dutch Rabbits (n=18)	Eye	-	Ophthalmoscopy	Electrode, 100 μm diameter, 20 Hz biphasic pulse	-	2.5 mA, 0.25 μC/phase	0.1 ms	Threshold (-0.614 mA/ms) determined by appearance of whitish spot around the electrode
							1.5 mA, 0.38 μC/phase	0.25 ms	
							1.0 mA, 0.5 μC/phase	0.5 ms	
							0.6 mA, 0.6 μC/phase	1.0 ms	
				Fluorescein Angiography	Electrode (as above)	-	1.6 mA, 0.16 μC/phase	0.1 ms	Threshold (-0.517 mA/ms) determined by appearance of dye leakage or hyper-fluorescence around retinal area where electrode was placed
							0.9 mA, 0.23 μC/phase	0.25 ms	
							0.6 mA, 0.3 μC/phase	0.5 ms	
							0.5 mA, 0.5 μC/phase	1.0 ms	
(Colodetti, Weiland et al. 2007; Ray, Colodetti et al. 2009)	Long-Evans Rat (n=20)	Eye	-	Histology (GFAP, H&E)	Electrode (9.35×10⁻⁵ cm² surface area)	-	No Contact	-	No Damage.
							No Contact, 0.09μC/ phase		
							Contact	-	Damage. Thinning of outer and inner nuclear layers
							Contact, 0.09μC/phase		

One of the primary concerns with correlating laser damage to damage that has occurred by conductive means (via an implanted prosthesis) are differences in absorption by the different tissues found within the eye. With a multi layered structure such as the eye, the potential for laser radiation and energy to penetrate through some layers to be absorbed by others could induce erroneous calculations of temperatures if one assumes that all the delivered power has induced thermal heating in one particular layer or structure. The potential for scattered energy to be absorbed by structures that are not directly in the path of the laser can also contaminate results, producing a wider region of heating (and potential damage) than would be expected.

A non-linear relationship between retinal injury and measured temperatures was observed by Welsh (1984), who used 488 nm Argon and 647 nm Krypton lasers to irradiate retinal tissue in over 60 Rhesus monkeys. Ophthalmoscopy was used to determine the threshold temperature at which thermal lesions were observed, with their results not displaying a linear correlation between the induced lesion size and either the temperature increase or the power used in the tests. His study used powers ranging from 7.5 mW to 142 mW and irradiation times between 0.002 and 1000 seconds, with temperature increases ranging between 8.5°C and 46°C as measured by a thin film thermocouple placed in the vitreous, 100-200 μm from the retinal surface.

This data is contrary to a report written by Marshall (1969) who also investigated the effects of dosage rate on rabbit retina lesion size using a 694.3 nm Ruby laser with a 100-800 μm spot size. He investigated the differences that occurred in lesion size between power absorption and incident energy, measuring the size of the induced lesions using histology (using a Toluene Blue stain). The increase in lesion size based on incident energy and the power absorbed were both reported to be linear.

Data from Welsh et al. (1984) is also contrary to recent studies performed by Jain et al. (2008) who investigated the effects that different laser powers and pulse durations would have on lesion sizes induced by neodymium yttrium aluminium garnet (Nd:YAG) lasers in rabbit retinal tissue. Pulse durations of 10, 20, 50 and 100 ms were combined with laser powers of 50, 100, 150, 200 and 250 mW, with analysis performed by fundus photography. They observed that retinal lesion sizes were linearly related to the laser power and logarithmically related to the pulse duration. Curves from their work are shown in Figure 1.7, with a dashed line representing a laser spot size of 132 μm on the retinal plane.

Publications using lasers, while they have shown relatively little information directly relating temperature increases to thermal damage (especially over a time frame

replicating retinal prosthesis operation), have indicated that there are differences that occur due to the time damage measurements are taken.
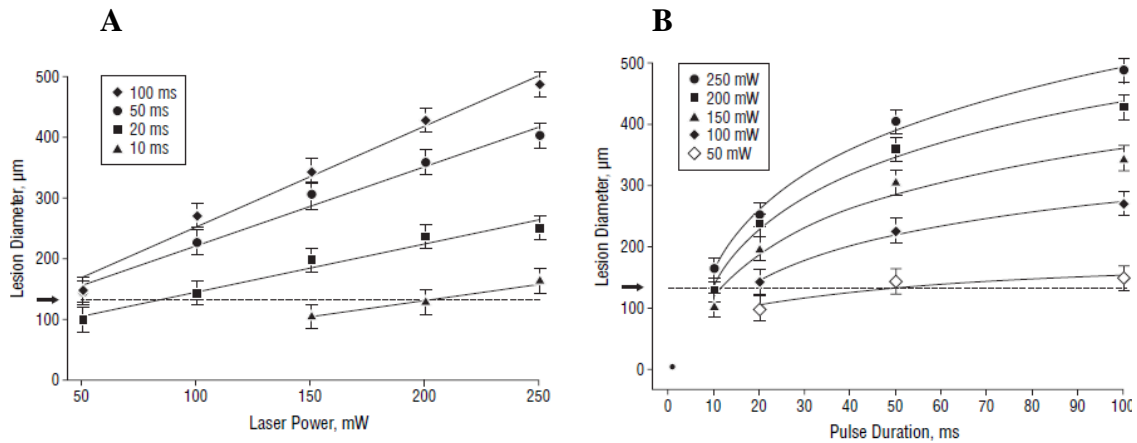
Figure 1.7. Rabbit retinal lesion sizes shown as **(A)** a linear function of laser power pulse durations of 10 ms (triangle), 20 ms (square) 50 ms (circle) and 100 ms (diamond) and **(B)** a logarithmic function of the pulse duration for laser powers of 50 mW (open diamond), 100 mW (closed diamond), 150 mW (triangle), 200 mW (square) and 250 mW (circle). Image used with permission from Jain et al. (2008)

Studies performed by Sailer et al. (2007) have indicated that a temperature increase of 3.2°C in a living eye should be expected when a subretinal implant is powered with 15 mW (4.8 mW/mm^2) of infrared energy (826.4 nm IR laser with a 3 mm spot size), the amount expected to be used by their group to supply a 1500 electrode implant. They expect that this should be able to be tolerated by retinal cells, and that an increase of retinal temperature from 36°C to 39.8°C for several weeks of continuous use should also be sufficiently low so as not to cause thermal damage to neighbouring neurons. At 40 mW of power dissipation (168.35 mW/mm^2), they measured a temperature increase of 4.5°C suggesting that for power irradiations of above 8 mW a compensatory mechanism came into place which strongly improved heat dissipation in the eye. Their tests, however, only had the IR beam focused on the sensor for between two and four minutes, far less than would be expected from a retinal prosthesis operating under normal conditions. Their results are shown in Figure 1.8, and did not mention whether the temperature increases induced by the irradiated power caused tissue damage.

Electromagnetic irradiation in the form of microwaves is becoming increasingly popular in the search to remove cancerous tumours by thermal ablation. Some studies that have investigated thermal damage and trauma caused by microwaves (both to kill cancerous cells and to investigate safe levels that can be tolerated by healthy tissue) have been discussed and are listed in Table A1.1 and A1.2 in Appendix 1.

Large discrepancies in thermal damage thresholds were observed due to differences in the animal models and tissues, the method and time of thermal damage analyses and the amount and duration of thermal energy supplied. While these studies can assist in determination of temperature and power increases that may cause damage, they should be used only as a guide, with experiments performed using conductive heating elements expected to produce slightly different results due to exacerbation of thermal trauma caused when combined with mechanical stress.
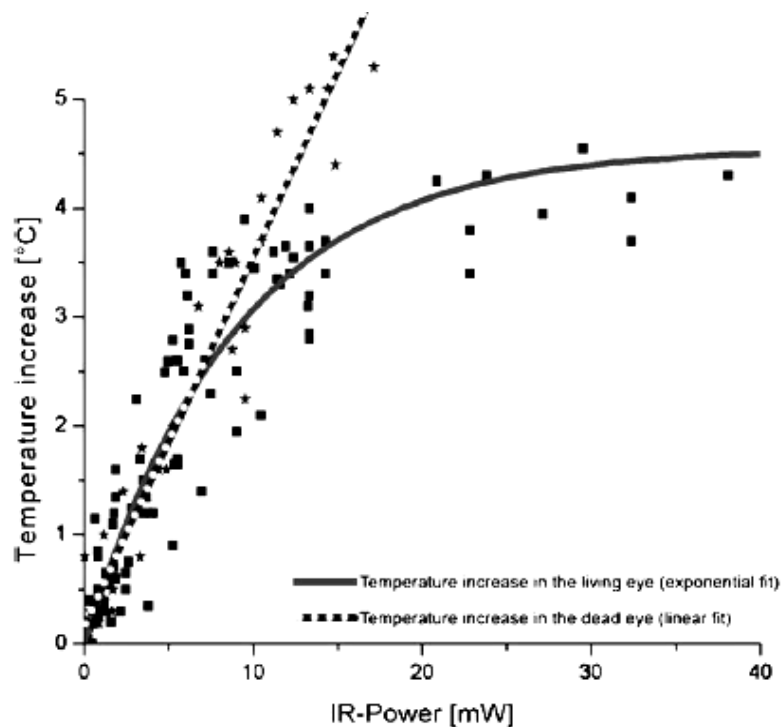
Figure 1.8. Temperature increase as a function of irradiated IR power in living and dead eyes, showing a linear fit between temperature and power in dead eyes and an exponential fit between the induced temperature increase and power IR-power dissipation in living eyes. The effect of perfusion is shown to occur at a temperature of 2.5°C to 3.0°C, where the curves for dead and living tissue branch. Image used with permission from Sailer et al. (2007).

1.5.3   Incubation Thermal Damage

Even without irradiation, biological tissue generally suffers irreversible damage when its temperature is raised by more than 10°C. Cells have been shown to die instantly when temperatures increase above 72°C, with delayed apoptosis occurring at 55°C to 58°C and delayed combinations of necrosis and apoptosis occurring at temperatures of 60°C to 68°C (Glickman 2002). Gerweck (1977) experimentally verified that the survival rate of hamster ovary cells heated for 300 minutes at 41°C was 60%, dropping

to 8% for cells heated to 42°C. This dramatic influence on increased temperature is exemplified by a survival rate of 70% after 35 minutes dropping to >1% after 150 minutes at a temperature of 43°C, with >1% of cells kept at 44°C surviving after only fifty minutes. This study was repeated by Jung (1994) with similar results. Jung found that at 43°C, Chinse hamster ovary cell numbers decreased to 80% of control after fifteen minutes, to 50% after thirty minutes and dropped to only 0.15% of control after two hours of incubation. Observations from Gerwick et al. (1977) and from Jung et al. (1994) are shown in Figure 19, indicating the exacerbation of cell trauma and death when high temperatures and long heating periods are combined.

Studies performed on Guinea Pig cortical neurons at temperatures of 37°C to 49°C by Fujii et al. (1982, 2002), showed no cellular damage throughout their five minute trial, although the N-potential was irreversibly blocked at temperatures greater than 47°C. Barbe et al. (1988) also showed a temperature dependence of rat eyes, with tissue heated to 40°C for sixty minutes not expressing heat shock proteins, with only fifteen minutes at 41°C or 42°C enough for the initiation of a cellular to respond.
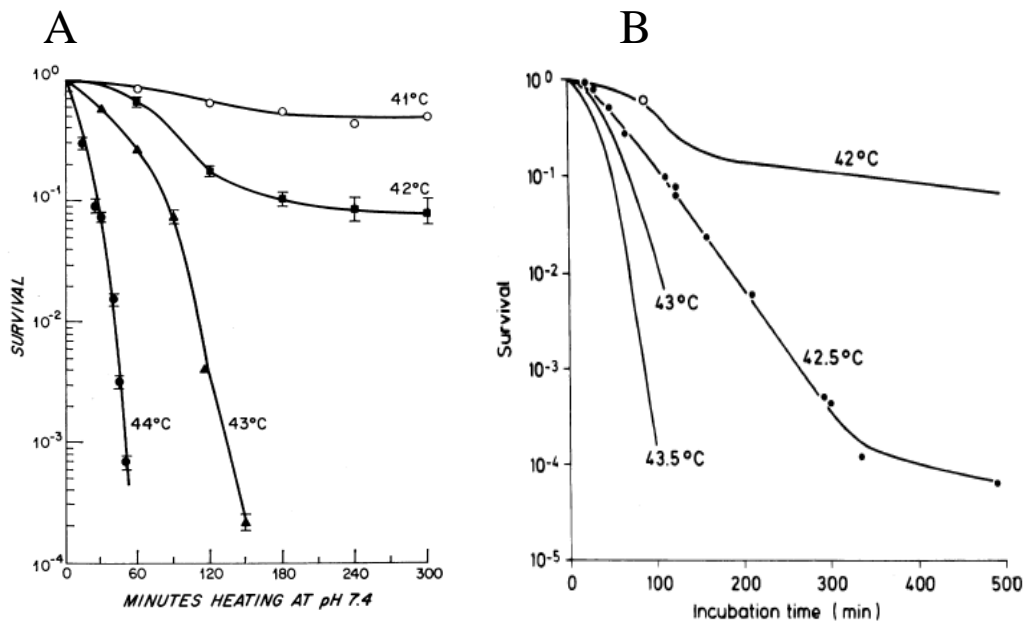
Figure 19. Cell death (indicated as a survival fraction) observed in Chinese hamster ovaries from continuous elevated temperatures from 41°C to 44°C. Images used with permission from **(A)** (Gerweck 1977) and **(B)** (Jung 1994).

Not only do these studies indicate the poor ability of cells to survive at increased temperatures, but also give a clear indication of the increased rate of cell death at elevated temperatures. For this reason, every precaution must be taken to ensure cellular elements are not overheated, and in the case where this is unavoidable, it must not occur

for extended periods of time with the degree of cellular damage depending on both the duration and the intensity of the heat stress.

Over a range of temperatures (42°C to 50°C) the degree of cellular damage increases with the duration of hyperthermia in an approximately logarithmic manner for many cell types (Harmon, Corder et al. 1990). Cell damage measured by Organisciak et al. (1995) showed that hyperthermia in rats accelerates retinal light damage compared with light exposure under euthermic conditions, and that hyperthermic light damage is related to the core body temperature and to the intensity of light used during exposure. Some of the other studies that have investigated thermal damage levels, both as a function of temperature and on exposure time are indicated in Table A1.3 in Appendix 1, and will be used to examine the effect that time and temperature (of whole body or whole cell incubation) has on thermal thresholds.

1.5.4   Other Thermal Damage

Other experiments investigating the effect of temperature increases on retinal tissue damage have been performed with ultrasound, TTST (transscleral thermotherapy), heated disks and drug administrations; although each of these methods uses temperatures much higher than would be expected to be used in a permanently implanted retinal prosthesis.

McDannold et al. (2000) used ultrasonic energy on rabbit thigh muscles and reported no damage occurring at temperatures up to 47.2°C, with lesions occurring at temperatures greater than 50.4°C. Their data indicated lesions were seemingly independent of power dissipated in the tissue, with powers ranging between 12-30W producing lesions in some experiments and no visible lesions in others. Damage was seen by Braakman et al. (1989), also using ultrasound in rabbit eyes, at all temperatures greater than 43°C for 30 minute irradiations. At 43°C, damage was reported to be representative of corneal local hemorrhagic keritis and local oedema in the retina and choroid with a 10% of cells measured being necrotic. This increased to almost 50% necrotic cells at temperatures in excess of 49°C.

When Lyons et al. (1986) used a 2.06 MHz lithium niobate ultrasonic transducer with a power of 200-300 mW/cm^2 to produce thermal lesions in cat cortical tissue from temperatures spanning 41-49°C for fifty minutes, his group found a linear relationship between the size of induced lesions and temperatures. In acute studies (termination and

histology performed between one and three days), they found thermal injuries including coagulation necrosis, polymorphonuclear leukocytes and pyknosis of grey matter neurons, oedema and vacuolation of white matter. Lesion size was shown to increase by 4.293 mm^2/°C·min, with an intercept at 42.2°C. In subacute studies (3 – 21 days) thermal injuries included coagulation, necrosis with liquefaction, fluid filled necrotic centres, lipid-laden macrophages, vascular proliferations and perivascular infiltration, with lesion sizes increasing by 2.495 mm^2/°C·min with an intercept of 41.1°C. The lesion size dropped again in chronic investigations, with a slope of 2.286 mm^2/°C·min with an intercept of 41.4°C, with damages in this 21-56 day period including reduction and shrinkage of the necrotic centres, fibrosis, gliosis and vascular proliferation.

Damage through the expression of heat shock protein 90 (Hsp90) was reported to be caused by sub-lethal injection of LSD to the brain and kidneys, with a temperature of 42.5°C for one hour published by Quarishi et al. (1995). A TTST thermal heating disk that consisted of hot water passing through a 6 mm diameter, 3 mm deep disk heater produced no damage for 60 seconds at 50°C, although 55°C and higher temperatures resulted in vascular occlusions of the retinal and choroid and retinal tears in rabbit eyes (Rem, Oosterhuis et al. 2003). While these techniques for inducing thermal damage are not directly related to temperature increases caused by conductive heat transfer, they do confirm other studies indicative of damages caused at high temperatures.

A list of studies and results from thermal damage thresholds investigating TTST, ultrasound and drug administration are listed in Table A1.4 in Appendix 1.

1.6 THERMAL DAMAGE COMPARISON

Results of thermal damage, damage thresholds and safe (undamaged) observations from all publications listed in Table 1.2 and Appendix 1 (Tables A1.1, A1.2, A1.3 and A1.4), irrespective of animal model or tissue used in experimentation, manner and method of damage analysis and whether pre-treatment or multiple stressors are combined, is shown in Figure 1.10 (with Figure 1.10B showing a magnification of Figure 1.10A with temperatures less than 50°C and thermal heating durations between 1 and 300 minutes).

With such a large overlap between observations of temperatures that do and do not induce damage, it is difficult to determine a power budget (or temperature threshold) to ensure the safety of permanently implanted retinal prosthesis. Results from published literature indicates damage can be caused across a large range of temperatures and durations, with temperatures from 36-70°C and durations spanning micro-seconds to months all inducing irreversible damage. Studies have also indicated that threshold damage can be anywhere from 0.00001-30 minutes with temperatures from 30-90°C. Safe measurements have been reported to span a wide range, with temperatures of 35-50°C and durations of up to 40 minutes reported not to induce observable retinal trauma.

To determine whether thermal damage measurements were not related or affected by time, Gaussian plots of safe, threshold and damaging temperatures were plotted using Minitab 15. Shown in Figure 1.11, these curves indicate that the average temperature at which damage was reported is 44.52±5.9°C (n=57), with most reports of safe temperatures around 40.27±.4.5°C (n=20). The threshold values however, were generally reported above the damage temperature, at a value of 52.61±13.3°C (n=32). The large standard deviations observed are due to the use of many different animal models, tissues and measurement methods as well as the very high temperatures (and very low durations) used in laser irradiation studies.
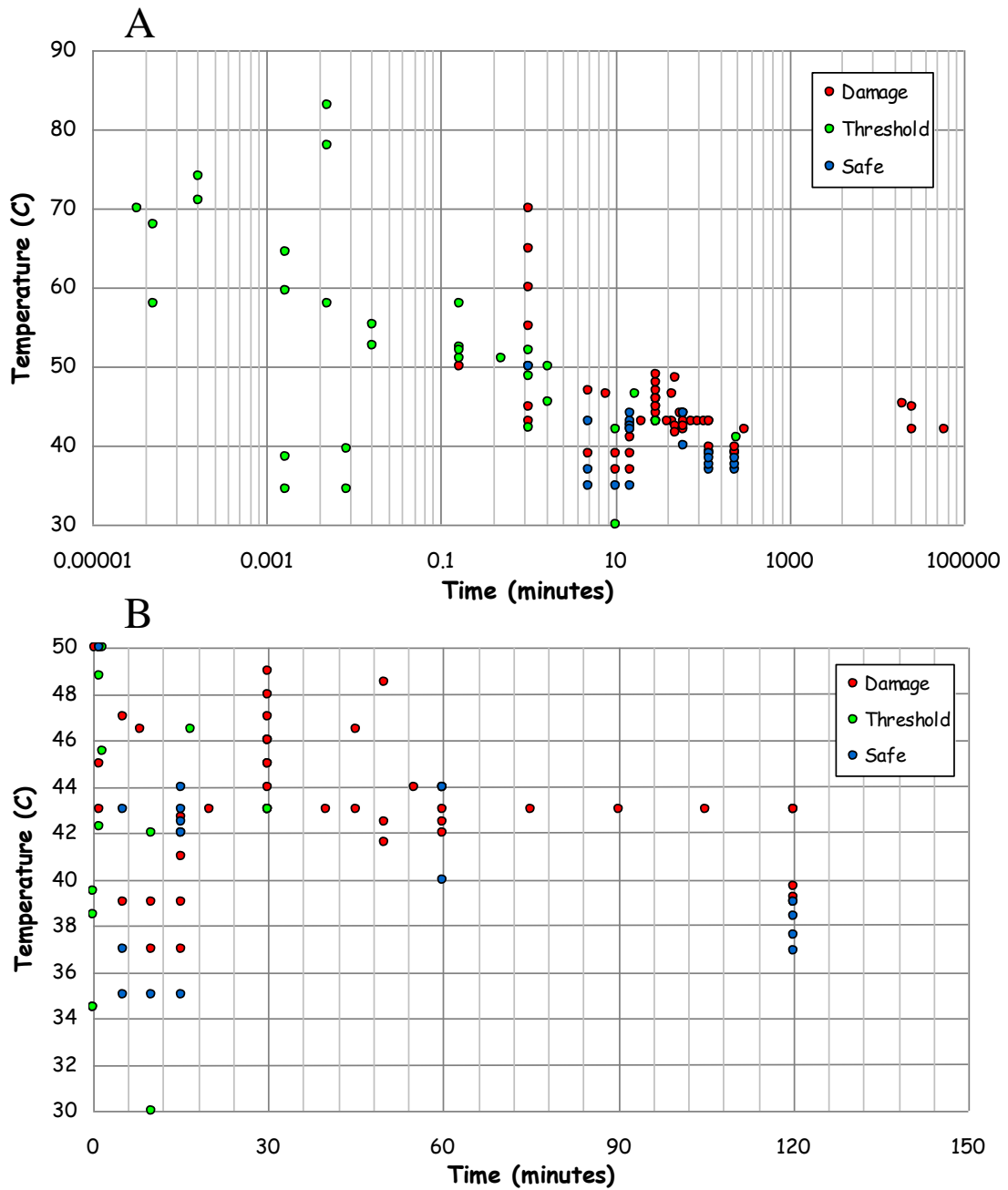
Figure 1.10. (A) Thermal damage experiment temperatures and test durations for studies listed in Table 1.2 and Appendix 1, inclusive of all thermal damage from studies performed using laser and electromagnetic irradiation, conductive heating, incubation, ultrasound and other methods and **(B)** for temperatures between 30°C and 50°C and durations between 1 second and 150 minutes. Red, green and blue data points indicate temperature-time values published to cause damage, be on the thermal damage threshold and that are safe, respectively.
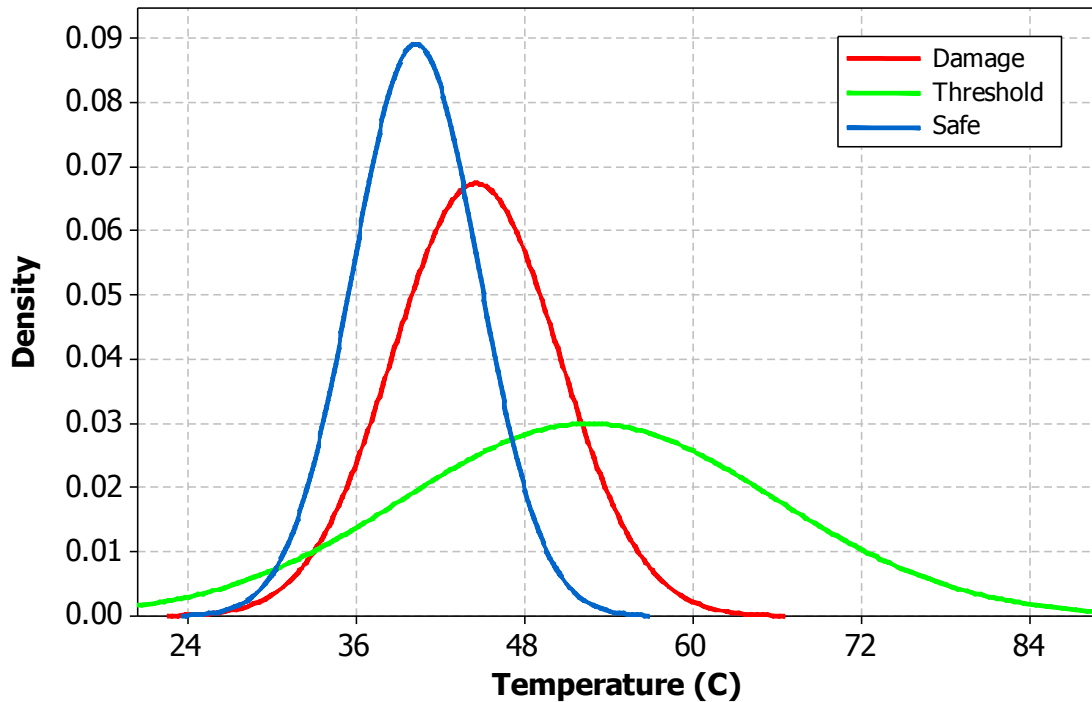
Figure 1.11. Gaussian plots of temperatures at which safe (blue), threshold (green) and damage (red) from publications listed in Appendix 1.

To enable an analysis of thermal damage occurring as a result of both the heat duration and temperature, published thermal safety, threshold and damage results were converted to a cumulative number of equivalent minutes at 43°C (*CEM* 43°C) by

$$CEM\,43°C = tR^{(43-T)}$$ (1.2)

where t is the time interval in minutes, T is the average temperature during the time interval t and R is a variable related to the number of minutes needed to compensate for a 1°C temperature change above or below the 43°C breakpoint (Dewhirst, Gross et al. 1986; Dewey 1994; Dewhirst, Vigilanti et al. 2003). The R values used in comparison between thermal damage literature reports are 0.23 when the temperature is below 43°C and 0.43 when the temperature is greater or equal to 43°C (Dewey 1994). Figure 1.12A indicates *CEM* 43°C values observed for all safe, damaging and threshold observations, clearly indicating a large overlap between research conducted to investigate thermal safety. A Gaussian plot for each of the damaged, threshold and safe *CEM* 43°C values for temperatures below 50°C and for durations between one second and 150 minutes shown in Figure 1.12B.
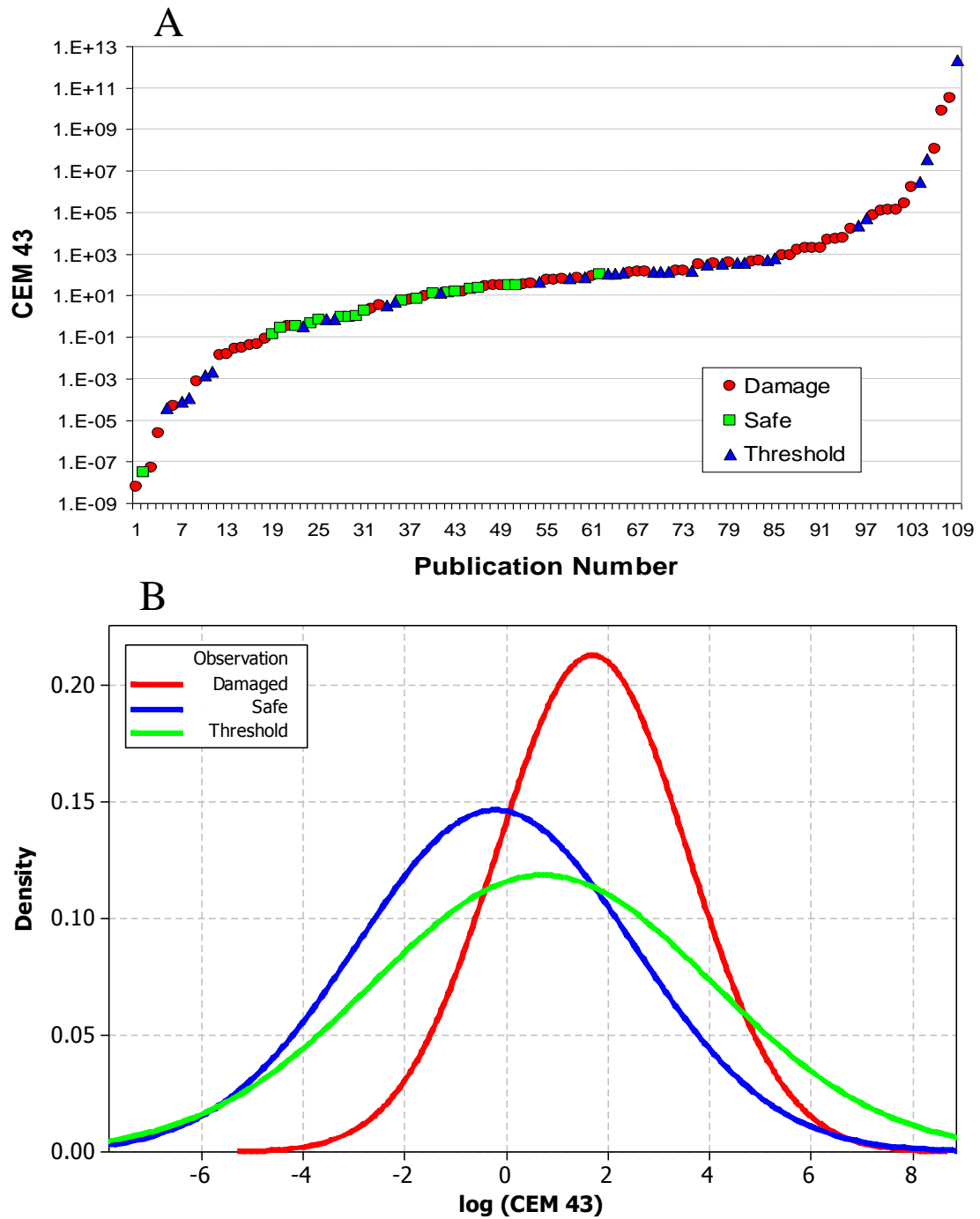
Figure 1.12. (A) Safe (green), damaging (red) and threshold (blue) number of cumulative minutes at 43°C observed from research listed in Appendix 1. **(B)** Gaussian fits the log CEM 43°C values for safe (blue), threshold (green) and damaged (red) published observations.

The safe, threshold and damaging number of cumulative minutes at 43°C was determined to be 0.60 ± 537 (n=57), 5.15 ± 4750 (n=32) and 48.4 ± 75 (n=20) minutes, respectively (log(*CEM*43°C) of -0.2228 ± 2.725, 0.7118 ± 3.365 and 1.685 ± 1.876, respectively). As would be expected, the number of equivalent cumulative minutes at 43°C to induce damage was greater than for safe observations and greater again than

observed thresholds. The ability to accurately use this data to ensure the safety of a retinal prosthesis is hindered by the very large standard deviations, arising from the different animals and tissues, endpoints and methods of damage analysis used between the studies.

A plot of the average (thick lines) and standard deviations (faint lines) of the published safe (blue), threshold (green) and damaging (red) thermal observations are shown in Figure 1.13, for temperatures between 30°C and 50°C and durations between one and 1000 minutes. This plot was derived from the mean and average *CEM*43°C data, again using an *R* value of 0.23. The data suggests that to ensure a retinal prosthesis does not cause damage, a temperature of 45.33°C should not be breached (even for one minute), decreasing to less than 41.12°C for durations in excess of 100 minutes.
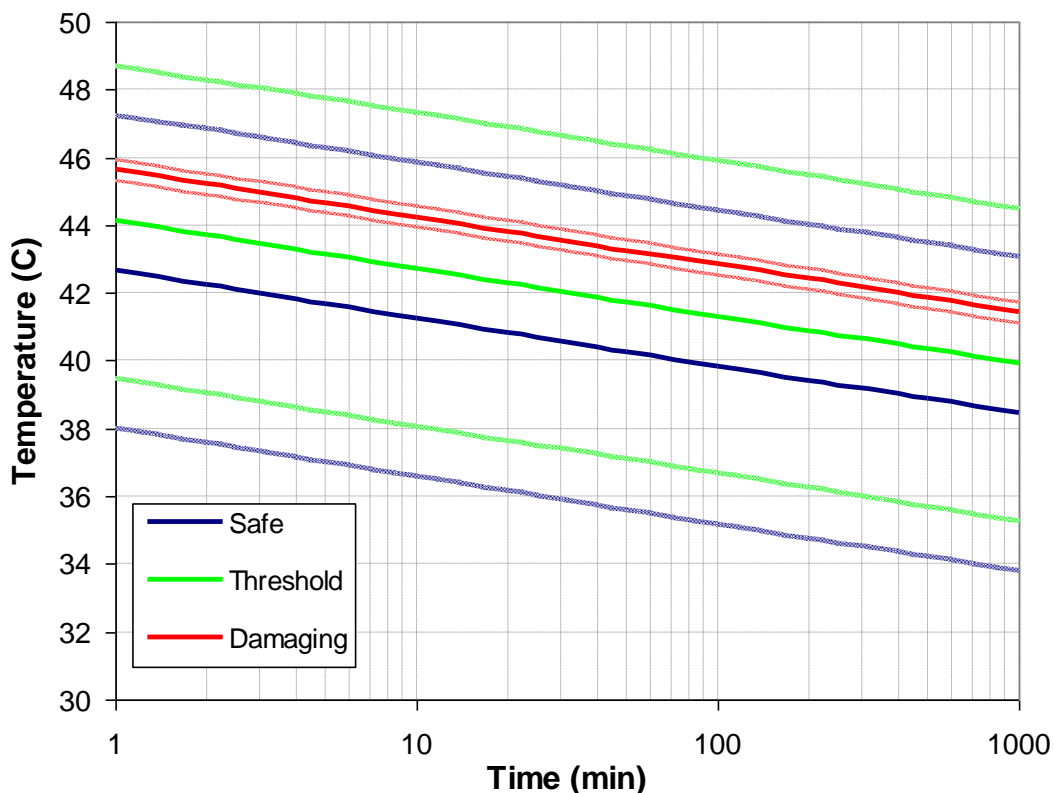
Figure 1.13. Time-temperature responses for safe (blue), threshold (green) and damaging (red) responses calculated from the mean CEM 43°C published data. Faint lines are indicative of observed standard deviations.

While it would be unwise to put too large an emphasis on the average thermal damage measurements accumulated from all of the listed publications, there are some very similar correlations that must be addressed when designing an experiment to investigate the thermally safe temperatures that retinal tissue can tolerate by conductive energy transfer from a permanent visual prosthesis.

The eight primary features (excluding mechanism of thermal injury) that were observed to alter the thermal resistance and affecting thermal damage thresholds are: 1) animal model; 2) tissue type; 3) simultaneous stressors (such as ischemia and mechanical damage); 4) temperature and duration of thermal insult; 5) method and timing of damage assessment and definition of thermal damage; 6) delayed damage and cellular recovery; 7) thermotolerance and repetition of thermally induced stress and 8) animal body temperature. Each of these parameters can have large differences in the assessed level of damage. As most of the published literature does not investigate thermal damage induced in retinal tissue already damaged by degenerative conditions such as retinitis pigmentosa and age-related macular degeneration by active operation of a permanently implanted retinal prosthesis, there is a large potential for retinal damage thresholds to be different than those published, which would render the published tolerances misleading.

The only way to ensure that no damage will be caused to a patient by a visual implant is to conduct experimental tests that match the proposed devise (in terms of size, location and power dissipation) and the usage (daily hours and pre-existing degenerative conditions) as close as possible. The acute thermal heating tests have been designed to mimic the use of a visual prosthesis, attempting to match these parameters as closely as possible. While important to ensure closely matched trials and end-stage prosthesis use, *in vitro* and *in vivo* animal trials can assist in initial damage determination and can help assess methods of damage analysis to improve correlations between chronic animal trials and those performed in human clinical trials.

1.6.1 Animal Model Variations

Almost none of the publications listed in Table 1.2 or Appendix 1 are tests performed on human retinal tissue, and while the temperature increases or damages measured can give indications of other key issues to be included in the testing protocol, a direct comparison between results could lead to erroneous judgement. Animals such as the mouse, rat and rabbit are often used for laboratory investigations and are relatively cheap and easy to maintain. The ability of these animals to be used as a model to investigate the effects of a 5×5 mm implanted heater, however, is nigh impossible. For these animals to be used, a smaller implant was designed to fit into the eye and the potential for differences in thermal elevations and damage caused by a significantly smaller heating element is an issue. These animals however, can be used to gain insight into appropriate endpoints and methods of damage and can be used to give

approximations on the amount of thermal trauma tolerated by retinal neurons (Chapter 6).

The importance of using an appropriate animal model was shown by Neumann et al. (1982) and by Glaze et al. (1986), who used identical heating apparatus (2 MHz RF, 50°C temperature increase of 7 W) to investigate thermal damage in horses and dogs. The dogs were reported to have thresholds occurring after ten seconds of stimulation, with thirty seconds required to produce the same effect in horses. A study by Dewhirst et al. (2003) examined differences in time required to produce epidermal necrosis as a function of temperature for mouse, pig, rat and human. They reported that while pig and human skin are almost identical, they are also more highly resistant to thermal damage than skins of mice and rats, shown in Figure 1.14.
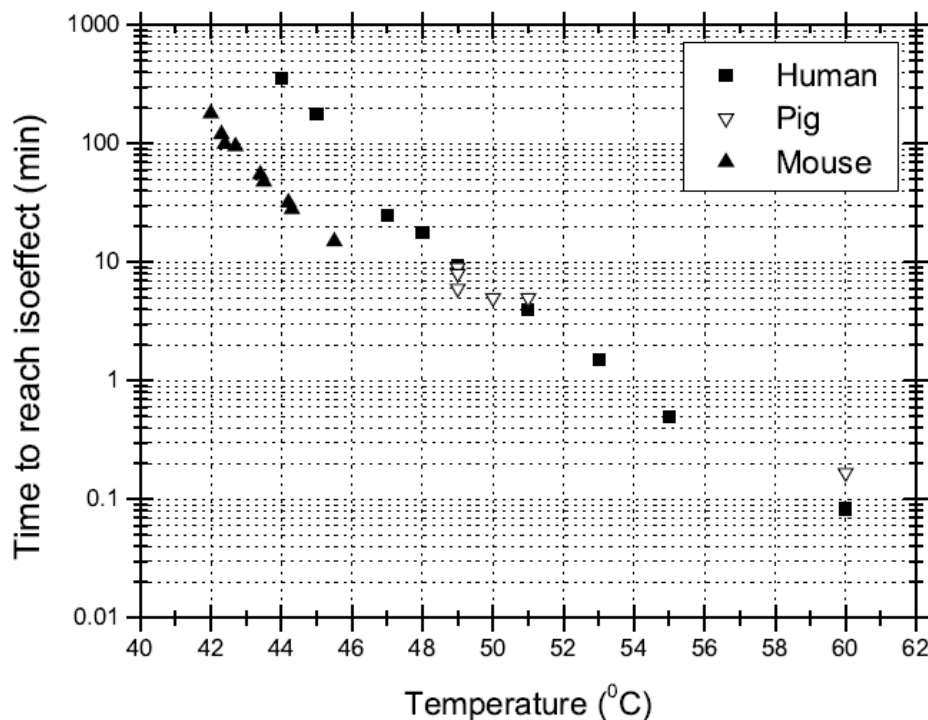
Figure 1.14. Observed thresholds of thermal resistance of human, pig and mouse skins, indicating dissimilarities occurring between animal models. Image used with permission from Dewhirst et al.(2003).

1.6.2   Variations in Tissue Types

Delicate retinal photoreceptors and neurons can easily be damaged. This damage has been shown to be caused by both an increase in temperature and by damage from mechanical pressure (Colodetti, Weiland et al. 2007; Ray, Colodetti et al. 2009). The

pressure required to cause irreversible retinal damage is magnitudes larger than pressure damage that can be tolerated by other tissues such as skin or bone and, likewise, thermal increases that can be tolerated by other tissues are not expected to correlate well with safe retinal tissue temperatures. Dissimilarities that occur between thermal damage thresholds have been observed by Dewhirst et al. (2003) on mouse tissue, with their results shown in Figure 1.15. They reported significant differences between the time-temperature relationship of spinal cord, small intestine, feet, testis and ear skin of mice, indicating that the skin of the ear and foot is more resilient to thermal stress than more complex tissues such as the testis and spinal cord. Differences, however, could have arisen due to inconsistencies in assessment methods with necrosis being the thermal damage endpoint for the feet and skin, stem cell survival used to determine intestinal damage and weight used to evaluate testicular trauma. The correlation between the endpoints is not identical, and care must be taken to acknowledge that these damage mechanisms may not be reflective of thermally induced damages to all tissue types.

Differences in thresholds for different cell types was observed by Sykes et al. (1981) who used white fluorescent light to determine a 195-361 μW/cm^2 threshold for cone damage and a 361-615 μW/cm^2 threshold for cone damage in primate eyes. Complex structures such as the eye have large differences in thermotolerant components, as indicated in Figure 1.16 where safe and unsafe observations of thresholds and damaging temperatures can differ by more than 2.5°C depending on the area the thermal stress is applied.
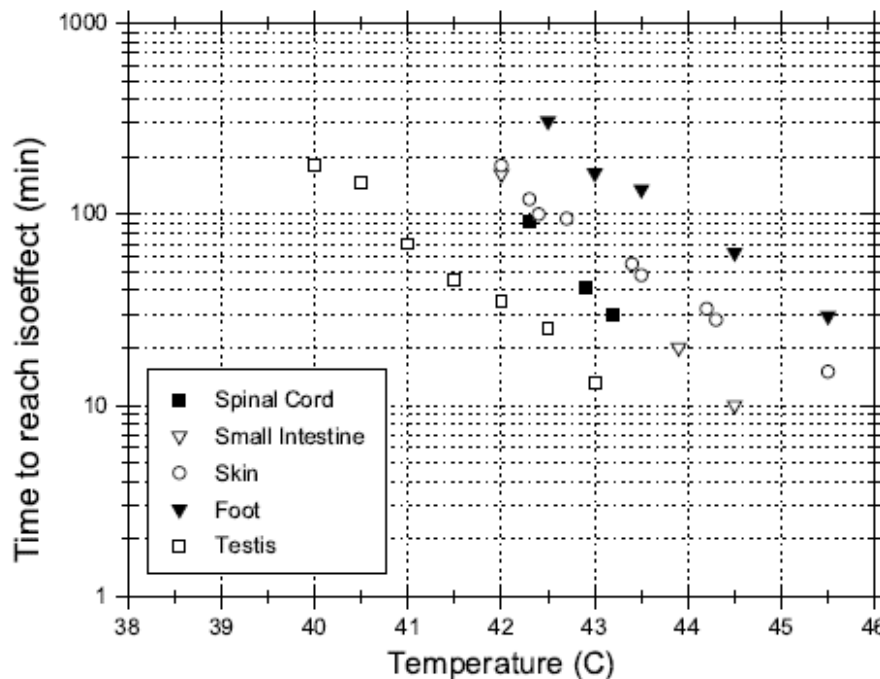
Figure 1.15. Observed thresholds of thermal resistance of mouse spinal cord, small intestine, skin, foot and testis, indicating dissimilarities occurring within different tissue types. Image used with permission from Dewhirst et al. (2003)
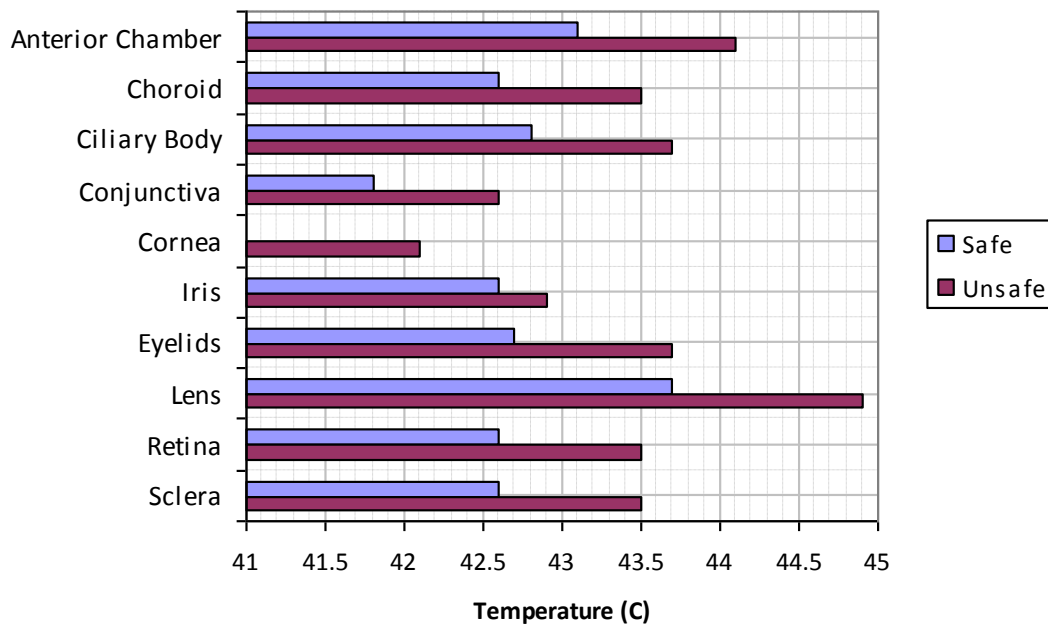
Figure 1.16. Temperature thresholds for common rabbit eye tissues indicating safe observations (blue bars) and unsafe observations (red bars) as a function of temperature, indicating dissimilarities occurring between different tissue types. Image adapted from data from Bollemeijer et al. (1989)

1.6.3 Simultaneous Stressors

Thermal energy dissipation in tissue that is already damaged or diseased can play a large role in the amount of damage induced by the temperature increase, exacerbating any damage that may be observed in an otherwise healthy eye.

Minamisawa et al. (1990) investigated the effects of increased temperature in combination with ischemia on cortical tissue in SPF-Winstar rats. The experiment measured the temperature with a thermocouple positioned in the bregma and aorta and used direct visual cell counting in the CA1 and subiculum in the hypothalamus to compare experiments. They found that both an increase in temperature and an increase in the ischemia time had significant impacts on the number of surviving cells. At a temperature of 35°C, ischemic conditions for 5, 10 and 20 minutes resulted in 1-5%, 25-30% and 30-40% loss of cells respectively. This increased to 15-20%, 45-55% and 80-90% at a temperature of 37°C and further increased to a cell loss of 30-45%, 80-90% and 90-95% cell loss for 5, 10 and 15 minutes under ischemic conditions and a temperature of 39°C. This highlights the impact of multiple simultaneous damage mechanisms exacerbating the total damage caused.

1.6.4 Temperature and Duration

While a large emphasis has been put on the animal model used, the type of tissue and the power source, perhaps the most important parameter that determines the thermal damage is the amount of energy the tissue must tolerate. The duration of the thermal exposure and the magnitude of the insult will have large consequences for any cell and animal type if these are too great. Laser irradiation looks at short time frames with pulses generally less than a second and thus publications that investigate the effects of temperature increases over a longer period are more valuable to correlate with expected damage from a retinal prosthesis.

As mentioned previously, survival rates of cells distressed by prolonged thermal increases are affected by both the duration of the insult and the magnitude of the thermal increase. This has been shown to occur in research conducted on Chinese hamster ovary cells by Gerwick et al. (1977) and Jung et al. (1994). Their work indicates the exacerbation of increased temperature-time combinations, with a marked decrease in cell survival as the temperature or duration increases. At a temperature of 41°C, the survival rate dropped and reached a plateau at approximately 50% from 180 minutes onwards. An increase in temperature by 1°C (to 42°C) decreased the cell survival rate significantly (to less than 10%) by 180 minutes. A further increase in temperature, by only 0.5°C, and the survival rate loses the ability to plateau (where cell survival and revival is balanced) and a survival fraction of less than 0.01% occurs after 300 minutes. Increasing temperature further, and the cell survival rate drops to below 0.01% after 120 minutes at 43°C, 100 minutes at 43.5°C and approximately 50 minutes for cells heated by 44°C. This sharp decline in cell survival will be deleterious if the temperature is allowed to reach levels where the rate of cell survival and regeneration are overshadowed by the rate of cell death. This sharp decrease, seen at higher temperature, was suggested to be a result of both the thermal energy insult as well as toxicity produced from the death of neighbouring cells. For this to be avoided, allowable thermal increases must be carefully selected and monitored.

The rate of heating is also an important factor that will determine the amount of cellular death and damage, having a large effect on the degree of cytotoxicity. In a study by Dewhirst et al. (1986), the threshold for arteriolar stasis was between 45°C and 46°C for heating rates from 0.1°C to 0.7°C per minute. At a higher heating rate (1.0°C/minute), the stasis temperature dropped to 42°C. This was also shown for venular stasis, dropping from 43.1°C to 42.1°C when 0.1°C/minute heating rates were compared to 1.0°C/minute respectively. The difference in temperature for damage onset occurs

because thermotolerance develops to a greater degree during slow versus fast heating rates (Herman, Gerner et al. 1981).

1.6.5 Damage Assessment

The way in which thermal damage is measured and assessed will play a large role in the determination of temperature thresholds. The observer and protocol used in each experiment is often different, with quantification of damage ranging from alterations in cellular function to complete and irreversible necrosis. While it would be unwise to ignore previous research performed, comparison between datasets is made more difficult through inconsistencies between what is considered to be safe, damaging and on the threshold.

Studies have been performed looking at a range of features and endpoints, with the primary endpoints of importance in the measurement of damage relating to operation of a visual prosthesis being only those damages which are reversible and do not impede on neuronal function. Differences that can occur due to measurement techniques have been reported for a wide array of measurement methods including electron microscopy, fundus photography, histology, fluorescein angiography and ophthalmoscopy (Birngruber, Puliafito et al. 1987; Bollemeijer, Lagendijk et al. 1989; Kremers and Norren 1989; Roider, Brinkmann et al. 2000; Framme, Schuele et al. 2004; Morimura, Okada et al. 2004; Nakauchi, Fujikado et al. 2007).

Histological assessment of tissues can reveal damage that may be sub-clinical and not measurable by fundus photography, ophthalmoscopy or fluorescein angiography, although these techniques may be able to measure subtle damage changes that occur during experimentation and only lead to significant thermal damage on accumulation of repeated thermal exposure. Studies by Birngruber et al. (1987) performed on Chinchilla Grey Rabbits using 825 nm Argon laser with an 80 µm spot size, indicate the importance of measurement equipment and methods in determination of accurate thresholds. They measured an E50 threshold (threshold at which damage would occur in 50% of trials) to be 0.75 µJ when measured by fluorescein angiography and 4.5 µJ when measured by ophthalmoscopy. This indicates an increased sensitivity of damage to fluorescein angiography when compared to ophthalmoscopy although the same end points (swollen photoreceptors, sub cellular structural damage and melanin granule disruption) were used to define damage.

Differences that occur between thresholds due to damage measurement tools was also reported by Roider et al. (2000) who indicated that photocoagulation of photoreceptors could be caused with 100-500, 30-130 µJ pulses at 500 Hz from a 527 nm, Nd:YAG laser in human patients with diabetic maculopathy, soft drusen and central serous retinopathies when analysed by fluorescein angiography, with no damage noticeable by ophthalmoscopy. Ophthalmoscopy has also been reported to be less sensitive than fluorescein angiography by Framme et al. (2004) who used pulses of 527 nm Nd:YAG lasers to irradiate rabbit retinal tissue and observed that damage thresholds seen ophthalmoscopically were consistently around 250 mJ/cm^2 greater than fluorescein angiographic thresholds.

Reports of threshold differences, occurring due to different end point measurements, was also observed by Jain et al. (2008) between measurements taken by histological and ophthalmoscopical assessments. On average, the fundus photographs required lesion sizes 23% greater than damage thresholds measured histologically using a toludine blue stain and light microscopy. This was shown to occur independently of laser power or pulse duration as shown in Figure 1.17.
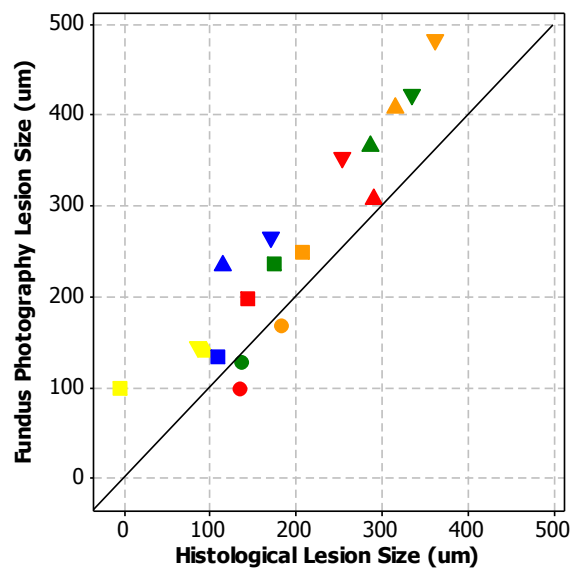
Figure 1.17. Comparison between histologically assessed and fundus photograph lesion sizes. Squares, circles, triangles facing up and triangles facing down represent 10, 20, 50 and 100 ms pulse durations respectively. Yellow, blue, red, green and orange data points represent 50, 100, 150, 200 and 250 mW laser powers respectively. Black line represents a 1:1 comparison. Adapted from data from (Jain, Blumenkranz et al. 2008)

Different thresholds for different analysis techniques was also reported by Bresnick et al. (1970) who looked at pathological thresholds and compared them to ophthalmoscopically visible damages. The finding was that pathological damage

assessment was more sensitive than assessment by ophthalmoscopy, and increased with increasing power with damage probability-power slopes of 1.77 and 1.65 for ophthalmoscopic and pathologic 12 ms pulse durations respectively and slopes of 1.69 and 1.52 for 125 ms pulse durations.

1.6.6 Delayed Damage and Cellular Recovery

Cell recovery is also an important factor to consider when comparing thermal damage. The ability of cells to recover has been published by Ben-Schlomo et al. (2006) who used 514 and 544 nm Argon Lasers to irradiate the retinas of pigmented rats. Flash ERG was used to measure the recovery, with an initial decrease in the B-Wave amplitudes recovering to almost normal (compared with control rats) after a 60 day period. Other studies have reported thermal damages that can both manifest after a given period of time or conversely be repaired after prolonged durations (Ham, Ruffolo et al. 1978; Lyons, Obana et al. 1986; Li, Zhou et al. 1987; Li, Qiu et al. 1988; Bollemeijer, Lagendijk et al. 1989; Ming, Algvere et al. 2004; Ben-Shlomo, Belokopytov et al. 2006; Kim, Park et al. 2006).

In the case of a retinal prosthesis, where any cell death is to be avoided, damage that manifests after a prolonged period must not be neglected by thermal measurement of data immediately following thermal trauma. Ham et al. (1978) used blue light at 441 nm from a 450 W Xenon Slit Lamp to determine damages that occurred to irradiated retinal tissue in Rhesus monkeys. Initially one hour post treatment to one day post treatment, with 1000 second pulses and powers ranging from 30-90 $\mu J/cm^2$ only slight visible damage was seen above the threshold level of 62 μW. Two days post trauma, damage could be characterised by retinal pigment epithelium disruption, choroidal damage, pigmentary changes in the lesion area and mild oedema. From tissue collected at five to six days post trauma, there was noticeable damage and disorientation of the outer segments, debris-laded macrophages in the subretinal space and disruption, proliferation and hypo-pigmentation of the retinal pigment epithelium. Recovery was reported to have occurred around ten to eleven days after the induced laser trauma, with hypo-pigmentation of the retinal pigment epithelium still present although there was no noticed cell proliferation and the outer segments of the rod and cone cells were almost normal (albeit slightly shorter), with a normal choroidal appearance. This recovery continued, and at 30 days after the initial trauma the retinal pigment epithelium,

photoreceptor outer segments and choroid were assessed as normal, with only a small amount of macrophages present in the subretinal space. Only a slight hypo-pigmentation of the lesion area was present 60 days post trauma, with a full recovery documented to occur after 90 days. This trial indicates the importance of long term assessment (chronic trials) as tests which do not allow for recovery and regeneration to occur may miss observing the return of morphology or tissue functionality.

A recent study performed by Paulius et al. (2008) investigated the healing of retinal photochemical lesions from rabbits irradiated with a 532 nm Nd:YAG laser with a power of 175 mW and pulse durations ranging between 5 and 100 ms, shown in Figure 1.18. Lesions were graded after 1 minute and assessed histologically after 1, 7, 30, 60 and 120 days. They found that with pulse durations greater than 10 ms, the retinal lesion size would stabilise at around 40% of the original size after a period of 60+ days. For pulse durations of less than 10 ms, the lesion size would decrease and heal completely within four months. This suggests that while initial trauma may be caused through mechanical insertion of a retinal implant, the damage (provided is minute) can be repaired. The ability to ensure that thermal trauma does not exacerbate damage caused mechanically, reducing the potential for the tissue to completely heal, is something which must be assessed prior to commercialisation of retinal prostheses.
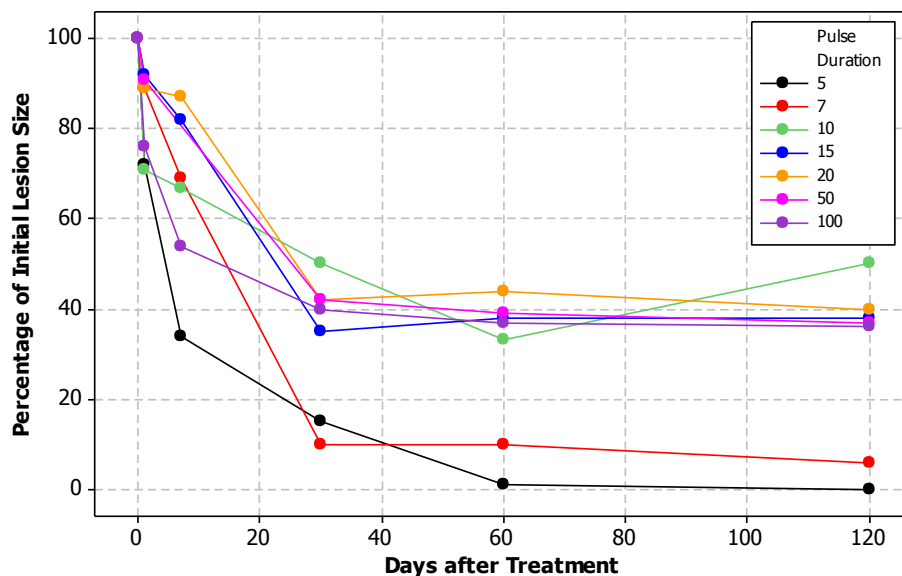
Figure 1.18. Healing response of tissue from laser induced damage from a 175 mW, 532 nm Nd:YAG laser with pulse durations of 5 ms (black), 7 ms (red), 10 ms (green), 15 ms (blue), 20 ms (orange), 50 ms (pink) and 100 ms (violet) shown as a percentage of the initial lesion size (after one minute) over time. Image adapted from data from Paulius et al. (2008).

For a retinal prosthesis, these types of longer term studies will give the best representation of damage that has occurred and recovery that has been made and can

allow for comparisons between the damage caused and functionality lost to a much higher standard. Moderate thermal stress may require 48-72 hours to become apparent, with cellular responses including inactivation of enzymes, cell shrinkage, and deformation of structural proteins and loss of birefringence. An experiment performed by stressing cultured primary striatal neurons for two hours at 43°C indicated that the first mechanism of damage visible by light microscope was the blebbing of processes, which was only visible 24 hours following stress termination (White, Luca et al. 2007). Condensed nuclei (probably indicative of apoptosis) appeared by 24 to 36 hours later, and by 48 to 60 hours post-trauma, most neurons were dead. Hyperthermia has been shown to produce a delayed, perhaps apoptotic death in cortical neurons (Vogel, Dux et al. 1997), cerebellar granule neurons (Lowenstein, Chan et al. 1991), dorsal root ganglion neurons (Uney, Kew et al. 1993) and septal neurons (White, Luca et al. 2007). This delayed reaction to thermal stress will reduce the ability of acute animal trials to accurately determine the amount of cellular degeneration. These short (up to 48 hour) experiments, while can be used to determine the ability of retinal tissue to dissipate heat (retinal flux measurements), they are not expected to give sound evidence towards the amount of damage that has been caused, emphasising the requirement of chronic trials to be undertaken.

1.6.7   Thermotolerance

Thermotolerance, an acquired resistance to thermal toxicity, occurs when cells and tissues are exposed to thermal stress. Most proteins are down-regulated during and after the heat stress, with the exception being heat shock proteins that are up-regulated during heating and act as chaperones to either target refolding or degradation of proteins (Burgman, Nussenzweig et al. 1995). The amount of thermal tolerance will depend on the severity of the thermal damage and the duration of the heat stress. This was investigated by Law (1979) who examined the thermal resistance of mouse ears to skin necrosis. An initial 43.5°C thermal injury was inflicted for 2-40 minutes, with second heat treatments administered over the next 1-160 hours. Using an endpoint of 50% necrosis, found that the time required to reach a maximum thermotolerance increased by 0.7 hours for each minute of initial heating, with maximal thermotolerant tissue requiring an additional 1-2°C temperature increase to produce isoeffects similar to single heated tissue.

Using Chinese hamster ovary cells, Hildebrandt et al. (2002) demonstrated an increase in the survival of cells after incubation at 43°C after an initial 1 to 16 hour incubation at

40°C, shown in Figure 1.19. There were less than 2% of cells remaining after approximately 1.5 hours of heating at 43°C without prior heat treatment, increasing to around 80% survival with 16 hours of thermal pre-treatment. While the amount of cell death was still significant (only 10% of cells remaining after 6 hours at 43°C with 16 hours of pre-treatment), at a lower thermal level (such as that expected in a retinal prosthesis), pre-treatment could act to retain a larger proportion of cells. This would have significant benefits if it were possible to reduce the magnitude of cell death by simply heating the region neighbouring a visual implant prior to use.
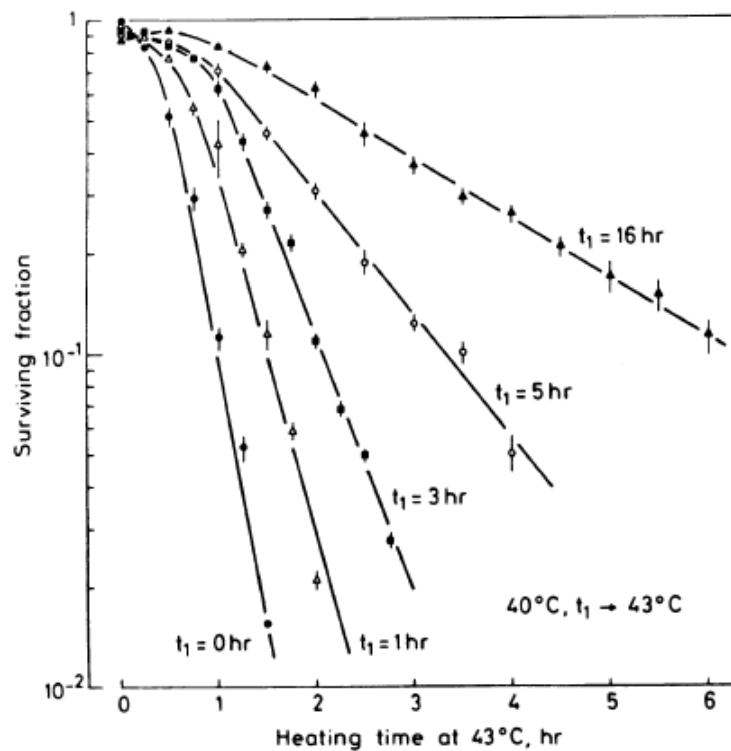
Figure 1.19. Survival rate of Chinese hamster ovary cells due to heating at 43°C after a 40°C heating pre-treatment (t_1) for 0, 1, 3, 5 and 16 hours. Image used with permission from Hildebrandt et al. (2002).

1.6.8 Body Temperature

Body temperature variations can also affect thermal damage thresholds. The degree of damage can be exacerbated by body temperature as shown by Polhamus et al. (1975) who reported thermal thresholds from 488 nm Argon laser irradiation with a 200 μm spot size in different rabbit eye tissues. The ophthalmoscopically determined threshold increased at a rate of -1.15 × the measured fundus temperature + 52.4°C. Body temperature dependence has also been published to be a prominent feature in retinal

thresholds by Gorgels et al. (1979), Ward et al. (1971) and by deLint et al. (1992). This emphasises the importance of ensuring animal body temperature is measured and maintained throughout experiments and is carefully matched over subsequent tests.

1.7   THERMAL DAMAGE MEASUREMENTS

To determine the extent of the damage caused at a cellular level by the dissipation of thermal energy from a heating element, a methodology that quantifies the resulting neuronal degeneration of the retinal tissue is required.

These procedures generally require fixation of tissue prior to enucleation, with the exception being rat *in vitro* tests which remove the globes prior to experimentation and fluorescein angiographic analysis which investigates the thinning of blood vessel walls *in-situ*. Following the fixation protocol, the eyes can be assessed by using many methods of immunofluorescence. The protocol used to fix, section and stain the cells will be discussed in more detail in Chapters 5 and 6, with background and publications on potential methods of assessing thermal damage discussed in the following sections. The primary methods investigated include stains for degenerating neurons (Fluoro-Jade), staining for microglia and stains used to immunofluorescence glial fibrillary acidic protein, a published and well documented marker of retinal damage and deterioration.

1.7.1   Fluoro-Jade

Fluoro-Jade C (and its predecessors Fluoro-Jade and Fluoro-Jade B) are anionic fluorescein derivatives that are useful for the histological staining of neurons undergoing degeneration (Schmued, Albertson et al. 1996; Schmued and Hopkins 2000; Schmued, Stowers et al. 2005). Although the exact ability of these stains to bind specifically to damaged neurons is still largely unknown, there have been many publications indicating the ability of Fluoro-Jade to stain all degenerating neurons and apoptic cells regardless of the specific insult or mechanism of cell death. Schmued et al. (1996, 2000, 2005) has investigated the use of Fluoro-Jade to stain degenerating neurons in rat and mouse cortical slices that had been damage from neurotoxic insult. Studies in mice and rats have confirmed the fluorescent staining by Fluoro-Jade to degenerated tissue (Chidlow, Wood et al. 2009), damage from ischemia (Olsen and McKeon 2004) and damage by cortical contusions and traumatic brain injury (Eisch,

Schumed et al. 1998; Colombo and Puissant 2002; Anderson, Miller et al. 2005; Duckworth, Butler et al. 2005; Hellmich, Eidson et al. 2007). Damage from mechanical lesions in primates and from cortical slices in Alzheimer's suffers has also shown positive results (Colombo and Puissant 2002).

Cell counts from images stained with Fluoro-Jade are used to determine the extent of damage compared to un-damaged controls. With the ability of Fluoro-Jade to be combined with other stains used for damage investigation (such as GFAP), Fluoro-Jade staining will be attempted. It is expected that Fluoro-Jade and its derivatives will be able to stain any cells that have been damaged by thermal insult as a result of heat dissipated directly into the retinal tissue even though processes of apoptosis and necrosis cannot be differentiated. This staining technique, in combination with other methods, is expected to allow quantification of the effects of sub-threshold heating over prolonged periods. Some publications using Fluoro-Jade as a damage analysis tool are listed in Table A1.5 in Appendix 1.

1.7.2 Glial Fibrillary Acidic Protein

Glial Fibrillary Acidic Protein (GFAP) is a 47000-54000MW cell specific intermediate filament protein whose expression is widely used as an indicator of glial cell response to neuronal injury. With virtually all forms of injury triggering reactive gliosis (a process characterised by changes in astrocyte and Muller cell morphology and increased GFAP production), this staining technique has been widely used as a histological marker of damage. As GFAP is expressed in Muller cells (the structural cells found within the retina) following retinal injury, the use of this marker is thought to be a good measure for thermally induced retinal damage.

Damage caused by inherited conditions such as diabetic retinopathy (Mizutani, Gerhardinger et al. 1998), age-related macular degeneration (Ramirez, Ramirez et al. 2001; Wu, Madigan et al. 2003) and retinal detachment (Okada, Matsumura et al. 1990) have been measured using expression of GFAP as a damage end-point in human tissue. Measurements of damage levels caused by hyperthermia (Caprioli, Kitano et al. 1996), by retinal degeneration and detachment (Erickson, Fisher et al. 1987; Okada, Matsumura et al. 1990; Nakazawa, Takeda et al. 2007; Chidlow, Wood et al. 2009), electrical stimulation (Colodetti, Weiland et al. 2007), retinal vascularisation (Downie, Pianta et al. 2007), electromagnetic irradiation (Eisenfeld, Bunt-Milam et al. 1984), mechanical damage (Bignami and Dahl 1979; Nolte, Matyash et al. 2001), hypoxia and

ischemia (Liu, Smith et al. 1999; Olsen and McKeon 2004) and by neurotoxic insult (Dyer and Cepko 2000; Schmued, Stowers et al. 2005) have all been reported using GFAP expression. This process has been shown to be consistent across species, from fish (Bignami 1984) to cats (Pardue, Stubbs et al. 2001) and humans (Mizutani, Gerhardinger et al. 1998).

With such a large number of species and injuries reported to involve the expression of GFAP, this is one of the methods that will be used to determine the extent of thermal injury that occurs due to the thermal heating of retinal tissue. Some publications using GFAP to determine thresholds of damage are listed in Table A1.6 in Appendix 1. GFAP has recently been used by Colodetti et al. (2007) to determine whether electrical stimulation from their device undergoing clinical trials triggers a glial response. They found that GFAP increased in normal rats as the frequency increased from 2 Hz to 300 Hz with a charge of 0.68 mA/cm^2 (from one hour of biphasic stimulation), increasing further with a charge of 0.1 mA/cm^2 (20 Hz). While GFAP expression was observed, no retinal detachment or disorganisation was seen after 3, 7 or 14 days post trauma.

1.7.3   Microglial Morphology

Microglia, one of the three types of glial cell in the central nervous system and retina, play a key role in mediating immune tissue protection against infection and neuronal insult through secretion of cytokines and other bioactive agents (Soltys, Ziaja et al. 2001; Santos, Martin-Oliva et al. 2009). Retinal microglia are cells restricted to the inner retinal layers (ganglion cell, inner plexiform and outer plexiform layers) and are largely absent from the region extending from the outer nuclear layer to Bruch's membrane. Figure 1.22 indicates microglial presence (labelled in green) in the outer plexiform layer (OPL) between the outer nuclear and inner nuclear layers (ONL and INL respectively) and within the inner plexiform layer (IPL) and ganglion cell layer (GCL).

Microglia exhibit a stratified distribution correlating to the organisation of the retina and have a small cell soma, little perinuclear cytoplasm and a number of fine, branched processes that are covered in numerous protrusions (Figure 1.20). Microglia are highly sensitive to environmental changes and rapidly alter their phenotype to even minor disturbance of nervous system homeostasis caused by infectious disease, inflammation, trauma and brain tumours among other stressors (Kreutzberg 1996; Davalos, Grutzendler et al. 2005; Nimmerjahn, Kirchoff et al. 2005). This activation of microglia

is associated with alterations in cellular morphology, tissue distribution, migratory characteristics, changes in process structure and expression of cell surface antigens (Nimmerjahn, Kirchoff et al. 2005; Lee, Liang et al. 2008) and has been published to occur through a wide range of induced stresses including retinal ganglion cell axotomy, ischemia, photoreceptor degeneration, laser induced retinal damage and endothelin-induced optic neuropathy (Streit, Graeber et al. 1988; Suzumura, Marunouchi et al. 1991; Kreutzberg 1996; Soltys, Ziaja et al. 2001; Davalos, Grutzendler et al. 2005; Nimmerjahn, Kirchoff et al. 2005; Langmann 2007; Ransohoff and Perry 2009).
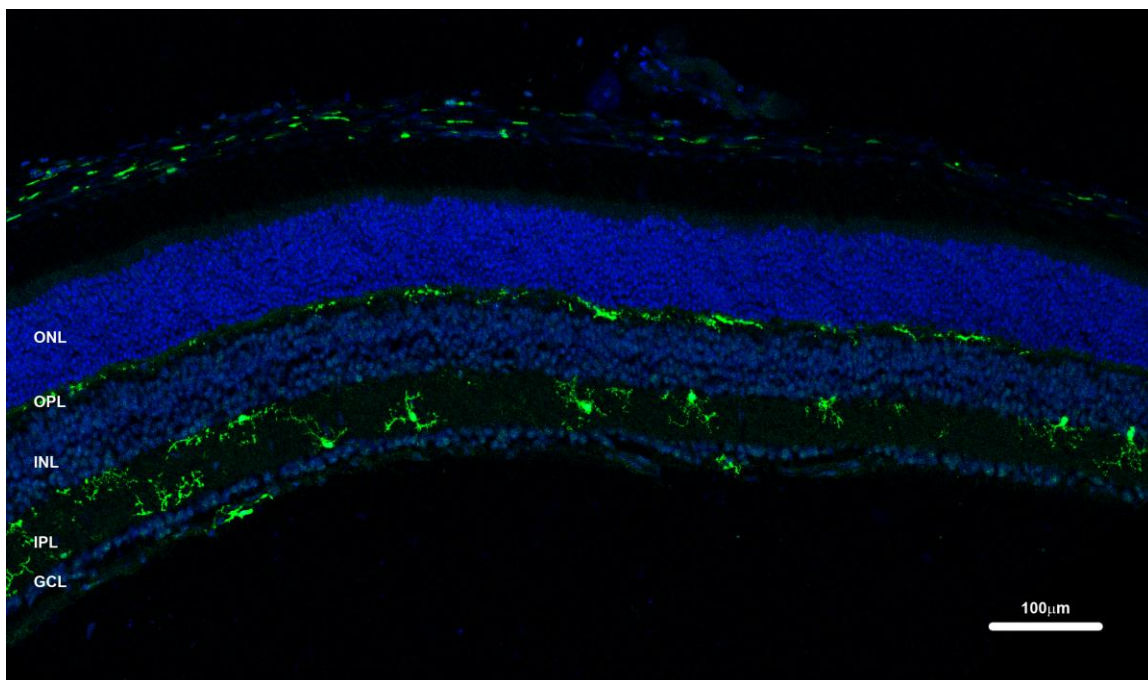
Figure 1.20. Presence of green labelled microglia in a rat retinal cross-section, located in the inner plexiform and ganglion cell layer (IPL, GCL) and in the outer plexiform layer (OPL) between the outer and inner nuclear layers (ONL, INL). Image courtesy of K.Vessey.

Once microglial cells have been alerted by endogenous triggers to disturbances of their local environment, they undergo proliferation, migration, enhanced phagocytosis and secretion of cytokines, chemokines and neurotoxins (Kreutzberg 1996; Langmann 2007). Morphological changes to normal, ramified microglial cells include a decrease in number and retraction of primary and terminal axonal processes, increases in soma volume, and a progressive loss of fine dendritic protrusions. This progression from a ramified (to hypertrophied) to a bushy microglia cell is shown schematically in Figure 1.21.
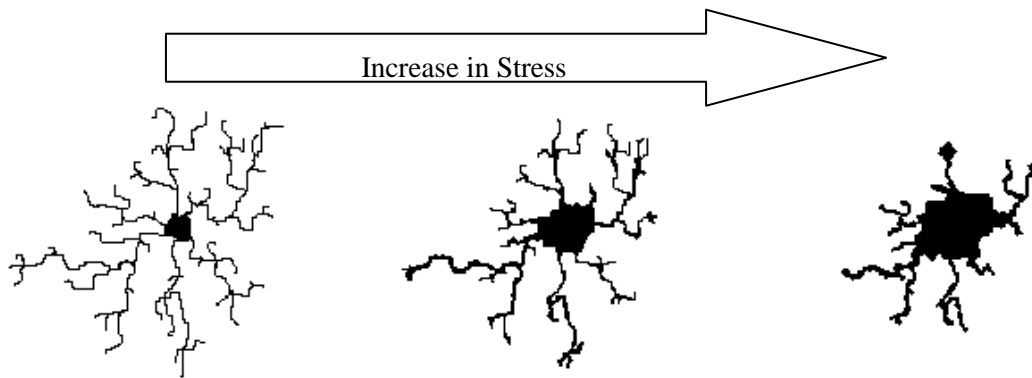
Figure 1.21. Examples of morphological types of microglia: ramified (left), hypertrophied (centre) and bushy cells (right), indicating an decrease in arbour area and an increase in soma area as the microglia alter their morphology due to stress.

Microglial protrusions have also been shown to be directed preferentially towards a site of injury. In a study performed by Lee et al. (2008) using Argon laser to induce retinal damage, microglial cells responded to the injury by directing processes towards the injury site and by extending new process towards the laser induced lesion, withdrawing processes on the side furthest from the injury. This is shown in Figure 1.22, with almost complete tropism occurring 393 seconds after the onset of injury.

Publications that have used microglial morphological changes to analyse damage occurring to retinal tissue has been performed in mice and rats over a range of stresses and some of these are listed in Table A1.7 in Appendix 1. It is expected that damage caused by thermal energy dissipation into retinal neurons will provoke the same activation response from resting microglia, changing their soma areas and dendritic spans in accordance with the degree of damage caused. Differences in the areas of microglia, combined with analysis of the arbour area will be used to investigate thermal damage thresholds and mechanical damage levels arising from the implantation of a heating element, assisting to determine safe power budgets for permanently implanted retinal prostheses.
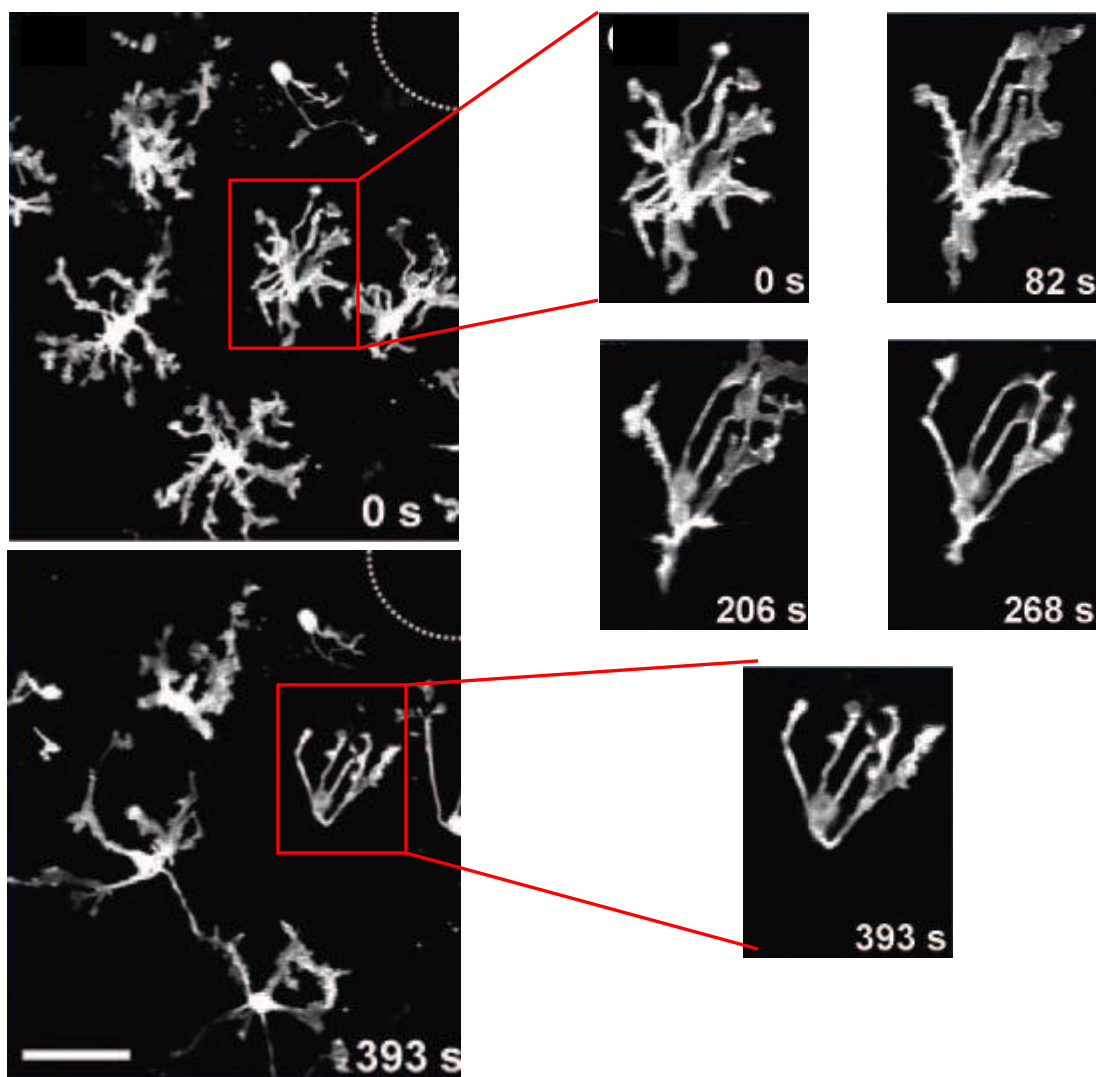
Figure 1.22. Morphologic responses of microglia to focal laser injury showing high magnification of microglia and site of laser injury (dotted circle) immediately and 393 seconds after laser injury and progressive morphological change in response to injury after 0, 82, 206, 268 and 393 seconds. Image adapted from Lee at al. (2006).

1.8   CONCLUSIONS

Light reflecting off objects in our visual scene is focussed and traverses through the accessory structures of the eye to the photoreceptors within the retina, where the membrane folds and disks in the photoreceptor outer segments convert light energy into electro-chemical signals by the process of photoisomerisation. These signals pass through the rich interconnectivity of horizontal, bipolar and amacrine cells, condensing information from over 100 million photoreceptor inputs to 1.2 million ganglion cell outputs, whose axons form the optic nerve and pass the signals from the eye to higher cortices where the signal is further refined and processed to give us our sense of vision. Persons suffering from AMD and RP have damaged photoreceptors, and will lose vision until completely blind. These patients however, do have many remaining interneurons and ganglion cells and it is these cells that are targeted by electrical stimulation to enable perceptions of the outside world.

There are three main target regions being addressed to enable phosphene perceptions of the visual field by electrical stimulation, each with their own advantages and disadvantages. Electrical stimulation of the cortex (and lateral geniculate nucleus in the thalamus) would enable perception to be delivered even in cases where the optic nerve or eyes have been completely damaged or removed, although lose the initial stages of processing that occurs within the retinal interneurons. Similarly, optic nerve stimulation is able to account for ganglion cell dystrophies, but is limited in the space and potential to stimulate a large number of independent neurons. Stimulation within the eye, either epiretinally, suprachoroidally or subretinally enables the use of interneuron processing. Each of these locations within the eye also has distinct advantages, from simplified surgical procedures (suprachoroidal and subretinal) to reduced charge requirements (due to the close proximity of an epiretinal implant to ganglion neurons), and disadvantages alike.

In each of the implant types, the number of electrodes will essentially determine the resolution that the device is capable of, with increased numbers leading to increased visual acuity (neglecting possibilities of current steering). As electrode numbers increase, the potential for neurons in close proximity to the electrodes or electronic circuitry have increased risk of being adversely affected by thermal heat dissipation. While current clinical trials have not suggested this is a major problem, future designs with an increased electrode numbers, reduced distances between electrodes, electronics

and neurons, and the use of the visual prostheses for up to eighteen hours of the day in an already diseased retina may be an issue.

Tests performed to investigate the threshold levels for electrical stimulation and temperature increases have been generally only applied to electromagnetic irradiation, whole body incubation, laser thermal damage and direct conductive heating. These types of tests have a large number of dissimilarities between the animal models and tissues used, the age and progression of any diseases, body and room temperatures, test durations, levels of anaesthesia, methods of inducing thermal stress and the damage assessment methods. Each of these factors can have large effects on thermal damage thresholds, particularly when attempting to determine a thermal threshold for a retinal prosthesis to be implanted permanently in a human with a predisposition to retinal damage. Thus, experiments performed to

Methods of damage analysis were also investigated, with many studies investigating cellular damage or change using histological techniques such as Fluorescein Angiography, Fluoro-Jade staining, up regulation of glial fibrillary acidic proteins and the changes in cell morphology occurring to microglial cells when they or neighbours were stressed. Each of these testing methods, combined with the knowledge gained from published experiments and data should allow the construction of equipment and testing protocols that give the best chance of being able to correlate thermal damage data, with thermal model simulations to ensure that normal operation of a retinal prosthesis is safe, both for the implant and the patient.

2

EQUIPMENT DESIGN AND CALIBRATION

The equipment that has been designed and constructed to accurately induce and measure thermal changes in the eye in order to assist with the determination of thermal damage thresholds is discussed in this chapter. The ability to ensure that the equipment is functioning properly and accurately is of high importance in determining the connection between the histologically measured damage and increases in retinal tissue temperature. The correlation between safe and potentially damaging temperatures can then be related to the amount of power dissipated by implanted circuitry in close proximity to the delicate neural tissue and can be used to guide retinal prosthesis designs via acceptable power budgets.

The major pieces of equipment required for temperature measurement include implantable temperature sensors and a high resolution temperature measurement system, capable of measuring and recording multiple temperature changes simultaneously and in real time. An implantable heating element and current sources are also required to deliver the power to the tissue to induce the desired temperature increases.

Due to the highly stable, linear and repeatable behaviour of platinum resistance temperature detectors (PRTDs), these sensors were chosen to measure induced thermal changes in retinal tissue.

Implants were designed and constructed to be as close as possible to current designs of epiretinal and suprachoroidal visual prosthesis. The implants, manufactured on a flexible polyimide substrate, were of similar dimensions to current designs, with heating element areas also similar to current sizes of electrode stimulating chips. The implants were designed to be able to be implanted using identical surgical techniques to current prostheses and were shown through cadaver trials to meet this criterion. To induce and measure temperatures from multiple sites simultaneously, devices were built with multiple sensor locations and heating locations, with a range of implants allowing up to 9 sensor measurements, 5 heating elements and the ability to alter the size of the heating elements if desired. Through infra-red thermography of the implants, it was observed that the power dissipated by the heating elements will remain contained to the area covered by the heating element. Lead wires connecting the current source to the implant were not shown to heat up to levels that would compromise thermal measurements along the implant shaft.

Calibration of the temperature measurement system, conducted over multiple independent trials and over heat bath temperatures ranging from 33°C to 44°C, indicated the linear voltage-temperature conversion equations were highly repeatable, with an average temperature error of ±0.002°C. Both the high and low current sources constructed were also shown to be repeatable and accurate, with the low power current supplies outputting currents with a maximum fluctuation of 2.4 mA.

The designed current sources, measurement system and implants were shown through cadaver trials (Chapter 4) to be able to induce and measure multiple thermal changes occurring within a cat eye, simultaneously and in real time and are expected to perform equally well when used in living tissue in which thermally induced damage can be analysed.

2.1   SENSORS

To accurately measure and record temperature deviations from the retinal cells at the back of the eye under the influence of dissipated heat from a retinal prosthesis, sensors must be chosen and positioned so as to cause minimal trauma while obtaining accurate measurements.

2.1.1   Infra-red Thermography

Infra-red thermography is one method of non-contact temperature measurement which can be performed without inducing additional mechanical damage. Measurements of implantable-device-induced thermal increments has been studied and published, indicating that this type of non-contact measurement can be very accurate and repeatable for measurements of cortical surface temperature increases (Jiang, Ng et al. 2005; Kim, Tathireddy et al. 2007; Kim, Tathireddy et al. 2007) corneal surface temperatures (Murphy, Patel et al. 2001) and retinal whole-mounts (Reitsamer, Groiss et al. 2000).

One drawback of using infra-red imaging to measure temperatures is the severely limited ability to record thermal increments at distant locations through a fluid filled cavity, such as the retinal tissue at the back of the eye. The ability of this method to accurately measure retinal tissue temperatures is also hindered by the possibility that back-scattering and absorption of the laser light may induce retinal tissue heating and damage in undesired areas. This was shown by Scott (1988) who reported that the cornea and aqueous humor strongly absorb infrared light in excess of 1400 nm, with temperature measurements recorded above the baseline temperature as a result.

2.1.2 Thermocouples

Thermocouples, one of the oldest and most common methods of temperature detection are becoming increasingly prevalent in the biomedical field with a plethora of alternative uses. Determination of the temperatures required to produce heat shock protein 90 expression in rabbits was measured using a rectal thermocouple probe (Quraishi and Brown 1995) with thermocouples also used to measure thermoregulation under anaesthesia (Kurz, Sessler et al. 1993), thermal tissue damage thresholds in rabbit muscle caused by sonications (McDannold, King et al. 2000) and the thermal ablation of tumours using transpupillary and transscleral thermotherapy (Miura, Nishiwaki et al. 2003; Rem, Oosterhuis et al. 2003; Ibarra, Hsu et al. 2004). Thermal increases have been measured with thermocouples investigating the effects of 2 MHz radio-frequency current induced hyperthermia on equine and rabbit corneas (Neumann, Kainer et al. 1982; Bhatt, Peyman et al. 1993), by high intensity light in rabbit fundus (Cain and Welch 1973; Welch 1984), infrared laser irradiance on rabbit retina (Sailer, Shinoda et al. 2007) and argon lasers in rabbit retina and rhesus monkey (Polhamus and Welch 1975; Welch and Polhamus 1984). Thermocouples have also been employed to measure thermal elevation of retinal prosthesis microchips implanted on the sclera in canines (Singh, Roy et al. 2008) and to measure the temperature increase of canine eye tissues under the influence of a heating element implanted in the posterior chamber (Piyathaisere, Margalit et al. 2003).

While thermocouples have a very broad temperature measurement range and are limited in manufacture size only by wire gauge (and a thin surrounding sheath), these types of sensors require a reference temperature, measuring the thermal differential between the reference and the source (Bronzino 2000; Bajzek 2005). The accuracy and stability of thermocouples can only be assured if the thermoelectric characteristics of the thermocouple conductors are uniform throughout experiments. Thermocouples have a non-linear temperature-voltage output and have a limited ability to be soldered to an implant, with the solder-copper wire connections also inducing temperature dependant voltage differences (Bronzino 2000; Bajzek 2005). Thermocouples can also have long term drifts with exposures to high temperatures due to oxidation-caused chemical changes and may express short term cyclic changes in thermal emfs generated by the heating and cooling of the base metal which can induce both magnetic and structural inhomogeneties (TC 2008).

2.1.3 Thermistors

Like thermocouples, thermistors have long been used as temperature measurement sensors. They have applications ranging from thermal measurements used to predict and detect cardiac arrhythmias (Philip 1984; Caudras 2006), safety measurements of the thermal increases caused by mobile phone usage (Tahvanainen 2007) and deep brain stimulator lead heating (Elwassif, Kong et al. 2006). Stimulus-activated thermal changes in the brain have also been studied using thermistors (LaManna, McCracken et al. 1989) as have measurements of blood pressure and perfusion rates (Valvano 1985; Anderson 1992). The effect that thermal energy has on tissue morphology caused by chronic heating has been reported with thermistors (Seese, Harasaki et al. 1998), with thermal gradients in rabbit eyes also being studied using thermistor temperature measurements (Schwartz and Feller 1962).

Thermistors and resistance temperature detectors (RTD) require a current to flow through the sensor for temperatures to be measured, and this power can be dissipated in the component causing additional heating. This heating effect in turn can cause the resistance of the thermistor to decrease and is known as the self-heating effect. While self-heating can be problematic, if the power level is moderate (using only small currents for measurement) this self-heating effect will not continue indefinitely as a thermal equilibrium with the environment will be reached (Sapoff 1963; Zurbuchen 2000). The power dissipated in a thermistor (and RTD) causes its temperature to rise above ambient according to:

$$\Delta T = \left(I^2 R_{RTD} \right) \times \theta$$

(2.1)

where the change in temperature, ΔT, is related to the square of the current passing through the thermistor, I, the thermistor or resistance temperature detector resistance and R_{RTD}, the self- heating effect, θ, in °C/mW.

Apart from having a non-linear response, another problem with the use of thermistors is reliability. Thermistors can tend to drift, changing resistance at a fixed temperature due to changes between the interface of the thermistor and its contacting mechanisms and oxygen transport phenomenon. This was shown by Trolander (1962) to cause a thermal

shift of up to a quarter of a degree over a twenty hour period, with the amount of shift also related to the temperature being measured.

Thermistors however do have high sensitivity to small temperature changes, small mass and a good thermal conductivity. By varying the types of oxides, their ratios in combination with each other and the temperatures at which they were sintered, different thermistors can be made to have ranges of levels and tolerances, with accuracies an order of magnitude or more sensitive than common thermocouples (Bronzino 2000).

2.1.4   Resistance Temperature Detectors

Resistance temperature detectors are one of the newest types of sensor to be used and, as such, there are very few publications on biomedical applications. These sensors, while having an inherently simple method of temperature detection, are more difficult to make than thermocouples and thermistors, especially in the size required for implantation into the eye. Operation of the RTDs essentially involves the measurement of the electric resistance of a piece of metal or a wire, which generally increases as the temperature of the electric conductor increases. This enables temperatures to be recorded through measurement of resistance in a linear fashion.

The most common metals and alloys used for resistance temperature detectors include platinum, gold, silver, copper, constantan and nichrome. These metals, chosen for their linear temperature-resistant behaviour, have temperature coefficient of resistances between 0.0002%/°C (constantan) to 0.3%/°C (copper) and a resistivity of between 108 mΩ·cm (nichrome) to 1.629 mΩ·cm (silver). Noble metals are preferred for RTDs as they do not corrode easily and, when drawn into thin wires, their cross section will remain constant and can avoid measurement instabilities caused by a change in resistance over time (Bronzino 2000). Platinum is an ideal material for RTDs as it is has a very wide un-reactive temperature range, a high resistivity and has a linear temperature-resistance relationship due to the superior thermal and temperature characteristics of platinum (Chung 2008). Further, it can be obtained in a highly pure form which reduces impurities (and thus resistive variations) within the RTD (TC 2008).

There are many types of platinum RTD sensors (PRTDs) with one of the most common being in the form of a thin wire wound in helical form around a ceramic bobbin, supported by frictional contact in a closely fitting, thin walled glass tube. This design aims at making a strain free thermometer which can expand and contract on heating and cooling without the wire rubbing or being stretched by its support. Smaller, more recent PRTD construction, involves deposition of platinum onto a ceramic substrate, and can be of two types: thick film and thin film. Thick film sensors are produced by silk screen printing a glass/platinum paste onto a substrate while thin film production uses vacuum semiconductor fabrication techniques to evaporate platinum onto the substrate.

Due to the small size of these sensors, they have an increased thermal response, are generally more insensitive to vibration and are cheaper than common wire wrapped PRTDs. Disadvantages over this type of PRTD includes the inability to expand and contract as easily as wire wound RTDs (and hence there may be stability concerns over large temperature ranges and extended use) and are more prone to contamination as they require less metal. Manufacture of thin film sensors may also produce irregularities, with annealing temperature and film thickness affecting the temperature coefficient of resistance (Kim 2001; Imran 2006). A representation of a thin-film and wire-wound RTD is shown in Figure 2.1, indicating the placement of the platinum on the ceramic substrate.
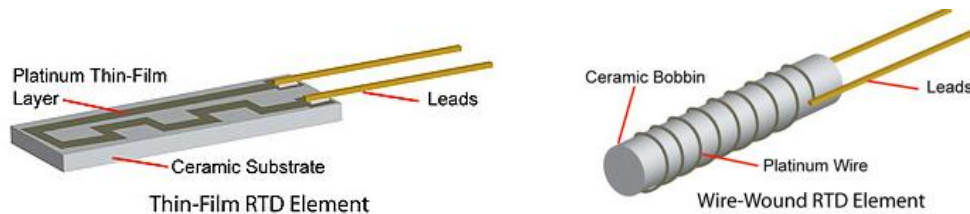
Figure 2.1. Thin-Film and Wire-Wound platinum resistance temperature detectors showing the platinum wire embed in a ceramic substrate or wound around a ceramic bobbin and connected to lead wires (WTWH-Media 2009)

International standards regulating the manufacture of PRTDs reduce these potential errors and provide an approximately linear resistance-temperature profile governed by the Callander-Van Dusen (CVD) equation for temperatures over 0°C,

$$R_t = R_0 \times \left(1 + At + Bt^2\right)$$

(2.2)

where R_t is the resistance at temperature t, R_o is the resistance at a temperature of 0°C and the coefficients A and B are equal to 3.9083×10^{-3} °C^{-1} and -5.775×10^{-7} °C^{-2}, respectively.

While this gives an accurate resistance values for a known temperature, the ability to devise a method of interpreting temperatures based on resistance measurements will be required. Relating temperature to a resistance measured from an RTD can be erroneous if self-heating errors and lead wire connections are not taken into account, with uncompensated leads increasing resistance and hence altering the actual temperature measured. This can be reduced by appropriate connectivity, with a four wire Kelvin connection essentially negating any differences in lead wire resistance.

2.1.5   Sensor Choice

While all the fore-mentioned sensors would be appropriate in measuring temperature elevations in retinal tissue, the chosen sensor will have to sufficiently fulfil the following primary requirements. These include having a high level of accuracy, a predictable and repeatable performance, the ability to be implanted in identical positions over trials, low cost and reliable performance and small enough size for multiple sensors to be inserted to simultaneously record temperatures in an eye of similar size to that of a human.

All sensors mentioned have a high level of accuracy within the temperature range used in these experiments (between 35°C and 45°C), with thermistors having a much larger change in resistance to changes in temperature than either an RTD or a thermocouple junction. However, thermistors and thermocouples both have a highly non-linear temperature-resistance (or temperature-voltage) profiles when compared with PRTDs. While all the sensors can be produced small enough to fit into the orbital cavity, the ability to be soldered onto a backing board will allow for stable placement and a more repeatable design, which favours both the thermistor and RTD sensors. Reliability of the sensors also favours RTDs with current international standards ensuring quality of PRTD manufacture. PRTDs however are the most expensive of the three sensor types. Table 2.1 lists properties of sensors desired for use in measurement of retinal tissue temperatures for all three sensor types.

Table 2.1. Comparison between thermistors, thermocouples and platinum resistance temperature detectors.

Consideration	Thermistor	Thermocouple	PRTD
Accurate	Yes	Yes	Yes
Suitable Temperature Range	Yes	Yes	Yes
Cheap	Yes	Yes	No
Fast Response Speed	No	Yes	Yes
Long Term Stability	No	No	Yes
Appropriate Size	Yes	Yes	Yes
Reference Required	No	Yes	No
Power Supply Required	Yes	No	Yes
Self-Heating	Yes	No	Yes
Surface Mounted	Yes	No	Yes
Linear Response	No	No	Yes

Surface mounted platinum resistance temperature detectors fit all criteria for sensor selection, ability to be soldered, have internationally standardised performance, linear characteristics, small, cheap and do not require an additional, known, temperature reference. The primary drawbacks, however, include the cost, the requirement of a power source and self-heating effects. As the long term drift is almost negligible, the sensors can be re-used in experiments which will reduce the costs required, and by ensuring the sensors have reached thermal equilibrium within the immersed medium, the effects of self-heating can be accounted for. Some specifications and dimensions of the surface mounted Platinum Resistance Temperature Detectors, manufactured by Heraeus Sensor Technologies Inc. are provided in Table 2.2.

Table 2.2. Properties of Heraeus 0603 platinum resistance temperature detectors (Type 2B)

Property	Specification
Length	1.7 ± 0.1 mm
Width	0.85 ± 0.1 mm
Depth	0.45 ± 0.1 mm
Temperature Range	-50°C to 130°C
Temperature Coefficient	3850 ppm/°K
Class	2B
IEC Specification	DIN EN 60751-1998
Reaction Time	$t0.5 < 0.1$ seconds
Self-Heating Effect	< 0.4 °K/mW
Measuring Current	0.1-0.3 mA
Tolerance	$\pm (0.1 + 0.0017 \, |t|)$ °K
Nominal Resistance (R_0)	1000Ω (at 0°C)

The length and width of the PRTD is considered acceptable for thermal measurements within the small confines of an eye, with a 0.45±0.1 mm maximum height (or depth)

experimentally shown to be acceptable for implantation in the suprachoroidal space of cadaver eyes (Chapter 4). The fast response time will allow for almost instantaneous thermal measurements and the well regulated temperature coefficient will ensure that all sensors are accurate, interchangeable and will measure temperatures consistently. Using the recommended measuring currents of 0.1-0.3 mA, the self-heating effect of the 1000Ω PRTD will be between 0.004°C and 0.036°C, with a tolerance of between 0.1595°C and 0.1765°C within the desired 35°C to 45°C temperature range and follow a very linear profile with the resistance increasing by 3.8505Ω/°C.

2.1.6   Second Order Linearisation

While the accuracy of the PRTD can be assured through international standard IEC-EN 60751-1998, this standard only provides a resistance-temperature profile for intervals of 1°C. To be able to optimally determine thermal elevations that cause retinal damage, temperature deviations of at least 0.1°C are desirable. To enable smaller intervals than those of 1°C specified, a process called second order linearisation can be employed. This process assumes a linear relationship between successive points and allows for approximations of temperature to the tenth of a degree (or better where required).

The second order linearization program shown in Appendix 2 was written in Matlab 7.0.4 (Mathworks Inc.) for fast and easy translation between measured resistances (as specified by Heraeus) and absolute temperatures. This allows for calculations of temperature to within the desired 0.1°C accuracy for resistances spanning a one to sixty degree temperature range. To ensure that this second order linearization is as accurate as the Callander-Van Dusen equation used by the international standards, differences between resistances calculated by the two methods over the temperature range expected to be used are compared. Figure 2.3A and Figure 2.3B indicates the resistance-temperature profiles between the two methods, with Figure 2.3C indicating a maximal difference between the two methods of less than 0.005 Ω (0.0013°C) over the range 31 to 47°C.

A   B   C
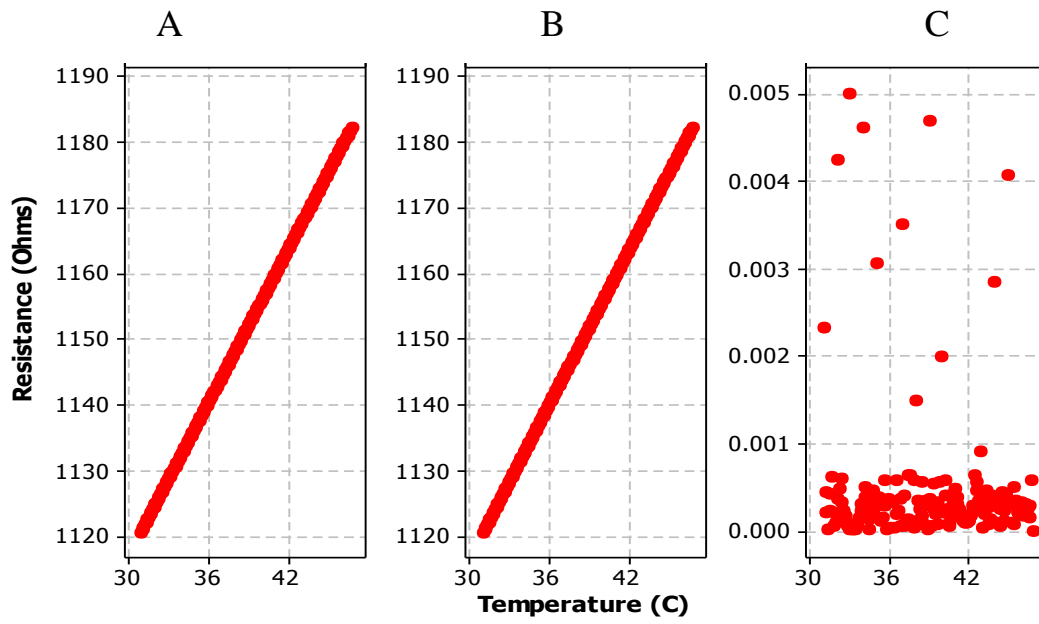
Figure 2.3. Resistance temperature profiles from **(A)** the second order linearization method, **(B)** the Callander-Van Dusen equation and **(C)** the resistance differences between the Callander-Van Dusen and second order linearisation temperature correlation methods over the temperature range 31°C to 47°C.

2.2   IMPLANT DESIGNS

To mimic the potential retinal temperature increases that may occur due to normal operation of a permanently implanted visual prosthesis, a device that imitates the current prosthesis designs is required. Both the size and implant location must be similar to expected commercial devices, with the ability to induce thermal changes over an area similar to the dimensions of a prosthesis of high importance. For the heating element to be effective in assessment of maximal power budgets and safe temperature increases allowable by a retinal prosthesis, the following design parameters have been set:

1)   The implant must have the versatility to replicate both suprachoroidal and epiretinal implants, and must have the ability to be inserted using surgical techniques identical to those used in the current retinal prosthesis implantation. The implant should also conform to current electrode designs in terms of implant stiffness, width and thickness and should imitate current prostheses regarding the active electrode area and the implant area as a whole, whist having the versatility to adapt to future retinal implant designs. Further, the implanted device must be able to withstand the harsh environment of the eye without effecting its performance or ability to imitate a retinal implant, and similarly must not cause any adverse and uncontrolled biological reactions while implanted (with the exception of induced mechanical and thermal trauma).

2)   The heating element must be able to deliver powers comparable to current literature and designs (detailed in Chapter 1) and should directly affect tissue temperature through conductive transfer of thermal energy, in temperature increments of 0.1°C or less.

3)   The measurement system must be able to run without requiring mains power and should be small and light enough to be portable. The measurement system should have a resolution of at least 0.1°C, be reliable, repeatable and reusable for the duration of the project and must be designed to allow for multiple simultaneous recordings of temperature measurements in different locations

surrounding the heating element and able to record the measurements accurately and in real time

The implant designs were constructed using Altium Designer 6 (Altium Ltd.) and were manufactured by The PCB Company Pty. Ltd. using 15 oz copper tracks embedded into a polyimide substrate. The thickness of each of the layers as specified by the PCB Company, are shown in Figure 2.4 for a two-sided board. The top (and bottom) layers include 12 μm solder masks on 35 μm layers of copper (18 μm base copper layers on 17 μm copper plate layers), which are joined to 25 μm polyimide layers via 20 μm of adhesive. This gives a total thickness of 159 μm for both layers and has been shown though initial cadaver trials to be an appropriate thickness: not too thick that flexibility is compromised and not too thin that surgical implantation would require an inducer to avoid implant buckling.

	Thickness (μm)	
	12	Solder Mask
	18	Plate Copper
↑	17	Base Copper
Layer 1	20	Adhesive
	25	Polyimide
Layer 2	20	Adhesive
	17	Base Copper
↓	18	Plate Copper
	12	Solder Mask

Figure 2.4. Layer dimensions of the double sided flex-PCB implants, with two copper layers (each made from a base and plate copper layer) separated by two layers of adhesive. Each side is also coated in a solder mask.

All the implants take advantage of the strong and flexible printed circuit boards whose mechanical properties are similar to current implants used in animal trials (Sachs, Schanze et al. 2005; Seo, Paik et al. 2006; Burkitt 2010; Suanning and Lovell 2010). In addition to the above layers, some of the PCBs have a gold overlay to reduce the potential for the copper tracks to corrode and allow for a much more durable solder attachment.

A schematic example of the desired function of an implant is shown in Figure 2.5, where 30 mW of power dissipation through the red heating element induces a region of damage (yellow). Tissue temperature, measured by PRTDs located along the implant

shaft, allows for a correlation between tissue damage and temperature and thus a power budget can be created to advise retinal implant designers.
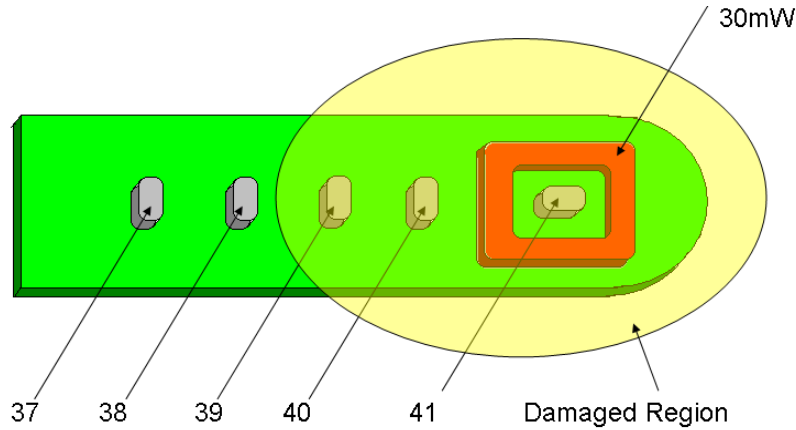
Figure 2.5. Schematic of how 30 mW of thermal energy dissipated by the heating element (red) may induce temperature increases of 41°C at the central temperature sensor (grey) and 40°C, 39°C, 38°C and 37°C at temperature sensors located down the flexible PCB shaft (green). A possible area of damage is shown as a yellow area and comprises of temperatures above 39°C.

2.2.1   Copper Coil Heating Element Implants

The initial heating element designs used current flowing through thin copper tracks embedded within the polyimide substrate to increase the temperature of retinal tissue. Single and multiple heating element implants were designed, with effective areas (circumference of the heating elements) ranging from 5 × 5 mm to 5 × 8.5 mm. Two designs were constructed using copper coils as heating elements. The initial design (CC − 1) was used to determine the feasibility of a copper coil heating element to induce thermal alterations in tissue, with the second design (CC − 2) enhanced with additional locations for temperature measurements, superior connections to current sources and measurement equipment and an additional heating element.

2.2.1.1   CC - 1

The initial manufactured heating element design used a 0.25 mm wide copper coil track as a heating element to induce temperature increases in adjacent tissue. The heating element had a total length of 72.57 mm, spanning an area of 5.08×8.50 mm with a total active area (area covered directly by the copper heating element) of 18.14 mm^2.

The element was connected to external leads through 1 mm solder holes for connection to current sources and temperature measurement equipment. The implant had a total width of 5.5 mm with an implantable shaft 75.35 mm long, designed to easily accommodate for a 17 mm insertion into the globe and to allow ample room for a connection pad and mid-shaft anchorage to a stereotaxic frame, if required to maintain a stable head position during *in vivo* trials. To reduce the potential for the lead wires that carry current to the heating element themselves heating up and inducing thermal damage to retinal tissue, these wires were positioned on the opposite side to the heating element, facing the vitreous fluid. These tracks were twice as thick as those used in the design of the heating element, 0.5 mm, which increased the surface area and reduced the resistance (and thus power) by a factor of four.

Six Heraeus SMD 0603 platinum resistance temperature detectors (sensors) could be attached to the implant, one in the centre of the heating element, one 2.78 mm from the heating element (heating element edge to sensor edge), and then at 2.1 mm intervals to allow temperature measurements across a 20.28 mm distance. With multiple sensors located at increasing distances from the generated heat, it is expected that this implant will be able to measure temperature gradient from the heating element and diffusion properties of the tissue and intermediate fluids. A photograph of the manufactured copper coil implant is shown in Figure 2.6.

Initial implant trials on cat cadaver eyes have shown the heating element thickness is such that no buckling of the implant occurred during insertion whilst being flexible enough to conform to the curvature of the eye. These trials also demonstrated that the differences in dimensions of the heating element when compared to current electrode arrays (additional height compared to electrode arrays due to addition of sensor elements) do not compromise the surgical implantation procedure, with a thin layer of conformal coating sufficient to taper the sensor height so as not to catch on neighbouring tissue while being inserted.
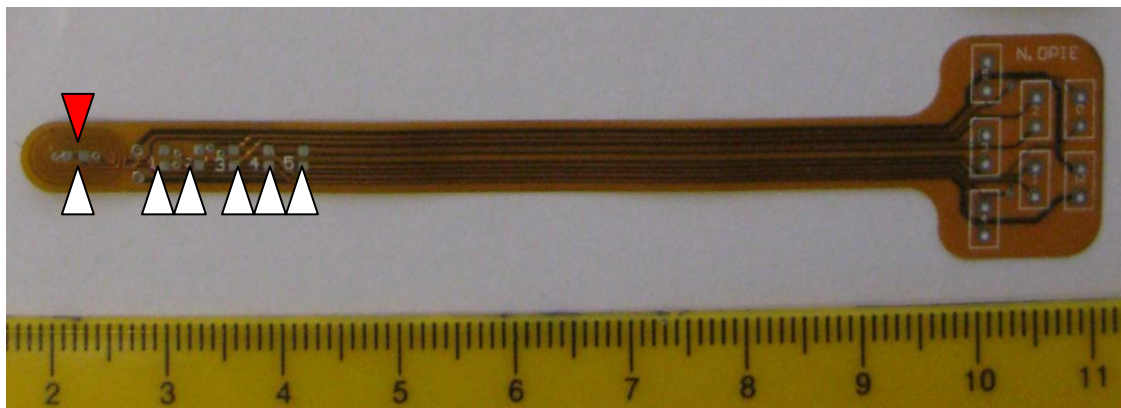
Figure 2.6. Single copper coil heating element implant showing the heating element (red marker) and the locations of the six temperature sensors (white markers).

Pre-trial testing of the implant was carried out using infra-red thermographic analysis. This was performed to ensure that the heating element implant could heat up to the temperature levels expected to be on the threshold of thermal damage limits and thus ensure that the implant would be an appropriate representation of the stimulating circuitry required to be built on the implanted retinal prosthesis chip. Excessive heating of the lead wires, however, was a concern using this design with wires passing current through from the current source to the copper coil observed to heat up. This is shown in Figure 2.7, and while the level of heating is not as substantial as that of the copper coil, the ability to restrict thermal dissipation to the heating element only is compromised with tissue adjacent to the lead wires also being heated.
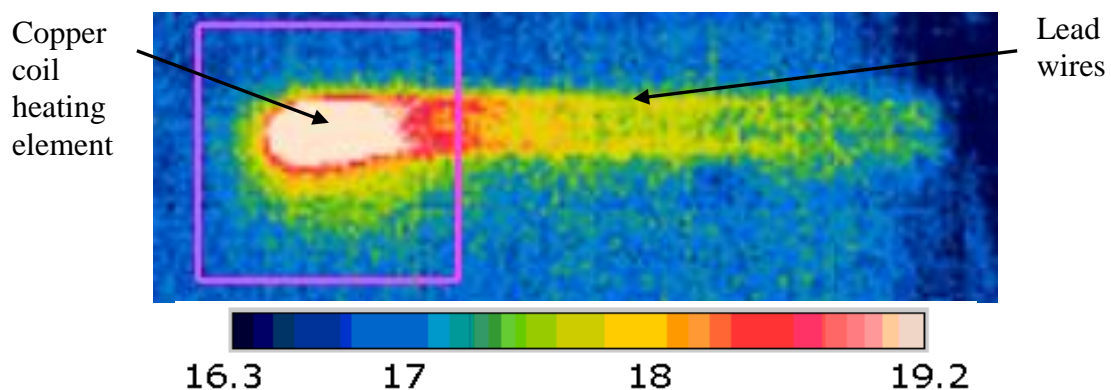
Figure 2.7. Thermographic image of the copper coil heating element implant, indicating the temperature increases observed at the site of the heating element (white region) with clearly defined lead wire heating (yellow tracks). Pink outline represents camera focus area.

2.2.1.2 CC - 2

To reduce the potential for lead wire heating to cause erroneous damage measurements, an implant was constructed with a 0.1 mm thick copper coil heating element, increasing on 0.25 mm steps to a 1 mm lead wire. A schematic diagram of this design is shown in Figure 2.8 with the red tracks indicative of the heating element and connections to the attached current source.

Retinal tack holes were positioned at a distance of 2 mm from the edges of the heating elements to assist in anchoring the device in place when used in an epiretinal setting, and at intervals corresponding to the locations of the PRTDs. The attachment of an implant to the retina to ensure that contact is made when the eye moves is more difficult in an epiretinal scenario compared to a suprachoroidal setting. To overcome this, titanium tacks are currently being used and are common practice for use in repairing retinal detachments prior to laser surgery (DeJuan, McCuen et al. 1986), with tacks having been reported to induce a loss of photoreceptor outer segments and retinal disorganisation within a 750 μm radius (Ohira, deJuan et al. 1991; DeJuan and Crittenden 1994; Majii, Humayun et al. 1999; Gerding, Taneri et al. 2001; Seo, Paik et al. 2006). The tacks used to anchor the implant to the retina, produced by Geuder (Heidelberg/Germany (No. 33437T)), are composed predominantly of titanium (90.02%), are 2.4 mm long with a 1 mm long rectangular spike (0.8×0.35 mm) that penetrates into the tissue (Gerding, Taneri et al. 2001). Retinal tack holes used had a 0.6 mm internal diameter and were surrounded by a 0.1 mm copper ring for additional support. To ensure that the damage caused by the tack insertion does not influence the thermal damaged caused by the heating elements, the tacks have been positioned at least 1 mm (and up to 2 mm) away from locations where tissue will be sampled. Cadaver trials using the retinal tacks have indicated that circuit board vias of 0.35 mm diameter are sufficiently large to allow penetration of the tack through the implant and tissue while ensuring a firm clamping of the heating element to the tissue (the implant cannot slide off the tack).

Seven sensors, located centrally to the two 5×5 mm heating elements and at 1.16 mm intervals from the edge of the heating elements, were positioned on the opposite side of the implant to the heating elements. This allows for a flush contact between the implant and the retinal tissue surface. The lack of any components on the heating element side should reduce the mechanical trauma caused by insertion and tacking of the implant to a

minimum, with the damage measured from histological sections representing damage caused by thermal energy dissipation only. While it may be expected that placing sensors on the opposite side to the heating element (and retinal tissue) would cause slight variations in temperature measurements, saline bath experimentation indicated this was not the case, with no difference in temperatures observed when PRTDs attached in identical positions on opposite sides were measured.
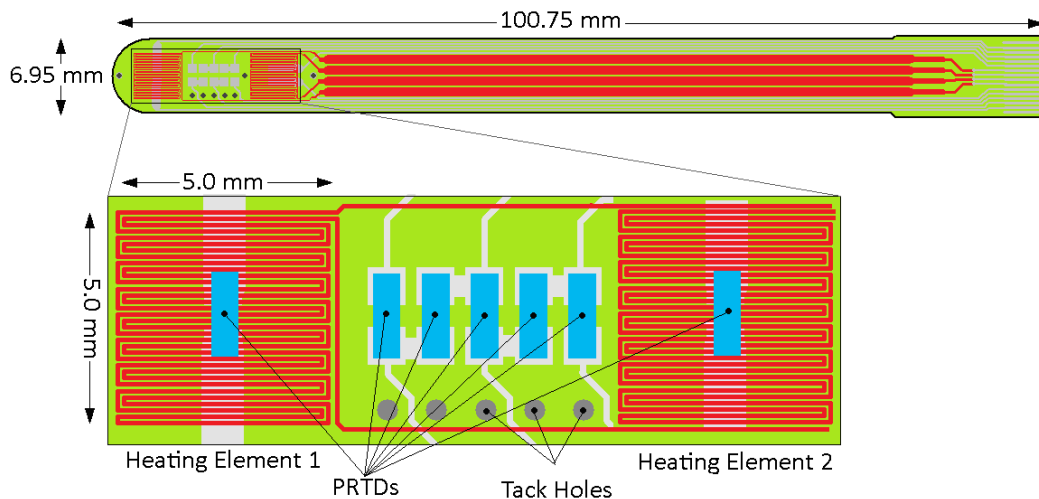
Figure 2.8. Double copper coil heating element epiretinal implant, indicating the entire implant length (100.75 mm) and width (6.95 mm) and the two 5 × 5 mm heating elements (red) and the centrally located PRTD temperature sensors (blue) and tack holes (grey).

The double copper coil heating element design also utilised zero impact force (ZIF) connection pads, allowing for easy attachment and removal of the implants to current sources and measurement equipment. Four wire Kelvin connection was available through use of a designed splitter attached to the ZIF connector, and while mismatches in lead wire resistance within the implant will not be accounted for, these minute dissimilarities are expected to be negligible as the implant leads are symmetrically identical in widths and lengths. This implant was used in the *in vivo* cat tissue experiments (Chapter 5) and indicated that the size, flexibility and ability to be anchored securely (once with retinal tacks required and once without) was appropriate for use in determination of thermal damage thresholds.

2.2.2 Surface Mounted Resistor Heating Element Implants

While CC − 2 was able to decrease the lead wire heating observed in CC − 1, large currents were required to induce relatively small thermal increases. To reduce the power supplied to the heating element (and also reduce the potential for lead wire heating to induce erroneous results), implants using 0402 size surface mount resistors were designed. The resistors were attached to the flex-PCB tracks through 0.6×0.5 mm solder pads, arranged to maximise the number of resistors that could be attached in a 5×5 mm area. Multiple devices were designed using resistors, allowing for alterations in heating element size to be investigated as well as allowing for chronic tests to be performed by reducing the overall implant size. Devices were also designed to have multiple heating elements, aimed at reducing the number of animal trials required.

2.2.2.1 SMR - 1

In addition to changing the heating element to a resistor array, the copper coil heating element implants are also limited in ability to investigate thermal damage thresholds with a range of heating element sizes. A variable size heating element array was created using 0.25 mm spacing connection pads, allowing for a range of heating element sizes to be used. A schematic diagram of this design is shown in Figure 2.9, indicating the total heating element area (6.00×4.65 mm) and sensors located centrally to the heating element and at a distance of 2.8, 4.7, 6.6 and 8.5 mm from the heating element edge. Lead wires connecting the heating element array to the current sources was through a 0.5 mm copper track, located on the opposite side of the flex-PCB to the temperature sensors and heating element.

Combinations of resistors can be placed on the heating element array to vary the total size of the heating element. This is shown in Figure 2.10, where altering the location of resistors changes the size of the heating element.
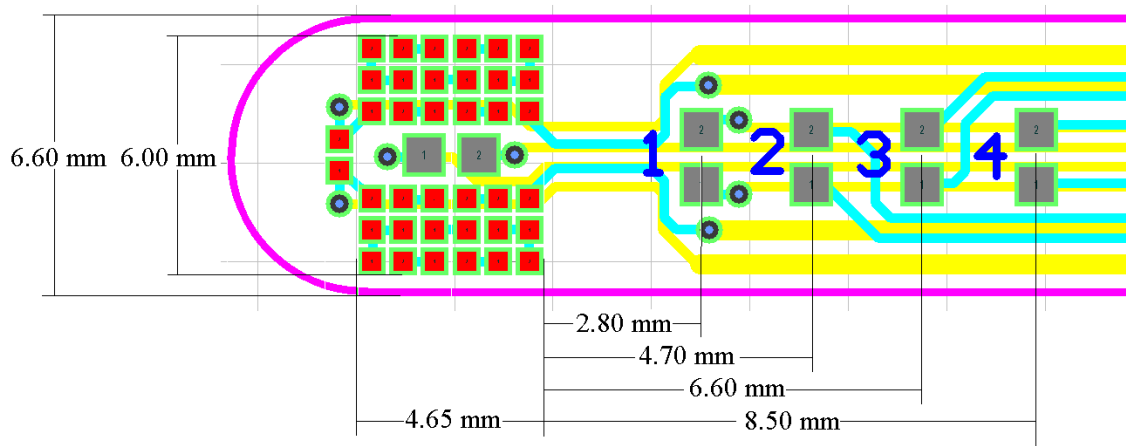
Figure 2.9. Schematic diagram of the implanted end (23.0 mm) of the variable size heating element (total length of 77.0 mm). Temperature sensors pads (grey squares labelled '1' and '2') are shown at distances of 2.80, 4.70, 6.60 and 8.50 mm from the edge of the heating element (red), and centrally to the heating element array (distance of 0 mm). The maximum width of the heating element is shown (6.00×4.65 mm), with the width of the implant being 6.60mm. Yellow tracks are on the opposite side of to the heating element with blue tracks (and temperature sensors) located on the heating element side.
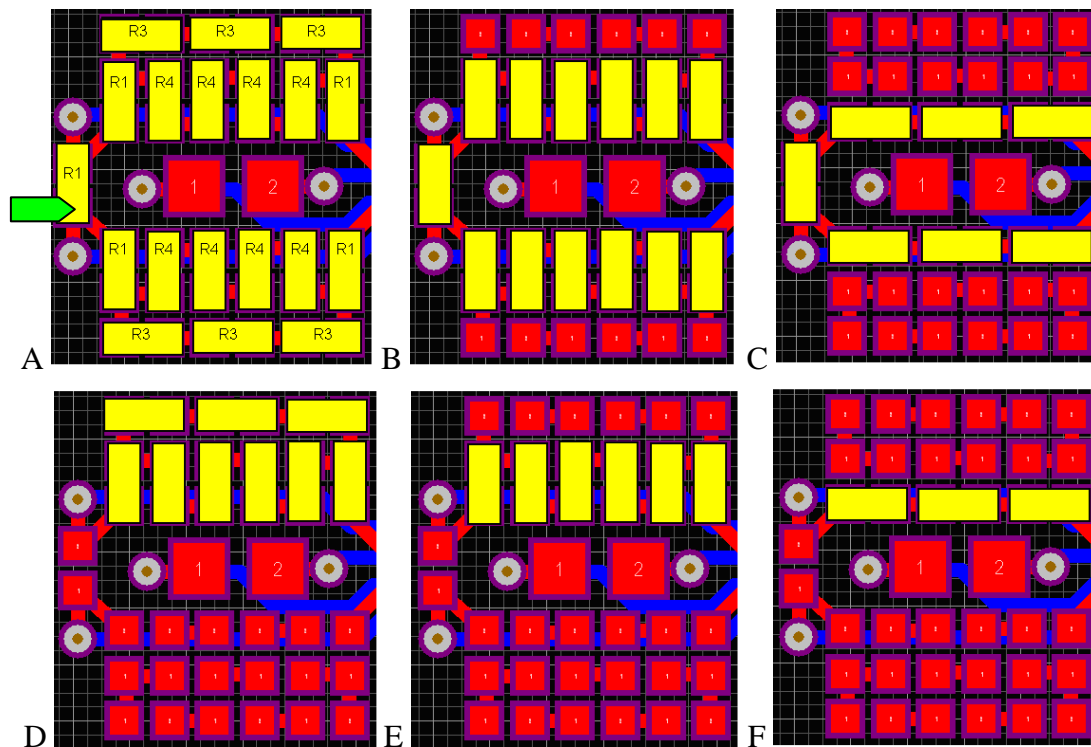
Figure 2.10. Combinations of resistors that can be used to alter the active area of the variable size heating element implant, showing connection of **(A)** 19 resistors (6.0×4.65 mm^2), **(B)** 13 resistors (3.0×4.65 mm^2) , **(C)** 7 resistors (2.0×4.65 mm^2), **(D)** 9 resistors (1.5×4.65 mm^2), **(E)** 6 resistors and (1.0×4.65 mm^2) and **(F)** 3 resistors (0.5×4.65 mm^2). It should be noted that other combinations are available although they are not expected to be used and by the removal of resistor R1, panels A, B and C can produce two independent heating elements in identical size to panels D, E and F. Green arrow indicates location of R1, the resistor used to divide (when absent) or join (when present) the heating element array halves.

The heating element array can also be divided into two independent heating elements by removal of resistor R1 (green arrow). This implant was one of the implants used to investigate temperature–power correlations in cat cadaver tissue (Chapter 4) and indicated that the flexibility and length of the implant was appropriate and surgical insertion could be performed in identical fashion to current suprachoroidal implantation techniques. The temperature sensors and heating elements were able to induce and measure thermal elevations effectively.

2.2.2.2　　　SMR - 2

A small epiretinal implant, with a total length of 15.3 mm was created to increase the ease of surgical implantation. These implants have a reduced number of sensors (four), although they are spaced closer together (1.2 mm from the heating element to the first sensor, and then 1.2mm sensor edge to sensor edge intervals). The heating element was reduced both in size and complexity, with a 13 resistor series combination being used to heat an area of 5.18×4.60 mm. The epiretinal implant is shown in Figure 2.11 (each grid line is separated by 2.53 mm), with gold connection pads overlayed on the copper tracks. The red tracks on the retinal side of the implant have been hidden by almost identically placed tracks on the opposite side of the board. This allowed for connection to the tracks from either side, reducing the mechanical trauma.

Thermographic analysis was performed to ensure the resistive heating element could induce the required magnitudes of thermal elevation. The currents used to induce temperature increases up to 8°C above the ambient temperature are listed in mW/mm^2 beneath each image in Figure 2.12. A current delivery of less than 4 mA produced very minor thermal increases, with all power dissipations from current levels above 9.7 mA shown to increase the temperature of the heating element to above 25°C (shown as white) corresponding to an increase of at least 7.5°C above ambient.

Cadaver trials have indicated that this device would be suitable for suprachoroidal stimulation and for epiretinal implantation, though care must be taken to ensure that the connection wires do not compromise the flexibility of the implant or cause unwanted damage to the delicate retinal tissue. This implant was also used in the determination of temperature-power relationships in cat cadaver eyes, with similar success to tests performed using the variable size heating element implant.
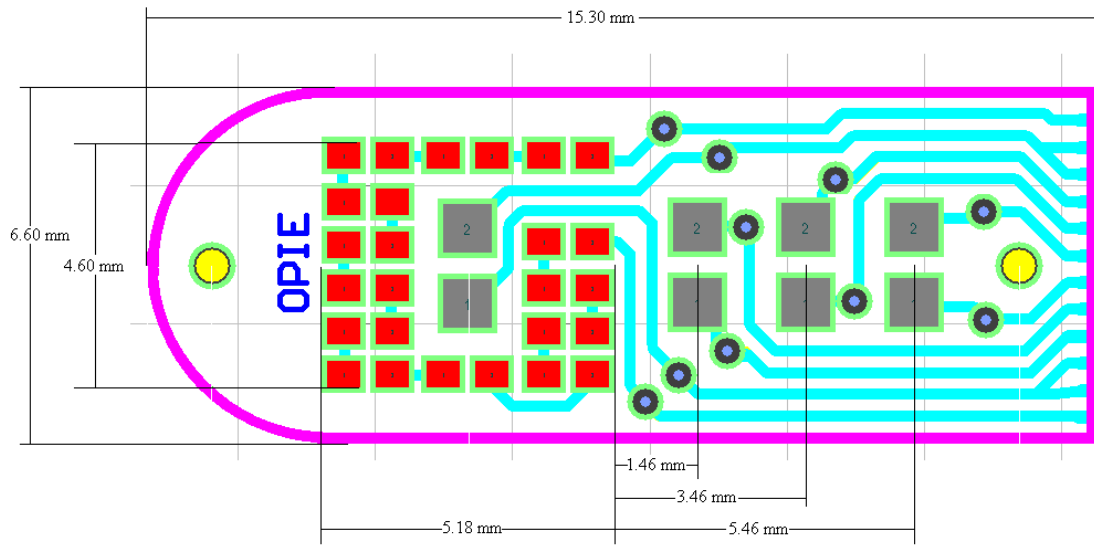
Figure 2.11. Small epiretinal implant, indicating red heating element area $(5.18 \times 4.60$ mm) and four platinum resistance temperature detector solder pads central to the heating element and at 1.46, 3.46 and 5.46 mm from the edge of the heating element. Total length and width of the implant is 15.30 mm and 6.60 mm respectively, with retinal tack holes (yellow circles) located 2 mm (centre to centre spacing) from the heating element edge and the furthest sensor. Blue tracks (and temperature sensors) are located on the heating element side with identical tracks located on the opposite side to the heating element.
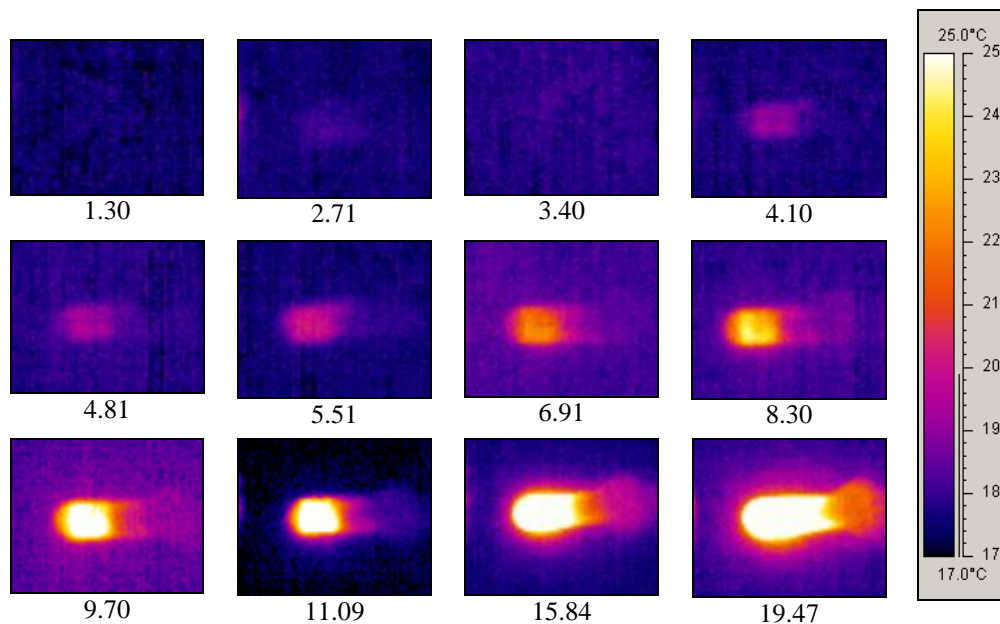
Figure 2.12. Thermographic images of temperature increases shown for the small epiretinal implant heating element as a function of current dissipated through the heating element (mA) shown underneath each panel
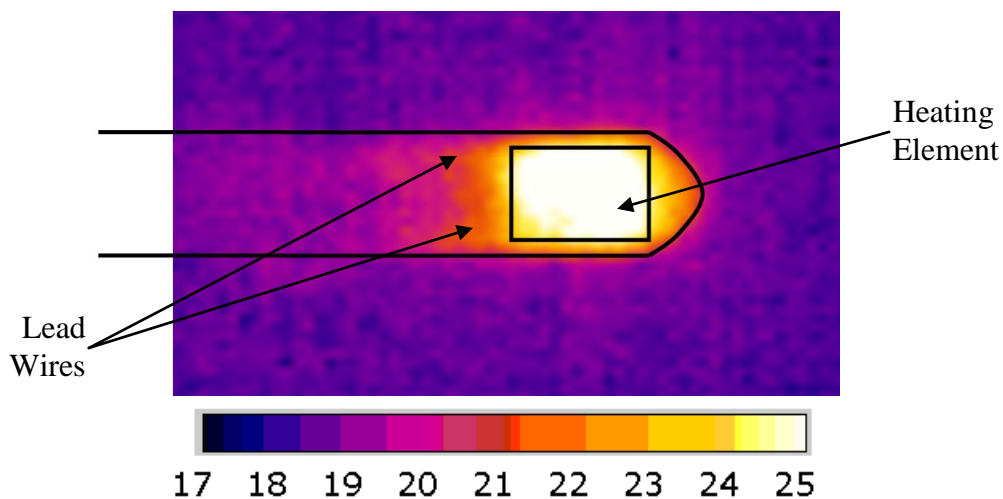
Figure 2.13. Thermographic analysis of double heating element implant with one active heating element indicating reduction in lead wire heating with superimposed approximation of heating element area and implant width.

2.2.2.3   SMR - 3

A chronic epiretinal and suprachoroidal implant was designed to be used in thermal testing over longer periods and is shown in Figure 2.14. This implant design has the ability to be completely implanted within the eye (with the exception of lead wires) and can thus enable closure of the globe, reducing damage caused by intraorbital pressure decrease and retinal collapse. While this implant still requires lead wires to be attached, they can be attached on either side of the implant with only two wires required for the heating element and two or four wires (for four wire Kelvin connection) to the temperature measurement system.

The dimensions of the heating element are identical to the small implant's heating element, as is the distance between the heating element and the retinal tack holes. The total length of this implant is 13 mm, with a 6.6 mm width. Similar to the small epiretinal implant (CC – 2), the underlying blue track hide identically located tracks on the top layer, allowing for connection to the implant leads from either side.

Cadaver trials using this implant have indicated that the flexibility and the size of the implant will be adequate for a chronic experiment, although the ability of the lead wires to be surgically passed through the cornea or sclera and choroid for an extended period will have to be investigated further.
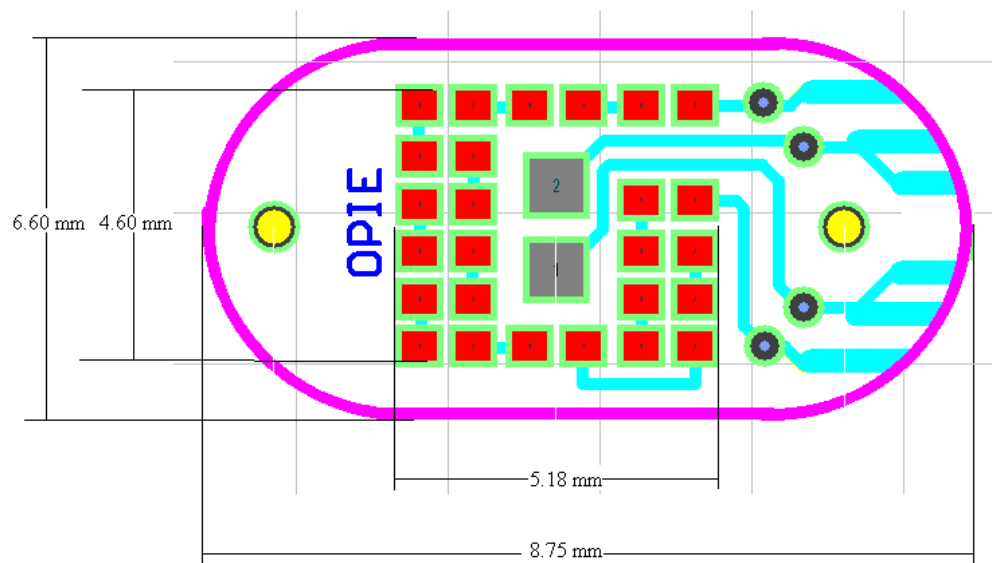
Figure 2.14. Small epiretinal chronic implant, indicating the red 5.18×4.60 mm heating element (and central grey temperature sensor) on the curved 6.60×8.75 mm polyimide implant substrate. Yellow circles represent 1 mm tack holes located 2 mm (centre to centre spacing) from the heating element edge.

2.2.2.4   SMR - 4

To increase the number of independent trials that can be performed on any one animal, another implant was designed. This epiretinal implant has the ability to induce up to five different temperatures with the all-series resistor heating element areas being 4.57×5.08 mm. These implants can measure temperature deviations at up to nine locations, one at the centre of each of the heating elements and one midway between. The sensors' edge to edge separation is 3.18 mm with a 4.57 mm centre to centre separation. The implant has been designed for the four 10.04 mm long and 5.97 mm wide arms to conform to the curvature of the inner retina, allowing a reasonable degree of separation between each of the heating elements. This is shown in Figure 2.15.
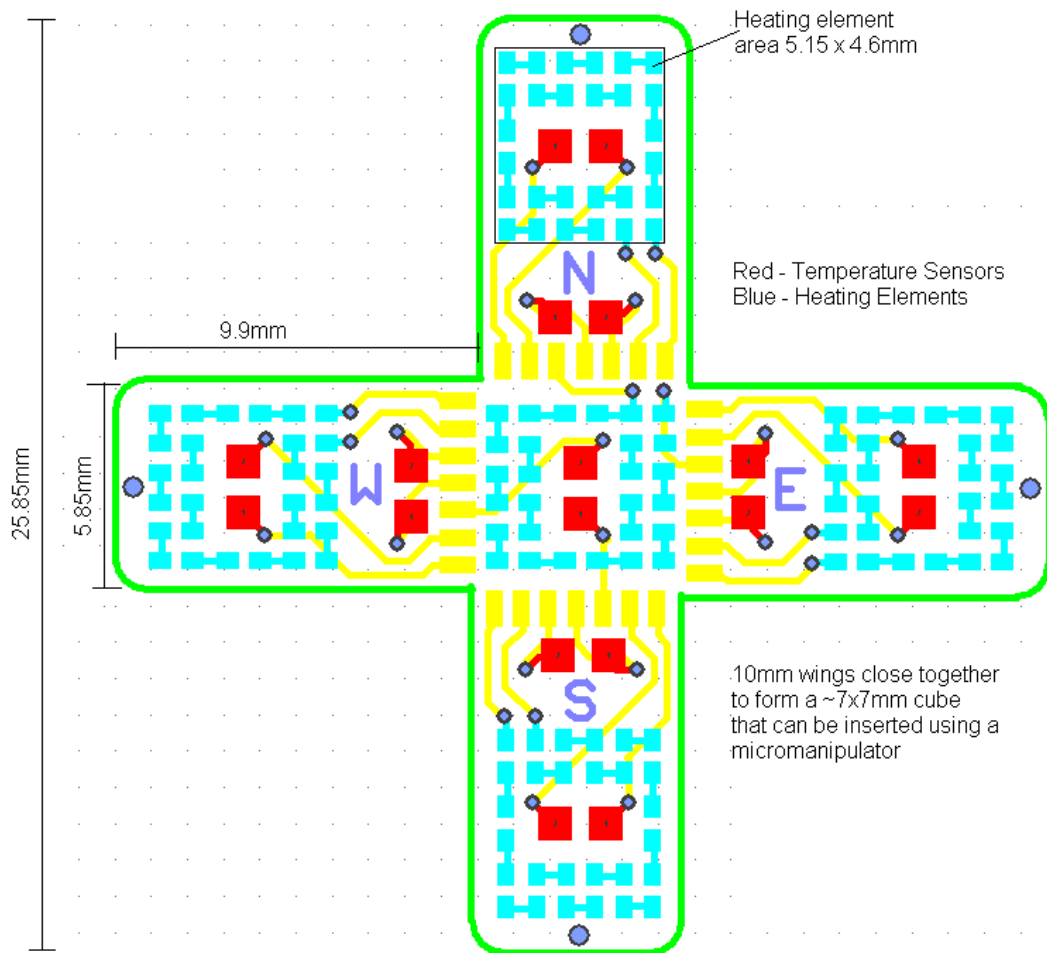
Figure 2.15. Multiple heating element epiretinal implant design showing the 5.15 × 4.60 mm heating element area (blue solder pads) and the locations of the nine temperature sensors (red solder pads). Each of the four wings are 9.90 × 5.85 mm, with a total width and height of 25.85 mm. Dark blue holes located at the end of each of the wings allows wings to be retracted to form a 7 × 7 mm cube that can be inserted into a cat eye.

When the implant is bent to conform to the curvature of the retina, the distance between opposite heating elements is 9.00 mm, with adjacent heating element centres separated by 7.06 mm, all heating element centres are 6.35 mm from the central heating element, with finite element model simulations indicating that this separation will be sufficient to ensure thermal cross talk is avoided (Chapter 3). The ability of the implant to curve around the retina is shown schematically in Figure 2.15, where a retract wire is used to fold the implant arms up for insertion, folding the arms back down to the retina once the implant is within the eye. In this design, the heating elements (located on the retinal side) are on the opposite side of the flex-PCB to the measurement sensors, although these are still located centrally to each heating element.
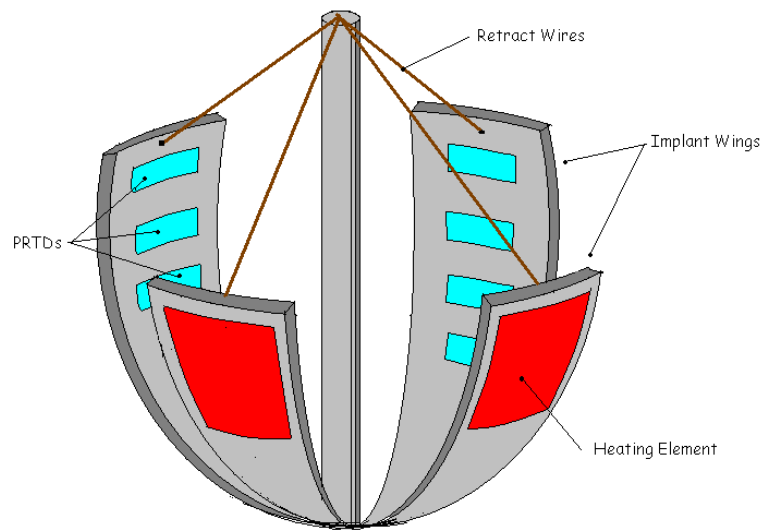
Figure 2.16. Multiple heating element implant after retraction of the implant wings to allow for orbital insertion.

Cadaver tests using this implant indicated the implant was able to fit almost perfectly into the eye of the cat after the cornea, lens and vitreous fluid had been removed. The slight pressure from the wings as they unfolded and lay on the retinal tissue was also enough to ensure flush contact between the heating elements and sensors and retinal tissue was made and maintained without the requirement for retinal tacks.

To reduce the wires required to be implanted within the eye, a splitter was used. This splitter, shown in Figure 2.17, essentially converts the two wire measurement system into a four wire Kelvin connection, removing resistance errors from the long lead wires between the implant and the electronics. While there is still the possibility of resistive differences occurring between the splitter and the implant, these errors have been drastically reduced with all wires of equal length (±1 mm). As this implant has nine PRTDs and five independent heating elements, the total number of wires required for a four wire Kelvin connection is 46, reduced to 28 wires with the Kelvin connection beginning from the splitter. With this implant consisting of nine independent sensors and five heating elements, a switch matrix was required to enable current delivery and temperature measurement from the four current sources and high resolution temperature measurement boards. The switch matrix takes into account the symmetry of the implant, and allows for a control (no current delivery) to be located either centrally or in one of the heating elements located on the implant wings.
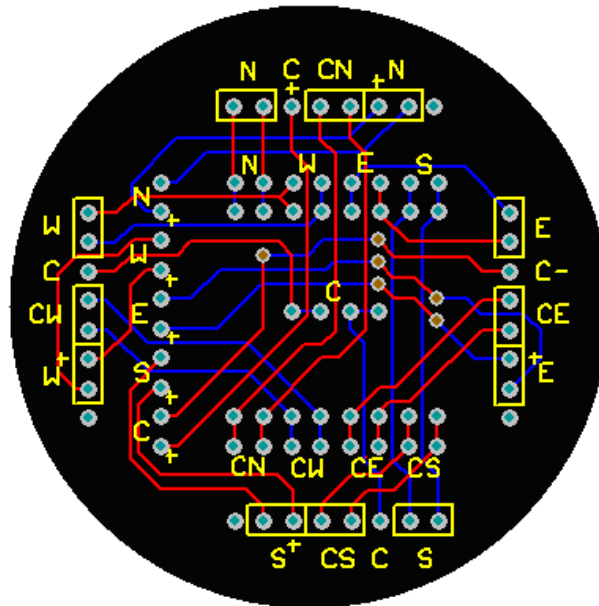
Figure 2.17. Splitter used to reduce the number of wires connected to the implant from 46 to 28. Peripheral pins (yellow squares) connect to the implant with internal circles (not bounded by yellow squares) connecting to the temperature measurement system via four wire Kelvin connection.
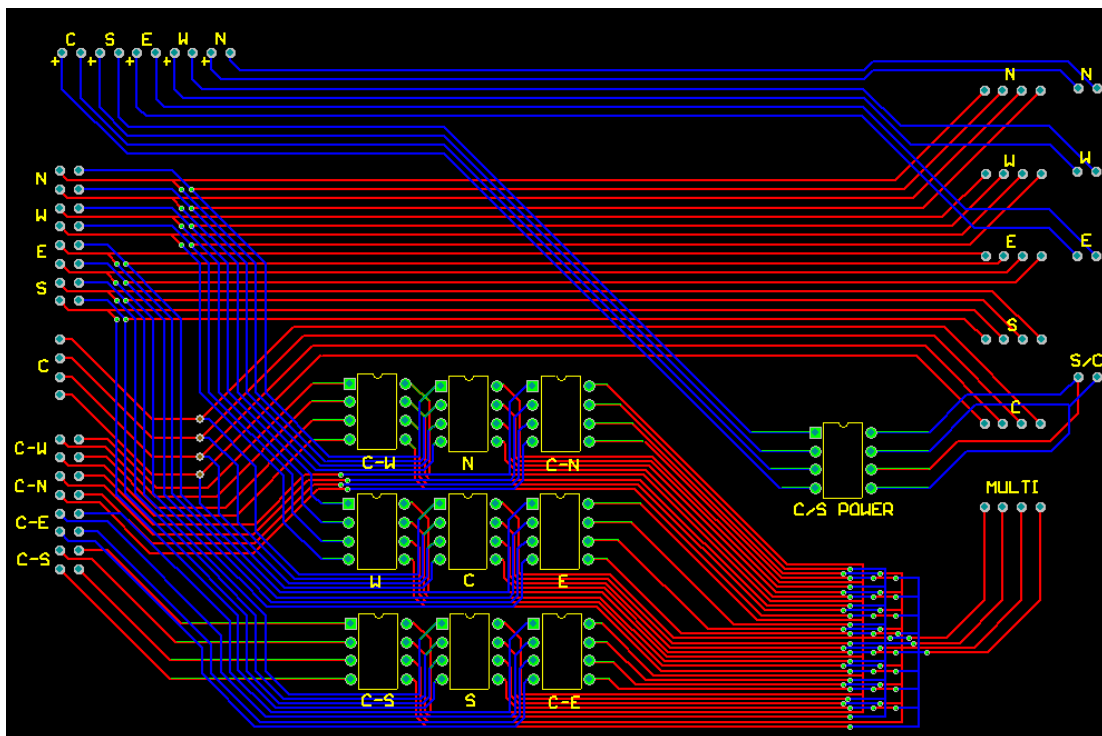
Figure 2.18. Switch matrix used to enable measurements from the nine implanted current sources (in each eye) and deliver and measure power to and from the five heating elements (per eye). Left hand circles represent connection points to the implant sensors, with central switches (denoted C-W, N, C-N, W, C, E, C-S, S, C-E) used to control senor measurement through four wire Kelvin connections. Connection pads on right hand side and top connect to current sources and heating elements (on implant) respectively.

Temperature sensors located in the centre of three of the heating elements located on the wings are connected to a temperature measurement board. The other two central censors and the four sensors located midway between two heating elements are measured through manual switching of the appropriate switch matrix components. The fourth board also has the ability to measure any of the sensors, reducing the potential for board or wiring failure to disable temperature measurements. Sensor temperature measurements are thus obtained from the sensors located on the north (N), west (W) and east (E) wings, as well as from any predetermined sensor (MULTI) located on the right hand side of the switch matrix (Figure 2.18). Similarly, the power supply to the heating elements is delivered to the north, west and east wings (N, W and E, respectively) and to either the central (C) or south (S) elements as determined by the S/C switch. Each of the switches used are four way rocker switches which all allow for four wire Kelvin connection to any of the sensors. In a similar fashion, any of the five heating elements could be connected to a current source through the C/S POWER switch, which essentially switches between the central heating element and the south heating element.

This implant was used in the initial *in vivo* cat experiment with poor results (Chapter 5). Due to the heavy fixing of the cadaver eyes, they did not replicate anaesthetised animal tissue behaviour. While the tissue in the cadaver eyes maintained the spherical shape upon removal of the cornea, lens and vitreous fluid, once this was performed in the acute eyes, the eyes collapsed upon themselves. This was caused by the reduction in intraocular pressure that was required to maintain the spherical shape. Once the eye had collapsed, the ability to insert the implant was very difficult, even with the implant folding to almost a 5×5 mm size. The insertion of the implant was also made more complicated by the attachment and all the connecting wires and as a result, the implant caused severe damage to both the eyes on implantation and rendered the eyes useless for histological analysis.

Further, the implant connections failed in many cases and resulted in a loss of ability to both record retinal temperature and to induce thermal elevations due to the over-folding of the implant causing detachment of the implant pads from the substrate which was not seen in saline or cadaver trials. The ability to induce five different temperature elevations in a 5×5 mm area using this implant, while would have reduced the number of animals required for experimentation (able to performed more independent trials simultaneously) was deemed to be unsuccessful due to the overall size of the implant, and a smaller, multiple hating element implant was designed accordingly.

2.2.2.5   SMR - 5

This implant was designed to allow for multiple heating elements within a single eye (and thus increase the number of tests possible per animal) whilst paying particular attention to the overall implant size. By removing three of the heating elements from the multiple heating element design, this design could be reduced to a total width of only 7.10 mm, similar to previous design widths.

This implant, similar to its predecessors having gold pads, ZIF connection, a SMD resistive heating element and being of similar thickness to other double sided implants (159 μm), had additional 0.6 mm diameter holes adjacent to each of the sensors. These holes could be marked and would allow for orientation of the implant once the tissue had been sliced and prepared for histological processing and damage evaluation. These holes could also be used as retinal tack holes to ensure the implant is flush against the retinal tissue, although care would need to be taken to ensure mechanical damage caused by tack insertion was not combined with the thermal damage measurements.

All lead wires connecting the implant heating elements and sensors to the ZIF connection are on the back (opposite the retinal tissue) and are thus all in direct contact with the vitreous fluid, improving heat dissipation away from retinal tissue that is not immediately beneath the heating elements. The implant has a total length of 100.75 mm, a 20.35 mm distance between the two retinal tack holes closest to the heating elements and a heating element separation of 7.5 mm.

The implant design is shown in Figure 2.19, with each gridline representing a 1 mm interval. The numbers and letters corresponding to the heating elements and sensor lead wire connections are mirrored to allow viewing from underneath as the implant side will be facing the retina. To enable measurements from the five temperature sensors located between the two heating elements with only four wires, combinations of the wires were used. The use of a common ground would have reduced the potential of measurements to be made simultaneously and was avoided.

This implant was also designed to be used in conjunction with a splitter to increase the 0.5 mm pitch ZIF tracks to larger tracks for manual soldering. The splitter was also designed to have three rectangular (0.75×2.0 mm) connection pads, two on the top side and one underneath. This was done to allow for four-wire Kelvin connections

to be implemented with ease which could not be performed on the implant without increasing the implant width to an unacceptable degree.
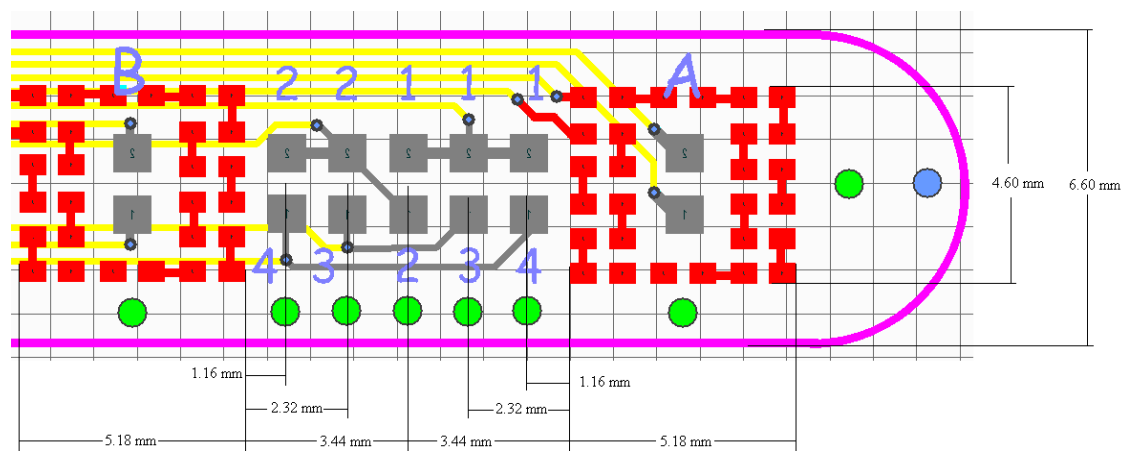
Figure 2.19. Double heating element epiretinal implant showing two 5.18 × 4.60 mm heating elements (red, marked A and B) with centrally located sensors (grey) and sensors located between the two heating elements (3.44 mm distance from the heating element edges) and at a distance of 1.16 and 2.32 mm from the edge of the closest heating element. Implant was 6.60 mm wide and had a total length of 100.75 mm. Retinal tack holes (green) are used to anchor the implant as well as for marking the location of the temperature sensors and heating element centres. Numbers indicate the leads connecting to each of the temperature sensors.

As this implant design has up to seven independent temperature sensors, a check panel was created. The two sensors that are central to the heating elements may be measured and recorded in real time with the high resolution temperature measurement system, with a total of four measurements in each acute test (two each eye).

Cadaver trials with this implant have shown that the implant requires at least one retinal tack in order to be in good contact with the retinal tissue. The separation between the heating elements was not a problem provided only a thin layer of conformal coating was used (50 μm), as thicker layers compromised the flexibility and thus the ability of the tacks to maintain retinal contact.

2.2.2.6 SMR - 6

A version of the double epiretinal heating element implant was created to allow for enhanced flexibility in the region between the two heating elements. This implant is identical to its predecessor but has only one temperature sensor located between the two heating elements. This reduces the number of lead wires and retinal tack holes

required. All parameters of thickness, width, length and dimensions of the heating elements are identical to the double epiretinal heating element implant. Measurements of the central sensor can be done through the measurement board or directly by connecting the wires to the DMM. Real time measurement of resistance changes can thus be taken, connecting the DMM to a computer and using the Fluke ViewForms software.

2.2.3   Conformal Coatings

To ensure that there is no shoring of the flex-PCB board components, either of the temperature measurement sensors or the resistor combinations used to induce thermal changes, the whole board must be hermetically sealed. The encapsulation of the implanted device is comparable to methods published by Millard and Shepherd (2007) (Millard and Shepherd 2007)where conformal coating is applied to the flex-PCB after cleaning the board with iso-propanol alcohol.

The conformal coating of electrical contacts has been tested in a balanced salt solution (almost identical ionic composition to that of a human eye) with promising results. This method is suitable for acute use; however, the 50 µm thick silicon coating may need to be increased by multiple applications for chronic studies. A further coating of flowable silicone sealant (Permatex) was used to further reduce the likelihood of saline shorting connections during acute trials.

2.2.4   Implant Comparisons

By designing and manufacturing a number of implants, the ability to determine to determine thermal changes caused by induction of power dissipation that result in damage to retinal tissue can be achieved for epiretinal, suprachoroidal, acute and chronic situations. The implants could dissipate power over a range of areas and magnitudes reducing the number of animal trials required through constructing implants with multiple temperature sensors and heating elements. A photograph of all the sensors and connectors produced are shown in Figure 2.21, with Table 2.3 listing all the properties of each of the implants to be used to guide decisions as to which implant would be most appropriate for a particular use.
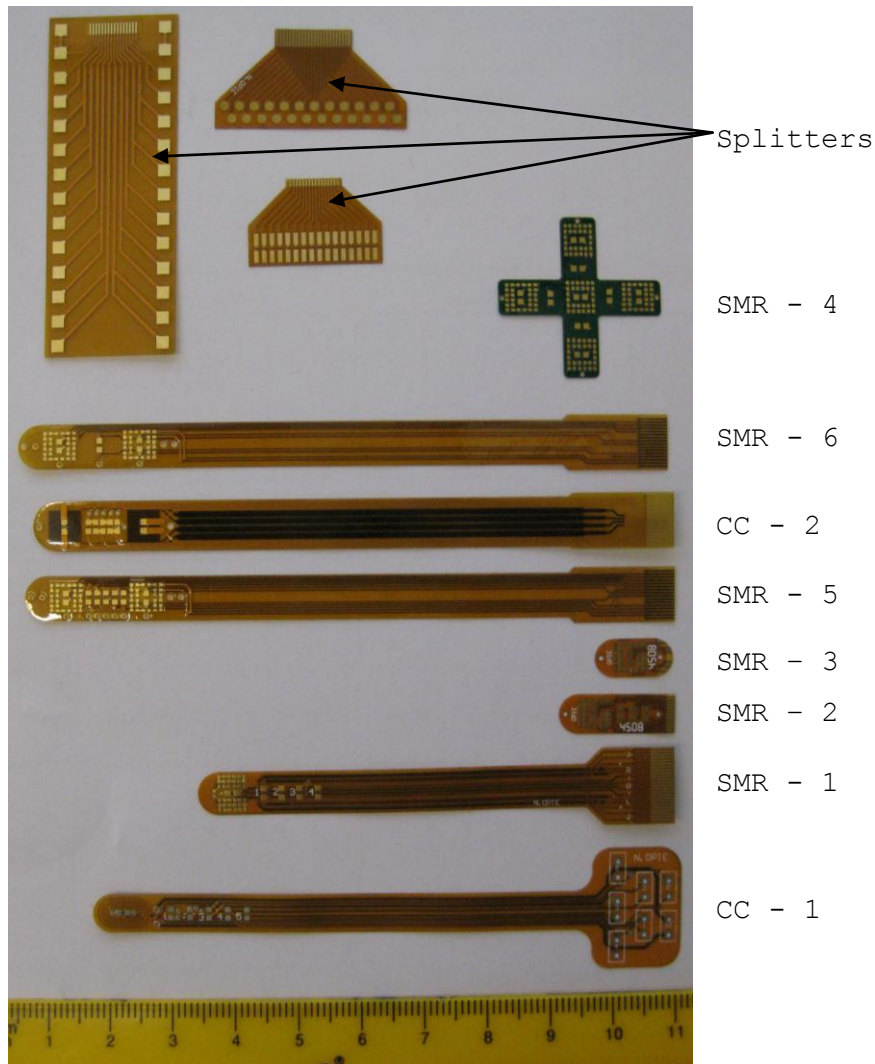
Figure 2.21. All implant designs and connection pads produced. Heating elements are facing the left hand side with connections to the high resolution temperature measurement system and current sources on the right.

Table 2.3. Comparison between all designed and produced implants

Properties	Implant Design							
	CC - 1	CC - 2	SMR - 1	SMR - 2	SMR - 3	SMR - 4	SMR - 5	SMR - 6
Total Length (mm)	75.35	100.75	76.981	15.3	8.75	25.896	100.75	100.75
Width (mm)	5.5	7.95	6.6	6.6	6.6	26.0	6.6	6.6
Thickness (um)	159	159	159	159	150	159	159	159
Substrate Material	Polyimide	Polyimide	Polyimide	Polyimide	Polyimide	Polyimide	Polyimide	Polyimide
Pad Material	Copper	Copper	Copper	Copper	Copper	Copper	Copper	Copper
Gold Overlay	No	Yes	Yes	Yes	Yes	Yes	Yes	Yes
Connection Type	Soldered	ZIF	ZIF	ZIF	Soldered	Soldered	ZIF	ZIF
4 Wire Kelvin	Yes	At Splitter	Yes	Yes	Yes	At Splitter	At Splitter	At Splitter
Suprachoroidal	Yes	Yes	Yes	Yes	Yes	No	Yes	Yes
Epiretinal	No	Yes	No	Yes	Yes	Yes	Yes	Yes
Acute	Yes	Yes	Yes	Yes	Yes	Yes	Yes	Yes
Chronic	No	No	No	Yes	Yes	No	No	No
Sensor Number	6	7	5	4	1	9	7	3
Sensor Distances (mm)	0, 2.10, 4.20, 6.30, 8.40, 10.50	0, 1.16, 2.32, 3.48, 4.64, 5.80, 6.96	0, 2.80, 4.70, 6.60, 8.50	0, 146, 3.46, 4.46	0	0, 1.65	0, 1.16, 2.32, 3.48, 4.64, 5.80, 6.96	0, 3.48
Heater Number	1	1 or 2	1	1	1	5	2	2
Heater Type	Coil	Coil	Resistor	Resistor	Resistor	Resistor	Resistor	Resistor
Distance Between Heaters (mm)	-	7.4	-	-	-	7.5	7.4	7.4
Heater Area (mm x mm)	5.08×8.50	5.00×5.00	0.50×1.00 - 4.65×6.00	5.18×4.60	5.18×4.60	5.18×4.60	5.18×4.60	5.18×4.60
Lead Wire Location	Back	Front	Back	Back	Back	Back	Back	Back
Lead Wire Thickness (mm)	0.5	1	0.5	0.5	0.5	0.25	0.5	0.5
Tack Number	0	8	0	2	2	4	11	7
Tack Location	-	1 mm Ends, Sensors	-	2 mm Ends	2 mm Ends	0 mm Ends	1, 2 mm Ends, Sensors	1, 2 mm Ends Sensors

2.3 HEAT BATH

In order to ensure that voltages from the high resolution temperature measurement system correlate accurately with the absolute temperature being measured, measurements were made in a heat bath. Not only does the use of a saline heat bath remove the potential for turbulent air flow of different temperatures across the sensors to induce erroneous measurements, but can also allow for fine control of temperatures and temperature increases.

To calibrate the equipment, the heat bath temperature was increased from room temperature (well below resting body temperature) to at least 45°C (maximum temperature for thermal damage analysis). The body temperatures of active animals over a two hour period has been reported to vary by ±0.9°C, and a stability of no more than this is required if a heat bath is expected to accurately replicate body temperature conditions (Dawson and Hilbert 1970).

Thermal models were constructed to analyse temperature distributions within the saline bath (Chapter 3), and indicated that a stirring device would be required to ensure no hot spots were generated at the vessel boundaries. A motor connected in series with a variable resistor allowed for a continual stirring whilst ensuring minimal heat was generated by water movement (4 rotations per second). This was shown to reduce temperature hot-spots, maintaining a constant temperature throughout the saline bath.

Initially an Electrothermal MH-503 cryogenic heat bath was used and while this device was able to heat the saline bath over the desired range, the ability to produce a stable temperature was inadequate. Over a 4 hour period, the temperature of the water within the heat bath was shown to range from between 35.109°C and 41.306°C. This 6.2°C difference, well above animal body temperature fluctuations, was due to the heat bath thermistor turning on and off as water within the bath was heated and cooled around the desired temperature. This can be seen graphically in Figure 2.22, with measurements taken using a Fluke 289 True RMS Multimeter (with a resistance accuracy of 0.05%) connected to FlukeView Forms 3.3 Logging software. Measurements were taken at 1 second intervals.
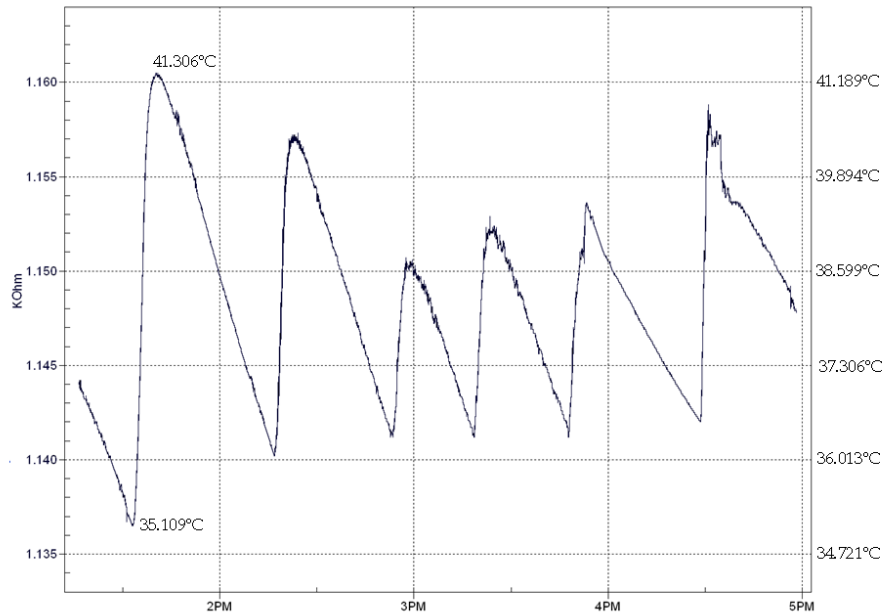
Figure 2.22. Temperature fluctuations observed when using a commercial heat bath set to 37°C.

A simple heat bath was designed using between one and six 60W, 240V E8 light globes (Philips) to heat and stabilise the temperature of saline contained within a 1L glass vessel, without deviating by more than ±0.9°C over a two hour period. The glass vessel was placed through an opening in the lid and was encompassed by globes positioned at 60° intervals (Figure 2.23). The internal walls of the pine heat bath were lined with aluminium foil to reflect the scattered light and assist to distribute thermal energy evenly into the glass chamber. The heat bath had a variable resistor allowing for accurate control of the amount of energy supplied to the clear glass vessel.

Using 3 globes and a medium brightness, the linear temperature-time graph shown in Figure 2.24 was produced, enabling the calibrations of sensors and temperature measurement over the desired range (room temperature to >45°C). Using two globes at a very low brightness, stability of the heat bath was achieved (less than ±0.9°C over a two hour period). Figure 2.25 shows the temperature fluctuation of the custom made heat bath set to maintain a temperature of 41.7°C over a 7000 second period. Over a two-hour duration, the custom made heat bath was observed to deviate by less than ±0.35°C.

The ability of the constructed heat bath to operate at body temperature ranges and to hold a constant temperature for at least 3 hours (deviating by 0.104°C) makes it ideal for imitating body temperatures. The heat bath will be used in conjunction with the designed and manufactured implants used during *in vitro* testing. Cadaver eyes implanted with one of the designed heating element-sensor combinations and connected

103

to temperature measurement equipment and a current source will allow investigations into the heat flux that is present when retinal tissue is heated under conditions simulating retinal prosthesis operation.
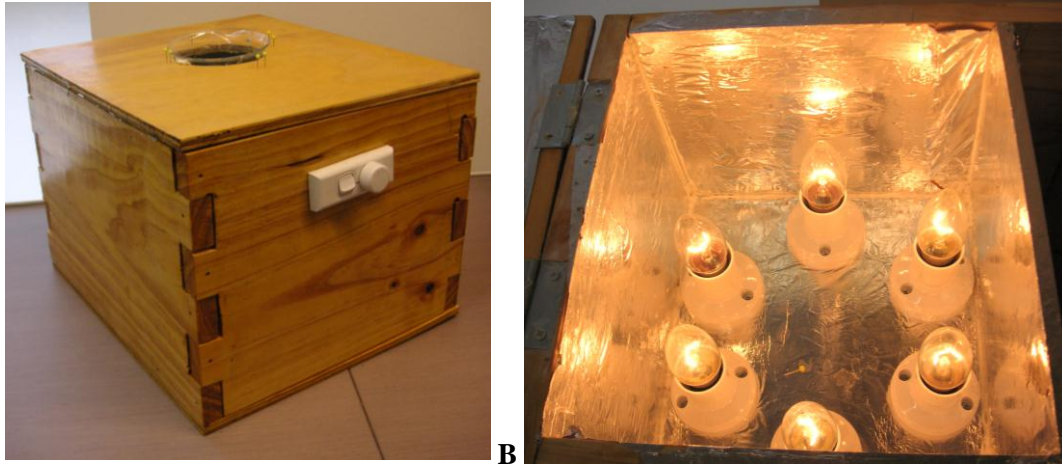
Figure 2.23. **(A)** External photograph of the custom made heat bath, indicating the white dimmer switch and the placement of the saline containing vessel on top of the pine box. **(B)** Inside the heat bath, showing aluminium foil layered on pine walls and six globes which would surround the clear glass saline containing vessel at 60° separations.
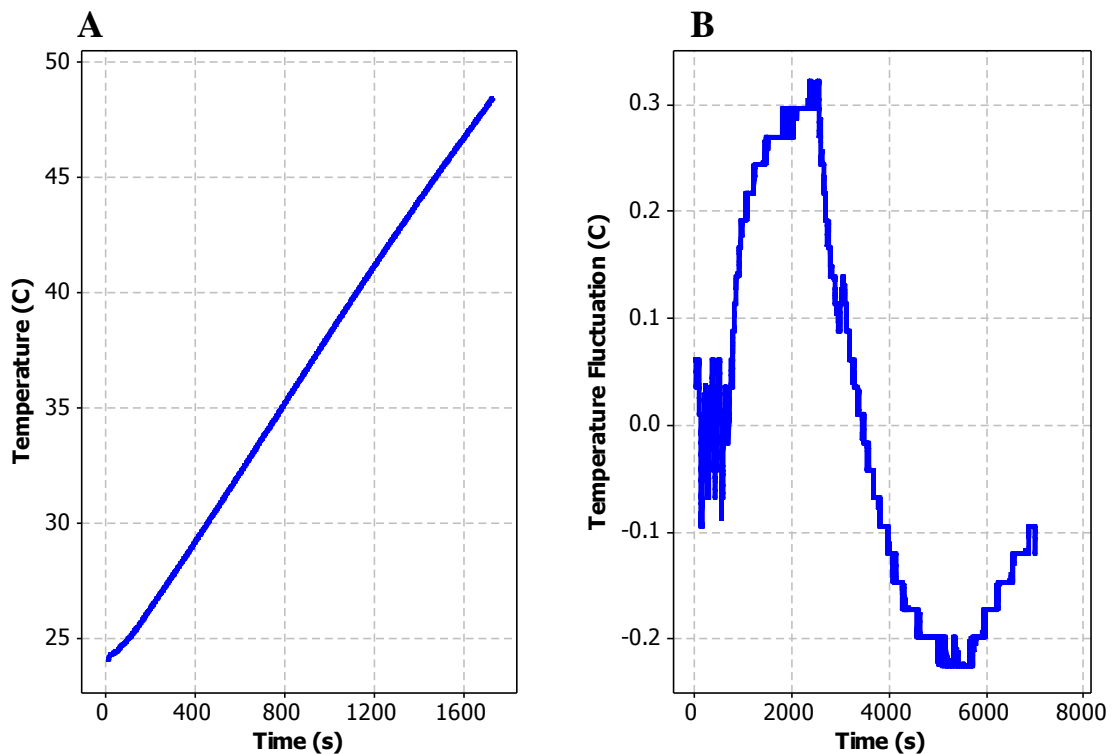
Figure 2.24. **(A)** Linear increase measured within the custom made heat bath for temperatures ranging from room temperature (~25°C) to >45°C observed over 1800 seconds. **(B)** Temperature fluctuations over a 7000 second period for the custom made heat bath deviating by less than ±0.35°C over a two hour period.

2.4 ELECTRONICS

To measure and record thermally induced alterations occurring in retinal tissue, current sources and high resolution temperature measurement equipment must be designed, constructed and calibrated. Equipment was designed to be used in conjunction with experiments that are sensitive to electrical mains noise, and as such, batteries were used to reduce the potential of inducing electrical mains artefacts.

Current sources were built to deliver power to the heating elements, with multiple types built for the copper coil and resistive elements, allowing for a large range of available currents to be used. The high resolution temperature measurement system was designed to enable multiple and simultaneous temperature measurements to be recorded and stored in real time.

2.4.1 High Power Current Source

A current source designed to supply power to implants using copper coils as a heating element requires a much larger current supply than one used for surface mounted resistors. The current source was designed to be powered by a Laboratory DC Power Supply (GW) that is connected to mains, although can also be powered by lead acid batteries if the mains noise produces large signal artefacts. A schematic for the current source design is shown in Figure 2.26. When the switch S1 is closed, power supplied by the DC voltage source, regulated by R1 and R2, flows through the heating element (RH) with current supplied to the heating element measured as the voltage (Vout) across R3.

A 10 turn 10kΩ variable resistor has been used for R2, and has been placed in parallel with R1, a 0.1% 1.15kΩ current limiting resistor. For a combined resistance of approximately between 50Ω and 1150Ω and a voltage supply of between 1 and 30 V, the current that can be delivered to the heating element will be in excess of 600 mA, more that enough to achieve the desired temperature increase. The current passing through the heating element can be calculated using Ohms Law:

$$I = \frac{V}{\left(\dfrac{R1 \times R2}{R1 + R2} \right) + RH + R3}$$

(2.3)

where *I*, the current in Amps, is a function of the voltage, *V*, and the resistance, *R*, (equivalent to a parallel connection of resistors *R1* and *R2* in series with the heating element, *RH*, and a sense resistor *R3).* A 0.1%, 1W, 1Ω resistor has been used as the sense resistor (*R3*) with the measured voltage (*Vout*) equal to the current flowing through the heating element. This current source is highly versatile, with a change in *R1* allowing for a much larger range of currents. To allow the use of both sources, the heating elements, measurement leads and the variable resistors are interchangeable using a series of pins to alternate between the two sources. This removes the requirement to provide multiple variable resistors and leads to connect to the measurement device and reduces the space and pin requirements for the heating element attachments.
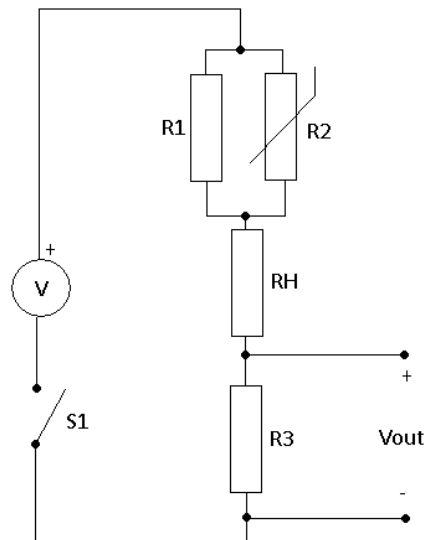
Figure 2.26. Schematic diagram of the high power current source. When switch S1 is closed, current from the batteries (V), controlled by variable resistor R2 is supplied to the heating element (RH) and measured as a voltage (Vout) across the sense resistor (R3). The current limiting resistor (R1) is used to ensure excessive power is not delivered to the heating element when R2 becomes very low.

Saline bath trials were conducted to investigate the amount of current that is required to heat water. The heating element used was a 3Ω, 0.25 mm wide copper coil track (double heating element implant). Temperature increases measured by the sensors located centrally to the heating elements (on the reverse side of the 159 μm thick polyimide board) were plotted as a function of current supply, which had current steps of 50 mA from 50 mA to 300 mA. The temperature increases that occurred as a result were 0.222°C, 1.22°C, 2.44°C, 3.94°C, 5.44°C and 6.61°C respectively, shown in Figure 2.27. The blue trace is indicative of the current and the green trace represents the temperature measured. The current was measured through a 0.1%, 1Ω resistor, and

hence 1 mV is equivalent to 1 mA. The temperature measurement has an approximate 1 V to 1°C conversion.
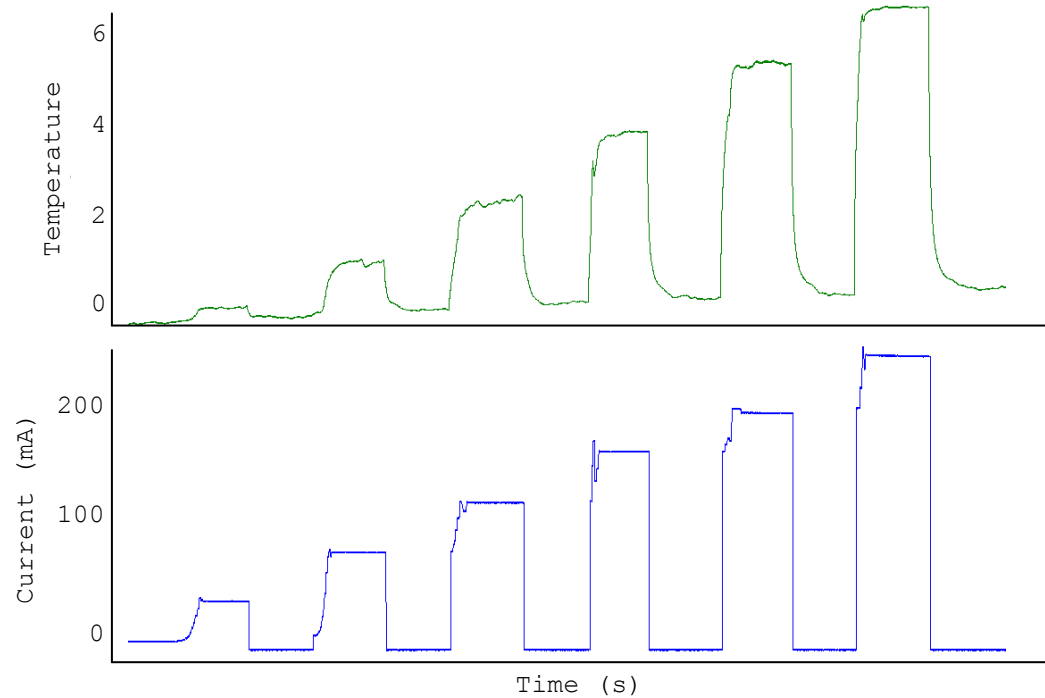
Figure 2.27 Plots of a saline bath test relating the induced current through the heating element (blue trace) to the resulting temperature increase (green trace). Current is increased in 50 mA steps from 50 mA to 300 mA.

Average results comparing the current and temperature increase from the saline bath tests are shown in Figure 2.28 when the temperature was set (red data points, obtained by fine tuning the current source until the desired temperature was reached and had stabilised) and when the current was set (black data points). A linear fit to both data sets indicated that the current induces a temperature increase of 38.15 mA/°C, and should be suitable for use in the determination of current and power thresholds that induce thermal damage through *in vivo* and *in vitro* heating experiments.
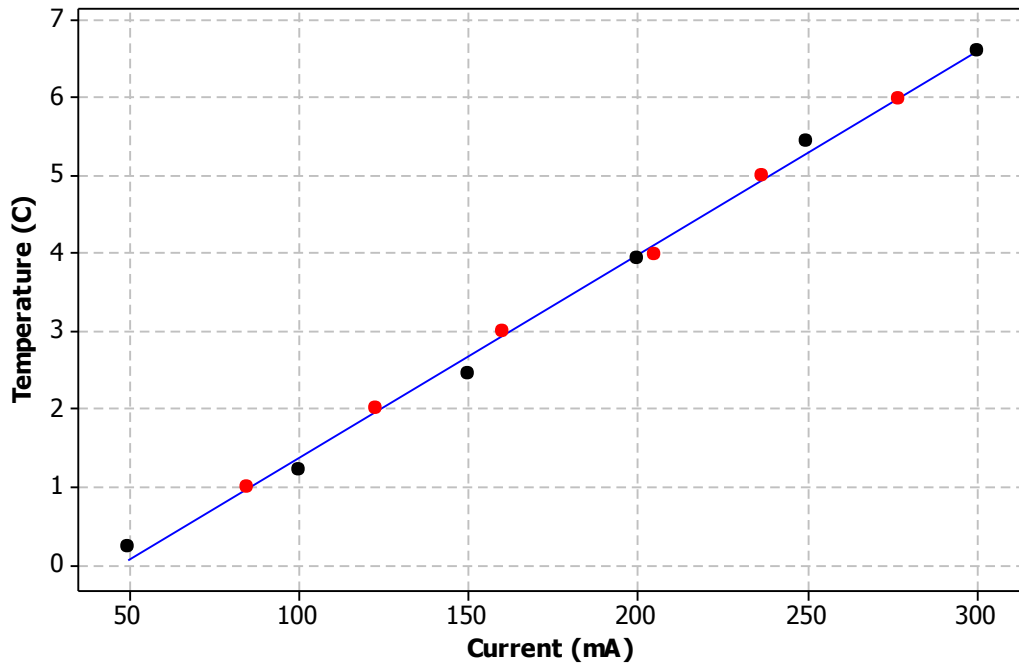
Figure 2.28. Temperature-current relationship for the initial saline bath current source experiments. Black data points represent average results obtained when current was fixed and red data points give averages obtained when the temperature was fixed. Blue line is a linear fit of both sets of averaged data.

2.4.2   Low Power Current Source

A current source was built to supply the resistive heating element with enough power to induce retinal heating. The requirements for this current source included portability, the ability to be constructed from off-the-shelf components, the ability to supply currents up to 40 mA to four independent heating elements, reasonable stability and a power supply that did not require connection to mains. A current mirror design was chosen as shown in Figure 2.29. While this design has limited stability at higher current levels compared with sources using feedback loops through op-amps, it does not require much power to operate and can be easily controlled through a variable resistor.

The operation of this simple circuit essentially supplies current through a 100Ω current limiting resistor (R1) and a 10kΩ variable resistor (R2) with a magnitude related to the input voltage and the total path resistance. The current passing through the BC337 transistor to ground is mirrored in the opposite side passing through the heating element and a 1Ω sense resistor. The maximal currents that can be obtained can are:

$$I = \frac{V_{in} - V_{Q1}}{R_1 + R_2}$$

$$I = \frac{V_{in} - 0.7}{R_T}$$

(2.4)

where V_{Q1} is the BC337 transistor collector emitter voltage drain, I is the current supplied to the heating element, R_T is the total resistance (sum of the current limiting resistance, R_1, and the resistance set on the variable resistor, R_2, as a function of the input voltage, V_{in}). The maximum amount of current that can flow through R_1 and R_2 is not, however, the maximal current that can flow through the heating element, which will be dictated by the voltage compliance. The maximal current that can flow through the heating element for a heating element resistance of 300Ω the current is

$$I = \frac{V_{in} - V_{Q1}}{R_{HeatingElement} + R_{Sense}}$$

$$I = \frac{V_{in} - 0.7}{300 + 1}$$

(2.5)

As the current flow will depend strongly on the rail voltage, this needs to be regulated to ensure that stability can be maintained as the battery deteriorates. To ensure the voltage through the current source does not change as the batteries flatten, series connections of 12 V lead acid batteries are passed through 5 V or 12 V voltage regulators, with the power supply to the high resolution temperature measurement system using a 24 V regulator.
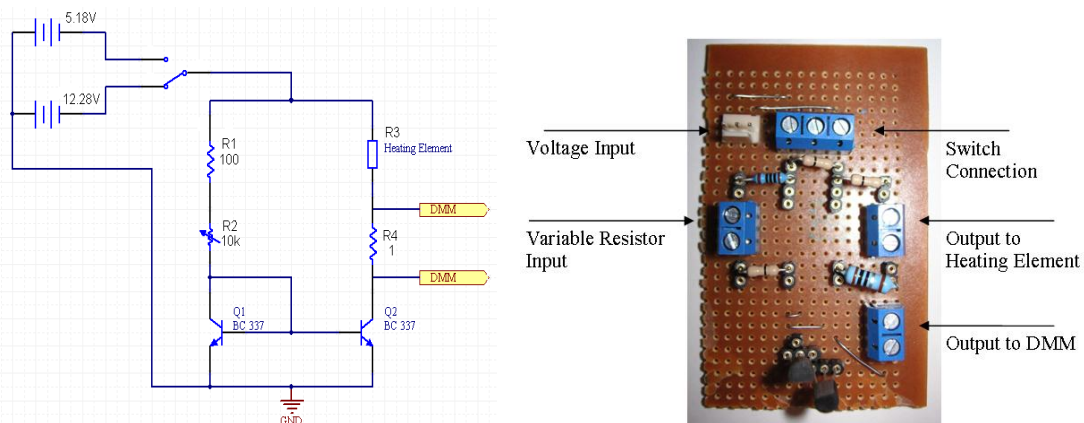
Figure 2.29. (A). Current source design utilising current mirror transistor to supply current to the heating element (R3) through control of the variable resistor (R2). **(B)** Photograph of the built current source showing the connections form the source to the input voltage, variable resistor, switch, heating element and DMM for measurement of current through the sense resistor.

Figure 2.30 indicates that to ensure stable voltage outputs of 5.18V, 18.12V and 23.89V, the input voltage must be at least 6.4V, 22.1V and 26.0V, respectively. Measurement pins, used to ensure the input voltage is above the stable threshold will be constructed into the measurement system design.
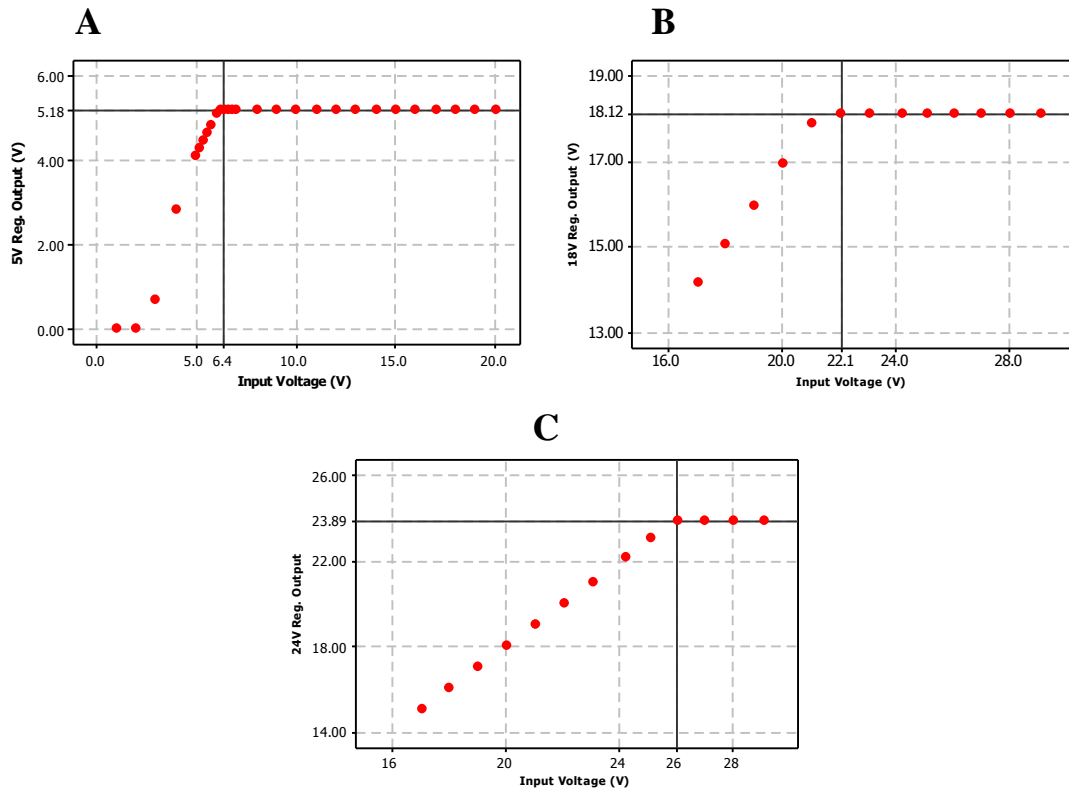
Figure 2.31. Output voltage as a function of input voltage for an **(A)** LM7805, 5V regulator, **(B)** LM7818 18V regulator and **(C)** LM7824 24V regulator showing voltage stabilisation at 5.18, 18.12 and 23.89 V, requiring input voltages of at least 6.4, 22.1 and 26.0V, respectively.

The theoretical current through the heating element using the voltage regulators is shown in Table 2.4 ranging from 0 mA to 14.88 mA (using 5.18 V regulated supply) or 38.47 mA (for the 12.28 V regulated supply). In practice, however, the range will depend on the exact resistance values used and the intrinsic transistor properties. To reduce variation amongst sources and to reduce errors (resulting in non-precise current output), resistors have been chosen with a 0.1% tolerance and a thermal coefficient of 15 parts per million. The current flowing through the heating element can be recorded during the experiments by connecting a digital multimeter across the sense resistor terminals. These values can be increased by altering the resistances within the circuits with these currents used to drive implants using resistors rather than copper coil heating elements

Table 2.4. Comparison of actual and theoretical maximum and minimum current deliveries for LM7805 and LM7812 voltage regulators.

Current Output (mA)	LM7801, 5.18V		LM7812, 12.28V	
	Minimum	**Maximum**	**Minimum**	**Maximum**
Theoretical	0.00	14.88	0.00	38.47
Current Source 1 (P1)	0.26	17.23	0.98	40.76
Current Source 2 (P2)	0.43	17.27	1.28	41.09
Current Source 3 (P3)	0.52	16.09	1.42	40.84
Current Source 4 (P4)	0.48	17.47	1.72	41.54

A current of 40 mA through a 1×0.5 mm 20Ω resistor will supply a power of 64 mW/mm^2, which is expected to be well above thermal safety limits and it is thus expected that this current source will be sufficient to provide the power required by the resistive heating element to induce temperature increases in retinal tissue that are damaging. Tests conducted to determine the reliability of current delivered by the current sources are shown in Figure 2.31. Current deliveries of between 1 and 34 mA were supplied to the heating element for five minutes, with the average error margin (magnitude of current deviation observed over a five minute interval) shown to be less than 2.4 mA for all sources. The error was shown to increase with increasing current supplied, with error margin percentages (on average) measured at 2.8%, 3.0%, 3.1% and 3.5% for the four constructed sources, respectively.
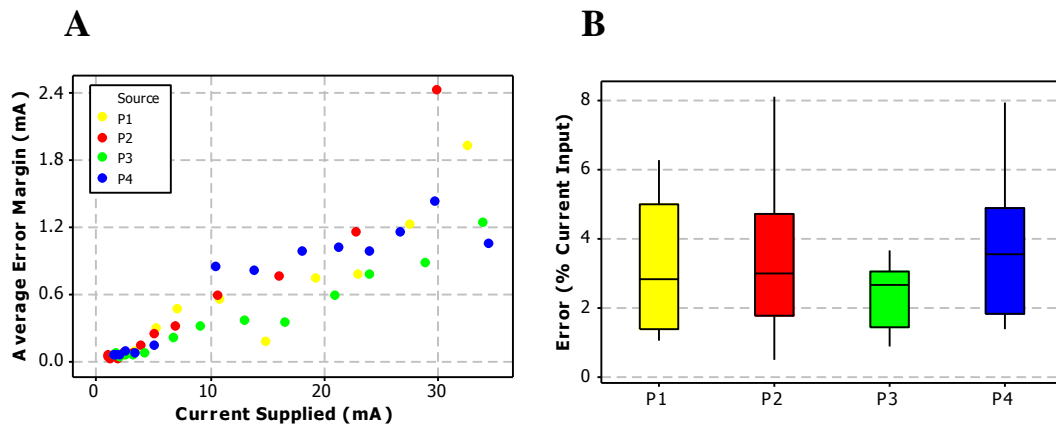
Figure 2.31. (A) Average error margin as a function of supplied current and **(B)** the error as a percentage of the current input for all four current sources (P1, yellow; P2, red; P3, green and P4, blue).

2.4.3 High Resolution Temperature Measurement System

Measurement equipment was constructed to simultaneously measure and record the resistance of all the PRTDs attached to the shaft of the implanted flex-PCB. These measurements of PRTD resistance would then be converted into absolute temperatures and temperature variations that result when the retinal tissue is heated.

A high resolution temperature measurement system (HRTMS), designed by Gavin Pearce (NICTA), was used to convert the measured resistances into temperatures. A photograph of the completed board is shown in Figure 2.32 indicating input locations for the current setting resistor (R_{Iset}), the reference resistor (R_{ref}), the PRTD (R_{PRTD}), the voltage input (V_{in}) and the output voltage (V_{out}) which is converted to measures of temperature. This board requires a DC power of between 9 V and 27 V enabling it to be used in conjunction with other experiments without introducing mains noise. A 24 V regulator was used to ensure a constant and repeatable power delivery to the board, with input voltages greater than 26.0 V producing a stable 23.89 V output.

Some of the design advantages of the HTRMS include the use of alternating current (to remove the thermocouple effects that can occur between dissimilar metals (Benedict 1969), the use of four wire Kelvin connection (reducing the potential for mismatched lead resistances to effect measurement results (Garvey 2007; Kester 2007; MAXIM 2008) and the use of a precision current pump to ensure the current passing through the temperature sensor can be accurately controlled for self-heating analysis (Valvano 1985). The resistors and components used in the construction of the board have a tolerance of 0.1% and a low thermal coefficient (maximum 15 ppm).

To generate an accurate output voltage that relates to the resistive difference between the reference resistor and the PRTD, the circuit initially produces a 1kHz triangular waveform from the input voltage across AD706 operational amplifiers. OP213 components filter this signal through a 1 kHz, 0.25 dB third-order Chebychev filter, which is then supplied to the precision current pump. A resistor with a value of 4.020 kΩ (±0.1%) was used as the current setting resistor, which when supplied with the 1.00V, 1 kHz sine wave (from the Chebychev filter) ensured the current through the PRTD and reference resistor was limited to 250 μA. The circuit diagram of the HTRMS can be found in Appendix 2. This current, well within the specifications given by PRTD

manufacturer Heraeus, is expected to induce a self-heating error of less than 0.05°C through the 1kΩ PRTD, with the specified self-heating coefficient of 0.8°C/mW.

Figure 2.32. Photograph of high resolution temperature measurement device indicating voltage input, measurement output, current setting resistor, sense resistor and PRTD attachment.

As temperatures between 33°C and 44°C are of most importance (body temperature plus additional induced heat), a reference resistor must be chosen to correspond with the PRTD resistance within this range. The circuit uses a difference amplifier to enhance the signal, comparing the reference resistance to the resistance of the PRTD, with resistances of 1.12kΩ to 1.15kΩ (corresponding to PRTD measured temperatures of approximately 31°C to 39°C) shown in Figure 2.33.

In Figure 2.33, the zero crossings (temperature at a measurement of 0 V) increase from 31°C to 33.5°C and then to 39°C as the reference resistance of increases from 1.12kΩ to 1.13kΩ and to 1.15kΩ. The linear range of the HTRMS, in which there is the greatest change in measured voltage for a given PRTD resistance change, also shifts with increases reference resistance, with ranges of 25.5°C to 37.5°C, 27.5°C to 39.5°C and 33.0°C to 45.0°C for the 1.12kΩ, 1.13kΩ and 1.15kΩ resistances respectively. A resistance of 1.15kΩ was chosen as the reference resistance, as the 33°C to 45°C allows for temperature measurements slightly below body temperature (as may be expected within the eye) to well above a temperatures shown to cause retinal burns. Calibration of the PRTD sensors with the HTRMS was performed to ensure the equipment was adapted to function optimally around the 33°C to 45°C range, to reduce any noise

artefacts and to determine the correlation between measured voltage and tissue temperature.
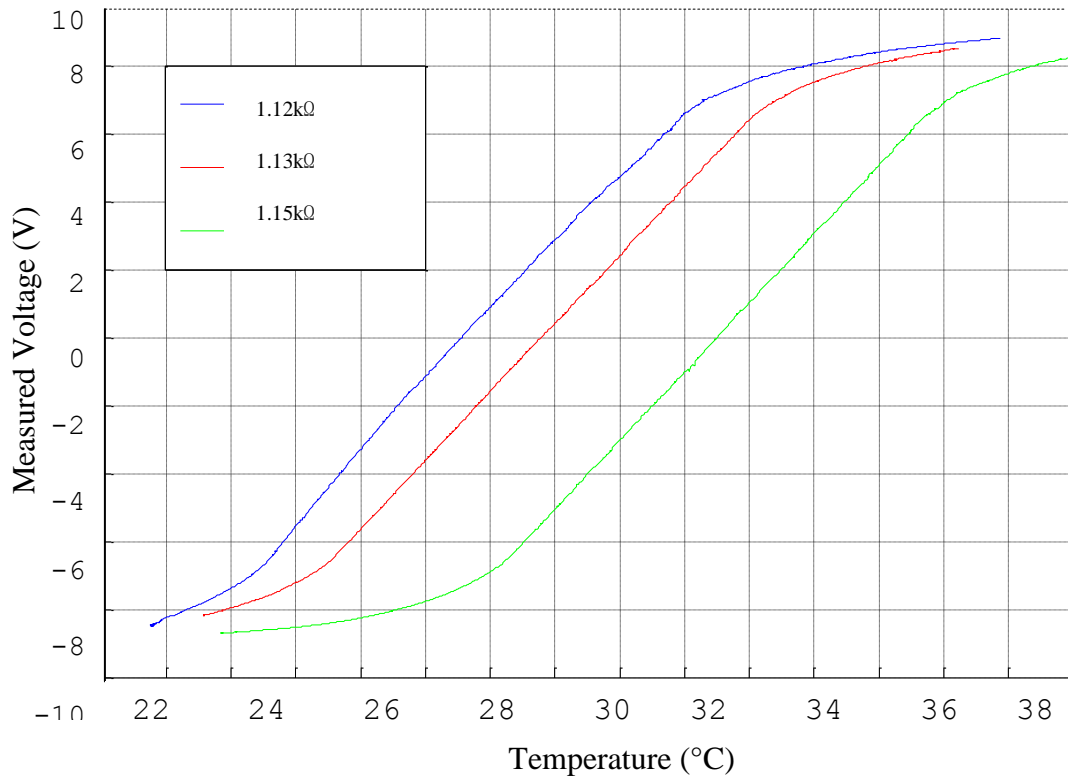
Figure 2.33. Effect of reference resistance on the HRTMS dynamic range (linear portion of temperature-voltage curve) for reference resistances of .112kΩ (blue), 1.13kΩ (red) and 1.15kΩ (green) for temperatures between 22 and 50°C

The experimental set-up is shown in Figure 2.34 and involves the submersion of the implant containing the heating element and sensors within a saline bath. The fluid temperature is measured by an independent PRTD sensor connected to a digital multimeter and is moderated by controlling the brightness of light globes contained within the reflective heat bath chamber. A fan is used to ensure no hot spots occur within the saline solution, particularly at regions closer to the walls of the glass vessel. Temperature measurements from the implant sensors are sent via a splitter to the high resolution temperature measurement device before passing through the data acquisition hardware to a computer for real time voltage recording. A box was built to house the required splitters, current sources and high resolution temperature measurement devices and allow easy control and measurement of the currents supplied to the implanted heating elements. A photograph of the constructed box is shown in Figure 2.35.
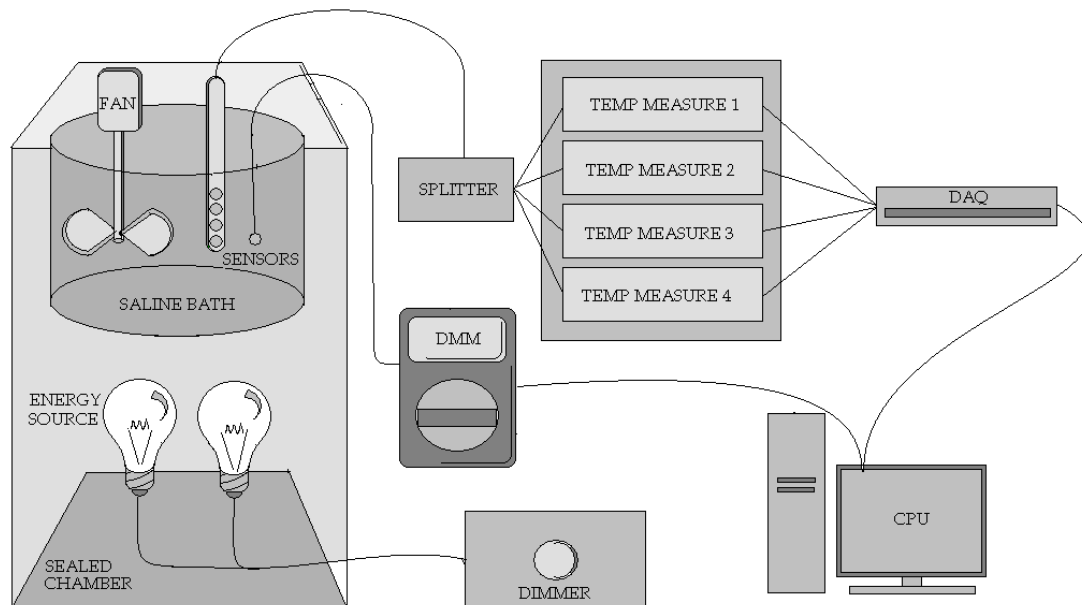
Figure 2.34. Experimental set-up for calibration sequences where an implant containing temperature sensors and current sources is immersed in the saline bath. Temperature of the saline bath is measured by a digital multi-meter (DMM), with the light globe energy sources contained within the sealed chamber of the custom made heat bath controlled by the dimmer. A fan is used to uniformly distribute thermal energy within the saline bath. The implant temperature sensors are connected to a splitter and the four high resolution temperature measurement devices (Temp Measure 1-4) are digitally acquired and recorded simultaneously and in real time by the computer (CPU), which also records temperature measured by the DMM.

To calibrate the high resolution temperature measurement device, the saline solution within the heat bath was heated through the 32°C to 45°C temperature range at rates varying from 0.2°C/minute to 2.6°C/minute. Voltage measurements corresponding to sensor temperatures were recorded by LabVIEW Signal Express at rates varying from 1Hz to 1kHz. These voltages were compared to resistance measurements recorded by the digital multimeter corresponding to heat bath temperature after conversion to temperature using the second order linearization method.

Seven independent recordings were taken over the temperature range 32°C to 45°C for each of the high resolution temperature measurement boards. A sample of data collected from at least seven tests (performed on different days allowing for ambient temperature deviations to be negated) is shown in Figure 2.36 for each of the four high resolution temperature measurement systems. The tests performed on each of the boards, suggests a highly linear and repeatable temperature-voltage profile. While there are slight differences between each of the boards due to minute component differences, these results indicate the ability of the devices to determine tissue temperatures to within 0.1°C.
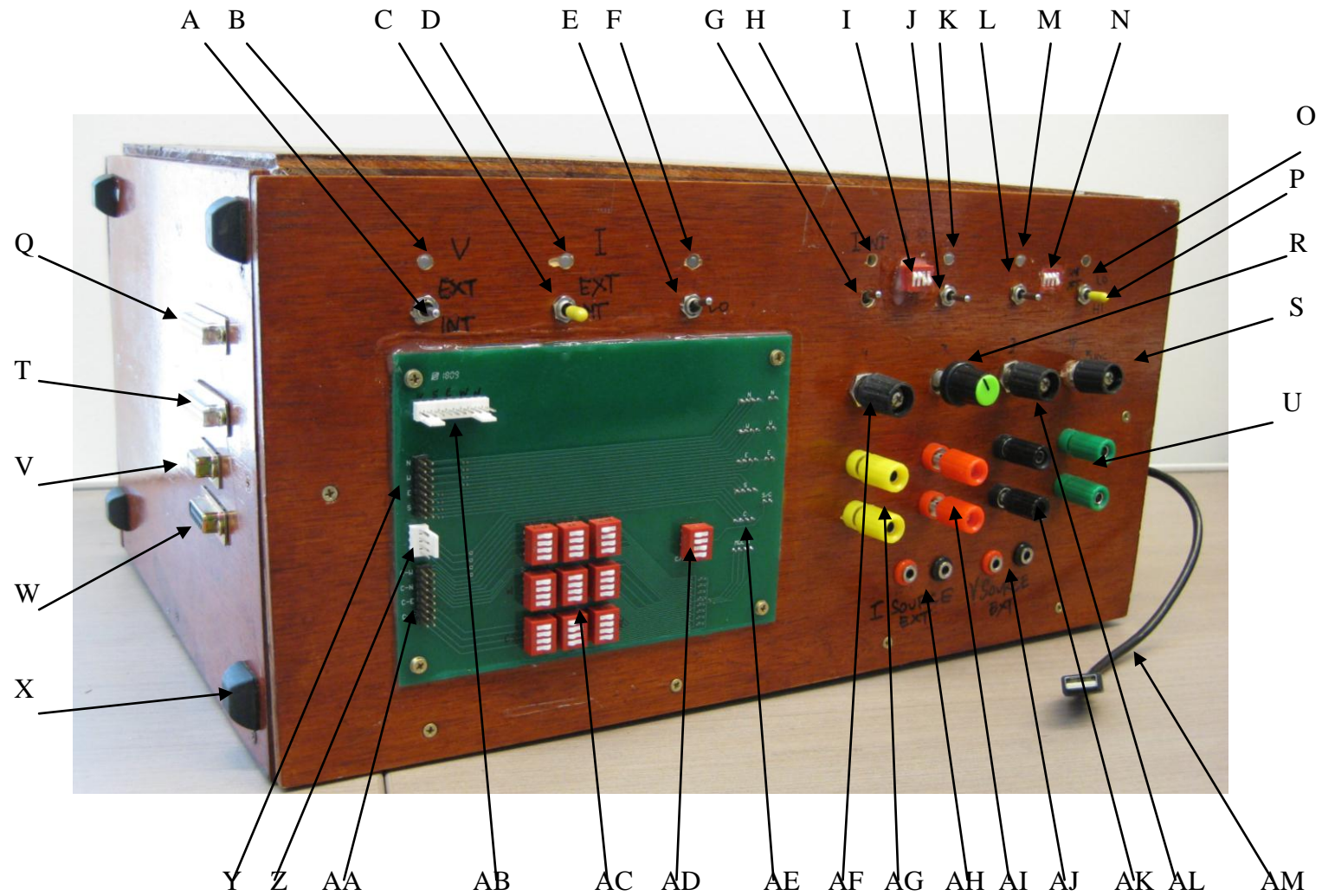
Figure 2.35 (opposite page). Custom made box designed to house temperature measurement and current source devices. **(A)** Switch to supply voltage to the high resolution temperature measurement system from either an internal regulated battery or external source or none. **(B)** Two colour LED showing whether high resolution temperature measurement system is being supplied from an external or internal regulated voltage source. **(C)** Switch to supply current sources from internal regulated battery or external supply. **(D)** Two colour LED to indicate whether power to current sources is supplied from an internal regulated battery or external voltage source. **(E)** Switch to enable a high or low voltage to be supplied to the current sources. **(F)** LED indicator to show whether high or low power is being supplied to current sources. **(G)** Switch to turn on current source 1 to either the high or low source setting. **(H)** Two colour LED to indicate whether current source 1 is powered by a high or low current source setting. **(I)** Four-way switch to enable or disable recorded measurements from any of the four current sources. **(J)** Switch to turn on current source 2 to either the high or low source setting. **(K)** Two colour LED to indicate whether current source 2 is powered by a high or low current source setting. **(L)** Switch to turn on current source 3 to either the high or low source setting. **(M)** Two colour LED to indicate whether current source 3 is powered by a high or low current source setting. **(N)** Four-way switch to enable any of the four heating elements to be directly supplied by an external current source. **(O)** Switch to turn on current source 4 to either the high or low source setting. **(P)** Two colour LED to indicate whether current source 1 is powered by a high or low current source setting. **(Q)** Attachment point for implant with up to four current sources and four temperature sensors (in four wire Kelvin connection). **(R)** Variable resistor used to control current supplied from current source 2. **(S)** Variable resistor used to control current supplied from current source 4. **(T)** Additional attachment point for implant with up to four current sources and four temperature sensors (in four wire Kelvin connection). **(U)** Connection point for recording of current supplied by current source 4. **(V)** Connection point for additional ten PRTD measurements using device designed for when using CC - 2. **(W)** Connection point for additional ten PRTD measurements using device designed for Implants SMR - 5 and SMR - 6. **(X)** Stability feet. **(Y)** Connection point for leads to connect to north, south, east and west PRTDs to measurement system using Implant V and four wire Kelvin connection. **(Z)** Connection point for central PRTD to measurement system using SMR - 4 and four wire Kelvin connection. **(AA)** Connection point for leads to connect to north-west, south-west, north-east and south-east PRTDs to measurement system using SMR - 4 and four wire Kelvin connection. **(AB)** Connection point for leads to north, south, east, west and central heating elements using Implant V. **(AC)** Nine four-way switches to control four wire Kelvin measurements from all implanted PRTDs using Implant V. **(AD)** Switch to change current source from central to north. **(AE)** Additional measurement points for current sources and centrally located PRTDs. **(AF)** Variable resistor used to control current supplied from current source 1. **(AG)** Connection point for recording of current supplied by current source 1. **(AH)** Connection point for external current source. **(AI)** Connection point for recording of current supplied by current source 2. **(AJ)** Connection point for external voltage source. **(AK)** Connection point for recording of current supplied by current source 3. **(AL)** Variable resistor used to control current supplied from current source 3. **(AM)** Attachment from data acquisition card to computer for simultaneous real time recording.

117
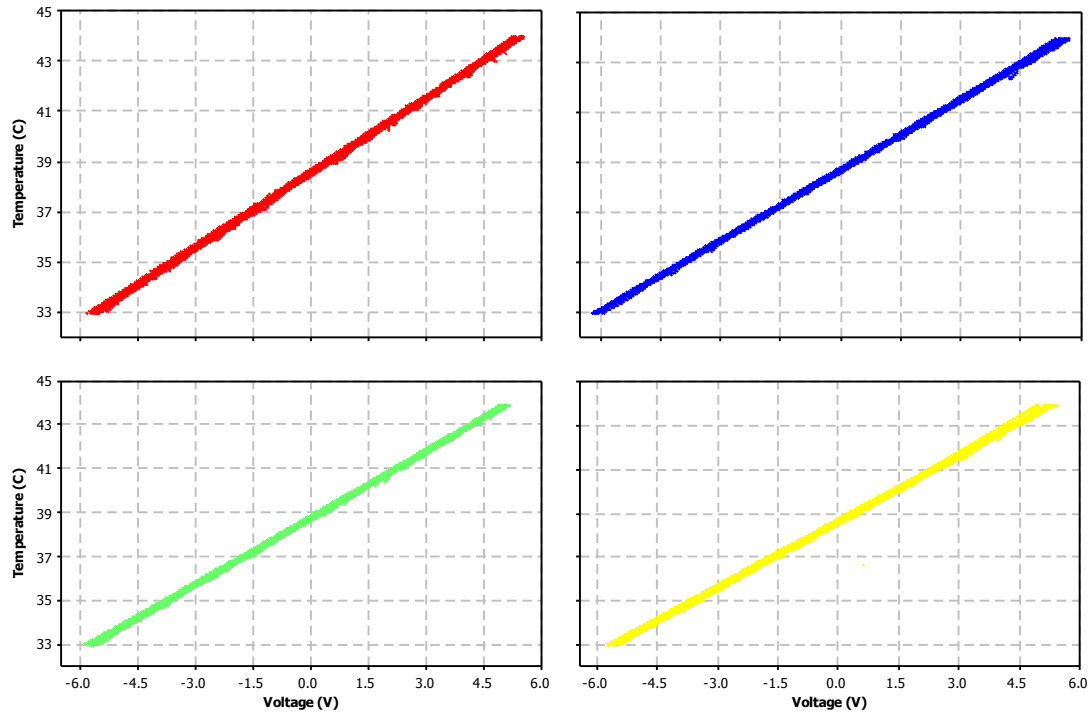
Figure 2.36. Temperature voltage measurements obtained experimentally for Boards 1 – 4 over the temperature range of 33 to 44°C.

The gradients of each of the boards were designed to be 1°C/V. This was to allow simple determination of the measured temperatures during experimentations in which the output would be in volts. The zero-crossings of each of the boards, set using 1.15kΩ (±0.1%) were between 38.6°C and 38.82°C for each of the boards, allowing the linear range to be maximised surrounding body temperatures and expected temperature elevations (33°C to 45°C). The differences between the measured results and the linear equations (Temperature = Zero Crossing + Gradient × Voltage) are listed in Table 2.5. The average differences suggest that each of the boards will measure temperatures accurately and within a tolerance of 0.1°C. Differences between equations and the experimentally measured data are shown in Figure 2.37 for each of the four boards.

For each board, the R^2 value (calculated by Minitab 15, Minitab Inc.) was 99.9%, with all S-values (standard distance the data values fall from the linear regression line) within 0.1°C. This indicates that the boards can be used to reliably and repeatable measure temperatures and thermal elevations observed in retinal tissue.

Table 2.5. Linear conversion factors, offsets and R^2 values for the four high resolution temperature measurement boards.

	Board			
	1	**2**	**3**	**4**
Gradient (V/°C)	0.9914	0.9417	1.017	1.009
Zero-crossing (°C)	38.60	38.75	38.82	38.66
Maximum Difference (°C)	0.31	0.32	0.31	0.27
Minimum Difference (°C)	-0.22	-0.23	-0.21	-0.34
Average Difference (°C)	-0.002±0.08	-0.002±0.07	-0.003±0.07	0.003±0.08
S-Value	0.0896	0.0705	0.0798	0.0933
R^2 Value	99.9	99.9	99.9	99.9
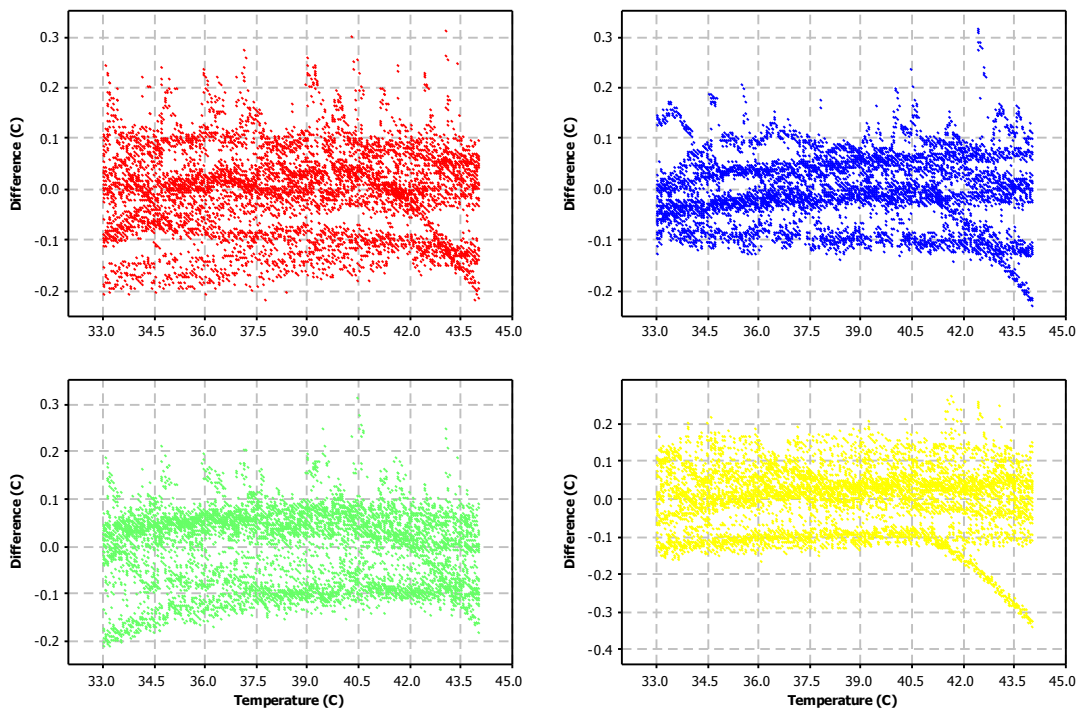
Figure 2.37. Histograms of residuals for all board equations indicating differences between theoretical calculations and experimentally obtained data over multiple successive trials over the temperature range 33 to 44°C.

2.5   CONCLUSIONS

This chapter discussed the equipment required to induce and detect thermal alterations occurring to retinal tissue. Different sensors were investigated, with platinum resistance temperature detectors chosen due to their reliability, accuracy, small size and ability to be soldered on to constructed implants. These implants, capable of monitoring thermal changes in a number of areas were constructed to be specialised for different test durations and for evaluation of different implantation locations. The implants also had varied number and size of heating elements, aimed at reducing the number of animal trials required whilst allowing different heating element sizes (imitating different sizes of retinal prosthesis electronics) to be evaluated.

The heating elements were shown using infra-red thermography to heat up to desired temperatures in the desired regions, without inducing thermal elevations in retinal regions in contact with the heating element lead wires. The heating elements were powered by custom made current sources, capable of delivering a large range of currents and thus able to induce a wide range of thermal elevations. The current sources were observed to be accurate, deviating by less than 8% over a five minute duration.

High resolution temperature measurement equipment were constructed and calibrated and were able to be monitored and recorded in real time through connection to computer. A heat bath was also constructed to ensure an animal's body temperature can be accurately replicated for use in cadaver trials.

3

FINITE ELEMENT THERMAL MODELS

In order for visual prosthesis to enable patients the ability to read, recognise faces and be independently mobile, prosthesis electrode numbers will have to increase significantly (Cha, Horch et al. 1992; Cha, Horch et al. 2000; Margalit, Maia et al. 2002; Eckhorn, Wilms et al. 2006). Additional electrode numbers will increase the power required by the implants, which may cause thermal damage to retinal neurons if the implanted circuitry induces large retinal tissue temperature increases. While there is a reasonable amount of literature investigating the use of finite element models to predict the temperature distributions around human eyes during steady state conditions (Scott 1988) and from laser and radiofrequency irradiation (Scott 1988; Bernardi, Cavagnaro et al. 1996; Hirata, Matsuyama et al. 2000; Hirata 2005; Ng and Ooi 2006; Flyckt, Raamakers et al. 2007; Ng and Ooi 2007; Wainwright 2007), there is a clear deficit of thermal models constructed to investigate temperature increases caused during retinal prosthesis operation.

To accurately assess temperature increases that cause damage to retinal neurons by thermal energy dissipation from a retinal implant, animal experiments need to be performed. The number of animal experiments can be greatly reduced by replacing animal trials with simulations performed using thermal models, provided the thermal models are accurate. While many studies have constructed thermal models of human eyes, the ability and accuracy of these models to predict temperature distributions caused by implanted heating elements in a cat eye remains largely unknown. Thermal models of cat eyes, designed to be used in conjunction with both epiretinal and suprachoroidal experiments, have been constructed. To ensure the thermal models can

accurately replicate experimental conditions used in cadaver tests and *in vivo* experiments, alterations in body and room temperatures, thermal conductivity of the retinal and choroidal tissue and the presence of choroidal blood perfusion have been investigated.

To ensure the safety of retinal prosthesis recipients, experiments have been performed on cat retinal tissue to investigate thermal damage thresholds. To reduce the number of animals required, two- and three dimensional finite element thermal models (FEM) were constructed using COMSOL Multiphysics (COMSOL AB) to investigate temperature distributions that are induced within the eye by energy dissipation from suprachoroidal and epiretinal implants.

The accuracy of the constructed FEMs can be validated through cadaver trials, with simulations investigating the effects of room and body temperature fluctuations, perfusion rates, implant positions, changes in choroidal and retinal thermal conductivities as well as the effect of increasing implant temperatures used to reduce the number of required animal experiments.

Finite element simulations indicted that while room temperature, body temperature and metabolically generated heat had little effect on retinal tissue temperature, there would be significant differences between excised and fixed cadaver eyes and experiments performed *in vivo*. Primary differences included the thermal conductivity of the tissue and blood perfusion, with the placement of the heating element also altering the thermal profile and potential safety of an eye.

Results from the finite element models, cadaver trials (Chapter 4) and *in vivo* experiments (Chapter 5) have been accepted for publication in the IEEE Transactions on Biomedical Engineering (Opie, Burkitt et al. In Press).

3.1 FINITE ELEMENT MODEL CONSTRUCTION

The finite element thermal models used to simulate the experimental protocols have been designed in size and structure for direct comparison between model simulations and cat experiments. The main components which make up the global volume and structure of the eye were included (lens, cornea and sclera) as well as the retina, the structure most important in thermal damage investigations, and the choroid, the major blood supply and thermoregulatory structure within the eye.

The overall shape of the eye was constructed as the combination of a global ellipsoid with a 21 mm anteroposterior axis, a 20 mm transverse and vertical axis and a connecting corneal sphere with a radius of curvature of 8 mm, as shown in Figure 3.1. Between points A and B, the 0.6 mm cornea is modelled as a room temperature boundary condition, with predetermined ambient temperatures set along this arc. In a similar fashion, the remaining segment of the globe (comprising the sclera and the remaining cornea) is set to a desired body temperature boundary condition. The 0.08 mm thick choroid lies on top of the sclera and stretches almost to the horizontal meridian, as does the 0.6 mm thick retina. The lens, modelled with an 8 mm anterioposterior dimension and a nasotemporal diameter of 12 mm, has a steeper anterior curvature and sits just posterior to the centre of the globe. An intersection between the lens and the cornea and sclera divides the remainder of the eye into anterior and vitreous chambers, filled with their respective fluids. Measurements of cadaver eyes were used in conjunction with dimensions observed by Prince (1960) to construct the cat model.

The model is designed to be used for investigating thermal increases that can occur in one of two currently proposed retinal prosthesis locations: suprachoroidally (within the suprachoroidal space between the sclera and the choroid) and epiretinally, (positioned in the posterior chamber in direct contact with the retinal neurons). The epiretinal implant has been placed in the macula lutea, a 6 mm diameter area located almost along the vertical midline, as this area is responsible for the majority of useful vision (Roberts 2002). Due to the ganglion cell axons forming the optic nerve passing through the retina and choroid, the suprachoroidal implant has been positioned 0.5 mm temporally from the vertical midline following the scleral curvature. The heating elements are set to the

thermal conductivities of the materials they replace when not in use (are essentially invisible): the vitreous humor for epiretinal implants and scleral tissue for the suprachoroidal implant.

While the eye has many other structures (such as the pupil, iris, ciliary muscles, etc.), most of these components are located within the anterior portion of the eye and have been omitted as it is expected that any thermal damage occurring due to the thermal energy dissipation from an implanted heating element (either placed on the retina-vitreous margin or choroid-scleral interface) will occur in the posterior segment of the eye at a distance far enough from the frontal accessory structures so as not to cause deleterious effects. While some damage may occur to the tapetum, a 86 μm thick reflective cellular layer behind the retina, it has been excluded as this structure is not present in primates (Shen, Cheng et al. 2006). A schematic of the thermal model is shown in Figure 3.1, with all dimensions indicated in millimetres. Different regions of the eye are modelled as isotropic, homogeneous masses that allow a continuous flow of heat flux across and between the component intersections.
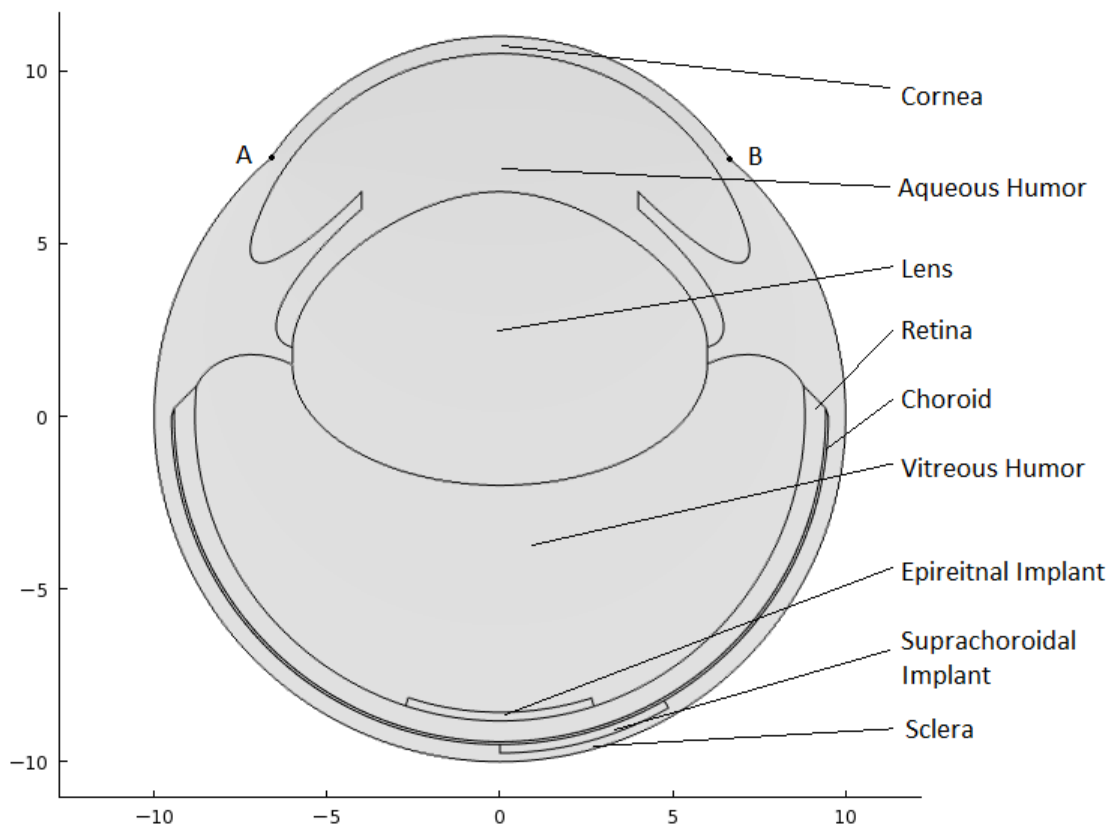
Figure 3.1. Schematic of the designed cat eye model indicating the primary global components (cornea, lens, aqueous and vitreous humor, retina, choroid and sclera) and the locations of an epiretinal and suprachoroidal implant. Anterior to points A and B, the corneal boundary condition is set to a predetermined room temperature, with a body temperature boundary condition set on the sclera.

The largest difference between human and cat eyes is the lens, with the human lens significantly smaller (Liou and Brennan 1997; Narasimhan, Jha et al. 2010). Temperature increases required to induce damage to the lens would need much larger implant power dissipations than would be safe for retinal tissue and as such, the size difference is not expected to compromise thermal model accuracy or the ability to relate these temperature increases to human situations. Other differences include thicknesses used for the retina, choroid and sclera in which there is a tapering down of these layers towards the limbus, with the tissues being thickest at the optic nerve. This has not been accounted for in the finite element model although as the implants are positioned centrally, a significant reduction in thermal damage is expected to occur at the horizontal poles. In each of these regions, a uniform thickness was used, taken as the average of the extremes.

Table 3.1. Dimensions of human and cat eye components used in the finite element thermal model.

Component	Property	Dimensions (mm)	
		Human	**Cat**
Choroid	Thickness	0.1 – 0.2	0.08
Cornea	Thickness	0.52 (centre) 0.89 (limbus)	0.60
	Radius of curvature	7.8	8.00
	Horizontal diameter	-	16.0
	Vertical diameter	-	16.0
Globe	Anterioposterior axis	21.0 – 26.0	21.0
	Transverse axis	24.0 – 23.0	20.0
	Vertical axis	24.0 – 25.0	20.0
Lens	Anterioposterior radius	3.75 – 7.69	8.00
	Nasotemporal radius	3.55 – 4.50	12.00
Retina	Thickness	0.50 (posterior) 0.10 (limbus)	0.60
Sclera	Thickness	0.60 (limbus) 0.50 (equator) 1.00 (optic nerve)	0.50
	Radius of curvature	12.0	10.0

Two models were designed to investigate thermal increases that can occur in the two currently proposed retinal prosthesis locations, epiretinally (positioned in the posterior chamber in direct contact with the retinal neurons) and suprachoroidally (within the suprachoroidal space between the sclera and the choroid). In both cases, the centrally placed implants were modelled as 5 mm diameter, 0.25 mm thick cylinders, and conformed to the curvature of the underlying tissues. While retinal prostheses would generally not be operated in a fashion in which all electrodes are stimulated simultaneously (due to power constraints and the amount of thermal energy that would be dissipated into neighbouring tissue by doing so), the entire implant has been

modelled as a constant temperature source, providing an upper limit of temperature increase and potential thermal damage. This also assumes that power, generated by the stimulating circuitry, will affect the entire implant uniformly, which is also a worst-case scenario.

The models have assumed that the aqueous humor in the anterior chamber and the vitreous humor in the posterior chamber have the same thermal conductivity, with the average value of 0.59 mW/mm·°C used in the finite element models. All thermal conductivities of the orbital tissues used in the finite element model were obtained from published sources (Lagendijk 1982; Scott 1988; Scott 1988; Liou and Brennan 1997; Hirata, Ushio et al. 1999; Oyster 1999; Hirata, Matsuyama et al. 2000; DeMarco, Lazzi et al. 2003; Gosalia, Weiland et al. 2004; Hirata 2005; Lazzi 2005; Flyckt, Raaymakers et al. 2006; Hirata, Fujimoto et al. 2006; Hirata, Watanabe et al. 2006; Ng and Ooi 2006; Flyckt, Raamakers et al. 2007; Ng and Ooi 2007; Ooi and Ng 2007; Wainwright 2007; PCB 2009; Matweb 2010; Narasimhan, Jha et al. 2010), with average values taken where discrepancies occurred. A full list of thermal conductivities, dimensions and other material properties (and respective references) are listed in Appendix 3, with Table 3.2 providing component properties of human eyes and those used in the cat thermal model.

Table 3.2. Tissue properties (thermal conductivity, density and specific heat) used in the construction of the finite element model of a cat eye.

Tissues	K W/m°C	ρ kg/m^3	C J/kg°C
Anterior Chamber	0.600	1009	3430
Lens	0.400	1100	3000
Vitreous Body	0.600	1009	3430
Retina	0.565	1039	3680
Choroid	0.600	1050	4178
Cornea and Sclera	0.580	1075	4178
Epiretinal Implant	400.0	8700	385
Suprachoroidal Implant	400.0	8700	385

The model was constructed with 437444 tetrahedral elements, with stationary nodal point temperatures calculated using a linear solver adhering to the bioheat equation (Lazzi 2005)

$$C\rho \frac{\partial T}{\partial t} = \nabla \cdot (K \cdot \nabla T) + A - B(T - T_b) + Q \tag{3.1}$$

where C is the specific heat [J/(kg °C)], ρ is the tissue density (kg/m^3), T is the temperature (°C), K is the isotropic thermal conductivity [W/(m °C)], A is metabolically generated heat (W/m^3), B is the blood perfusion coefficient [W/(m^3 °C)], Q represents the power dissipated by an implant (W/m^3) and T_b is the blood temperature, assumed

constant at 37˚C. Simulations in which temperatures were imposed on the implanted heating elements were also performed, indirectly accounting for power dissipation. In cadaver models, there was no metabolically generated heat ($A=0$) or blood perfusion ($B=0$) with *in vivo* temperature dependence of metabolism within the retina modelled as

$$A = A_R (1.1)^{(T-T_0)}$$

(3.2)

where T_0 is the basal temperature (˚C) and A_R is the retinal metabolic rate of 10000 W/m^3 (Lazzi 2005). Blood perfusion to the choroid and retina was represented in models by setting the choroid to a temperature of 37˚C, or through

$$B = \begin{cases} B_R & \text{for } T \leq 39^o\text{C} \\ B_R[1+0.8(T-39)] & \text{for } 39^o\text{C} \leq T \leq 44^o\text{C} \\ 5B_R & \text{for } T \geq 44^o\text{C} \end{cases}$$

(3.3)

where B_R is the retinal blood perfusion rate of 35000 W/(m^3 ˚C). A 20˚C room temperature boundary condition was imposed anteriorly to line A (Figure 3.1) or the cornea, with a convective boundary condition imposed on the remaining, posterior segment of the globe (Ng and Ooi 2006)

$$k \frac{\partial T}{\partial n} = h_b (T - T_b)$$

(3.4)

where n is the normal direction to the surface boundary and h_b is the convection coefficient between the head and eye with a value of 65 W/(m^2 ˚C). To identify the thermal increases that occurred in response to increased implant temperatures or power dissipations, temperatures were measured along the vitreous-retinal margin, at the retinal centre and on the retinal-choroidal interface from the posterior axis of the globe forward, shown in Figure 3.2.

Previous research has indicated that increasing the number of elements within finite element models of human eyes (Ng and Ooi 2006; Ooi and Ng 2007) and of brain surface temperatures (Kim, Tathireddy et al. 2007; Kim, Tathireddy et al. 2007) has only minor impact on temperature measurements (less than 0.07°C), with these models using over 100000 elements. Two-dimensional suprachoroidal thermal models of temperature fluctuations were investigated using a fine mesh with 7776 elements and an extremely fine mesh with 28047 elements. The extra elements between the scenarios were predominantly located within the areas of primary interest, the choroidal blood vessels and the retinal layer.
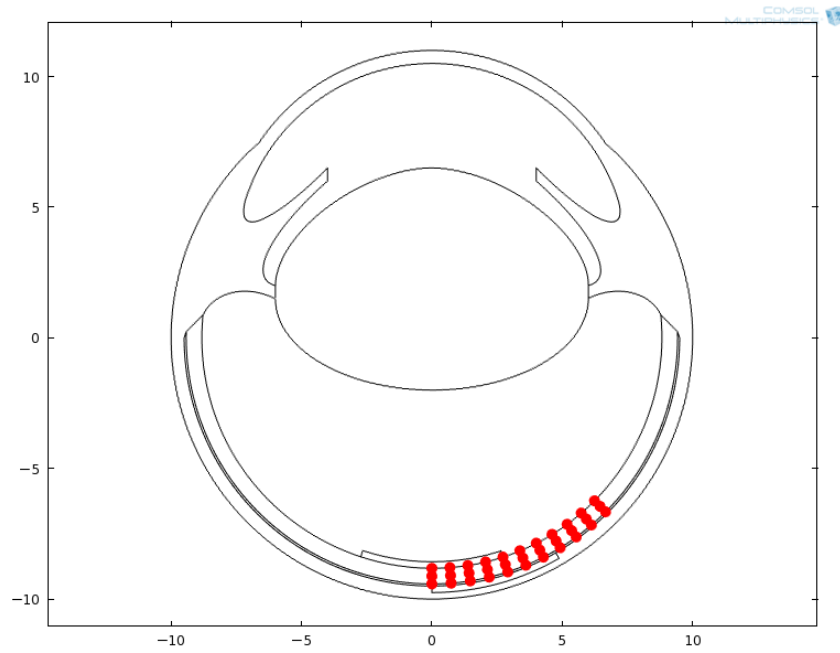
Figure 3.2. Finite element thermal model of a cat eye indicating points (red marks) at which temperatures were measured

| Fine Mesh | Extremely Fine Mesh |
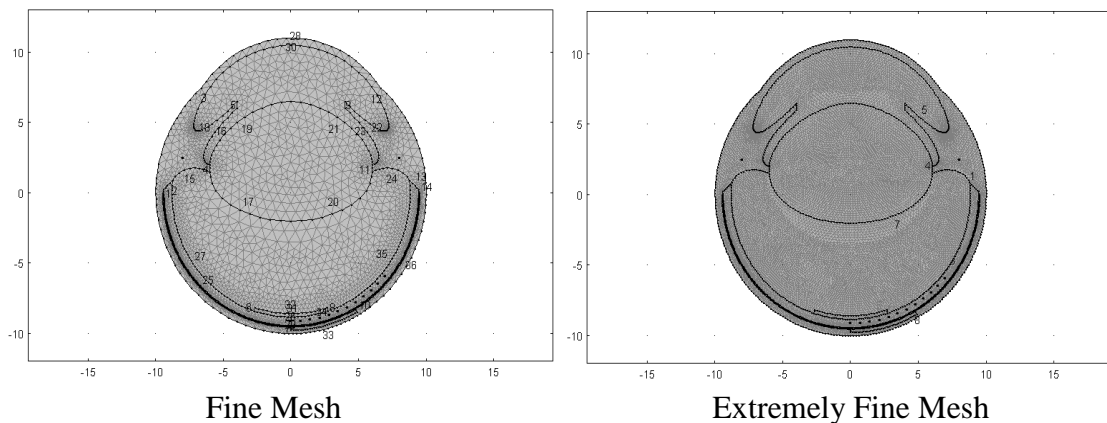
Figure 3.3. Representation of the elements used in a two-dimensional **(A)** fine and **(B)** extremely fine mesh of the cat eye model

To determine the effect that element size had on thermal measurements, analysis was performed in a suprachoroidal setting, with the heating element set to body temperature (37°C) and one, two and three degrees above body temperature (38°C, 39°C and 40°C, respectively). A body temperature of 37°C was set to all nodes situated on the external boundaries of the sclera and cornea up to the height of the iris, approximately in line with the most anterior position of the lens. The corneal temperature above this point was set to a room temperature of 20°C, consistent with room temperatures used in other finite element thermal models (Scott 1988; Ng and Ooi 2008). All tissues were assumed to have an isotropic thermal conductivity. There was an average difference of less than 0.002°C occurring between simulations with fine and extra fine meshes.

To ensure even smaller differences would be observed in a three dimensional model, the 4245 mm^3 three-dimensional finite element model was created with over 437444 tetrahedral elements. The numbers of elements used in each major component of the eye are listed in Table 3.3, with Figure 3.4 showing the FEM with a section removed to allow visualization of the internal components.

Table 3.3. Tissue volumes and element numbers used in the construction of the three-dimensional finite element model of a cat eye.

Tissues	Volume (mm^3)	Elements
Anterior Chamber	572.9	6910
Lens	613.0	4265
Vitreous Body	1534	8343
Retina	346.6	263951
Choroid	45.57	133389
Cornea and Sclera	1123	79305
Epiretinal Implant	4.783	410
Suprachoroidal Implant	4.771	871
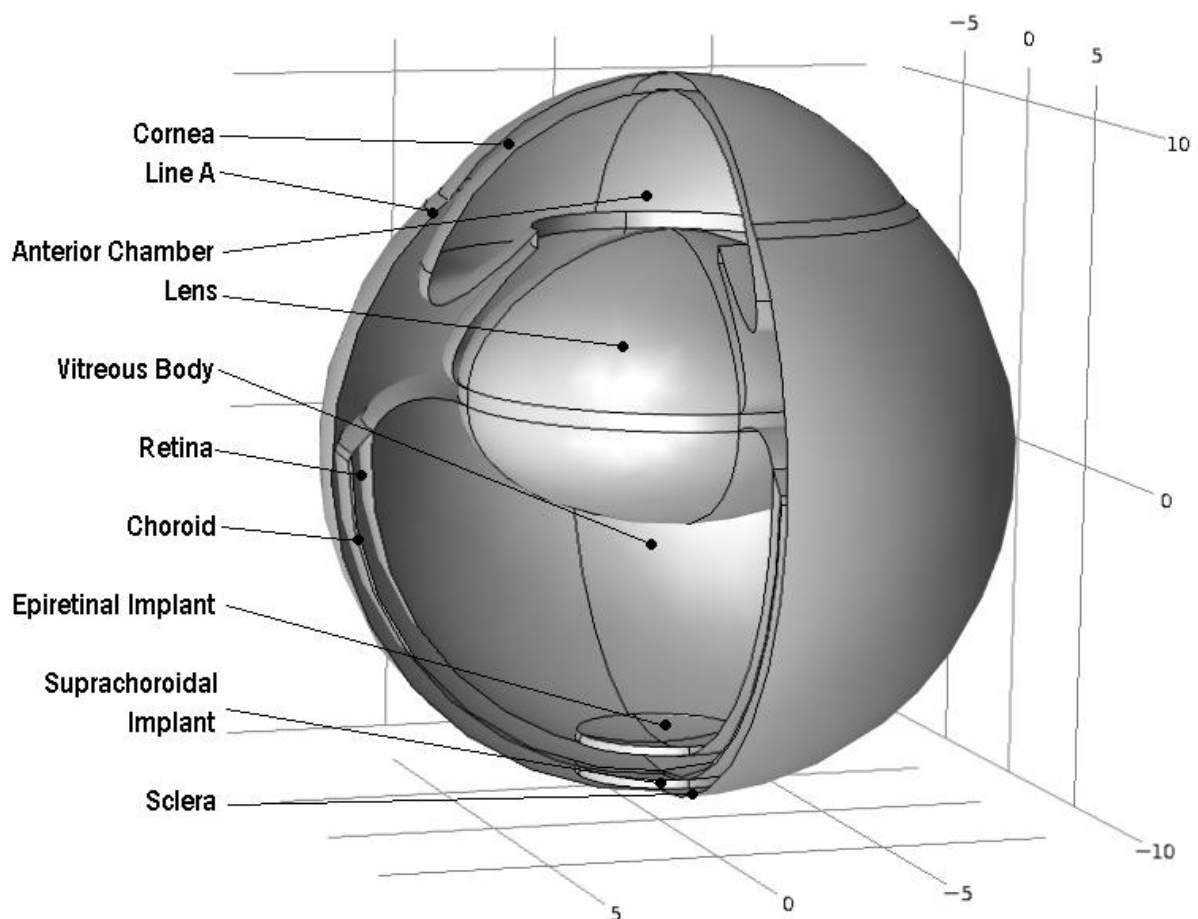
Figure 3.4. Three-dimensional, cut-away schematic of the designed cat eye model indicating the primary orbital components (cornea, lens, aqueous and vitreous humor, retina, choroid, and sclera) and the locations of an epiretinal and suprachoroidal implant. Line A indicates the intersection between the anterior scleral and posterior corneal forced boundary conditions.

3.2   MODEL ALTERATIONS

Comparative evaluations of the thermal models will assist in finding controllable and uncontrollable factors that may act to increase the damage caused to retinal tissue by a visual prosthesis. Factors such as the implant type (epiretinal or suprachoroidal) and the power dissipated through the implant (causing the implant to heat up) can be controlled, and a relationship between these factors and the induced temperatures can be used to guide implant designers. Effects such as body temperature, room temperature, thermal conductivity, perfusion and metabolically generated heat cannot be directly controlled by the device designers and must be analysed to ensure variations in these parameters do not exacerbate the induced temperature increase to the point where thermal damage to the neurons becomes irreversible. Control simulations, designed without either suprachoroidal or epiretinal implants were compared to simulations in which an implant was present to assist in the determination of implant influence. A schematic diagram of the temperatures observed in a control simulation is shown in Figure 3.5.
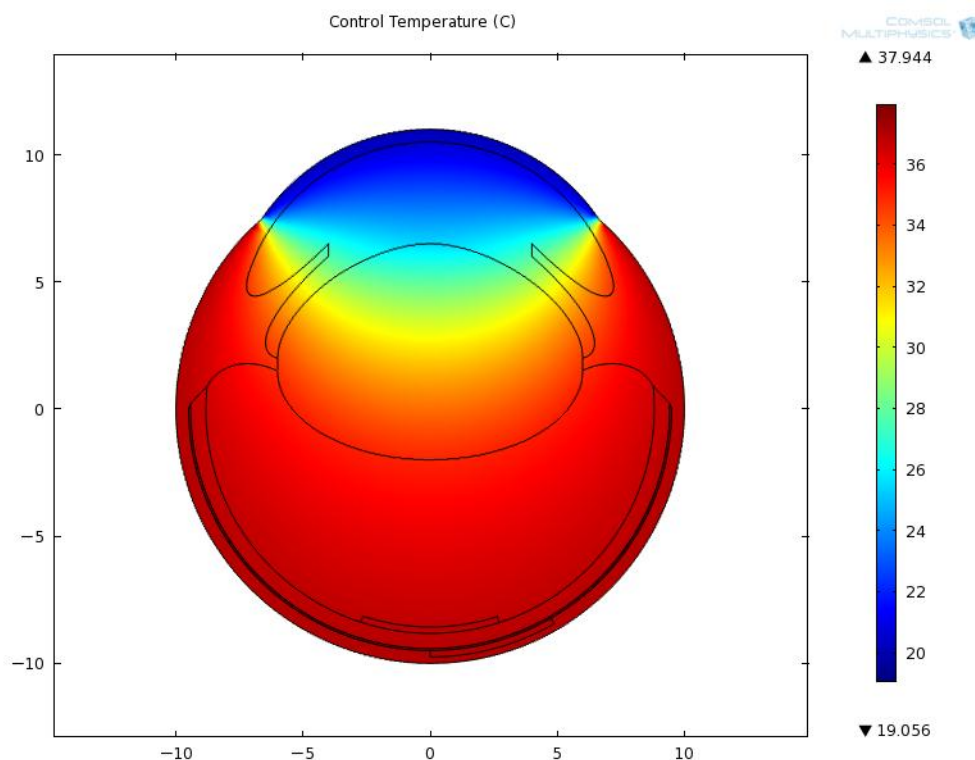
Figure 3.5. Finite element model constructed without influence from epiretinal or suprachoroidal implants indicating control temperautres.

Retinal tissue temperatures obtained from three-dimensional FEM simulations performed in the absence of either epiretinal or suprachoroidal heating elements, were 36.977°C, 36.965°C, and 36.938°C along the retinal-vitreous interface (anterior retina), mid-retina and retinal-choroidal margin (posterior retina), respectively, decreasing slightly as the distance from the horizontal midline increased.

3.2.1 Two- and three- dimensional models

To determine the effect that an additional dimension would have on retinal tissue temperatures in the presence of an active heating element, simulations were performed for heating element temperatures of 37.5°C, 38.0°C, 39.0°C and 40.0°C. A comparison between the temperatures observed along the retinal-vitreous interface for two-and three- dimensional epiretinal thermal models is shown in Figure 3.6.
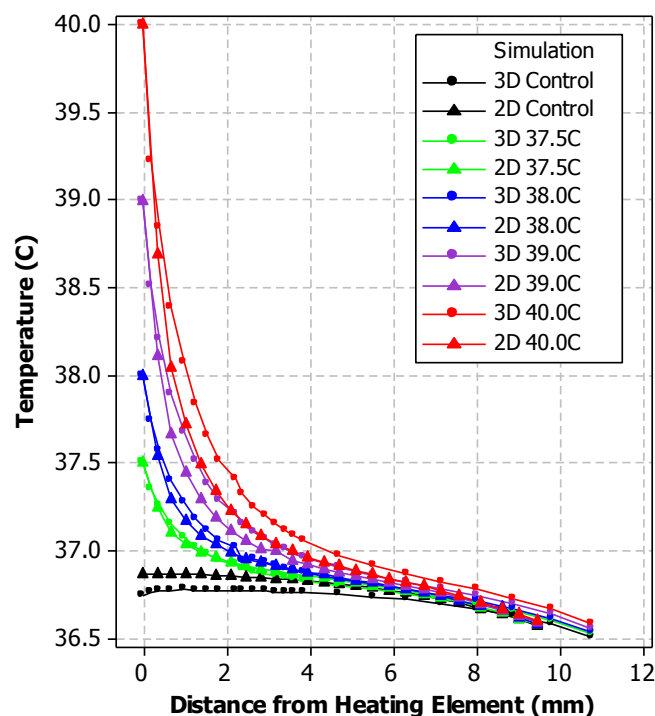
Figure 3.6. Two- and three- dimensional model simulations (triangles and circles respectively) of temperature measurements along the retina-vitreous interface for control scenario (black) and heating element temperatures of 37.5°C (green), 38.0°C (blue), 39°C (purple) and 40°C (red).

The difference in temperatures measured from the two- and three- dimensional model simulations is shown in Figure 3.7A (three dimensional model temperature minus two dimensional model temperature), with Figure 3.7B showing the temperature differences as a percentage of the heating element temperature. The greatest difference (12% of the heating element temperature) occurred at a distance of 0.68 mm from the heating element edge for all heating element temperatures. At a distance of 3 mm, the difference between the two- and three-dimensional models is less than 6%, dropping to below 2% at a distance of 8 mm. Figure 3.7C shows the temperature-distance profile occurring for all two- and three-dimensional models when the temperature increase is normalised, indicating that the two dimensional model will give an over-estimation of the temperatures along the retinal-vitreous interface by up to 12% of the heating element temperature. The retinal tissue temperature in the three dimensional model simulations are observed to cool faster than the two dimensional model, decreasing to 27%, 13%, 7%, 4% and 3% of the heating element temperature at a distances of 1, 2, 3, 4 and 5 mm from the heating element (compared to 37%, 22%, 13%, 8% and 6% for the two-dimensional model), respectively.
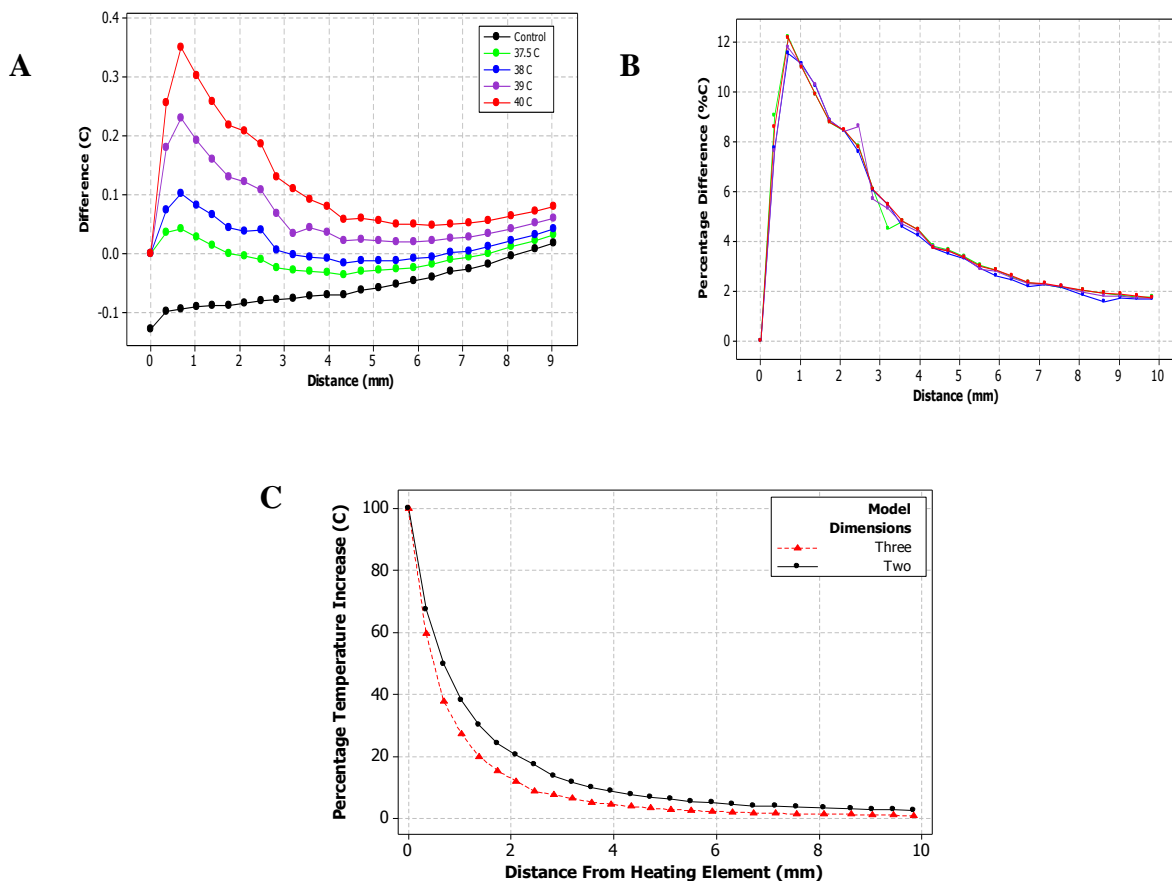
Figure 3.8. Comparison between two- and three- dimensional thermal models as **(A)** a temperature difference and **(B)** the difference as a percentage of the heating element temperature for heating element temperatures of control (black), 37.5°C (green), 38°C (blue), 39°C (purple) and 40°C (red). **(C)** Percentage temperature increase–distance profile relating to all two- and three-dimensional models after normalisation.

3.2.2 Effect of Room Temperature

While room temperatures of between 20˚C and 24˚C can be used to simulate corneal temperatures in cadaver tissues, corneal temperatures of 32.0˚C to 36.7˚C are expected to occur during *in vivo* experimentation (Ng and Ooi, 2006). Simulations performed to analyse retinal tissue temperature alterations induced by changing ambient temperatures have been conducted by Scott (1988) and Ooi (2007), indicating that retinal tissue temperatures would change by less than 0.05°C and 0.27°C, respectively, for room temperatures between 20°C and 30°C.

To ensure thermal models can be directly compared with suprachoroidal cadaver trials, simulations have been performed with corneal temperatures of 20°C, 22°C and 25°C. These simulations are shown in Figure 3.8 for a control scenario and conditions where the heating element is set to 38°C and 39°C.
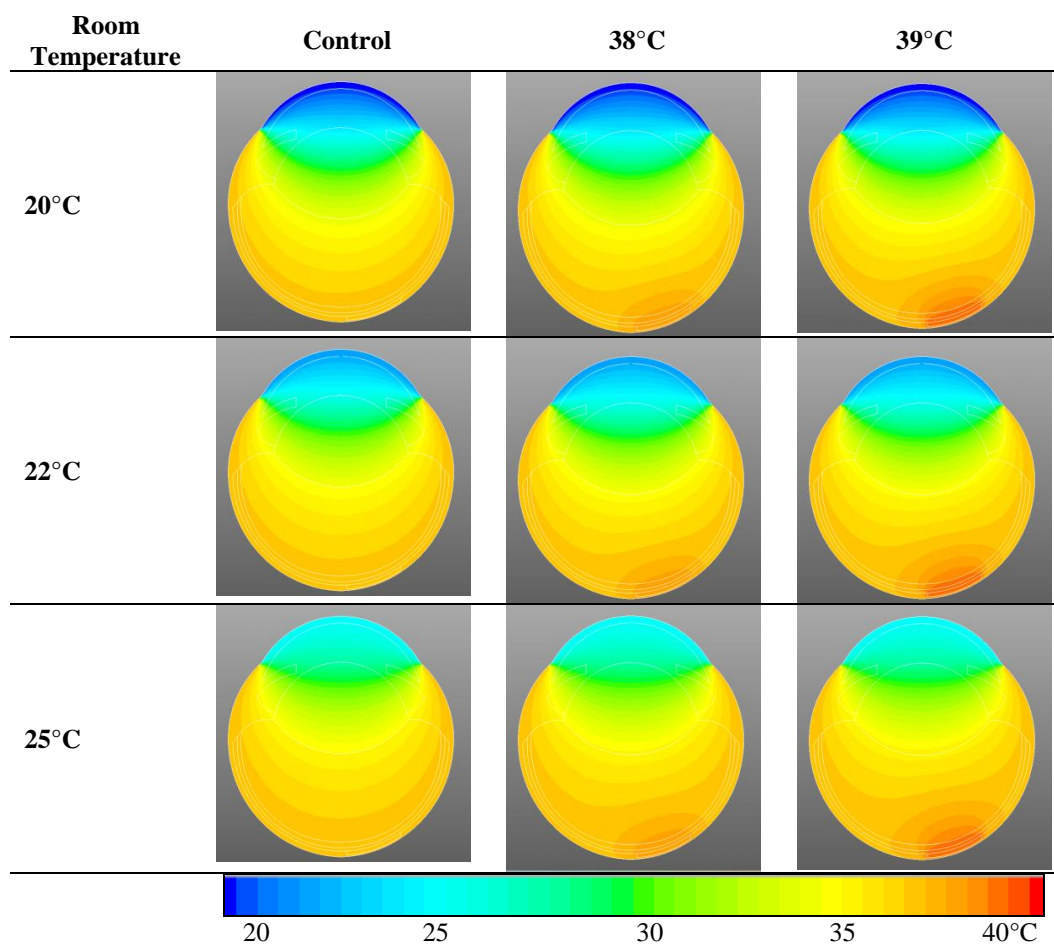
Figure 3.8. Thermal models indicating effects of room temperature (left hand side) and heater temperature (top temperatures). The first column is representative of the control condition with no heater influence.

The effect of alterations in room temperature on retinal tissue temperature (measured at the central retinal-vitreous interface) can be seen in Figure 3.9 for a control simulation (H0) and for heating element temperatures set to 38°C (H38) and 39°C (H39). In each case, the effects of room temperature variations are negligible.
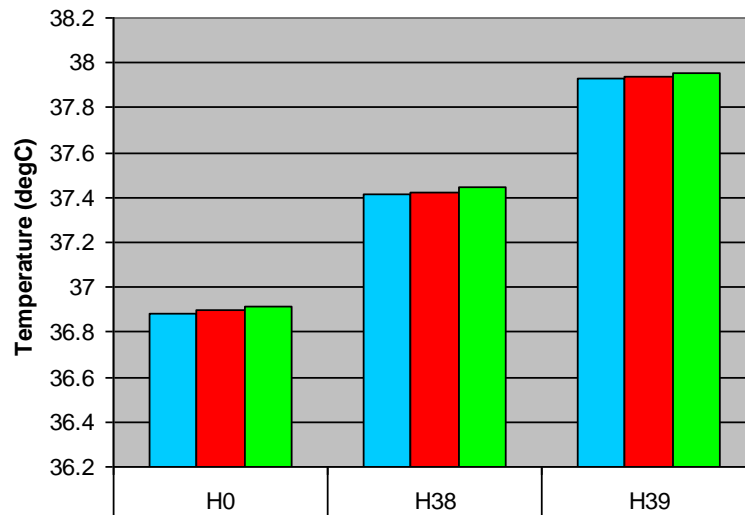
Figure 3.9. The effects of room temperature on the retina-choroid interface under influence of a heating element set to 38°C (H38), 39°C (H39) and a control (H0). Room temperatures of 20°C, 22°C and 25°C are indicated as blue, red and green bars respectively.

To ensure the thermal models can also be used in conjunction with *in vivo* experiments, in which the corneal temperate is higher than the room temperature, simulations were performed investigating corneal temperatures up to 36.4°C. The extent to which variation in corneal tissue had on retinal tissue temperatures was investigated, with the average retinal tissue temperature difference (in the anterior, mid- and posterior retinal layers) less than $0.033 \pm 0.01°C$ over a 26.4°C temperature range (10.0°C to 36.4°C). Thus, variations in room temperatures were considered negligible. Further, model simulations of retinal temperature performed with a convective boundary or a forced 37°C scleral interface were observed to differ by less than $0.035 \pm 0.01°C$, so the forced condition was used for simplicity.

The lack of temperature variation within the retina was expected to be caused by the large volume of intermediate structures (such as the large fluid filled anterior and posterior chambers) that act to thermoregulate retinal tissue and allow visual processing to occur in a homeostatic condition, regardless of the highly variable ambient temperature. The lower thermal conductivity of the lens also acts to prevent significant heat flow from the posterior to anterior regions of the eye.

3.2.3 Effect of Body Temperature Variations

Body temperature is expected to play a large role in the ability of the retina and choroidal vessels to regulate temperature and to prevent damage from occurring. Ward and Bruce (1971) investigated the effect that body temperature had on retinal irradiance in primates and reported that an increase in body temperature correlates with a decreased irradiance required for threshold burn. This is similar to studies done in rats by Noell (1966) and deLint (1992) who also indicated increased body temperature led to a decreased burn threshold. The use of a heat blanket to more closely regulate body temperature has been suggested by Siloski (2007) for use in experimentation with rabbits, and has been employed as part of the *in vivo* experimentation protocol (Chapter 5).

Thermal models were created to investigate the affect that body temperature fluctuations would have on measurements, both along the anterior-posterior axis and across the choroid-sclera interface. Simulations performed under control conditions and with thermal energy induction via an implanted heating element are shown in Figure 3.10 for a constant, 20°C room temperature.

While there is a clear increase in temperature surrounding the heating element caused by an increase in thermal energy dissipation, the general thermal gradients surrounding the heating element are almost identical irrespective of body temperature.

Increasing the body temperature by 1.0˚C (to 38.0˚C) induced an average retinal temperature increase of 1.000 ± 0.004˚C, with a one degree decrease in body temperature (to 36.0˚C) decreasing the average retinal tissue temperature difference by 0.998 ± 0.001˚C. Thus, to extract the effect an implanted heating element has on increasing retinal tissue temperature, temperatures were measured as an increase above resting body temperature.

Body Temperature	Heating Element Temperature (Above Body Temperature)		
	Control	+1°C	+2°C
36°C			
37°C			
38°C			
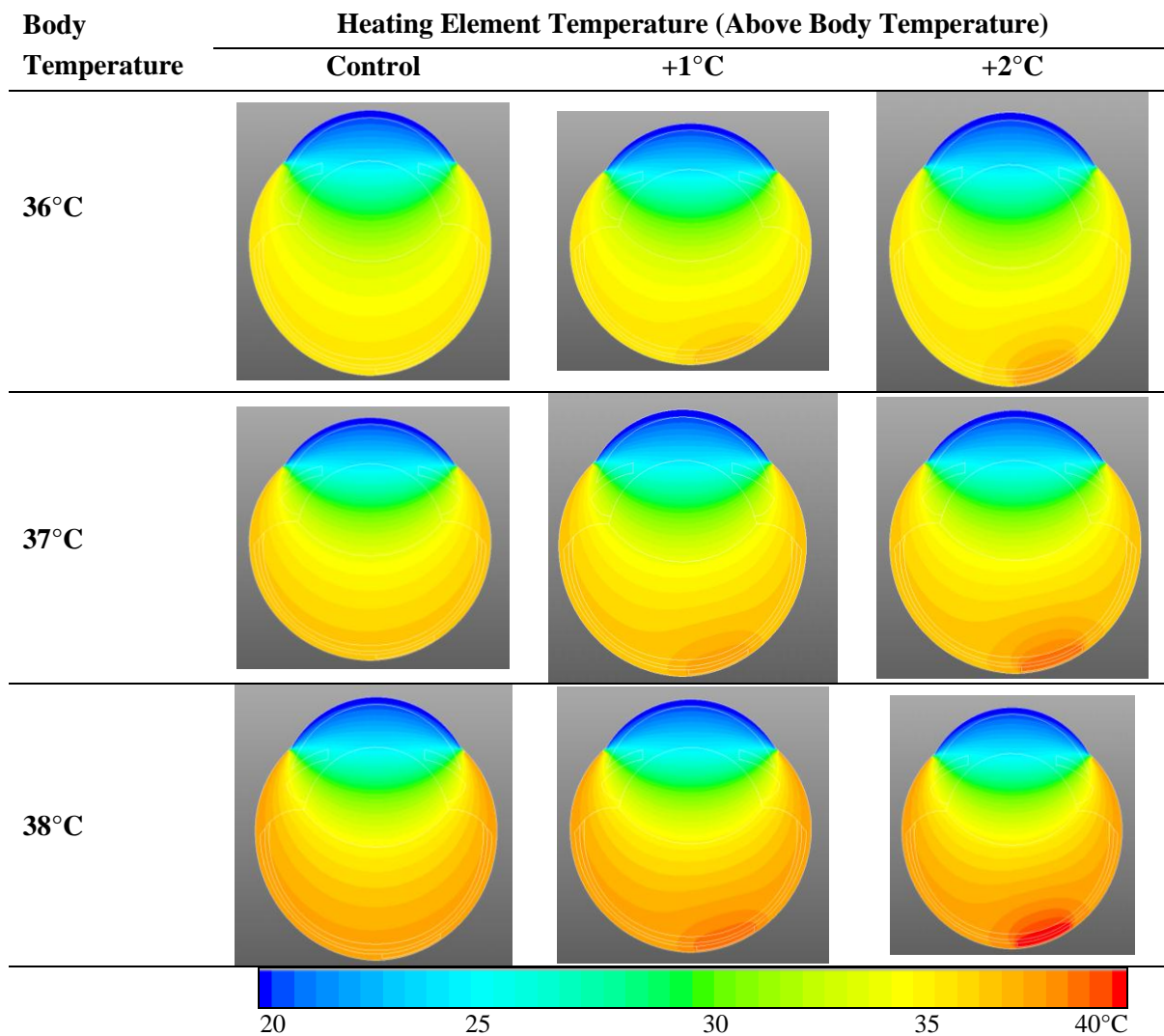
Figure 3.10. Thermal models indicating effect of body temperature fluctuations. Body temperatures are listed on the left hand column, with heating element temperatures given as the body temperature plus one or two degrees (top row)

The effect of orbital temperatures as a function of body temperature was also investigated by Ooi and Ng (2006, 2007) who reported that for blood temperatures of 35°C, 37°C, 38°C and 39°C, the tissue temperature in the anterior vitreous chamber would be 34.66°C, 36.60°C, 37.57°C and 38.54°C, respectively. Their results were similar to the thermal model simulations and indicated a close match between the temperature of the posterior vitreous and the blood temperature. It should be noted that the blood temperature flowing through the choroidal layer is closer to the retinal tissue than a body temperature boundary condition set on the outer sclera wall and thus it would be expected that temperature differences in this region can affect retinal tissue temperatures more easily.

A graphical representation of the temperatures measured along the retinal-vitreous margin is shown in Figure 3.11 for an epiretinal thermal model with body temperatures

of 36°C, 37°C, 38°C and 39°C, and heating element temperatures of 37°C, 38°C, 39°C and 40°C, respectively. In each case, the normalised temperature increase was identical as a function of distance from the heating element edge. This was also identical for heating element temperatures 2°C and 3°C above body temperatures of 36°C to 39°C.
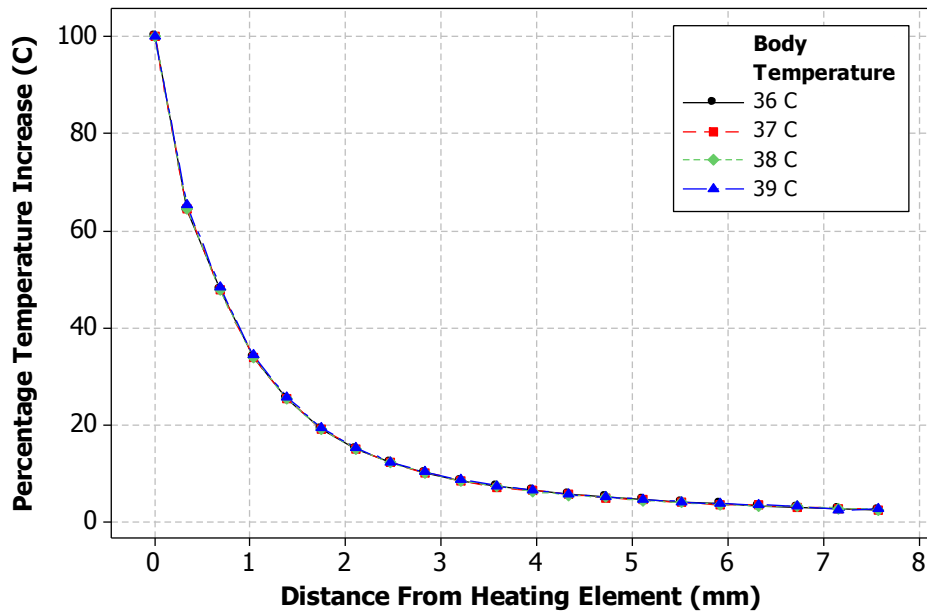
Figure 3.11. Temperature increase above control simulation for an epiretinal thermal models with heating elements one degree above body temperatures of 36°C, 37°C 38°C and 39°C as a distance from the heating element along the retinal-vitreous margin.

Results from different tests (and expected slightly different body temperatures) can be directly compared provided the body temperature is measured, and the thermally induced temperature increases caused by the heating elements are measured as an increase above body temperature. Thus, any thermal damage that occurs in the tissue can be compared to a control and thermal damage caused only by the heating element only should be apparent.

3.2.4   Effect of Implant Location

Correlations between thermal analyses performed on epiretinal models and on suprachoroidal models indicate that, due to the thermal conductivity of the vitreous fluid, the thermal spread in the epiretinal scenarios is slightly larger. This can be seen in Figure 3.12 (epiretinal implant) and Figure 3.13 (suprachoroidal implant), where both epiretinal and suprachoroidal models were simulated for a control scenario (no heating

elements) and for heating element temperatures of 38.5°C, 39°C and 40°C. The suprachoroidal implants are shown to induce lower retinal tissue temperature elevations than the epiretinal implant, for all heating element temperatures. This is due in part to the additional tissue layer (the choroid) that is present between the suprachoroidal implant and the retinal layer and in part due to the additional distance from the room temperature boundary condition (with the suprachoroidal implant positioned closer to the anterior surface of the eye).
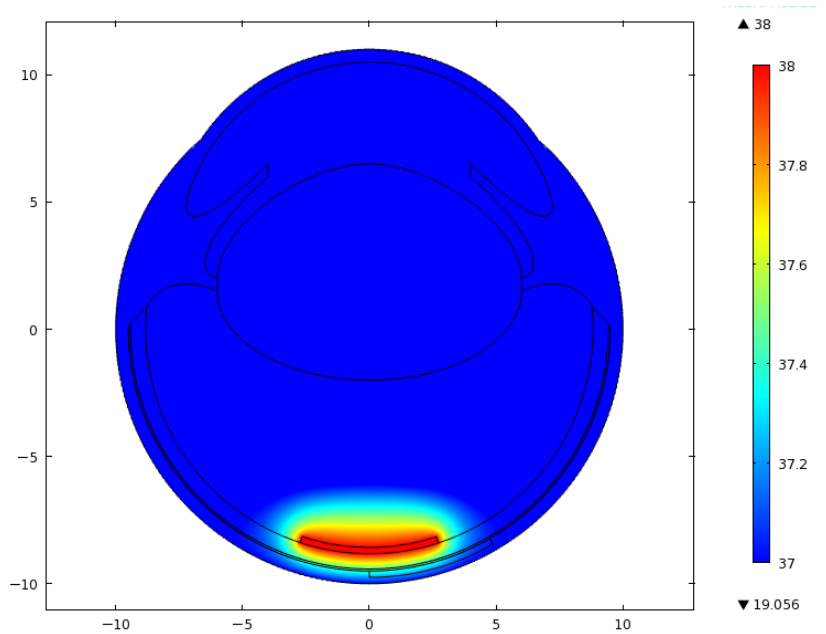
Figure 3.12. Finitel element model with an epiretinally implanted heating element set to a temperautre of 37°C.
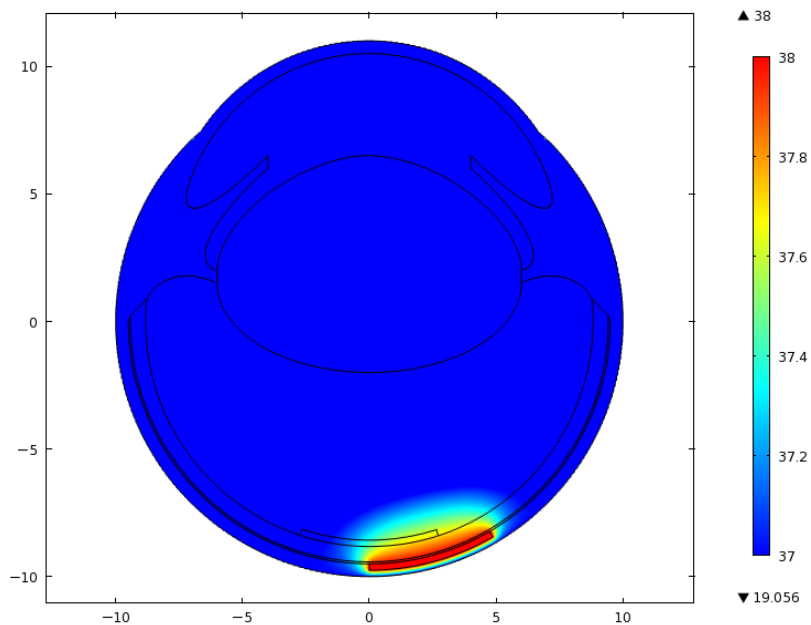
Figure 3.13. Finitel element model with an suprachoroidally implanted heating element set to a temperautre of 37°C.

Simulations performed with an epiretinal or suprachoroidal heating element set to a steady-state temperature of 38°C (emulating an unknown power dissipation) are shown in Figure 3.14 as a function of distance from the horizontal midline. All tissue temperatures were observed to decrease to less than 37°C (equivalent to a control condition) at a distance of 5.45 mm from the vertical midline (approximately 2.5 mm from the heating element edge). Due to the influence of the boundary condition imposed on the sclera being countered by the suprachoroidally implanted heating element, the observed temperature differences between the anterior and mid- retina and between the mid- and posterior retinal layers were greater during epiretinal simulations.
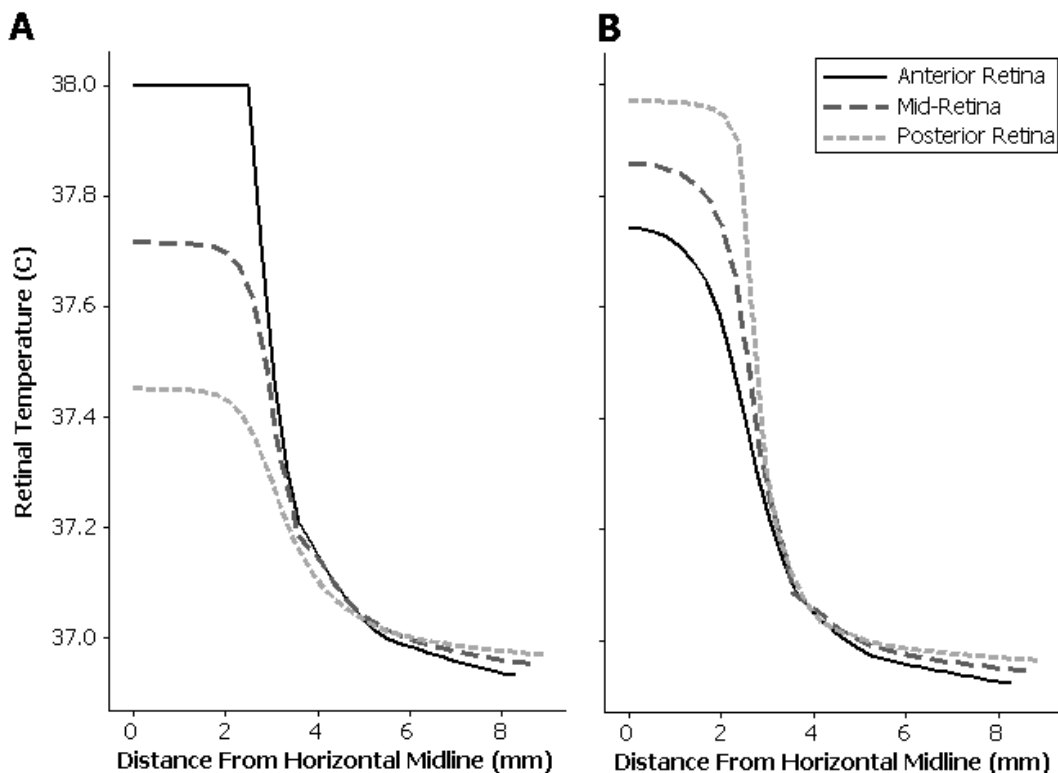
Figure 3.14. Simulations of anterior (solid black line), mid- (broken grey line) and posterior (dashed light grey line) retinal tissue temperatures from 38°C heating elements implanted **(A)** epiretinally and **(B)** suprachoroidally.

3.2.5   Effect of Choroidal Perfusion

Blood perfusion through the choroidal blood vessels not only acts to enrich the retinal neurons with nutrients and oxygen but also assists in maintaining a homeostatic temperature of the eye. By altering the rate at which blood flows through the choroid layer and choriocapillaries, the amount of thermal energy removed by the blood can be well regulated.

Circulation of blood within the choroidal layer of the eye has one of the highest perfusion rates in the body with blood passing through the choriocapillaries at a rate of 0.001 g/cm^2·s in primates (Welch and Polhamus 1984) and 2000 ml/mg/100g in rabbits (Sailer, Shinoda et al. 2007). This highly perfused tissue layer acts to ensure that heat generated metabolically by activation and stimulation of neurons within the retinal layer and heat in the form of non-visible light that is absorbed within the choroid and the retinal pigment epithelium does not increase the temperature of the eye to a magnitude that may reduce the functionality of activated neurons. The choroidal layer with its large perfusion rate can be modelled as a heat sink operating at, and with little deviation from, the animals' body temperature (Lazzi 2005; Hirata, Fujimoto et al. 2006).

Rawson and Hardy (1967) studied the effect of heating sheep abdominal tissue with a constant current and found that the temperature decreased by 0.8°C and 1.8°C (for initial temperature increases of 42°C and 45°C, respectively) caused by heat stimulus induced vascularisation. Seese (1998) reported that the capillary density increased by 3-4 times as a result of heating, consequently dropping the initial steady state temperature by 3°C. Temperature decreases were also reported in sheep muscle and lung tissue heated to 42-50°C (Liu, Saidel et al. 2003) and cat cortical tissue by Kim et al. (2007a), who demonstrated the effect of perfusion was to reduce the induced temperature increase from 0.089°C/mW to 0.051°C/mW. Sailer et al. (2007) reported that a linear temperature increase was seen in rabbit retina up to 40 mW (4.5°C) before a thermoregulatory mechanism came into place which stabilised the temperature and strongly improved heat dissipation within the tissue.

The effects of perfusion have been investigated using thermal models with Scott (1988) indicating that perfusion rates of between 65 and 100 W/m^2·°C would alter the temperature at the retinal-vitreous interface by 0.06°C (36.89°C to 36.95°C respectively). This was similar to findings by Wainwright (2007) who observed that increasing the choroidal perfusion rate from 0 to 30 ml/kg·s decreased the peripheral and central temperatures by approximately 0.04°C.

Mid-retinal temperature increases induced by an epiretinally implanted heating element in simulations with blood perfusion, modelled by (3.3) and by enforcing a 37°C, steady-state body temperature on the choroid, were compared. At low power dissipations (<100 mW), the effect of bioheat perfusion on mid-retinal temperature is similar to simulations performed in the absence of choroidal perfusion (Fig. 3.15). Increasing the power dissipated by the implant, increasing the retinal temperature, enhances the ability of choroidal perfusion to remove heat towards a condition in which the choroid acts as a 37°C heat sink. Thus, power dissipated into the retinal tissue by an implanted heating element or electrical device will increase the mid-retinal tissue temperature by between

1°C per 45.0 mW and 1°C per 59.2 mW. Immediately adjacent to the implant on the retinal-vitreous margin, powers of between 17.8 mW (no perfusion) and 27.4 mW (37°C choroid) were required to increase the temperature by 1°C, comparable to observations of implant-induced thermal elevations in cat cortical tissue (Kim et al. 2007).
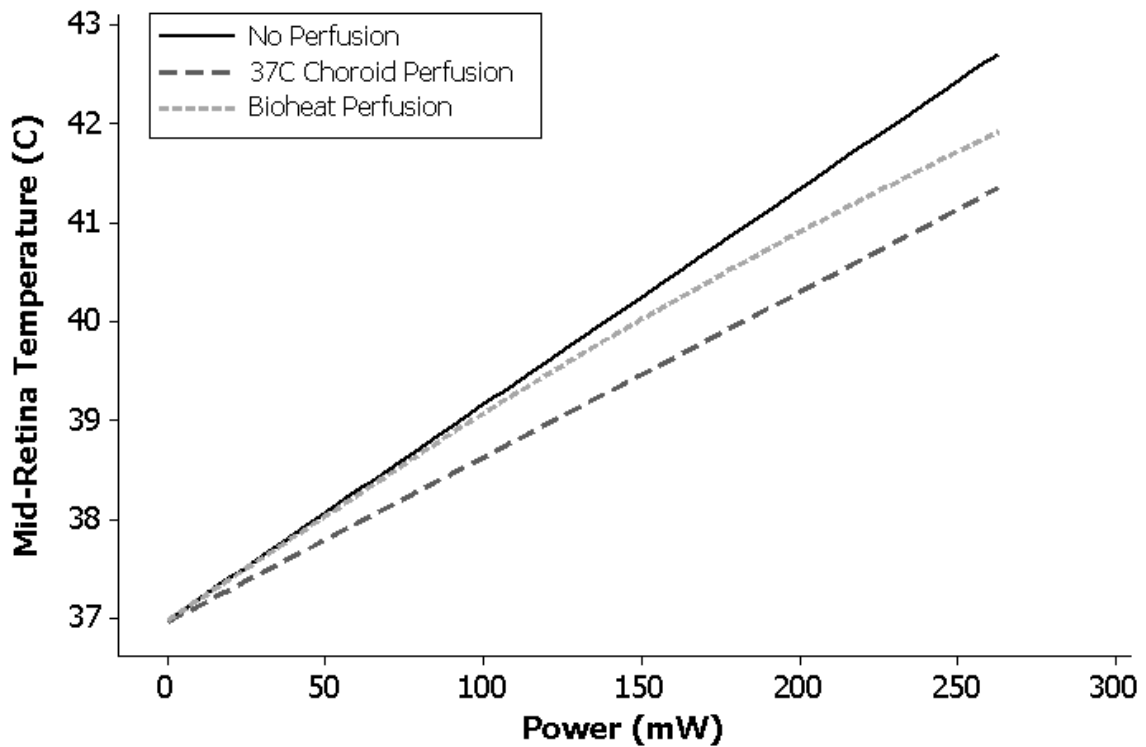
Figure 3.15. FEM simulations of mid-retinal tissue temperature increases with no perfusion (black line) and with perfusion modelled as a 37°C choroid (dark grey line) and by using the bioheat equation (light grey line) as a function of power dissipated by the epiretinally implanted heating element.

3.2.6 Effect of Altering Thermal Conductivity

As a person ages, the composition of the vitreous fluid within the eye will change resulting in a decrease in thermal conductivity (Scott 1988). Ng and Ooi (2006) investigated the differences in temperatures along the horizontal axis of the eye (anterioposterior axis) for different lens thermal conductivities. They showed that a worst case temperature difference occurring with a thermal conductivity difference between 0.21 W/m·°K and 0.54 W/m·°K was 0.12°C on the corneal surface, 0.13°C at

the anterior of the aqueous humor, 0.25°C anterior of the lens, 0.16°C anterior of the vitreous, 0.03°C posterior of the vitreous and 0.02°C within the sclera. This was similar to findings by Scott (1988) who altered the lens thermal conductivity by 0.334 W/m^2·°C (from 0.21 to 0.544 W/m^2·°C) and found no change in retinal tissue temperature. These studies however, did not investigate thermal conductivities that may occur within the retinal tissue layer.

Thermal conductivity was altered in the suprachoroidal model to determine differences that may occur due to retinal reorganisation and loss of cells and photoreceptors in late stage retinal degeneration, as well as to enable thermal models to be compared with fixed cadaver tissue. Models were analysed with a room temperature of 20°C, a body temperature of 37°C and heating element temperatures set to a steady state temperature of 37.5°C, 38.0°C, 39.0°C or 40.0°C. The thermal conductivities that were used in the analyses were applied to the retinal tissue and the choroid, increasing from normal (thermal conductivities of 0.565 W/m·°C and 0.600 W/m·°C for retinal and choroidal tissue respectively) to 20 W/m·°C. All thermal conductivity profiles followed the same curve, with negligible differences occurring due to alterations in heating element temperature when normalised.

A graphical representation of the normalised results for thermal conductivities increasing to 20 W/m·°C is shown in Figure 3.16, clearly indicating the extent at which alterations in thermal conductivity can have on thermal energy dissipation within the retina. While drastic thermal conductivity changes are not expected to occur in living tissues, even relatively small changes (0.435 W/m·°C in the retinal tissue and 0.400 W/m·°C in the choroid) can induce temperature differences of up to 7% (0.07°C for a heating element 1°C above body temperature). Differences between thermal models with conductivities of up to 20 W/m^2·°C are shown in Figure 3.17.
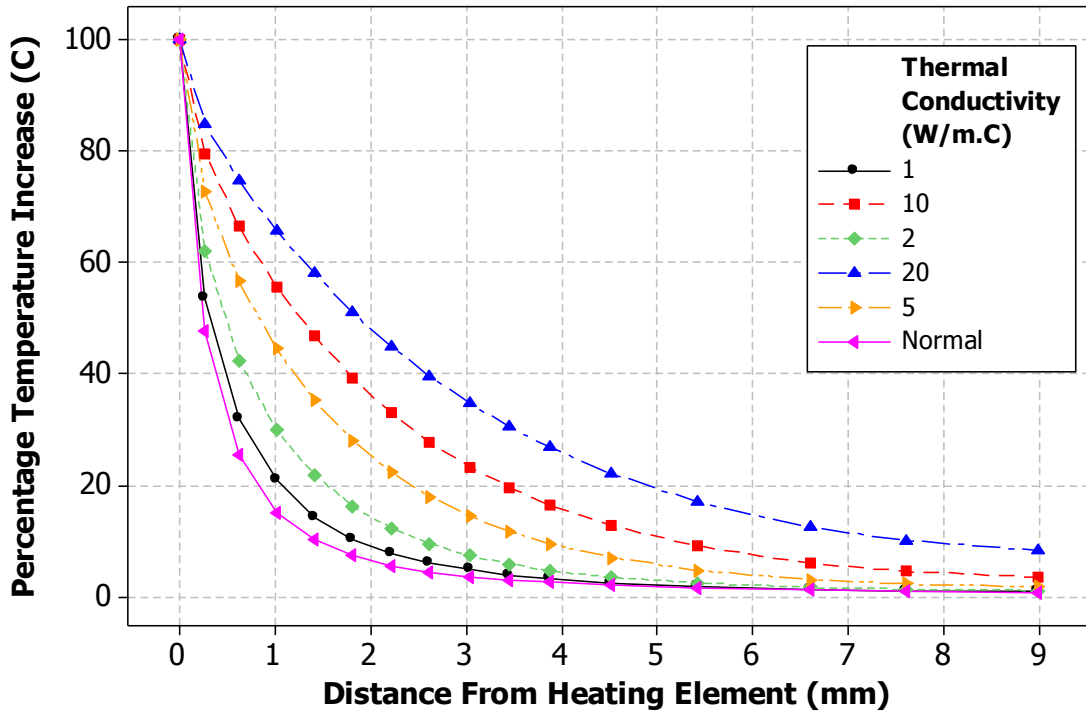
Figure 3.16. Effect of thermal conductivity on temperature distance profiles for heating element temerpatures of 1.0°C above body temperature
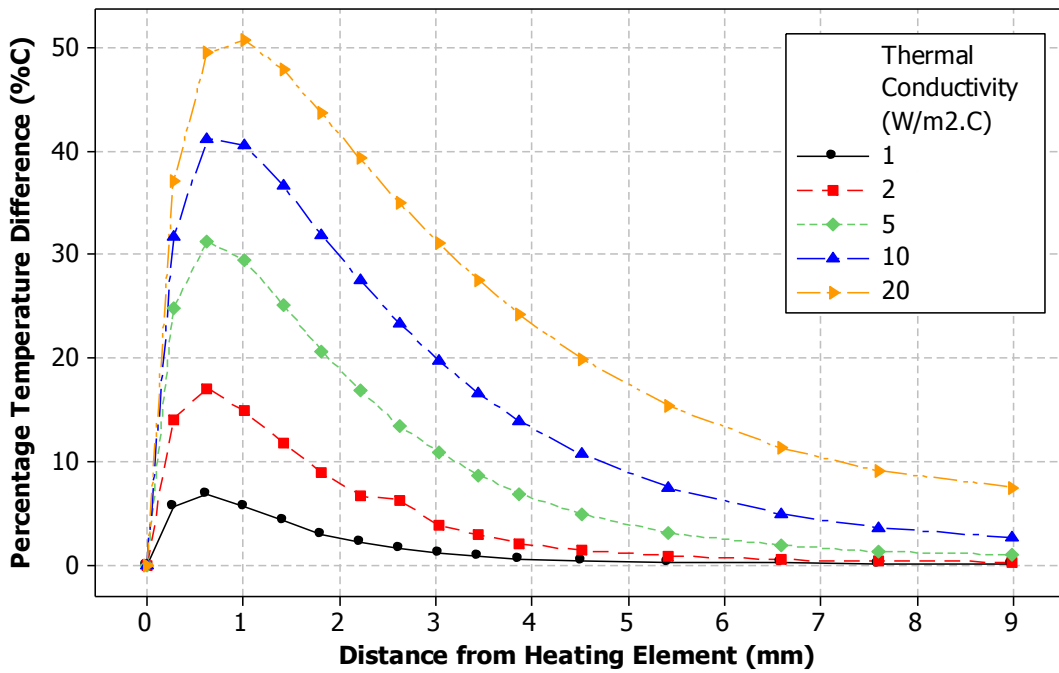
Figure 3.17. Differences observed in control simulations and suprachoroidal thermal models with thermal conductivities of the retinal and choroidal tissue increased to 20 W/m$^{2\cdot}$°C as a percentage of the heating element temperautre and the distance from the heating element edge.

3.2.7 Other Possible Effects

Other effects that may contribute to thermal differences between model results and those produced under experimental conditions include evaporation rate at the cornea-ambient interface (alterations in convection), blinking and pupil size (Scott 1988). While these parameters are not expected to play a significant role in the alterations of temperature at the posterior retinal tissue layer, it is important that these features be mentioned as possible discrepancies between models and experimental data. Ooi and Ng (2007) have investigated the effects of evaporation rates on the temperature variations in their eye model and indicated that while there will be a marked change in temperatures measured at the cornea, the effect of changing the evaporation rate from 20 W/m^2 to 320 W/m^2 will only have a 0.52°C effect on retinal tissue temperature. For normal conditions, with evaporation rates of 20-70 W/m^2, the temperature difference in the retina was observed to be 0.09°C. From this study and given the laboratory conditions in which model validations will take place, the effect of evaporation rate will be considered negligible. Metabolically generated heat is also a source of potential error, particularly in cases where perfusion and thermoregulation is hindered, although only a negligible effect has been reported (Kim et al. 2007s, 2007b).

It is expected that due to the lower heart rate (and thus lower perfusion rate) of animals under anaesthesia, that measured temperatures will be higher than those seen under normal conditions. While the metabolic rate will also be reduced, the overriding factor of less blood being able to remove excess heat and limit the homeostatic thermoregulatory ability of retinal tissue is expected to play a large role in temperature elevations seen in experiments. As all animals undergoing acute experimentation are required to be anaesthetised for the entirety of the experiment in accordance with the NHMRC guidelines (NHMRC Australian Code of Practise for the Care and Use of Animals for Scientific Purposes, 2004), the effects of anaesthesia, and its effect on thermoregulation must be considered. Hirata (2006) investigated the effects of anaesthesia on laser induced temperature increases in rabbit eyes and documented that the thermoregulatory response was inactivated and that blood flow and basal metabolism was reduced, reducing not only the blood flow, but the efficiency of the animal to thermoregulate. This has also been documented by Kurz et al. (1993) with Schwartz and Feller (1962) indicating that there is an expected temperature decrease of 0.2°C in the anterior chamber and 0.6°C of the core body temperature when using Nembutal.

3.3   CONCLUSIONS

This chapter investigated thermal models designed to be used in conjunction with acute and chronic, *in vivo* and *in vitro* animal experimentation. While the construction of the models will not be able to answer the question of thermal damage thresholds, these models can be used to dramatically reduce the animal trials required to investigate the many variables that can occur during experimentation.

Thermal models have been constructed for correlation with epiretinal and suprachoroidal implants and investigated the potential for uncontrollable factors (such as perfusion rates, room and body temperatures and tissue thermal conductivity) to induce large alterations in retinal tissue temperature. All thermal models indicated a rapid decrease in tissue temperature as the distance from the heating element (or retinal prosthesis chip) increased, suggesting that the primary region of concern would be tissue in direct contact with the implant. Simulations indicated that there was a direct correlation between temperature increase and power dissipation by the implant, and although implants used in patients would not have all electrodes simultaneously activated (and thus the temperature / power distribution along the implant-retina boundary) would not be uniform, these simulations investigate the worst-case scenario. Further, as retinal prosthesis stimulating circuitry is known to dissipate thermal energy, these heat generating components are usually implanted at a distance from the delicate retinal neurons. In this case, the simulated temperatures would be an overestimation of those observed in a practical application, however, provided these temperatures are not surpassed, the potential to induce thermal damage should be avoided.

The influence of a heating element in the two-dimensional epiretinal thermal model with a room temperature of 20°C and a body temperature of 37°C was reduced to 37% (0.37˚C increase for a heating element 1˚C above body temperature), 22%, 13%, 8% and 6% of the heating element temperature at 1, 2, 3, 4 and 5 mm from the heating element edge, respectively (a heating element 2˚C above body temperature would induce a thermal elevation twice as large as a heating element 1˚C above body temperature). Compared to a three-dimensional model, (in which the heating element influence dropped to 27%, 13%, 7%, 4% and 3% of the heating element temperature at distances of 1, 2, 3, 4 and 5 mm from the heating element edge), temperature differences of 0.48°C for a heating element 4°C above body temperature would be observed and thus, it is not recommended that models be created and used in two dimensions.

The finite element thermal models have indicated that while there may be a small amount of deviation occurring to an animal's body temperature, the effect of the heat dissipated by the implant is expected to supersede any changes in homeostasis. The ability to maintain a constant body temperature is not required (provided the temperatures are within a normal range and are not causing hyper- or hypothermia), as long as the temperature of the animal and that of the heating element is known. Even in the absence of accurate body temperature measurements, the effect on the retinal tissue is minimal when comparing control situations without the presence of a heating element to conditions where a heating element induces temperature elevations in surrounding tissue. Increases or decreases in body temperature resulted in almost identical increases or decreases in retinal temperature, and thus to extract the influence an implanted heating element has on increasing retinal tissue temperatures, temperatures should be measured as an increase above resting body temperature.

Models constructed with room temperatures varying between 10°C and 36.4°C have shown a negligible difference to retinal tissue temperature (< 0.033°C), and the effect of a convective or forced boundary condition also having a minimal difference (< 0.035°C).

The location of the implant will be one of the greatest influences of thermal damage (a maximum temperature difference of 26% of the heating element temperature at a distance of 0.69 mm from the heating element edge), with a greater distance between the retina and suprachoroidal approaches being preferable for heat dissipation. However, this is expected to be countered by an increase in charge required to deliver current to retinal neurons so as to initiate a response. Whether the additional distance and increased charge requirement will essentially cancel each other out in terms of power dissipation within the retinal neurons is yet to be determined. The heating element influence on the two-dimensional suprachoroidal thermal model, with room and body temperatures of 20°C and 37°C, was reduced to 14%, 8%, 4% 3% and 2% of the heating element temperature at distances of 1, 2, 3, 4 and 5 mm from the implant, respectively.

While metabolically generated heat was also negligible in the thermal models (<0.001°C), the effect of thermal conductivity and perfusion are two primary influences of heat dissipation within the retinal tissue. While it is not expected that the thermal conductivity will change to an extent seen through the fixation process of enucleated eyes, changes occurring due to retinal diseases and remodelling are factors that implant designers need to be aware of. Thermal conductivity changes of greater than 50% of the heating element temperature were observed when altering the thermal conductivity of

the retinal and choroidal tissues to 20 W/m^2.°C, with a 7% difference observed when the tissues were set to 1 W/m^2.°C.

The effect of perfusion is expected to greatly increase the rate and proficiency of thermal heat removal, although the potential for diseased retinal tissue to be poorer than healthy eyes at removing excessive energy is expected although not well understood. Blood perfusion, modelled by both the bioheat equation and as a forced, 37°C choroidal boundary condition indicated at low power dissipations (<100mW), the effect of bioheat perfusion was similar to simulations performed in the absence of choroidal perfusion (such as a cadaver eye). As the power dissipated by the implant was increased, the ability of choroidal perfusion to remove heat from the retina was enhanced and the temperatures measured from the retinal-implant interface were lower.

These models have been used in conjunction with cadaver, *in vitro* and *in vivo* experiments to assist with the determination of thermal damage thresholds and allow a significantly increased number of trials to be performed without required additional animal sacrifice (Opie, Burkitt et al, In Press).

4

CAT RETINA CADAVER TRIALS

In this chapter, results from cadaver trials are presented. Cadaver trials were designed to test implantation procedures and methods, enable final device improvements before acute and chronic animal trials, and allow investigation of the likely relationship between current dissipation and tissue temperature increases.

While saline bath trials using cadaver eyes do not account for thermal energy removal by choroidal blood perfusion or metabolically generated heat, these trials can be used to guide acute experiments by indicating powers that will cause extreme temperature increases (and likely severe retinal damage) and give insight into the expected spread of the induced thermal energy to the neighbouring retinal neurons. The measured temperatures are expected to be greater than for equivalent power dissipations in living tissue due to the inability to remove heat through blood circulation and thus, the primary aim of the cadaver trials was to determine an approximation of thermal damage thresholds from power dissipated in retinal tissue. This was achieved by investigating the power-temperature and temperature-distance relationships in cadaver eyes, allowing for an initial distance-power-temperature profile to be created. These experiments also investigated the delay between the current dissipated by the electronics through the tissue and steady state temperatures reached, whilst ensuring the equipment, measurement and recording system was suitable and reliable prior to acute or *in vitro* experimentation.

The initial set of experiments was performed using cat cadaver eyes that had been heavily fixed in 10% formalin or 4% paraformaldehyde. Due to the fixation process, these eyes did not retain their original material properties such as thermal conductivity, flexibility, elasticity and strength. This is expected to induce significant differences in the ability of the eye to dissipate heat identically to a healthy unfixed eye, although the size remained the same and identification of problems arising from surgical implantation were corrected and used to assist with *in vivo* experimentation.

Results from the trials indicated that cadaver retinal tissue will increase linearly with power, at a rate of 1°C per 0.01479 mW and would decrease according to a two phase equation as the distance from the heating element increased. The temperatures observed in the cadaver trials could be closely matched to finite element simulations (average differences less than 0.03°C) using an increased choroidal and retinal tissue thermal conductivity. The mechanical changes occurring to the cadaver tissue were observed to be caused during the fixation process.

The induced temperature measured along the retinal tissue margin was observed to drop below 50% of the heating element temperature at a distance of 0.27 mm, to below 25% at a distance of 0.62 mm and was less than 10% at distances greater than 1.41 mm from the heating element edge. Thus, in order to stay below the international standard applied to the surface temperature of implanted devices (2°C), a power of less than 140 mW (at the edge of the heating element), or a distance of greater than 0.75 mm (for powers greater than 650 mW) would be required.

These tests indicate that the designed implants and electrical equipment (discussed in Chapter 2) are able to be surgically implanted using methods and locations similar to current visual prosthesis designs, and can be used to accurately induce and measure temperature increases within a cat eye.

4.1   METHODS

The equipment and experimental set-up used in the cadaver experiments is similar to the experimental methods used in the equipment calibration trials (Chapter 2), albeit using an improved implant that has more closely spaced temperature sensors (PRTDs).

4.1.1   Implantation

The suprachoroidal heating element was personally implanted into the cadaver eyes with   surgical procedures similar to methods used by Australian and international groups for subretinal and suprachoroidal implantation (Schwan, Gekeler et al. 2001; Sachs, Schanze et al. 2005; Yamauchi, Franco et al. 2005; Schanze, Sachs et al. 2006; Gekeler, Szurman et al. 2007; Wong, Chen et al. 2009). This procedure involved making a small incision the width of the implant (7-8 mm) approximately 7 mm from the limbus, posterior to where the sclera and corneal tissues intersect. The implants were designed to be flexible enough to be thread through this opening into the suprachoroidal space, and stiff enough to be implanted without the requirement of an introducer. The implants were positioned in the desired position above the macula, with a 17 mm length sufficient to reach the optic nerve. In this manner, the heating elements were positioned within the fovea, posterior to the photoreceptors, tapetum and choroidal blood vessels. The surgical placement is indicated in Figure 4.1, with the red line representing the suprachoroidal implant beneath the choroidal vessels (yellow) and the retina (orange).
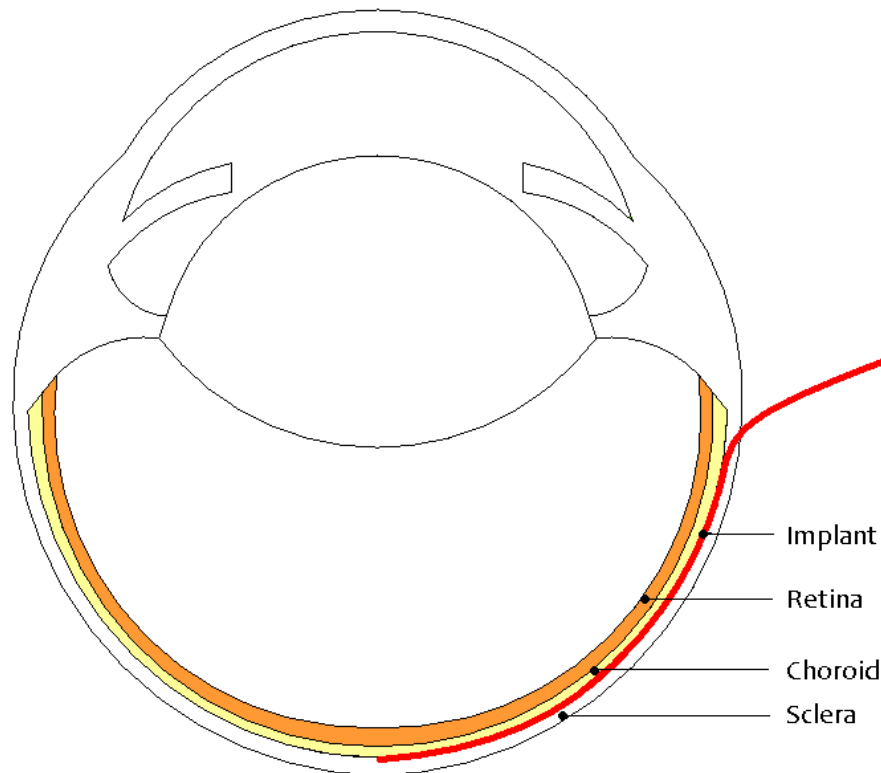
Figure 4.1. Schematic indicating the suprachoroidal insertion of an implant (red), designed to induce thermal elevations in the retinal tissue, in the foveal region of a cat cadaver eye in the suprachoroidal space between the choroid and the sclera

4.1.2   Equipment and Experimental Set-Up

A current source was used to deliver currents to the heating elements which comprised of 13 × 10-20 Ω 0603-size surface mounted resistors, soldered onto the flexible polyimide substrate (flex-PCB). At least four PRTDs were soldered down the 159 μm thick flex-PCB shaft at 1.2 mm intervals and were connected to the high resolution temperature measurement system, which connected through digital acquisition hardware to a computer, allowing multiple, simultaneous, temperature recordings.

The same heat bath was used as in the calibration trials (Chapter 2), with the temperature of the heat bath controlled by altering the power passing through the light globe heat sources. Temperature differentials within the heat bath were minimized through the use of a fan, with heat bath temperature measurements made through an immersed PRTD connected to a digital multi-meter (DMM) and recorded using Fluke View-Forms (National Instruments, TX), shown in Figure 4.2.
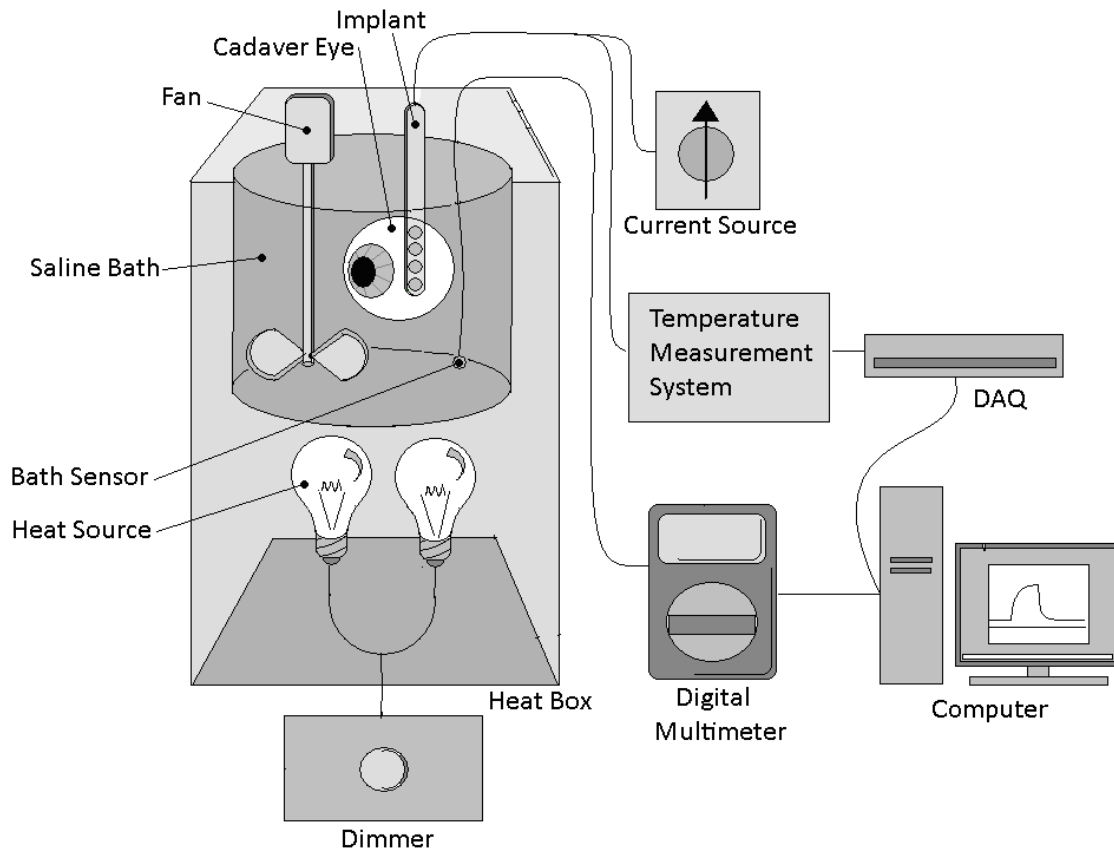
Figure 4.2. Cadaver trial equipment set-up indicating the implant inserted into the cadaver eye immersed in a saline bath. The saline bath temperature is controlled by a dimmer, with the light globes acting as the heat source and the fan ensuring thermal uniformity. A current source delivers power to the implants' heating element whose temperature is measured by the high resolution temperature measurement system before passing throug ha data acquisition card to be recorded simulataneously and in real time by the computer. The temperature of the saline bath, measured by a digital multimeter, is also recorded by the computer.

4.1.3   Experimental Protocol

Prior to the onset of retinal heating, the heat bath was stabilized at 37°C, to imitate the normal body temperature of a cat. The Lab-View software was set up to simultaneously record from the four sensors in RSE mode, with current sources recorded in differential mode. The magnitude of the currents delivered to the heating elements, measured as a function of the voltage across a 0.1%, 1Ω sense resistor, were recorded and displayed at a rate of 1 sample per second at the same frequency as PRTD measurements. Measurements of the saline bath, obtained from the DMM, were also recorded at a rate of 1 sample per second, with a common clock used to ensure simultaneous recording times of heat bath and tissue temperatures.

Following implantation, the cadaver eye was immersed in the heat bath (up to the height of the lens) with a no-recording period of at least fifteen minutes to allow for the cadaver eye to adjust to the temperature of the heat bath. Once the cadaver temperature had stabilised, five minutes (minimum) of baseline retinal temperatures were measured and recorded from each of the sensors. The current source was then turned on, with adjustments to the variable resistor used to pass the desired current through the heating element.

The currents delivered and the resulting tissue temperature increases were measured and recorded by the computer until a steady state temperature was observed (generally requiring at least 300 seconds). The current source was then turned off, the retinal tissue was allowed to cool and re-stabilise at the baseline temperature, and the experiment was repeated. Each current level was repeated at least five times with the temperature increase induced averaged over the repeated trials.

Comparisons performed between the induced temperature increases measured at the central sensor and the measured current and power dissipated by the heating elements enabled the construction of a temperature–power relationship for the cadaver tissue. Temperature measurements from the sensors located down the implant shaft were used to examine the influence of the heating element as the distance from the heating element edge increased.

4.2   RESULTS

Each of the measurements performed on cadaver eyes used the second order linearisation program (Chapter 2) to convert the measured and recorded voltages, observed from each of the PRTDs located along the flex-PCB shaft, into temperatures.

4.2.1   Measurements of Temperature Increase

The direct influence of thermal energy dissipated by the heating element was determined as the difference between the peak response and the temperature increase from the measured baseline temperature (average temperature measured immediately prior to the onset of current induction). Figure 4.3 indicates the temperature increase measured as the difference between the blue baseline response and the peak response (red) observed after the heating phase had stabilized. The heating phase is shown to be directly influenced by power flowing through the heating element.

It can be observed in this trace (Figure 4.3) that the final resting temperature is not exactly the same temperature as the initial baseline response. The increase from initial to final baseline was the result the temperature of the fluid within the heat bath increasing slightly.
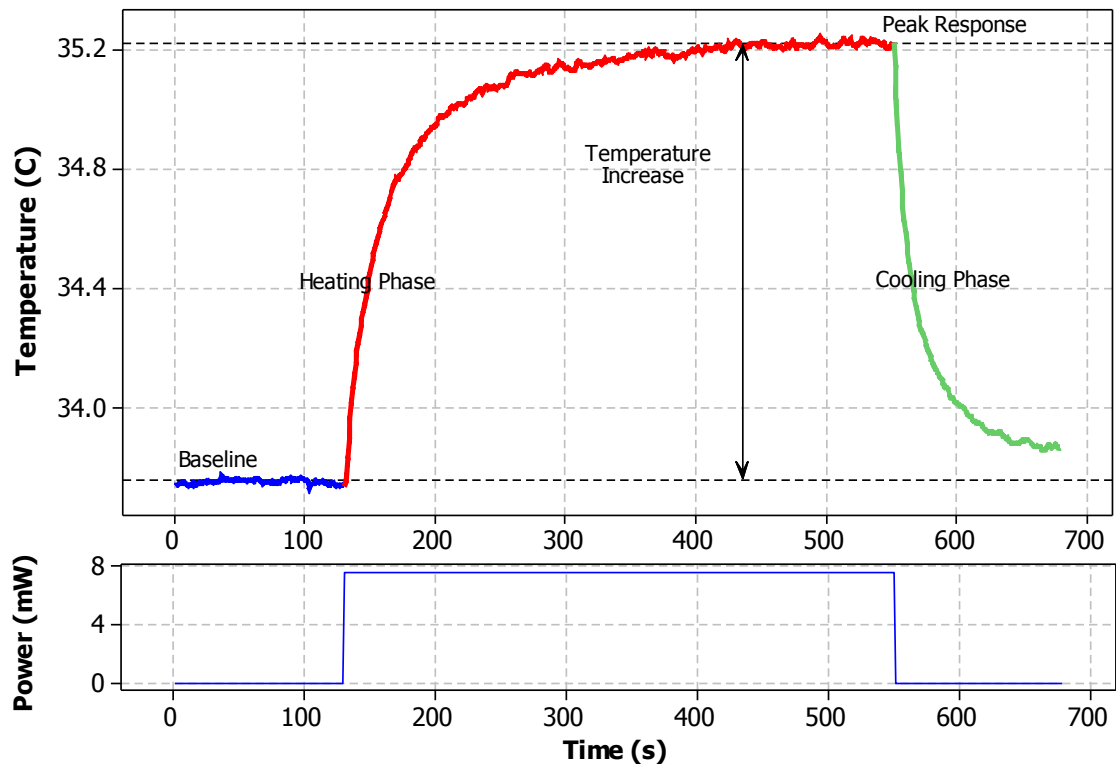
Figure 4.3. Example temperature increase observed due to power dissipation through an implanted heating element showing the baseline response (thick blue trace), the heating phase (red trace), the resulting temperature increase (from the baseline response to the peak response) and the cooling phase (green trace).

4.2.2 Effect of Bath Temperature

To ensure that measurements were not distorted by changes in animal body temperature, *in vitro* cadaver experiments were set up to investigate the effect that alterations in bath temperature would have on the increase in tissue temperature caused by a heating element with constant power dissipation. A series of seven recordings of thermal increases from 2 mW power dissipated through the resistive heating elements is shown Figure 4.4A. The measured and recorded voltages, converted to temperatures using the second order linearisation program indicated that the temperature of the saline bath increased linearly. By subtracting the influence of the heat bath, the effect of temperatures induced by the heating element only, could be observed.

The heat bath artefact was removed by subtracting the baseline temperature (red trace in Figure 4.4A) from the measured tissue temperature, with sensors measuring a thermal increase of 0.31 ± 0.2°C for each of the tests (Figure 4.4B). These tests also highlighted the importance of allowing at least 300 seconds for the tissue to reach a steady-state

temperature. This was not performed in the above example, and tissue temperatures measured without allowing for a steady-state temperature to be reached were lower. This can be seen in the 3rd to 6th heating phases in Figure 4.4B.
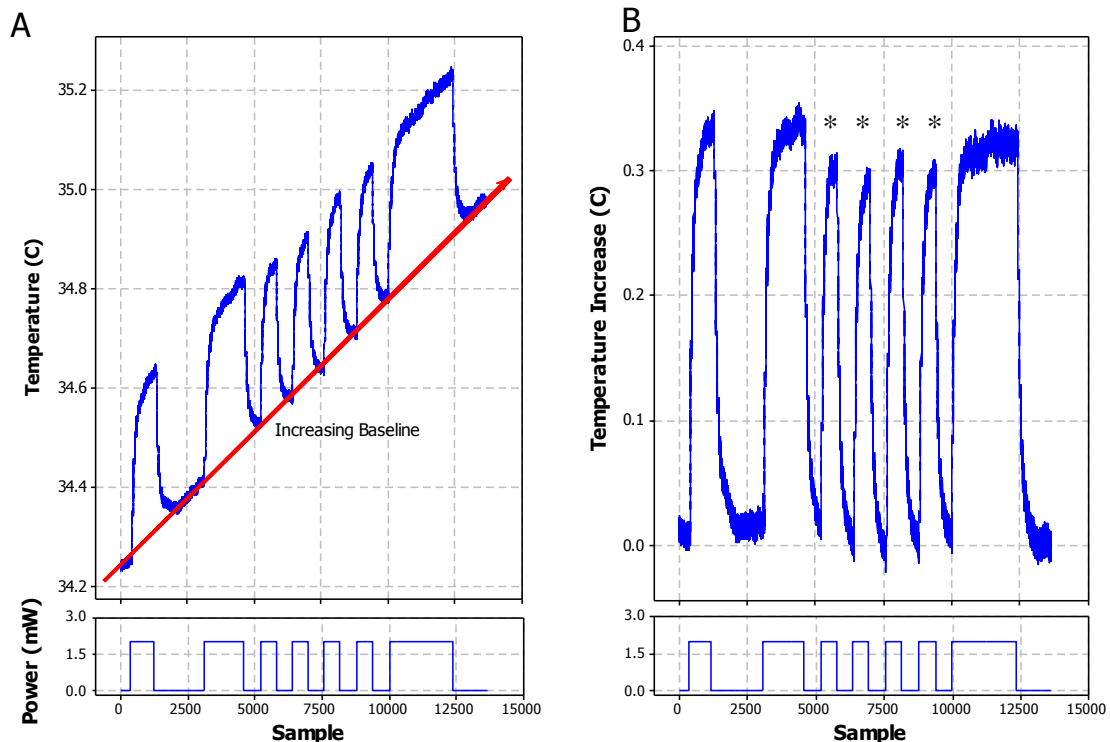
Figure 4.4. (A) Set of seven measured temperature increases observed due to a power dissipation of 2 mW passing through the heating element indicating the increasing baseline (red trace) and **(B)** the temperature increase caused by the heating element only after the heat bath temperature was subtracted. The trials marked with an asterisk (*) are indicative of tests that did not allow steady state to occur (were less than 300 seconds in duration)

In all future experiments (used for determination of temperature power relationships and of temperature distance relationships), at least 300 seconds was given after the onset of heating to ensure that the maximum temperature had been achieved, with a period of at least 500 seconds allowed for tissue cooling.

To further investigate the effect of heat bath temperature on cadaver measured temperatures, tests were conducted with a heat bath (body temperature) of 24°C and 34°C, with results shown in Figure 4.5. Heating elements were set to 1°C and 2°C above the heat bath temperature as measured by a central PRTD. At each temperature increase, three cadaver eyes were used with each data point representing an average of at least three tests. The results from these tests indicate that while there will be an obvious difference in the temperatures measured at each of the PRTDs due to an increased distance from the heating element, the effect of altering the heat bath temperature is negligible, with results from both the 24°C and 34°C cases being

equivalent. This suggests that as long as the artefacts caused by body temperature fluctuations is accounted for (both during trials and between trials), temperature elevations measured should correlate directly with the temperature increase induced by the heating elements. This was also shown through thermal model simulations (Chapter 3). While data observed from the cadaver trials suggests that temperature increase is independent of body temperature, this does not take into account damage that may occur, with increased temperatures published to drastically decrease damage threshold temperatures (Ward and Bruce 1971; Polhamus and Welch 1975; deLint, vanNorren et al. 1992; Gorgels, VanBeek et al. 1997).
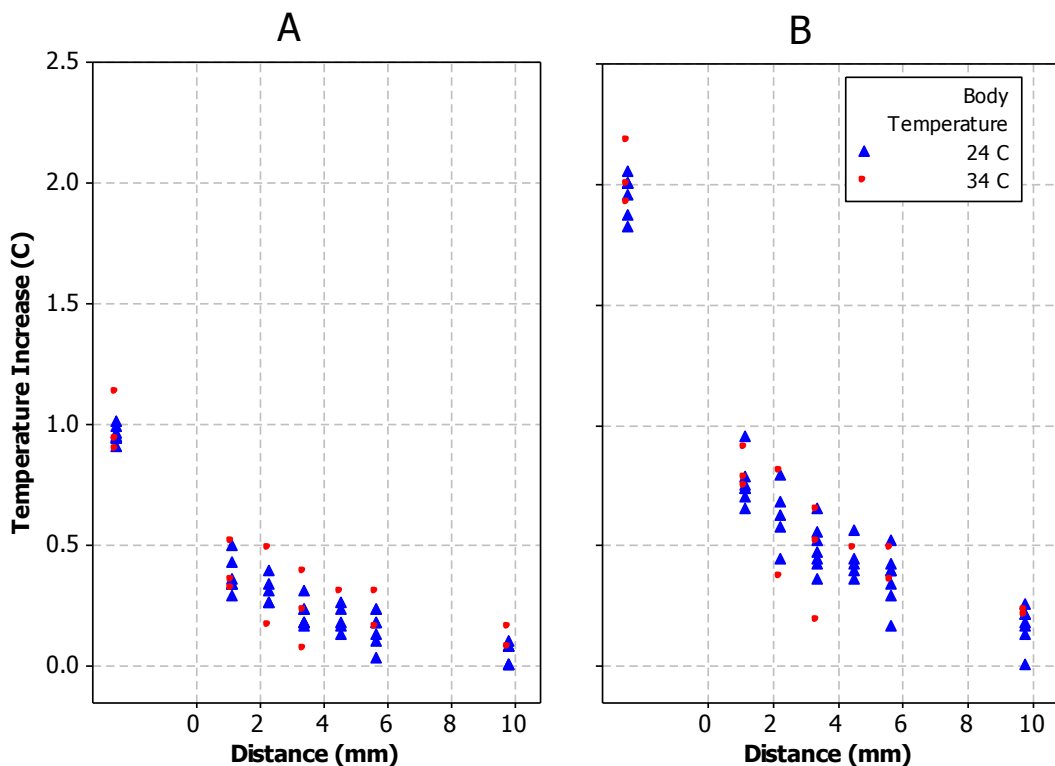
Figure 4.5. Temperature increase as a function of distance from the heating element for heat bath temperatures of 24°C and 34°C and heating element temperatures of **(A)** 1°C and **(B)** 2°C above the measured baseline temperautres.

4.2.3 Power Versus Temperature

To investigate the effect that power has on increasing the temperature of the sensor (and hence of the tissue adjacent to the heating element), measurements were taken over a series of cadaver tests across a range of power dissipations and current levels. In each of

the seven cadaver tests, the artefact caused by the heat bath was removed and individual heat trials were allowed at least 300 seconds to reach a maximum steady state increase.

To determine the effect that power dissipation had on increasing the temperature of the sensors located along the suprachoroidally implanted heating element shaft (and hence of the tissue adjacent to the heating element), measurements were taken over multiple cadaver tests across a range of power dissipations and current levels. Results, listed in Appendix 4, are the average results from at least three tests repeated with identically supplied power. Tests used currents ranging from 2 to 50 mA, with a total power dissipation in the thirteen-series-resistor heating elements ranging from 0.2 to 650 mW. Cadavers 1, 2 and 3 used the variable size heating element (SMR - 1) comprised of 16Ω resistors and temperature sensors located centrally to the heating element and at a distance of 2.80, 4.70 and 6.60 mm from the heating element edge. Cadaver tests 4, 5, 6 and 7 used the small implant design (SMR – 2), which could measure temperatures at distances of 1.5 mm, 3.5 mm and 5.5 mm from the heating element, comprised of 20 or 40Ω resistors. Results for all the cadaver tests, shown as a function of the temperature increase at the central sensor for given power dissipations, are shown in Figure 4.6, with temperature increases occurring at the centre of the most apically implanted heating element in seven cadaver eyes were observed to obey a linear temperature increase-power dissipation relationship, increasing by 1°C per 67.6 mW with a correlation coefficient $r^2 = 0.965$ (Fig. 7). This is comparable to the suprachoroidal FEM simulations that increased by 1°C per 65.0 mW.

To create a safe power budget for retinal prostheses, the amount of power dissipated in the implanted chip must not exceed the temperature damage threshold for retinal tissue. Experiments can be used in conjunction with the linear power-temperature relationship to give retinal prosthesis architects a safety limit to the amount of power that can be dissipated. While factors such as retinal perfusion (heat extraction by choroidal blood vessels) and heat produced by metabolic activity cannot be accounted for in cadaver tests, these tests do give a first approximation of the relationship between power dissipated by a heating element and the resulting tissue temperature increase.
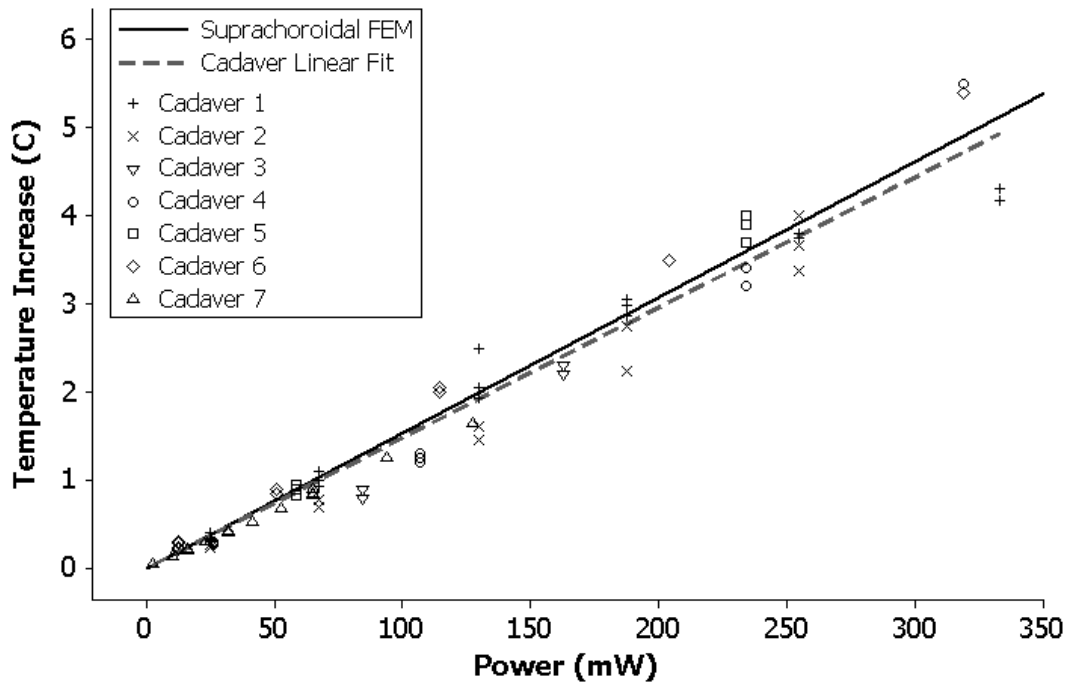
Figure 4.6. Suprachoroidal cadaver (data points) and FEM simulated data (solid black line) of temperature increase as a function of power dissipation. Broken grey line indicates linear fit to the experimentally obtained data.

4.2.4 Temperature Versus Distance

One of the primary questions investigated in the cadaver trials was how the induced temperature increase is affected by the cellular medium and the heat flux capacity of the tissue. This is essentially an investigation of the ability of a retinal implant to contain a thermal increase to the tissue immediately adjacent the heating element (or implanted circuitry). As the temperature induced by a heating element is in direct contact with the retinal tissue, then this tissue will be most affected and the results the most severe. Controlling this level of damage to within safe thresholds will thus ensure that the whole eye is safe from induced temperature increases.

To ensure that the FEMs were capable of accurately replicating experimental data, comparisons were made between FEM simulated temperatures measured along the choroidal-scleral interface and PRTD measurements in cadaver eyes, partially immersed in a 37□C heat bath and implanted with suprachoroidal heating elements. Fourteen eyes were used to compare the induced thermal elevations of retinal tissues with suprachoroidal heating elements set from 0.5°C to 4°C above a 37□C (body temperature) heat bath.

Post-sacrifice fixation of the cadaver eyes (performed with either 4% paraformaldehyde or 10% formalin) altered the thermal conductivity of the choroidal and retinal tissues, with the actual thermal conductivities of the cadaver eyes unknown. Each eye was tested at least five times at each heating element temperature using a single heating element (and without heating element influence) with all trials from both eyes from each animal averaged and normalized under the assumption that the fixation for both left and right cadaver eyes was identical. Across multiple measurements, the worst case standard deviation for any of the cadavers measured by the HTRMS was ±0.04°C. While care was taken to ensure the fixation process was uniform throughout cadaver trials where possible, discrepancies may have occurred from the use of other fixatives or from increased or reduced fixation times. The thermal conductivities of each of the cadaver eyes may be different, with temperature-distance results suggesting this was the case.

Individual cadaver eyes were observed to follow specific FEM simulations in which the retinal and choroidal thermal conductivities (K) ranged from normal ($K = 0.565$ and 0.600 W/(m $\square$C) for retinal and choroidal tissue, respectively) to 6 W/(m $\square$C). The average of all the tester eyes is shown in Figure 4.7, with the average differences between individual eyeball pairs and simulations with altered thermal conductivities shown in Figure 4.8.
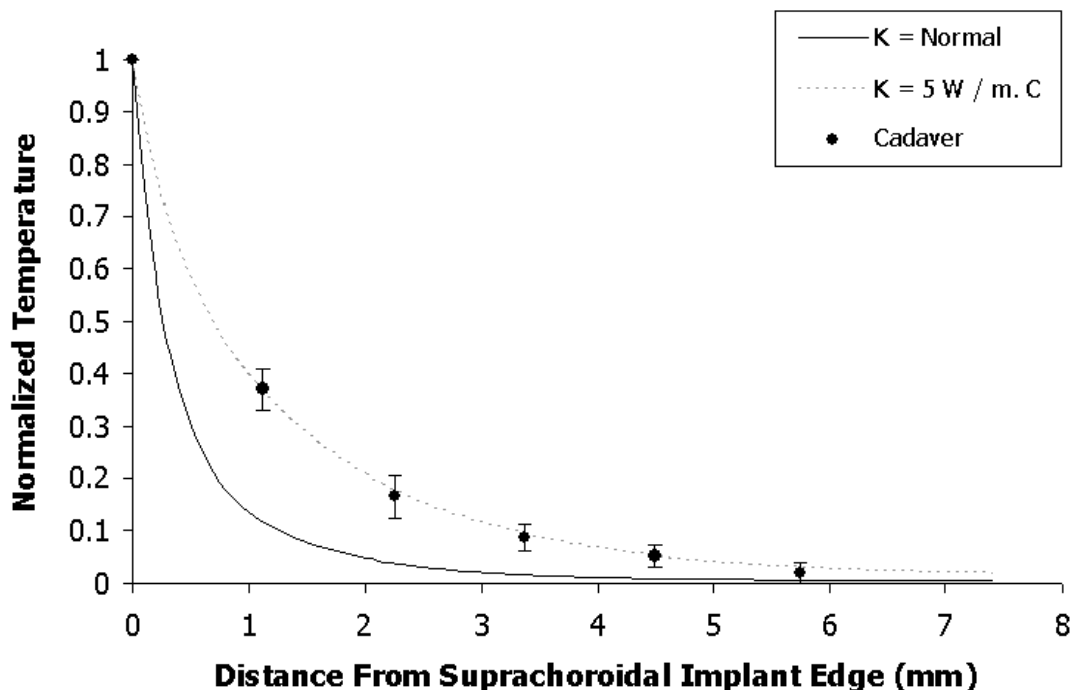
Figure 4.7. Comparison between cadaver tissue temperature increases (data points and error bars) induced by a suprachoroidally implanted heating element and FEM simulations with a normal (solid black line) and a 5 W/m·$\square$C (dashed light grey line) thermal conductivity (K) as a function of distance from the edge of the heating element.

The thermal model predictions and experimental data were very similar when FEMs with different thermal conductivities (K) were used. Cadavers 1, 2, 3, 4 and 5 were best represented by FEMs with thermal conductivities of 2, "normal", 4, 4 and 3 W/m·°C, respectively, shown as Cad1-Kx2, Cad2-KxN, Cad3-Kx4, Cad4-Kx4 and Cad5-Kx3 in Figure 4.8. The largest average temperature difference between a model-cadaver pair was between cadaver 4 and a model with a thermal conductivity of 4 W/m·°C (Figure 4.8, Cad4-Kx4), where a temperature difference of 0.033°C was measured.
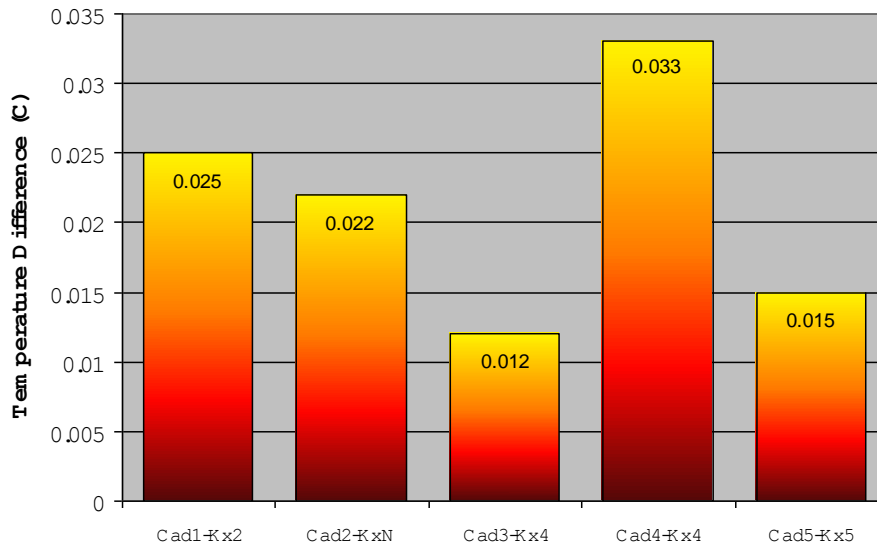
Figure 4.8. Average temperature differences between the cadaver measurements across the four measured distances and model simulations with varied thermal conductivity for each of the five cadaver eyes. Cadaver eyes used are denoted Cad1-5, with the associated thermal conductivity denoted by a prefix Kx. KxN implies a normal retina and choroidal thermal conductivity.

These results give strong evidence of the reliability of the finite element thermal models to predict temperature distributions along the retina for a range of heating element temperatures, with the largest average deviation from cadaver measurements less than 0.1°C.

While the actual thermal conductivity of the eyes used is unknown, the potential for the model to be used to analyse scenarios of altered thermal conductivity may be beneficial if alterations to retinal tissue caused by disease or structural changes are observed.

4.2.5   Thermal Safety

According to Australian and European standards for active implantable devices (BS-EN 45502-1:1998, AS-ISO 14708.1-2003, AS-EN 45502.1-2002), the thermally safe level of power dissipation is one which induces an implant surface temperature increase of no more than 2°C (BS-EN 1998; AS-EN 2002; AS-ISO 2003). By combining the power dissipation-temperature increase equation (Eq. 4.1) with the temperature-distance profile for the accurate thermal model, an approximation of the temperature increase can be determined for a given distance from the heating element surface and the power dissipated by an implant.

The FEM thermal models can be described as a two-phase exponential decay, with a fast exponential decay (F_E) occurring due to the thermal differential between the implant and the surrounding tissue and a slow exponential decay (S_E) occurring as the location of measurement moves away from the fovea towards the cooler lens. The fast and slow exponential decays are dependent on the initial temperature (T_H) and a plateau temperature (P) and the percentage of the distance taken up by each of the phases ($F_\%$). The equations for the two phases are:

$$F_E = 0.01 \times (T_H - P) \times F_\%$$
$$S_E = 0.01 \times (T_H - P) \times (100 - F_\%)$$

$$(4.2)$$

An equation for the temperature, T, at a given distance, d, can thus be described as a function of the two phases and their respective rate constants (K_F and K_S), by:

$$T = P + F_E e^{-K_F d} + S_E e^{-K_S d}$$

$$(4.3)$$

Using GraphPad Prism 5.03 (GraphPad Software Inc.), the values for the plateau temperature (P), fast and slow exponential phases (F_E and F_S) and the fast and slow rate constants (K_F and K_S) were calculated at 0.01207, 0.6672, 0.3202, 4.124 and 0.8874, respectively. Comparing the equation to the thermal model data (Figure 4.9) indicated a very high similarity between the equation and the simulations, with a R^2 value of 0.9998 and a sum of squares value of 1.566×10^{-5}. The difference between the plotted FEM model points and the equation has a median difference of 2.45×10^{-5}°C and an inter-quartile range of 5.75×10^{-4}°C.

By using the two-phase equation (Eq. 4.3) in conjunction with the temperature increase-power dissipation equation (Eq. 4.1), a thermal safety plot relating the distance from the

heating element and implant power dissipation to expected temperature increase was created. This plot, combining the accurate thermal model simulation data and cadaver trial measurements indicates that in order to stay below 2□C, a 5 × 5 mm heating element must not dissipate more than 135 mW (5.4 mW/mm^2) when in direct contact with retinal tissue. At distances greater than 0.5 mm from the retinal tissue, the heating element could dissipate more than 250 mW (10.0 mW/mm^2) without increasing the tissue temperature by more than 2□C. As the power dissipated by the implanted electrical equipment increases, the tissue temperature will also increase (Eq. 4.1). These temperatures, measured at a distance of 0 mm from the heating element, decrease with increasing distance in accordance with (Eq. 4.3).
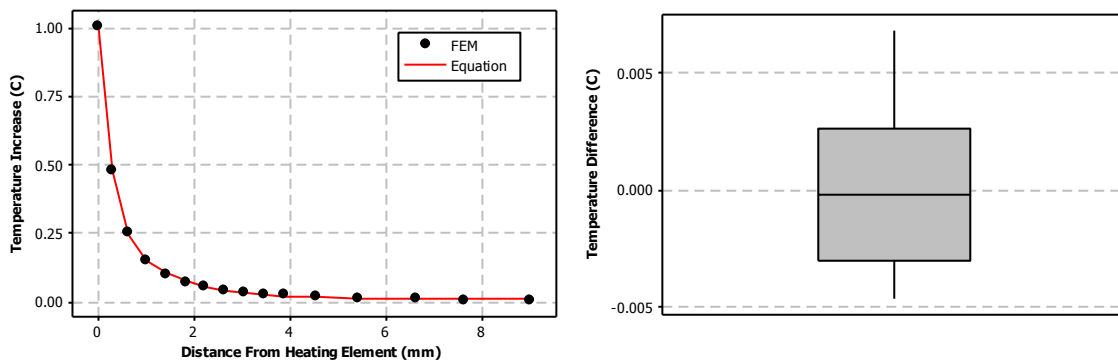
Figure 4.9. Comparison between the FEM simulation data points and the two-phase equation and a box-plot of the average differences between the two methods
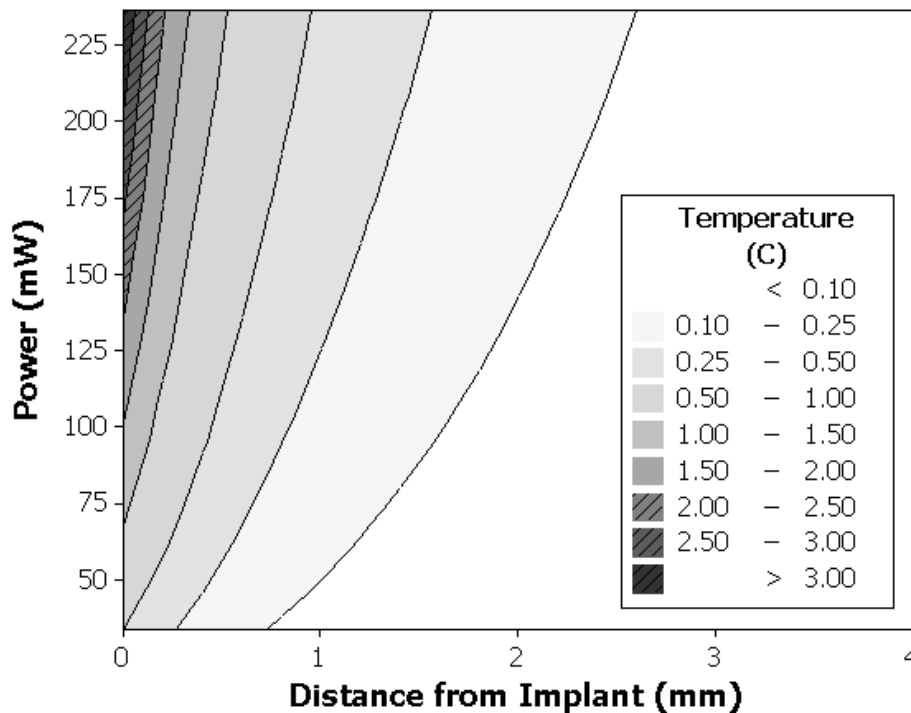
Figure 4.13. Predicted temperature-distance-power profile indicating safe ranges of thermal increase as a function of distance from the heating element edge and power dissipated by a suprachoroidally implant.

4.3 CONCLUSION

This chapter has investigated the use of cadaver eyes to determine the heat flux capacity of cat retinal tissue. Suprachoroidal implantations of a heating element and multiple sensors were used to investigate the temperature increases that are caused as the result of power dissipation through the resistive and copper coil heating elements, with a linear relationship observed, increasing by 1˚C per 67.6 mW. This is comparable to suprachoroidal simulations in which 65.0 mW induced a 1˚C temperature increase.

The affect the heat bath has on measurements of tissue temperature was investigated. Provided that the heat bath temperature is observed and recorded, subtraction of the heat bath temperature from tissue temperature measurements will give accurate and repeatable thermal measurements. There was no clear difference in induced temperature increases of cadaver tissue measured with heat bath temperatures of 24°C and 34°C, with retinal tissue temperatures more strongly influenced by the temperature of the heating element than that of the heat bath. While this can be controlled in cadaver trials, animal trials comparing temperature increases to thermal damage will need to regulate the animal's body temperature as closely as possible during and between tests, with published data strongly suggesting lower damage thresholds occur at increased body temperatures.

Cadaver tests were compared to simulations from the constructed finite element thermal model of a cat eye and indicated very similar results. Average temperature differences between the cadaver tests and thermal models were lower than 0.03°C, although, this was with thermal model simulations using altered thermal conductivities. Alterations in thermal conductivity are expected to occur in cadaver tests where the tissue is fixed but are not expected to be apparent in acute and chronic experiments to the degree observed in these trials.

By combining the temperature-power relationship with the temperature- distance relationship, a graphical representation of likely power dissipations and temperature combinations that cause damage was produced. This combination of results suggested that to stay below a temperature of 2°C, power dissipations of less than 135 mW when in direct contact with the retina. At a distance greater than 0.5 mm from the implant, the power dissipation could be increased to >250 mW, without inducing a temperature increase of > 2˚C. Thus, to ensure the thermal safety of a retinal prosthesis, the thermal safety profile must be adhered to by retinal implant architects.

5

THERMAL HEATING OF CAT RETINAL TISSUE *IN VIVO*

This chapter investigates the ability of retinal tissue to tolerate thermal insult caused by power dissipation though an implanted heating element in an *in vivo* setting. These studies followed on from trials using cadaver eyes (Chapter 4) to determine power-distance-temperature relationships, allowing for thermal energy removal by blood perfusion and other processes to be examined.

While the electrical equipment was identical to that used in the cadaver experiments, implants SMR – 4 and CC – 2 were used in attempt to increase the number of independent measurements (through implanting multiple heating elements) that could be obtained from a single animal.

Surgical techniques, identical to those being investigated for implantation of epiretinal prosthesis, were investigated and improved upon during the *in vivo* experiments, and while some data relating to the temperature increase (as a function of power dissipation) was obtained, immunology of the damaged tissue was not possible. Fluoro-Jade C and glial fibrillary acidic protein stains were attempted, with poor results observed in both *in vivo* cat retinal tissue and positive controls.

Results from the thermal heating tests indicated that tissue temperature increased linearly by 43.5 mW/°C up to a power dissipation of 78 mW, before increasing

dramatically to over 238 mW/°C, at temperatures 2°C greater than the recorded baseline temperature. While these tests were able to display the ability to maintain animal anaesthesia over an extended period (over 24 hours), and enabled surgical staff to gain experience in working with cat tissue, the ability to determine retinal tissue temperature thresholds was not possible.

From the difficulties observed during the *in vivo* cat experiments, further experiments were designed to be conducted on rat retinal tissue *in vitro* (Chapter 6). This would allow for a greater number of animals to be used and, while the thermal damage resulting from power dissipation would need to be performed with an implant that is not of the same size to that of current visual prosthesis designs (as was attempted in the cat experiments), the ability to assess methods of damage measurement and perform an increased number of trials at many different temperatures is expected to be highly beneficial.

5.1   INTRODUCTION

In vivo acute cat retinal tissue experiments were designed to give complementary information to the results obtained from the finite element thermal model simulations (Chapter 3) and cadaver trials (Chapter 4) to assist with the determination of safe power dissipation thresholds. Validation of the thermal model simulations, performed using cadaver eyes, indicated that the models accurately represented heat transfer around the eye in simulations without blood perfusion or metabolically generated heat. While little effect on tissue temperature increase is expected to be seen from metabolically generated heat, the extent to which perfusion will assist in ensuring the retinal temperature is homeostatically maintained can greatly increase the accuracy of thermal models designed to replicate permanently implanted retinal prostheses. The ability to ensure that induced temperature increases and power dissipation levels though-out the eye are not affected by inconsistencies in thermal conductivity (seen in the cadaver eyes through different fixation protocols) will also be of assistance in accurate determination of the amount of power that can safely be tolerated by retinal tissue.

By using cats as the animal model, direct comparisons of thermally induced damage could be made with human retinal tissue. The ocular sizes are very similar between cats and humans (Prince, Diesem et al. 1960; Scott 1988; Ng and Ooi 2008) which allows surgical procedures for human visual prosthesis implantation to be practiced and problems identified, but will also ensure the thermal energy dissipations within the eyes can be directly compared. While there are minor differences occurring in cat and human vasculature, these have been reported to be related to the choroidal thickness, with the function this highly perfused tissue remaining the same (Geeraets, Williams et al. 1962; White, Mainster et al. 1970; Welch and Polhamus 1984).

The majority of studies investigating thermal damage thresholds in retinal tissue were performed using laser irradiation. These studies, detailed in Chapter 1, used temperatures much higher than would be expected in a retinal prosthesis, with irradiation durations magnitudes shorter (sub-second insults). Thus, studies performed under these conditions are not expected to give an accurate correlation with thermal damage thresholds observed from normal use of a visual prosthesis.

There are few studies published using conductive heating elements to induce temperature increases within the eye. One study performed by Goldblatt et al. (1989) indicated the ability of rabbit retinal tissue to tolerate temperatures of 38°C for 45 minutes and 45°C for 5 minutes before damage was observed. Thermal damage was

observed to occur in canine retinal tissue due to a one second, 50 mW power dissipation (Piyathaisere, Margalit et al. 2003), although, like the study performed by Goldblatt, did not use durations up to 18 hours, the potential daily usage for a patient with an visual prosthesis. Nakauchi et al. (2007) and Ray et al. (2009) investigated pulses of electrical stimulation and their ability to be tolerated by, or cause damage to, the retina. While these studies suggested that mechanical damage would be present regardless of the amount of electrical stimulation, they did not assess temperature and thus these studies can not be used to assist in analysis of thermal damage thresholds.

Studies were performed by Kim et al (2007a) to assess the ability of perfusion to reduce thermal increases. While damage was not assessed in their studies, they indicated that cortical perfusion increased the ability of tissue to remove thermal energy, decreasing from 0.089°C/mW to 0.051°C/mW. The ability of perfusion to reduce temperature increase was also investigated by Sailer et al. (2007), who reported a linear temperature increase seen in laser irradiated rabbit retina up to 40 mW (4.5°C) before a thermoregulatory mechanism stabilised the temperature and strongly improved the heat dissipation within the tissue. The effect of perfusion is one aspect that could not be investigated through cadaver trials, and will be of great importance in the assurance of safe levels of thermal power dissipation by an implanted retinal prosthesis.

The primary aim of the *in vivo* pilot studies (other than to investigate the effect of choroidal perfusion) was to identify problems that may have occurred during the acute experiments. This included all aspects of surgery, animal maintenance and anaesthetic induction, issues concerning the induced thermal increase of retinal tissue, monitoring and measurement of thermal changes, enucleation and the histological process that followed.

Surgical experimentation involving the implantation and the placement of the heating element on the retinal surface (with as minimal mechanical trauma as possible) was investigated, and while this had been performed earlier on cadaver eyes, needed to be reassessed when using anaesthetised animal tissue. The surgery required to ensure the implant could remain in a stable position for the duration of the experiment, the ability to ensure the eye remained as close to normal as possible (without excessive changes to intraocular pressure or fluid within the anterior and posterior chambers) and the explantation of the device after experimentation were also investigated in the pilot trials and used to improve future experiments.

Equipment issues, both relating to the implant and connections and the measurement and recording apparatus were also trialled during the initial pilot test, pushing equipment capabilities to limit. Procedures involving the experiment duration, and

thermal heating protocol and the enucleation, fixation and histological analysis of the tissue after the experiment were also addressed and improved upon during the pilot studies.

5.2 METHODS

Animals used in experimentation must be treated with upmost care to ensure that they do not suffer needlessly. Further, to ensure that the experiments are accurate representations of the tests being performed, animals must be maintained in a consistent and repeatable manner. The animal maintenance and initial surgical procedures (insertion of intravenous lines and tracheotomies) were similar across all *in vivo* experiments and are detailed in the following sections. Details on the experimental protocol which changed due to alterations in inserted implant and the analysis tools investigated to determine the extent of cell damage are also discussed.

The approval of the use of cats was granted by Royal Victorian Eye and Ear Hospital, Animal Ethics Committee.

5.2.1 Animal Maintenance

All animals undergoing acute experimentation are required to be anaesthetised for the entirety of the experiment in accordance with the NHMRC guidelines (NHMRC Australian Code of Practise for the Care and Use Of Animals for Scientific Purposes, 2004) and adhered to the standard operating procedure 12 (Appendix 5).

Prior to the surgical and experimental procedures, pre-starved cats were weighed and given an initial subcutaneous injection of Xylazil (2 mg/kg), making the animal drowsy in approximately fifteen minutes. An intramuscular injection of Ketamine (20 mg/kg) followed and the animals were transported to the operating room where body temperature was regulated by placing the animals on a 37°C thermal blanket and covering with towels. Both eyes were lubricated with ocular lubricant and the tail, forearms and tracheal area were shaved. 22-gauge catheters were inserted into the cephalic veins of each of the forearms, with assurance of the correct locations of the catheters achieved by injection of sterile saline. Catheters were removed and reinserted if the injected fluid was observed to pool, with a three way tap attached and secured with tape to the correctly inserted catheters.

A tracheotomy was performed after a subcutaneous injection of antibiotic (Clavulox, 10 mg/kg), by making a longitudinal incision along the front of the throat of the animal.

Blunt scissors were used to expose the trachea and to clear the tissue and surrounding muscle. Two silk sutures were thread in a horizontal direction under the trachea, prior to cutting the trachea and inserting a 70 mm, tapered trachea tube with inner dimensions of 3 to 4.5 mm. The sutures were then tied to secure the tube in place and the animal was observed to be freely respiring. The incision was sealed, and a needle inserted into the tube was attached to a capnograph to monitor the animal's respiration rate. The end-tidal CO_2 should be 3-5% with a respiration rate of 5-25 breaths per minute. An ideal heart rate of between 140 and 250 beats per minute can be monitored by inserting recording electrodes or through the use of a pulse-oximitter attached to the cat's tail, forearm or tongue (Fallon et al. 2009).

Intravenous lines were attached to a three way plug and slow intravenous infusion of sodium pentobarbitone (60 mg/ml, 1:6 dilution) and Hartmann's solution (sodium lactate, 1.5 mg/ml. h) was automatically delivered using a Pegasus automatic anaesthesia pump, with a dose rate of between 0.5 ml/hour to 1.5 ml/hour depending on the animal's response. A higher rate was generally required at the beginning of the experiment when the effects of the Ketamine were wearing off. Hartmann's solution was delivered in 10 ml/kg bolus intramuscular doses every two to four hours, with vital signs (heart rate, respiration rate, CO_2 levels and body temperature) measured hourly throughout experimentation, with alterations to the anaesthetic dose performed accordingly.

5.2.2   Surgical Procedure

The surgical procedure used in the initial pilot trial was one of the first performed by the surgical staff on cats, and as such, many differences between human and cat eyes and retinal tissue became apparent. Two implantations were used to investigate thermal damage caused to retinal tissue, an open sky approach for the multiple heating element pilot study (pilot test I) and standard vitrectomy for the double heating element pilot studies (pilot tests II and III).

All surgical procedures followed immediately after the initial animal maintenance steps of anaesthetisation, attachment of intra-venous lines and the tracheotomy had been performed. All surgical equipment was sterilised in an autoclave, with implants sterilised with a fifteen minute, 70% ethanol wash.

5.2.2.1 Pilot Test I

The initial pilot study involved the stabilisation of a cat in a stereotaxic frame, with two ear bars, a chin bar and placement of eye bars so as not to disrupt the surgical procedure. This reduced any involuntary movements made by the animal, which could have caused an alteration in the position of the implanted heating element. The cat was inclined to approximately 60° above the horizontal meridian and supported with towels to reduce the pressure on the animal's neck and back.

Once the animal was secured within the stereotaxic frame, a small incision was made within the cornea and the cornea was removed. A lensectomy was performed to remove the lens and a vitrectomy was performed manually to remove as much of the vitreous fluid as possible.

This experiment used the multiple heating element implant (SMR - 4), which had five independent heating elements and nine temperature sensors located centrally and between each of the heating elements. To implant the device, the arms containing sensors and heating elements were folded to reduce the implant circumference and inserted into both globes where they were unfolded to lye on the retinal tissue.

After implant insertion and attachment to the stereotaxic frame to reduce movement, balanced salt solution was used to fill the eye cavity. The eye was then sealed to reduce evaporation and the requirement for additional fluid to be administered.

5.2.2.2 Pilot Tests II and III

The second and third pilot trials used the double copper coil heating element implant (CC – 2). This implant was smaller, having two independent heating elements rather than five. Due to the decrease in implant size, the second pilot study could be performed using standard vitrectomy techniques. This was also expected to greatly increase the ability of the eye to maintain intraocular pressure and reduce the potential for retinal detachments to occur due to collapse of the globe.

After the animal had been given the initial ketamine/xylasine injection and had intravenous lines attached, conjunctival connective tissue around the rims of the globe were cut. A lateral canthotomy and lid retraction was performed, followed by a

complete periotomy to provide trans-scleral access to the pars planar. Three transplanar port holes are then made about 2 mm posterior to the limbus, one for a balanced salt solution infusion line, one for the light probe and one for a vitrector, used to carry out a complete transplanar vitrectomy, removing the zonular apparatus and vitreous base above the retinal tissue to be in contact with the electrode array. Vitreous fluid was removed and the holes that were used for the light source and the vitrector were joined to form a full thickness retinal incision for implantation of the heating element and sensor array. The implant was inserted into the opening and moved into the desired location. A retinal tack was used to hold the implant in location during the initial double heating element pilot study (pilot test II), with no tack required for the second trial (pilot test III), as the implant had been pre-curved to conform to the curvature of the retina. The flexibility of the substrate allowed conformation, with the stiffness of the implant assisting to keep the implant overlying the retinal tissue.

During pilot test II, the implant touched the lens which became immediately cloudy, obscuring vision of the implant location. The mechanical stiffness of the lens made the lensectomy using the vitrector difficult, and retinal detachment was observed to occur during the lens removal. In the third pilot test, the lens was removed ultrasonically, maintaining the ability to visually inspect the location of the implant.

The implant insertion site was, however, problematic. In order to ensure the eye did not collapse, the eye was infused continuously with balanced salt solution. The fluid leaked out through the scleral incision was difficult to close. Sutures in a "handbag" type enclosure, zigzagging around the implant were used to reduce the amount of water leakage, allowing tightening of the sutures to close the wound. This had limited effect, with fluid being expelled at the implantation site. Super gluing the tissue closed did not work initially, with the fluid hindering the ability of the glue to set. This was attempted without the continual perfusion of balanced salt solution and was more successful, decreasing the amount of fluid being expelled through the opening. The eye was filled with heavy liquid which improved the structural integrity of the globe and stopped the expulsion of fluid.

5.2.3   Experimental Protocol

After surgical insertion of the implants, the animal was left to stabilise for at least one hour prior to temperature recordings. This also allowed the inserted implants to equilibrate to the temperature of the cat eye. The experimental protocol was changed

after the initial pilot study investigating five independent temperature sensors for the second and third pilot trials that used the double heating element array.

Implants were then connected via axon cables to the high resolution temperature measurement system (for PRTD temperature measurements) and current sources) for power dissipation through the heating elements). In identical fashion to the cadaver trials (Chapter 4), the measured temperatures and currents were monitored and recorded with at a sample rate of 1 Hz.

5.2.3.1 Pilot Test I

The initial pilot study, designed to investigate the ability of multiple implanted heating elements to independently induce retinal tissue temperature increases used a 4.5 kg, 16 month old female cat. The protocol for the acute pilot test included an initial 15-30 minute period of measurement without thermal induction which allowed for a recorded baseline temperature and to assist in the amount of power required to induce pre-determined temperature elevations.

The multiple heating element implant was used in this experiment (SMR – 4), which had five, 5 ×5 mm heating elements and a total of nine sensors (one central to each heating element and one in-between) on each implant, discussed in more detail in Chapter 2.

Following a thirty minute baseline measurement period, temperature elevations of 0°C (control), 1°C and 2°C were induced in the left eye (the central heating element acting as a control with two peripheral heating elements being heated) and elevations of 0°C (control), 2°C and 4°C in the right eye (the 2°C temperature increase induced in the central heating element, with the control (0°C increase) and the 4°C increase assigned to peripheral heating elements) were induced in the right eye. To obtain these temperatures, current was passed through the heating element in small increments until the temperature measured by the centrally located PRTD matched the desired temperature increase. A schematic of the desired heating element temperatures is shown in Figure 5.1.
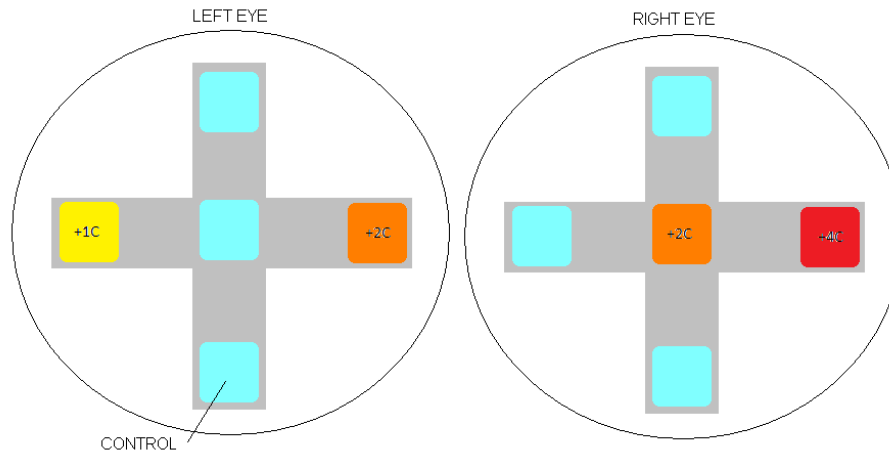
Figure 5.1. Desired thermal increases for the five heating elements implanted in both the left and right cat eyes in Pilot I. Blue squares are indicative of control (no power dissipation) with yellow square (left eye) indicating a temperature increase of 1°C, orange squares (both left and right eyes) indicative of 2°C increases and a 4°C increase (right eye) shown as a red square. Grey areas are representative of the implant locations.

A temperature increase of 2°C was used in both the left and right eyes as this is the thermal elevation allowed by international guidelines for surface temperature of implantable devices, with 1°C used to investigate half this temperature. A 4°C temperature increase has been reported to cause necrosis and cell death in 30% of Chinese hamster ovary cells when incubated at this temperature for one hour, and was used to give an initial measurement of thermal damage (Gerweck 1977).

Tissue taken from the control areas and from retinal locations not in contact with the implant would enable damage comparisons to be made between tissue subjected to thermal and mechanical trauma. These temperatures were intended to be maintained over a 24 hour period, with a final 30 minutes of baseline recording (all heating elements switched off) performed at the completion of the experiment.

5.2.3.2 Pilot Tests II and III

The second and third pilot tests were performed to investigate whether surgical and histological procedures using a smaller implant could be used to accurately determine thermal threshold levels in a cat eye.

Adult (20 month old) female cats were used, weighing 4.6 kg each. While changes were made to both the surgical procedure and to the equipment used in this experiment, the

thermal heating protocol (a thirty minute baseline recording followed by 24 hours of heating and a final thirty minutes of baseline recording) remained the same.

The double heating element pilot trials used the multiple copper coil heating element implant which had two independent heating elements (5×5 mm) made from coils of copper wire. The sensors were located on the opposite side to the heating elements, centrally and at 1.16 mm separations between the heating elements. The implant had a width of 7.5 mm and a thickness of approximately 159 μm with retinal tack holes located at the implant tip (1.5 mm from the heating element), 1.5 mm from the heating element midway down the polyimide shaft and 1.5 mm laterally from the sensors in the midline, discussed in more detail in Chapter 2.

In similar fashion to the initial pilot study, after a period of approximately one hour (allowing the animal to stabilise and the implants to equilibrate to the temperature of the cat eye), baseline temperature recordings were taken. These lasted for approximately ten minutes prior to the onset of current induction through the copper coil heating elements and the respective measurement of induced temperature increase.

5.2.4 Histological Analysis

After final temperature measurements had been taken, eyes were fixed using 4% PFA. As the animal was restrained in the stereotaxic frame, the ability to use whole body perfusion was limited. Instead, the 4% PFA was poured into the orbital cavities (with the implants remaining in place) for fifteen minutes prior to euthanisation and enucleation.

Following the surgical procedure in the second and third pilot trials, the animals were given sub-lethal intraperineal injections of Lethabarb and prepared for perfusion. Full body perfusion of the cats was then performed by opening the midline and exposing their hearts. Pericardial tissue surrounding the heart was removed and a perfusion lead was inserted into the left ventricle. A hole in the atrium was cut and one litre of saline was flushed through the animal until the fluid expelled from the atrium was almost clear. A 4% PFA mix was then sent through the infusion line to the left ventricle. The animals were euthanized upon this step and eyes were enucleated and kept in a PB mixture for histological processing.

5.2.4.1 Fluoro-Jade C

Fluoro-Jade C (and its predecessors Fluoro-Jade and Fluoro-Jade B) are anionic fluorescein derivatives that are useful for the histological staining of neurons undergoing degeneration (Schmued, Albertson et al. 1996; Schmued and Hopkins 2000; Schmued, Stowers et al. 2005) and it is thought that this may be a good measure of damage caused to cat retinal tissue through mechanical and thermal trauma. Although the exact ability of these stains to bind specifically to damaged neurons is still largely unknown, there have been many studies indicating the ability of Fluoro-Jade to stain all degenerating neurons and apoptic cells regardless of the specific insult or mechanism of cell death.

The ability of Fluoro-Jade C to measure thermal damage caused through implantation of a heating element was investigated using tissue from the initial pilot study. The stain has been effective in staining degenerated neurons caused by ischemia in the rat and mouse brain (Olsen and McKeon 2004; Duckworth, Butler et al. 2005), mechanical lesioning and traumatic brain injury in mouse and primate cortex (Colombo and Puissant 2002; Anderson, Miller et al. 2005; Bian, Wei et al. 2007) and degenerated rat retinal tissue (Fernandes, Maurer-Morelli et al. 2004; Chidlow, Wood et al. 2009). Additional research investigating neuronal death with Fluoro-Jade is listed in Table A1.5 in Appendix 1.

The enucleation of eyes used in the Fluoro-Jade staining was difficult due to the lack of intraocular pressure, with the retinal tissue appearing detached prior to fixation. Visual analysis of the retinal tissue and globe after removal of the implants indicated that the implant had punctured completely through the retinal tissue layer causing massive bleeding, retinal tears and detachment, resulting in mechanical damage that would far surpass thermal damage presented to the tissue. This was apparent on both eyes to different degrees, indicating that while the implant could be used for cadaver trials where the eye is more rigid, when the intraocular pressure drops in an acute setting (caused by removal of the cornea, lens and vitreous fluid) the eye collapsed upon itself and the retinal tissue was subsequently damaged by the implants.

The initial analysis of damage was performed using Fluoro-Jade C (FJC) in accordance with the manufacturer's recommended protocol, suitable for triple labelling of cell nuclei with DAPI and GFAP immunofluorescence. 15 µm sections of one of the cat retinas were taken along the retinal midline (along the naso-temporal axis) and placed

on polysine slides for analyses. Slides acquired from an aged retinal degeneration mouse (rd1 mouse) were also sectioned and mounted, to be used as a positive control.

A stock solution was made to 0.01% FJC by diluting 10 mg of the FJC powder with 100 ml dH_2O. Slides were twice rinsed in phosphate buffer (PB) for five minutes each before a final five minute wash in dH_2O. The slides were then coated in a 0.2% TritonX and phosphate buffered saline solution prior to a final five minute dH_2O rinse. The FJC stock solution was further diluted to a 0.0001% concentration by mixing 0.2 ml of the stock solution with 19.8 ml dH_2O, which was coated over the slides for ten minutes, prior to coating the retinal slides with DAPI (1.5 ml DAPI made from 0.05 µl of 1:3000 stock solution, combined with 1.5 ml dH_2O) for 10 minutes. Two final rinses were performed (5 minutes in dH_2O) prior to cover slipping the retinal slides.

Another analysis was performed using methodology from Schumed and Stowers (2005), which used potassium permanganate to open the cells to a greater extent and allow more FJC to penetrate. This protocol was also attempted on the damaged retinas of rd-mice. The protocol involved covering the slides in a mix of 1% sodium hydroxide and 80% ethanol (24 ml dH_2O : 6 ml ethanol : 0.3 g NaOH) for five minutes, then for two minutes in a 70% ethanol solution (21 ml ethanol : 9 ml dH_2O) and a two minute was in distilled water. A 0.06% potassium permanganate solution was used to increase FJC penetration and was add to the slides for 10 minutes prior to the addition of the FJC (0.0001% FJC made by combining 1 ml of 0.01% FJC stock solution with 99 ml of 0.1% acetic acid) for ten minutes. Three one minute rinses in distilled water was performed prior to air drying on a 50°C slide warmer for five minutes and cover slipping the retinal tissue.

5.2.4.2 Glial Fibrillary Acidic Protein

Glial Fibrillary Acidic Protein (GFAP) is a cell-specific intermediate filament protein whose expression is widely used as an indicator of glial cell response to neuronal injury. With virtually all forms of injury triggering reactive gliosis, this staining technique has been widely used as a histological marker of damage. Measurements of damage levels caused by hyperthermia (Caprioli, Kitano et al. 1996), retinal degeneration and detachment (Erickson, Fisher et al. 1987; Okada, Matsumura et al. 1990; Nakazawa, Takeda et al. 2007; Chidlow, Wood et al. 2009), electrical stimulation (Colodetti, Weiland et al. 2007), retinal vascularisation (Downie, Pianta et al. 2007), electromagnetic irradiation (Eisenfeld, Bunt-Milam et al. 1984), mechanical damage (Bignami and Dahl 1979; Nolte, Matyash et al. 2001), hypoxia and ischemia (Liu,

Smith et al. 1999; Olsen and McKeon 2004) and neurotoxic insult (Dyer and Cepko 2000; Schmued, Stowers et al. 2005), have all been possible using GFAP expression. This process has been shown to be consistent across species, from fish (Bignami 1984) to cats (Pardue, Stubbs et al. 2001) and humans (Mizutani, Gerhardinger et al. 1998) and is expected to be a good method of analysis thermal or mechanical trauma caused to cat retinal tissue through the implantation of a heating element. Additional studies using GFAP as an analysis tool are listed in Table A1.6 in Appendix 1.

Immunocytochemical labelling was carried out using the indirect fluorescence method. Sections from the control eye were defrosted within a sealed chamber with a wet paper towel floor (to prevent evaporation) for twenty minutes before being outlined with a wax PAP pen. The slides were washed in 0.1M PB three times for ten minutes each, prior to applying a blocking solution. The blocking solution, made by dissolving 2 ml of 10% normal goat serum (NGS), 0.2 g of 1% bovine serum albumin (BSA) and 16 ml 0.1M PB without heat under a fume hood prior to spinning the solution with an additional 2.0 ml of 0.05% Triton X-100 for one minute. The primary antibody (IBA-1; 09-19741, Wako Chemicals USA Inc.) was diluted (1:50000) in 3% NGS, 1% BSA, 0.05% Triton-X 100 in PB and applied overnight at room temperature. After the tissue was washed in PB (three washes for ten minutes per wash), goat-anti-rabbit IgG conjugated to Alexa TM 594 was applied for one hour (A-11037; Molecular Probes, Eugene, OR; diluted 1:800). Again the solution was washed in PB (3 x 10 minutes) and dried to remove excess solution. Mowiol was gently applied over the sections (2.4 g Mowiol, 6 g glycerol, 6 ml of dH_2O, 12 ml of 0.2M Tris Buffer and 0.65 g of 2.5% w/v DABCO), with cover slips placed over the Mowiol, ensuring no air bubbles remained. Slides were then taken to the confocal microscope for analysis.

5.3   RESULTS

Experimental results obtained from the three pilot experiments are discussed in the following sections. These results indicate the good ability to ensure animal comfort and maintenance for the duration of the initial 24 hour trial. Thermal damage results are discussed, and while limited from the initial pilot trials, the third pilot study was able to provide some information relating power dissipation and induced temperature increase occurring in the presence of perfused tissue.

5.3.1   Animal Maintenance

Animal maintenance results from pilot test I are shown in Figure 5.2, indicating a good ability to anaesthetise the animal and maintain the anaesthetic state for the duration of the experiment.

The anaesthesia profile is indicative of the rates administered automatically by the Pegasus pump, with bolus doses denoted by triangular symbols. The final bolus dose (for euthanisation) was 10 ml and is not shown. The dose required was relatively stable throughout the experiment, with very few changes needed to ensure animal comfort. There were almost no palperbral reflexes, indicating that the animal was properly anaesthetised throughout, with most of the reflexes that did occur (3 out of 4) occurring as the animal was transferring from Ketamine to Nembutal.

Respiration of the animal decreased from over 20 breaths per minute to around 10 breaths per minute after 1000 minutes and an increase in oxygen saturation from below to above 2.4% was simultaneously observed. The anaesthetic dose was maintained at 0.6 to 0.8 ml/hour for majority of the experiment to avoid an overdose occurring.

Hartmann's Solution was also injected sub-cutaneously in 10 ml bolus doses each 2-4 hours. These doses were administered in six locations around the animal, front left and right, middle left and right and back left and right as indicated in Figure 5.3, where the location of each dose is denoted by the time of injection. The protocol used for animal maintenance was verified in the initial pilot trial and was adopted in all future experiments without changes or alterations required.
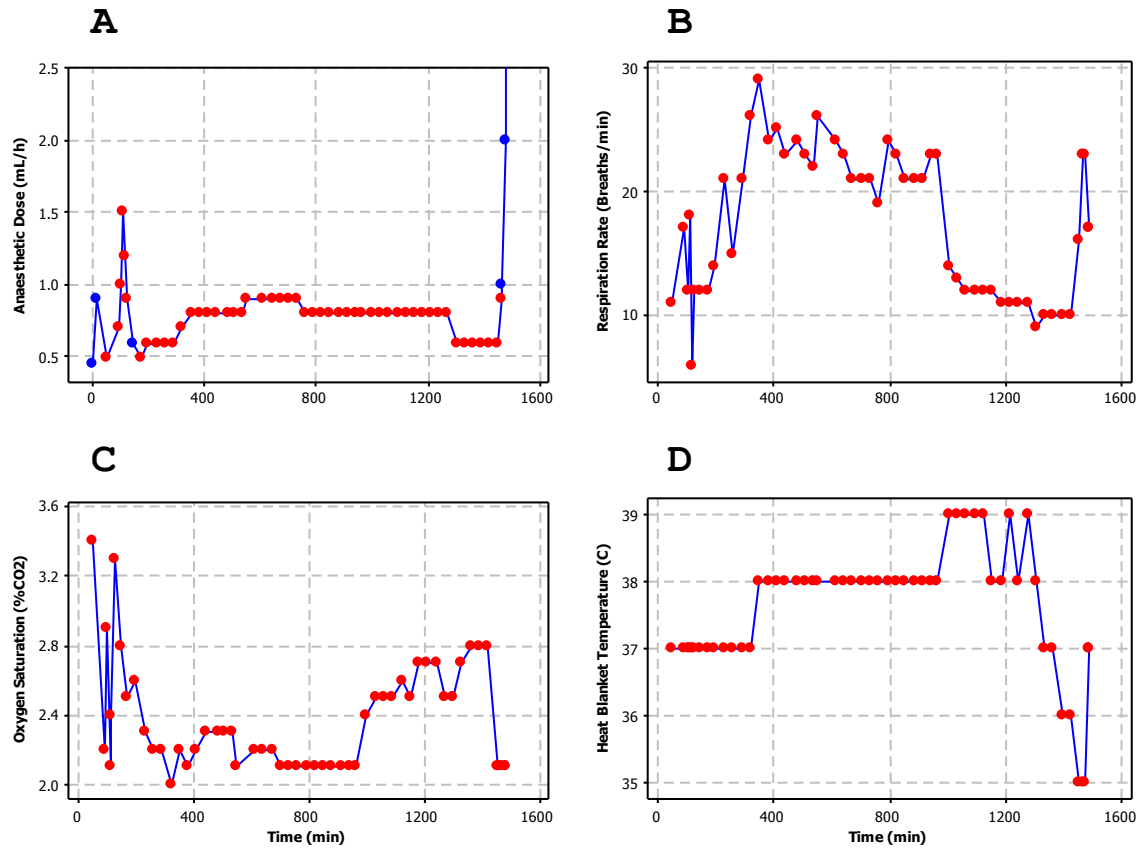
Figure 5.2. Animal maintenance results for the initial pilot trial using a multiple heating element implant, indicating **(A)** anaesthetic dose, **(B)** carbon dioxide levels, **(C)** respiration rate and **(D)** temperature throughout the experiment. Blue circles indicate the administration of a bolus anaesthetic dose.
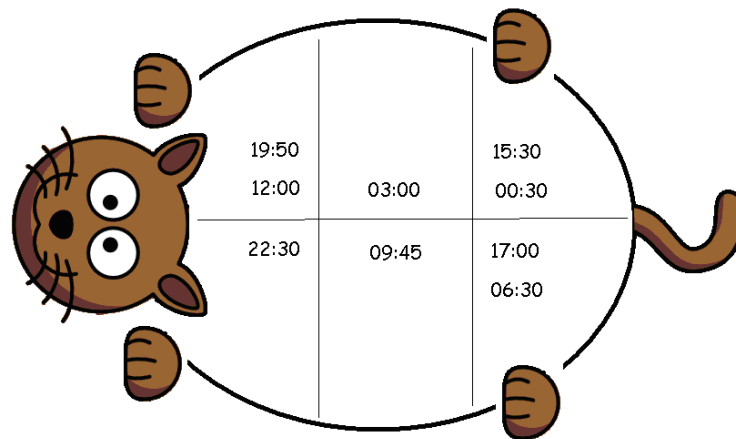
Figure 5.3. Hartmann's subcutaneous injection dose location and time for the initial pilot trial using the multiple heating element implant

183

5.3.2   Thermal Heating Results

5.3.2.1   Pilot Test I

As most of the lead wires connecting the implant to the measurement system fatigued and failed during implantation, almost all of the data that could be recorded was erroneous. Of the eighteen implanted sensors, only four of these could be recorded from and eight of the ten heating elements were also damaged. After experimental completion and explantation, it was observed that solder pads located on the implant (which connected the heating elements and temperature sensors to the measurements system and current sources) had detached from the polyimide surface, caused by the excessive bending required to insert the implant into the partly collapsed retina.

A sample of the current induction within the first four hours is shown in Figure 5.4, with an initial 1336 second baseline recording shown prior to the onset of a 20 mA current. The current is shown to be relatively stable for the first 5000 seconds, with no additional configuration required during this time. After approximately 6000 seconds, the current had reached a level of 19 mA (dropping by 1 mA or 5%) and was increased accordingly (to a current of 21 mA). This process needed to be repeated again at approximately 8000 seconds and again at about 9500 seconds, both times with the measured current flowing through the heating element falling below 19 mA. After this time, the current delivered through the heating element became unstable and this was thought to be caused either by mechanical failure of the lead wires (increasing resistance and hence decreasing the current flowing through the heating element) or by failure of the silicon coating designed to protect the circuitry from shorting.

The recorded voltages did not appear to correlate to temperatures in this initial pilot test. Initial baseline temperatures of 43.5°C were measured by three of the four sensors implanted centrally to the heating elements (sensors T2, T3 and T4), with the fourth sensor (T1) measuring a more plausible 35.5°C. Figure 5.5 shows an initial stabilisation that was observed to occur after 1100 seconds (for sensor T1), lasting for approximately 7000 seconds. This initial plateau indicated a temperature increase of 1.0°C from the baseline temperature with the second plateau, from 10000 to 14000 seconds, indicating a further 0.5°C increase.
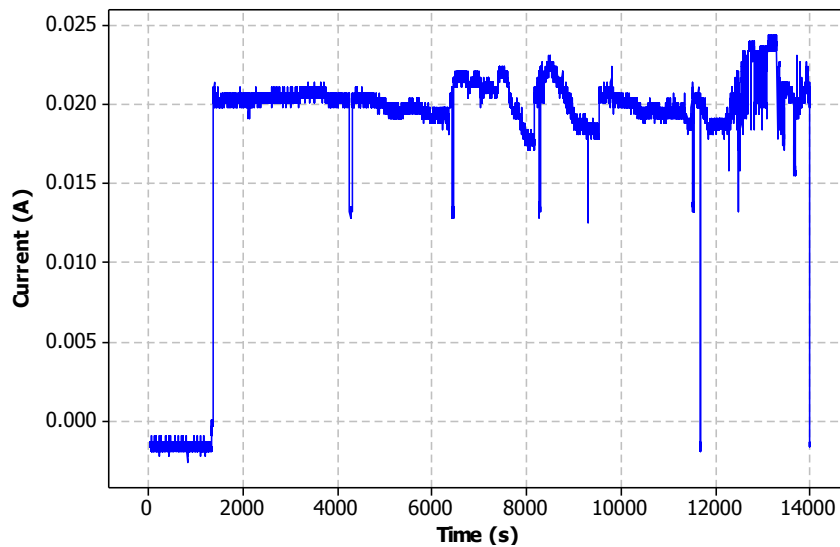
Figure 5.4. Current through a heating element in the left eye in the multiple heating element pilot study

While T1 provided temperatures that would be expected to be observed at the back of the eye (between 35.5°C and 36.5°C), the temperatures that were measured by the other sensors (between 43.5°C and 41.5°C) are highly unlikely. It is expected that shorting either in the leads connecting the high resolution measurement system to the polyimide substrate or between the implanted sensors was the cause of these erroneous results, with the detached solder pads expected to have been the primary cause of the short circuits.

The slight increase in temperature may be explained by fluid within the eye heating up from room temperature to that of the animal's body temperature. The body temperature of the animal and room was monitored and did not deviate significantly (by more than 0.5°C).

The major limitation that became apparent after this initial acute pilot experiment was the size of the implant. While the five heating element array worked well in cadaver eyes, this was primarily due to the increased rigidity as a result of eye fixation.

185
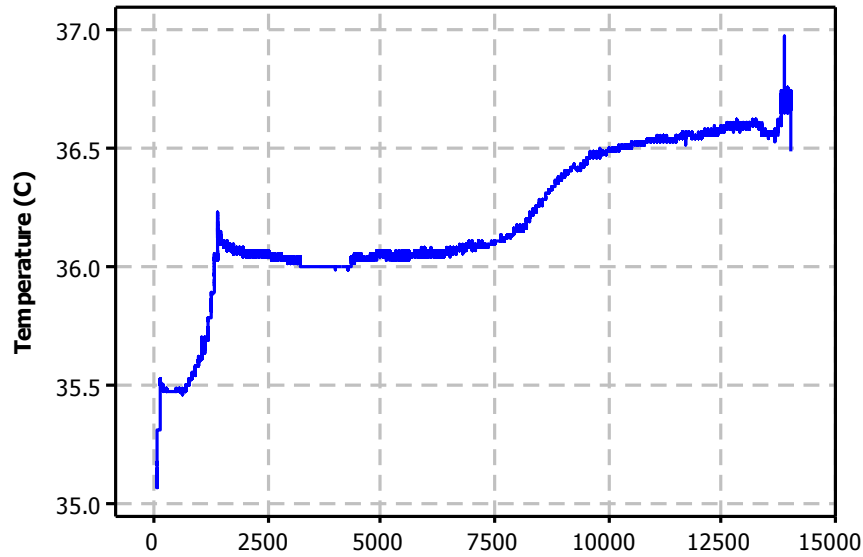
Figure 5.5. Multiple heating element pilot study test voltage measurements from sensor T1 implanted in the right eye.

5.3.2.2   Pilot Tests II and III

Due to retinal detachments and a loss of intraocular pressure required to prevent the globe from collapsing, measurements of thermal heating could not be performed during the second pilot trial.

During pilot test III, the implant was connected to the current source and measurement system and a baseline reading was taken over the initial 500 seconds. Heater 2 (located in the macula region) had an average reading of 33.63±0.02°C. This recording was slightly higher (0.4°C) than the average temperature measurements from the more peripherally placed heating element, with a baseline temperature of 33.23±0.02°C. Baseline recordings are shown in Figure 5.6 with recordings from Heater 2 having less noise than those obtained from a sensor measuring temperature of Heater 1, which is though to be related to the increased immersion and depth inside the animal.
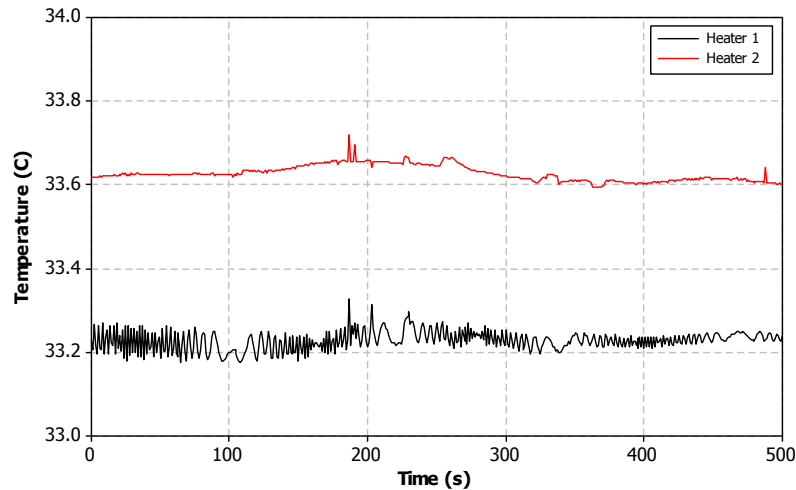
Figure 5.6. Baseline temperature measurements from the double heating element pilot trial for both implanted heating elements (red heating element is closest to the macula).

Results taken from the five implanted sensors between the two heating elements, measured with a DMM, had average baseline temperature readings of 34.57°C, 34.59°C, 34.59°C, 34.57°C and 34.61°C, with an overall average of 34.59±0.02°C. The maximum difference between the sensors was 0.2Ω, equivalent to a temperature difference of 0.052°C. A slight increase in the temperatures measured from the sensors was expected, with a poorer inherent resolution of the DMM determined from cadaver and saline bath experiments. All sensors were essentially identical in reading, suggesting that the baseline temperature was consistent within the eye and that the temperature of the heavy liquid used to ensure global integrity had reached a thermal equilibrium.

After baseline recordings, power was delivered to the heating element located in the macula with retinal tissue temperatures shown in Figure 5.7. Current was applied after 553 seconds (indicated by the dotted red line), and increased in steps to investigate the effect of power required to induce thermal temperature increase. The amount of current required to induce a temperature increase of 0.13°C, 0.97°C, 1.82°C and 2.48°C above baseline temperature averaged over the initial 553 seconds of recording was 30 mA, 103 mA, 157 mA and 271 mA, respectively. Power dissipations and resulting temperature increases are listed in Table 5.1.
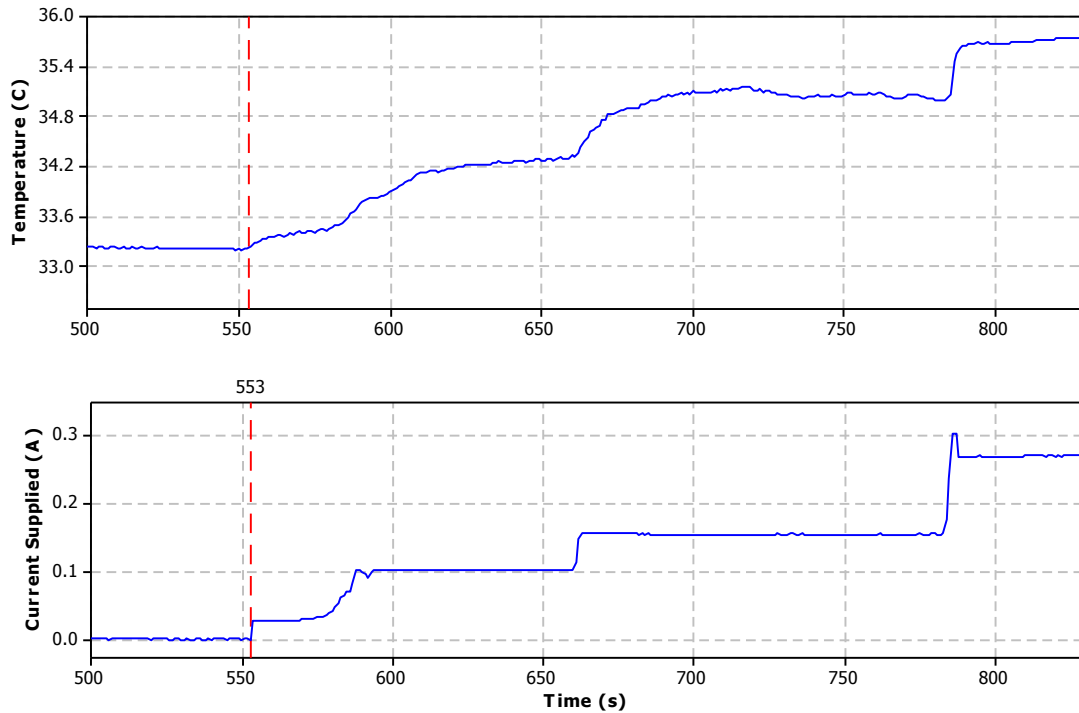
Figure 5.7. Tissue temperature and current measured through the sense resistor during pilot study III. Broken red line indicates timestamp where current was initially supplied to the heating element.

Table 5.1. Measured temperature and temperature increases as a function of current measured through the sense resistor in the double heating element pilot trial.

Time (s)	Current (mA)	Power (mW)	Temperature (°C)	Temperature Increase (°C)
Baseline (0-553)	-	-	33.23±0.02	-
555-570	30.260	2.930	33.36±0.04	0.13
600-660	103.00	33.95	34.20±0.09	0.97
670-770	156.55	78.43	35.04±0.08	1.82
790-830	271.83	236.5	35.71±0.03	2.48

As a function of power dissipated, the temperatures induced in cat retinal tissue was very similar to those observed using an identical heating element in saline bath trials, up to a temperature increase of 2°C, where additional power had a reduced effect on the temperature increase. This effect, which could be an early observation of increased perfusion removing thermal energy, is similar to observations reported by Sailer et al. (2007), and by Kim et al. (2007a). A comparison between power dissipation induced temperature increases for the copper coil heating element immersed in a saline bath, the results from the cadaver tests and in and results from the *in vivo* experiment are shown in Figure 5.8.
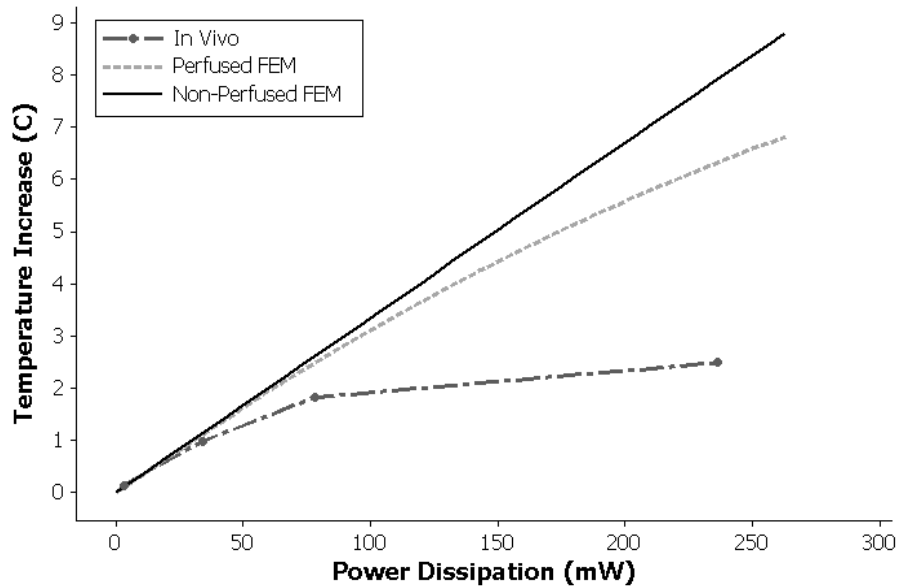
Figure 5.8. Comparison between temperature increases observed during *in vivo* experiments (dark grey line and data points) and FEM simulations with (light grey line) and without (black line) bioheat perfusion as a function of power dissipated by the epiretinally implanted heating element.

The temperature of the central heating element (Figure 5.9A) is shown to increase as current is injected through the heating element copper coils (Figure 5.9A). After 839 seconds, the current supply spiked, with the total current delivered increasing from 270 mA to 410 mA for 6 seconds, occurring again after 850 seconds where the current supply increased from 270 mA to greater than 400 mA (and one recording at 680 mA). It is thought that this spiking was the result of connection failure and shorting occurring between the leads carrying current to the heating element. Water was observed (post experiment) within the connection pads between the implant and the current source, and shorting occurring between these pads would have reduced the effective resistance of the heating element, increasing the current supplied (for a constant voltage source) as a result. This would also have increased the power dissipated within the heating element, increasing the retinal tissue temperature as a result.

The temperature measured at the heating element increased above 41°C as a result of the current spiking and the current source was turned off. The secondary current source was turned on at approximately 1000 seconds and increased to 350 mA in attempt to increase the temperature of the secondary heating element sensor (and neighbouring retinal tissue) to 35°C. This heating element was also shown to increase the temperature of the initial heating element sensor (located in the macula) by more than 1°C, increasing with time and following an almost identical response to the peripherally located temperature sensor. It is expected that due to water flowing across the ZIF connection pads during the surgical procedure, the heating elements were partially shorted, and induced identical power dissipations in both of the heating elements

simultaneously. This had the effect of inducing very similar temperature increase profiles as measured by the two sensors at times greater than 1000 seconds.

It is interesting that there was no increase in temperature measured at the site of the secondary heating element when the primary heating element was turned on, yet the opposite effect was seen when the secondary heating element 2 was turned on, inducing a temperature increase in the primary heating element. It is thought that additional shorting between these sensors could have occurred after the current spiking, with the two traces having similar behaviour after 1000 seconds. Baseline temperatures measured after the heating phase were 33.3°C and 34.1°C for the peripheral and centrally located sensors respectively and within 0.1°C of the initial baseline temperatures. This was also indicated by other sensor measurements made using the DMM with temperatures shown to decrease slightly to an overall average of 34.46±0.06°C with a maximum difference of 0.6Ω (0.16°C) between the sensors. The ability of the sensors to accurately measure temperature increases and baseline measurements was shown, and although additional work needs to be performed to ensure that any shorting that occurs within the connections through water contamination during the surgical procedure is properly removed.
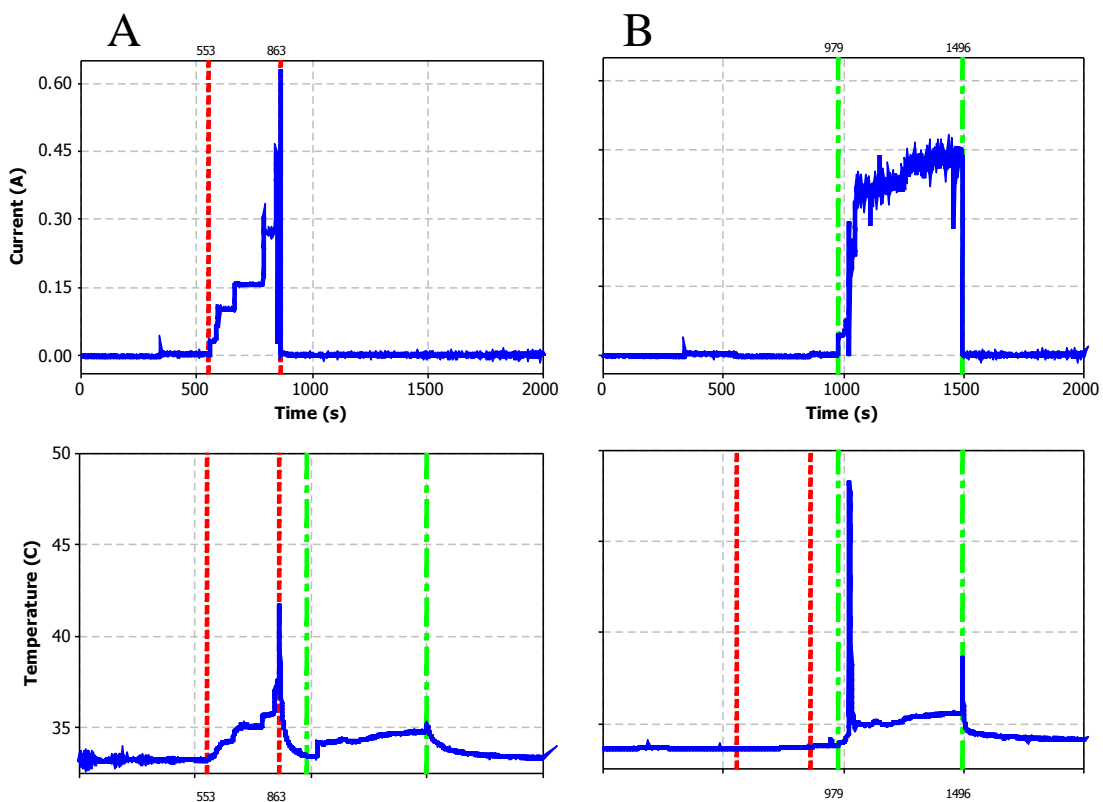
Figure 5.9. Measured tissue temperature and current induction through the **(A)** primary and **(B)** secondary heating elements. Red trace (from 553 to 863 seconds) represents time where primary heating element was switched on and green traces (979 to 1496 seconds) representative of the duration the secondary heating element was dissipating thermal energy.

5.3.3 Histological Results

Results using Fluoro-Jade C (FJC) were poor for both the positive control (rd1-mouse) and cat retinal tissue. Only a very small number of cells were stained with FJC and these were not considered to be representative of retinal damage. Using potassium to enhance the binding of the stain to damaged neurons also produced negative results, with no FJC staining noticeable for either the degenerated mouse retinal tissue samples or those from the thermal heating experiments.

Similarly, no results were observed using GFAP as a staining technique due to the large amount of mechanical trauma and the over-fixation of the tissue that occurred as a result of perfusion. This method of staining has been confirmed through immunofluorescence of retinal degeneration mice (data not shown) and is expected to be a good indicator of thermal insult in tissue that has not been severely damaged through surgery. Problems occurred during the fixation process, with large amounts of the fixative and solution exiting through the lungs. This is thought to have affected the ability of the tissue to be properly fixed, and hence may have impeded the stains from binding effectively. The enucleation of the control eye was achieved without surgical damage occurring although a small accidental incision in the tested eye caused a complete global collapse.

While gross mechanical trauma is expected to be one of the primary factors hindering the ability to visualise damaged neurons, other methods of analysing thermal damage will be assessed such as morphological changes occurring to microglia.

5.4   DISCUSSION

5.4.1   Pilot Test I

The initial pilot study clearly indicated that the implant, while suitable for fixed cadaver tissue, was not suitable for implantation into a living cat retina. The ability to accurately determine whether the implant was positioned on the retinal tissue layer was obscured by a large amount of blood pooling in the orbital cavities and it was unclear whether the blood had been a result of the initial vitrectomy or from the implant damaging the retinal tissue during implantation.

While having an implant able to induce temperature elevations in five separate 5×5 mm areas would drastically reduce the number of animals required for thermal heating experiments, the risk of excessive bleeding and gross mechanical damage rendering the histological data useless was deemed too great to continue with the multiple epiretinal implant design.

With the eye being open (cornea, lens and vitreous humor removed), the intraocular pressure of the eye decreased significantly, causing the eye to fold and collapse upon itself during the surgical procedure. The ability to restore the retinal shape through injection of balanced salt solution was limited, and the mechanical trauma caused by the retinal detachments is expected to have been significantly greater than any thermal damage measured. Due to the loss of intraocular pressure (and hence a reduction in the size of the scleral opening) the multiple heating element implant (SMR − 4) was badly damaged upon insertion. The loss of almost all the lead wire attachments that connected the measurement and current induction equipment to the implant was caused as solder pads detached from the polyimide substrate. This was not observed in cadaver trials where the fixation process stopped the retinal tissue from detaching and collapsing.

With a smaller number of larger tracks, and larger, repositioned solder connection pads, the potential for mechanical failure observed through connection wire breakage or detachment of the pads was greatly reduced. The manipulation of the implant was also reduced with the smaller implants, and these factors led to reduced mechanical damage and the ability to separate and determine the thermally induced damage.

The stereotaxic frame caused additional difficulty in performing retinal surgery and an inability to perform full body perfusion prior to enucleation, outweighing the benefits of maintaining a fixed head position.

There were no foreseeable problems with the high resolution temperature measurement system which was rechecked and calibrated after the experiment. Temperature measurements, while erroneous, were caused due to shorting and breakage of the leads, with the measurement system itself not requiring any alterations.

The large amount of retinal damage reduced the ability of the tissue to be used for histological analysis. Analysis performed using Fluoro-Jade C as a marker for degenerated and damaged retinal neurons was not shown to be feasible.

5.4.2 Pilot Tests II and III

Upon insertion of the array (CC – 2) in the second pilot trial, mechanical damage was caused to the lens when touched by the implant and the lens became immediately cloudy with cataract formation. This reduced the ability of the implant to be visualised through the front of the eye and a lensectomy was required to be performed using the vitrector. As the lens is much harder that the vitreous fluid, the ability to remove the lens using the vitrector was difficult and a partial corneal detachment was required for complete frontal lens removal.

Once the corneal wound was sutured, visibility of the implant location through the front of the eye was regained. Through the process of lens removal, the retinal tack had detached from the retina and a large retinal tear had formed, reducing the ability of this eye to be appropriate in measurements of thermal damage.

The nitrogen gas used by the vitrectomy machine to pump balanced salt solution into the eye to maintain intraocular pressure ran out and consequently the eye began to collapse upon itself. This removed the possibility of using the opposite eye to implant the heating element and sensor array, with the initial experiment finishing prematurely.

Confirmation of the ability to maintain intraocular pressure using a vitrectomy machine was gained, although the requirement for additional and backup nitrogen is required. The removal of the lens through a corneal incision reduced the intraocular pressure and made maintenance of the retinal integrity difficult which is not expected to occur in

future experimentations with the lens being removed via the ultrasonic vitrectomy. Bleeding caused when the cornea was incised will also be avoided using this method.

It is expected that the retinal detachment observed by excessive force applied to the implant while the lens was being removed, with the retinal tack pulling the retina away from the sclera. This indicated the ability of the retinal tacks to attach the implant to the retinal tissue, although care must be taken to ensure that the implants are not overly manoeuvred once anchored. The size of the implant appeared adequate and both heating elements could fit within the eye with retinal tacks sufficient to anchor the implant onto the retinal surface.

The second *in vivo* experiment using a multiple heating element design (CC − 2) was performed with similar surgical techniques to the previous trial. Again, the use of the vitrectomy machine in conjunction with a smaller implant reduced the potential for retinal detachments to occur as the eye collapsed with the intraocular pressure maintained through infusion of balanced salt solution. Using the ultrasonic vitrector to remove the lens enabled the implants to be properly inserted and laid on the retinal surface, allowing the implant to be monitored visually through the cornea.

The primary difficulty encountered in this study involved the sealing of the wound through which the implant was inserted. The infused balanced salt solution was continually expelled through the opening, with reductions in the perfusion rate causing a loss of intraocular pressure and collapse of the globe. A combination of superglue and heavy liquid was used to stop the fluid being expelled whilst maintaining ocular integrity. By drilling small holes through the polyimide implant substrate, sutures could be threaded through the implant, reducing the size of the wound and reducing the ability of fluid to flow out of the eye.

It appears that increased perfusion will act to stabilise the temperature of the retinal tissue to avoid thermal damage from occurring. The tissue temperature increased by 1.82°C due to the passing of 156.55 mA of current through the copper coil heating element, equivalent to a power of 78.43 mW. An additional 158.07 mW (115.28 mA) was needed to heat the tissue an additional 0.66°C, suggesting that some inherent mechanism came into place that increased the removal of thermal energy dissipated into the retinal tissue. While more tests need to be conducted to further investigate the potential of choroidal perfusion in removal of induced heat, this data is suggestive that regulatory mechanism will assist to reduce thermal damage.

Unfortunately, due to the condition of the tissue that was used for histological processing, damage could not be observed with either Fluoro-Jade C or GFAP. Thermal

damage can be observed in rat retinal tissue through analysis of microglial morphological techniques, and it is suggested that this method be employed to analyse retinal damage occurring in cat tissue after acute heating in an *in vivo* setting.

5.5 CONCLUSIONS

Acute, *in vivo* cat retinal tissue experiments were designed to investigate the thermal damage occurring to retinal tissue as the result of power dissipation through an inserted implant.

These trials showed the feasibility of the electrical equipment to accurately and reliably monitor and measure temperatures and temperature increases within the eye. Implants, designed to have multiple simultaneous heating elements (of similar size to current retinal prosthesis chips) were implanted epiretinally. The small implants (with two heating elements) were observed to be well suited for implantation, measurement and recording of cat retinal tissue temperatures.

Surgical procedures were greatly improved from the initial trial, with the use of vitrectomy machines and ultrasonic equipment showing promise in the removal of the lens and vitreous fluid. Infusion of balanced salt solution maintained the ocular integrity and avoided retinal detachments occurring through loss of intraocular pressure. The use of additional suture holes through the implant shaft are expected to greatly reduce the size of the wound required for implant insertion and will assist in ensuring the eye can be quickly and appropriately sealed.

Thermal measurements of the retina correlated well with saline bath trials using identical heating elements up to a temperature of 2°C (<100 mW), at which point a compensatory mechanism came into place to reduce the temperature increase for a given power dissipation. It is possible that this was caused by an increase in choroidal perfusion, removing thermal energy dissipated from the heating element. The tissue temperature was observed to increase by 2.48°C due to a power dissipation of 236.5 mW (increasing by 43 mW/°C up to 2°C, then at a rate of 150 mW/°C to 2.48°C).

In each of the tests, a high level of damage was caused mechanically, both through the surgical implantation, explantation and the fixation process. As a result, measurements of thermal damage could not be obtained using Fluoro-Jade C or GFAP.

To enable determination of the thermal damage thresholds of retinal neurons, additional tests will be required. To enable a larger number of experiments to be performed, analysing responses over a range of experiments, a more accessible animal will be used. Rats will be investigated as an animal model, and while the dimensions of their eyes will not allow the implantation of heating elements of similar size to retinal prosthesis,

the ability to conduct numerous tests over a wider temperature range will be investigated. These tests will look at morphological alterations occurring to microglial cells as a method for damage determination, to assist in ensuring retinal prosthesis are thermally safe.

6

IN VITRO RAT RETINAL TISSUE STUDIES

This chapter investigates thermal damage caused by a heating element implanted *in vitro* in rat retinal tissue, assessing thermal damage thresholds through immunofluorescent analysis of alterations occurring to microglia morphology. Mechanical trauma, caused through the implantation of a heating element and temperature sensor, was also assessed and shown to exacerbate microglia responses to thermal stress. By correlating the power dissipated by the implanted heating element with the resulting temperature increase and microglia response observed, a power budget, designed to assist retinal prostheses architects in ensuring implants do not induce thermal damage was derived.

Results showed that the first observable indication of thermal stress occurred as an increase in microglia soma areas. Incubation tests (tests involving thermal damage without the implantation of a heating element) indicated that soma areas would increase from a baseline size of 26.1 μm^2 to 42.1 μm^2, with a 50% damage threshold (a size of 34.1 mm^2) occurring at a temperature of 37.2°C. The incubation tests indicated a higher 50% temperature response for observable alterations occurring to arbour area (40.2°C). This higher temperature response is expected to be caused in part due to the sensitivity of the equipment, with observations performed looking at retraction of the larger branches rather than the many fine dendritic processes which were often difficult to observe using 20× magnification.

In thermal damage tests (performed with an implanted heating element dissipating thermal energy directly into the neighbouring tissue), soma areas, increasing at rates of

up to 0.21 m^2/mW, were first observed to increase above control (plus one standard deviation) in the peripheral ganglion cell tissue. This was observed at a temperature of 37.9°C (a temperature increase of 2.54°C), correlating to a power of 31.91 mW (power density of 23.46 mW/mm^2). Due to a large amount of mechanical damage caused by implantation of the heating element and sensor, soma areas in the central ganglion cell layer (directly beneath the heating element) were always greater in size than same temperature controls, with damage observed to be exacerbated when thermal insult was combined with mechanical trauma.

A correlation between microglia response from tissues subjected to increased temperature in a heat bath and tissue subjected to increased temperature through dissipation of thermal energy by an implanted heating element, indicated that mechanical damage induced an increase in soma area by at least 20% at all temperatures (baseline increase from 26 μm^2 in control tests to above 30 μm^2 in implanted tissue).

Cell counts were performed to analyse whether microglia migration was present, with the largest increase of 7.38 cells/mm^2/°C occurring in the central outer plexiform layer. However, this was not shown by two-sided t tests to be statistically significant.

This study indicates the importance of ensuring mechanical trauma through surgical implantation of a retinal prosthesis is kept to a minimum, especially when coupled with thermal stress such as power dissipation from the prosthesis chip. While there is no assurance that alterations in microglia morphology directly relate to neuronal damage (cells may restored or repaired and not permanently damaged), the ability to use alterations in morphology to indicate very early cellular responses to thermal stress can be of great assistance in ensuring the viability of neurons when eyes are implanted with retinal prosthesis.

6.1   INTRODUCTION

In vitro rat retinal tissue experiments were performed to ensure that a permanently implanted epiretinal neuroprosthesis, which dissipates power by implanted circuitry to electrical stimulate retinal neurons, operates at a temperature or power budget that is safe. Experiments were designed to investigate the threshold temperatures that induced retinal tissue damage, comparing the induced temperature elevations with power dissipated by an implanted heating element to provide power budgets to retinal prosthesis architects.

The four test categories used to investigate thermal and mechanical damage caused to rat retinal tissue immersed in a heat bath included control tissue (no thermal or mechanical stress), tissue subjected to thermal damage, tissue subjected to mechanical trauma and tissue subjected to both mechanical and thermal stressors. Mechanical trauma of tissue was induced by the insertion of a passive implant, in similar location (macula) to that of current epiretinal prosthesis designs. Thermal trauma was induced by the passing of current through the implanted heating element, with tests investigating thermal damage in the absence of mechanical damage inducing thermal stress through increased heat bath temperatures.

In vitro rat retinal tissue studies were performed because of the similarities that are present between rat and human retinal tissue. Both types of tissue have similar photoreceptors, interneurons (bipolar, horizontal and amacrine cells) and ganglion cells, with the primary difference between the two eyes being the size. A list of the size differences between human eyes (Liou and Brennan 1997; Oyster 1999) and rat eyes (Hughes 1979) are listed in Table 6.1, with the thermal damage results from these experiments expected to form a reasonable approximation of the amount of thermal energy that could damage retinal neurons and to help enhance and optimise acute and chronic studies performed on larger eyes.

Unlike the experiments performed *in vivo* on cat retinal tissue, the use of rats enabled many more studies to be performed and allowed a much larger number of temperatures to be investigated and repeated. While there are obvious differences in size and a smaller implant was required, the ability to assess many different types of stains and analysis methods over a larger range of temperatures was highly beneficial in the determination of thermally induced trauma.

TABLE 6.1. COMPARISON BETWEEN RAT AND HUMAN EYES

Key Measures	Human Eye	Rat Eye
Cornea to sclera length (mm)	24.00	6.29
Retina to lens length (mm)	16.78	1.40
Width (mm)	28.00	6.41
Aqueous volume (μl)	260.0	13.6
Vitreous volume (μl)	5200.0	54.4
Retinal subtense (μm/deg)	300	59
Retinal arc (mm)	51.0	10.6
Retinal area (mm^2)	1024	52

To determine the extent of thermal damage, analyses of microglia morphology were performed using immunofluorescence to visualise changes to microglial cells located in the ganglion cell and outer plexiform layers. These cells, which mediate immune tissue protection against infection and neuronal insult, have a small cell soma and a number of fine, branched processes that are covered in numerous protrusions (Lee, Liang et al. 2008; Rasohoff and Perry 2009).

Microglia are highly sensitive to environmental changes, rapidly altering their phenotype in response to even minor disturbances of nervous system (and retinal) homeostasis caused by infection, disease, inflammation, thermal stress and trauma (Kreutzberg 1996; Chen, Yang et al. 2002; Davalos, Grutzendler et al. 2005; Nimmerjahn, Kirchoff et al. 2005; Hanisch and Kettenmann 2007; Langmann 2007; Ransoff and Perry 2009; Santos, Martin-Oliva et al. 2009). Activation of microglia is associated with alterations in cellular morphology, tissue distribution, migratory characteristics, process structure and expression of cell surface antigens (Suzumura, Marunouchi et al. 1991; Soltys, Ziaja et al. 2001; Zhang, Lam et al. 2005; Hanisch and Kettenmann 2007; Lee, Liang et al. 2008; Ransohoff and Perry 2009), with morphological alterations observed in activated microglia including the retraction of processes, a loss of fine protrusions and an increase in soma area (Soltys, Ziaja et al. 2001; Davalos, Grutzendler et al. 2005; Zhang, Lam et al. 2005; Lee, Liang et al. 2008).

Measurements of microglial soma areas, arbour areas (area surrounding the microglia soma including dendritic branches and protrusions) and the ratio between the soma and arbour areas were investigated. Cell counts were also used as a tool to investigate changes occurring to thermally and mechanically damaged retinal tissue.

6.2   METHODS

Determination of thermal damage thresholds was performed *in vitro* using twelve week old Sprague Dawley Rats. Thirteen rats (26 retinae) were used to investigate the effects of incubation of retinal tissue on microglial response, immersing retinal tissue in heat baths at various temperatures. A total of eight rats (sixteen retinae) were used to investigate microglial response to mechanical trauma under normal temperatures and a further fourteen rats (28 retinae) were used to determine microglial responses to both mechanical and thermal insults.

6.2.1   Surgical Procedure and Experimental Set-Up

After the rats were weighed, they were anaesthetised with an injection of Ketamine (5 mg/kg) and Xylasine (60 mg/kg) in a 12:1 ratio, prior to sacrifice with a lethal overdose of Lethabarb. Both eyes were enucleated with the aid of a surgical microscope, using scissors to sever the optic nerve. The cornea, lens and vitreous humor was removed, taking care not to mechanically damage the retinal tissue. In cases where there was a strong bond between the vitreous fluid and the retina, a partial vitrectomy was performed to reduce the possibility of inflicting damage to the retinal tissue during the surgical procedure.

Enucleated eye-cups used in the incubation trials were placed in porous 5 ml containers that had been punctured to allow the movement of fluid. These containers, immersed in the heat bath fluid, ensured there was no direct contact between the tissue and the hot heat bath walls. The heat bath was filled with a solution of Ames' medium (A1420-1L, Sigma-Aldrich, MO, USA) and was bubbled with carbogen (5% CO_2, 95% O_2, BOC Medical, USA) which removed the requirement of a fan or stirrer to uniformly distribute. Control of the heat bath temperature was performed using a dimmer switch to vary the amount of power supplied to light globes surrounding the flask in which the eye-cups were immersed (Chapter 2). The temperature of the heat bath was monitored using an immersed platinum resistance temperature detector (PRTD) connected to a digital multi-meter (DMM) in identical fashion to the cadaver trials (Chapter 4) and *in vivo* cat retinal tissue experiments (Chapter 5).

In the thermal damage trials, water from the heat bath was syphoned into a smaller vessel on top of a commercial plate heater, which was also bubbled with carbogen and measured with a temperature sensor. Eye-cups from control tests were placed directly into the heat bath and allowed to move freely, in contrast to eye-cups used in mechanical control trials (trials where a heating element is implanted but not used) and heated trials (trials where a current was passed through the implanted heating element) that were held in position using a small ring (not shown). The ring enabled the use of a micromanipulator to carefully descend the implant directly into the eye-cup, ensuring a standardised level of depression and placement of the implants across trials. Contact was verified during initial pilot trials, with a distance of 2 mm between the heat bath chamber base and the implant enough to ensure gentle contact was made.

A schematic of the experimental setup (Figure 6.1) displays the position of a control eye-cup freely immersed in the heat bath fluid, a mechanical or thermal damaged eye underneath a micromanipulator-held implant and the carbogen and Ames' medium input and output tubes.
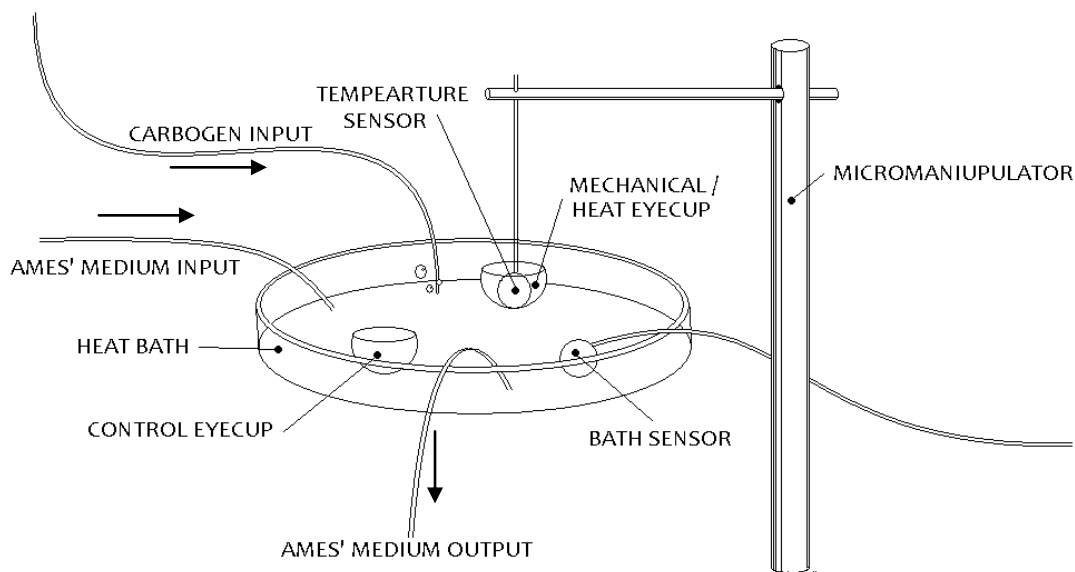
Figure 6.1. Experimental set-up for *in vitro* rat thermal damage tests showing the carbogen gas input and output tubes and the tube syphoning fluid from the custom made heat bath (Ames' medium input) into the heat bath. A free-floating control eye-cup and an eye-cup that has an implanted temperature sensor inserted by the micromanipulator are shown. Measurements from the implanted temperature sensor and the bath sensor are connected to the high resolution temperature measurement system (not shown).

The implant, inserted into the mechanical control and heated eyes, was constructed by attaching a 0603-size, 20Ω surface mounted resistor to one of the platinum resistance temperature detectors. Shorting was avoided by a thin layer of conformal coating, with the two 1.6×0.85 mm SMD components connected to form a cross. A final thin coating

of silicon was applied to ensure water resistance, with the implant thus able to induce thermal elevations in the constraints of the rat-retina while measuring thermal increments in real time. A schematic of the implant used in the *in vitro* rat trials is shown in Figure 6.2.

The PRTDs were attached to the high resolution temperature measurement system, with the heating elements attached to a current supply (discussed in Chapter 2). Calibration of the re-designed implants was performed, with changes in lead wire resistance having a negligible effect on temperature measurements.
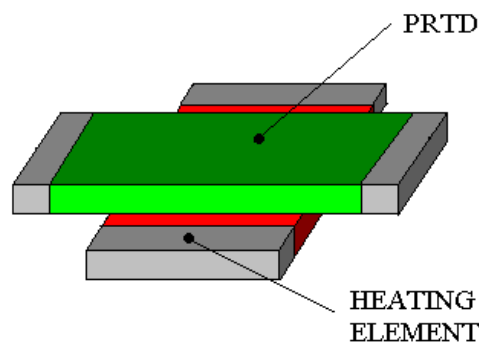
Figure 6.2. Implant used to deliver power (heating element) and measure temperature (PRTD) during *in vitro* rat retinal tissue tests. Conformal coating for water resistance and lead wires connecting the heating element to the current source and the PRTD to the high temperature measurement system are not shown.

Through pilot trials, it was noticed that the temperatures measured by micromanipulator-held sensors were strongly influenced by their immersion depth within the heat bath, with cooler measurements recorded when the sensors were closer to the room temperature air at the waters' surface. Subsequently, trials were performed after water had filled the heat bath to the point of overflowing.

6.2.2   Experimental Protocol

Prior to recording of temperatures and induction of current through the heating element, tissues were given at least 15 minutes to equilibrate to the temperature of the heat bath.

For the incubation trials, the desired heat bath temperature was obtained prior to immersion of the eye-cups. Tissues were then immersed within the heat bath for at least forty minutes with the heat bath temperature recorded at one second intervals. After the period of heating, tissues were removed for histological processing.

Eye-cups used in the heated trials were also immersed in a stabilised heat bath of a desired temperature. A fifteen minute baseline tissue temperature was recorded prior to the onset of any thermally induced energy dissipation, which lasted for at least forty minutes, similar to incubation trials. A final five minute baseline temperature was measured and the eyes were removed from the bath.

6.2.3   Immunofluorescence

Once the thermal experiments had been completed, the eyes were fixed for 30 to 40 minutes in 4% paraformaldehyde (4% PFA) to ensure that any damage that had occurred would be accurately maintained. The process of making 4% PFA, used to fix all rat retinal tissues, involved dissolving four grams of paraformaldehyde powder in 50 ml of dH_2O and spinning on a low heat within a fume hood. Two drops of 2M NaOH was then add, with spinning continued until the solution went clear. 50 ml of 0.2M phosphate buffer (PB, made by mixing 86.84 g di-sodium hydrogen orthophosphate ($Na_2HPO_4.7H_2O$), 10.48 g sodium phosphate monobasic ($NaH_2PO_4.H_2O$) and 2L dH_2O) was add and spun until the solutions were fully mixed.

The retinal tissues were immersed in 4% PFA prior to being washed in 0.2M phosphate buffer, three times for ten minutes each wash. Tissues were then sucrose protected to stop any remaining water from expanding and damaging the tissue while freezing. This process involved the washing the rat eye-cups for one hour in a 10% sucrose solution, followed by one hour in a 20% sucrose solution and an overnight wash in a 30% solution. Eye-cups were then frozen and thawed thrice, to enable easy removal of the retinal tissue from the sclera. Any vitreous fluid remaining in the eye was also removed to enhance the binding of the primary and secondary antibodies.

After another wash ($3\times$ 10 minutes in PB), the retinal tissue was immersed in a 50 µl 1:5000 dilution of primary antibody (IBA-1) in a primary antibody buffer. The primary antibody buffer used was made by dissolving 600 µl of 3% normal goat serum and 0.2 g of 1% bovine serum albumen into 17.4 ml of 0.1M PB, by stirring on low heat, prior to the addition of 2 ml of 0.5% TritonX-100. The retinal tissues were left in this solution for three days and re-washed before a secondary antibody (gt α rb 594, also mixed with the primary antibody buffer in a 1:800 ratio) was applied to the retinal tissue and left overnight.

6.2.4 Analysis

Once the staining was complete, the retinal tissue was flattened, mounted on polysine coated slides and carefully covered with slide covers to avoid trapping air bubbles. On the majority of tissue, the retina was flattened by making three incisions from the edge of the eye-cup towards the optic disk, splitting the eye into thirds.

6.2.4.1 Measurements of Microglial Areas

One 392×392 µm confocal photograph was taken in each of the thirds near the optic disk (central location) and taken between the optic disk and the edge of the eye-cup. Photos were taken both centrally and peripherally to enable microglia morphological changes caused by thermal and mechanical damage from directly underneath the heating element (centrally) and in the ganglion cell layer not in contact with the implant (periphery) to be distinguished. Photographs from cells taken in the incubation trials were not split according to central and peripheral regions, as the tissue in each of these layers was assumed to be the same.

Microglia images were observed using a Carl Zeiss Kaser Scanning System LSM 5 PASCAL (Carl Zeiss MicroImaging GmbH). An EC Plan-Neofluar 20X/0.5 M27 objective was used to photograph the images, with a 561 nm 21% wavelength through a 575 nm low pass filter with a 120 µm pinhole used to observe the fluorescent microglia. Six photos (three central and three peripheral), consisting of ten to fifteen slices each, were taken. These slices were separated into the ganglion cell layer and the outer plexiform layer, and superimposed to produce a single image of all the microglia within that region that was used to investigate thermal damage thresholds.

A quantification of the degree of thermal damage caused to the retinal cells was performed by analysing morphological changes occurring to the soma and the range of extracellular space approximated by the dendritic branches (arbour area). An example of how the soma and arbour area is determined is shown in Figure 6.3, with the green outline representing the soma area and the white line representing the arbour area. Using $20\times$ magnification, many of the very fine processes that sprout off the main dendritic branches cannot be observed. These processes, which greatly increase the surface area of the microglia (as well as the observed space) are not expected to cause large

deviations to the arbour areas measured, as they are often quite short and are expected to be contained within the traces connecting the large dendritic branches. The areas of the soma and arbour were calculated using Zeiss LSM Image Browser 4.2.0.121 (Carl Zeiss MicroImaging GmbH), with the number of pixels within the circumnavigated region indicative of the area. This method is similar to the method published by Slotys and Ziaja (2001), also investigating microglia morphological changes involving alterations in dendritic area.

Microglia soma and arbour areas from each image were averaged and recorded. A comparison between the soma areas, arbour areas and the ratio between the two (soma area divided by arbour area) was used to investigate differences that occurred between retinal tissue induced to thermal damage (incubation trials), mechanical damage (insertion of implant without power dissipation), both (implantation of heating element and power dissipation) and neither (control tissue).
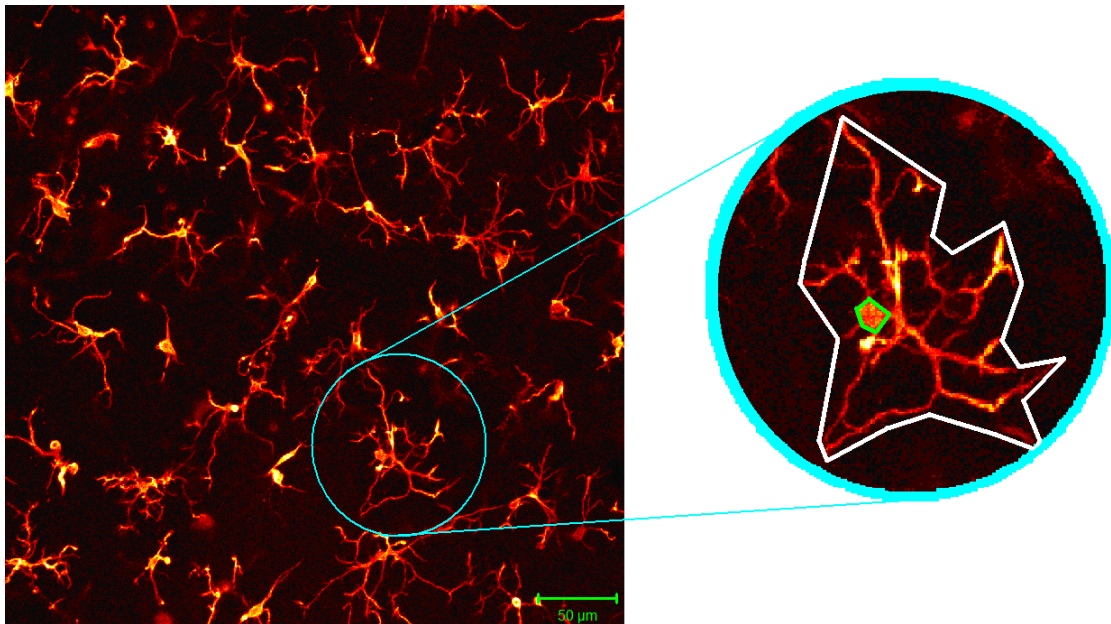
Figure 6.3. An example of a 392 × 392 μm confocal photograph of immunofluorescent microglia from the central ganglion cell region and (inset) a single microglia. The green trace represents the soma area with the white trace indicative of the arbour area.

6.2.4.2 Dose Response Curves

Dose response curves, calculated by GraphPad Prism 5.0.4 (GraphPad Software, Inc.) were used to determine temperature thresholds observed when tissue was subjected to both mechanical and thermal trauma:

$$S = B + \frac{U - B}{1 + 10^{T_{50} - T}} \qquad (6.1)$$

where S is the soma or arbour area (μm^2), as a function of the baseline soma or arbour area, B, (μm^2), the upper soma or arbour area, U, (μm^2), the temperature of the tissue, T, (°C) and T_{50}, the temperature (°C) at which the soma or arbour area was halfway between the basal and upper areas. The dose responses were assumed to have a standard slope (or slope factor) of 1.

Linear fits were used to investigate changes in soma and arbour areas in response to temperature increase, where the areas were related to the temperature difference between the baseline and induced temperatures measured in the tissue. These two tests were used to investigate whether thermal damage was a product of temperature or power dissipated within the tissue.

6.2.4.3 Microglia Cell Counts

The number of microglia within each image and region were counted to determine whether an influx of cells had altered microglial measurements. The number of cells in each 392 μm^2 confocal image were counted and multiplied to produce an average cell density as a number of cells per millimetre square.

For microglial cells to be counted the entire cell soma had to be visible, as did all the major dendritic branches. Cells that had finer processes obscured by the edges of the image were counted on the top and right hand sides only, if it appeared that the majority of the cell was within the image. All cells that were counted were also used in microglial analysis of soma and arbour area.

6.3 RESULTS

Results from the incubation tests as well as tests that investigated thermal and mechanical thresholds through implantation of the constructed heating elements are discussed in this section. These tests also investigate whether tissue temperature or thermal energy dissipation (temperature increase) is responsible for thermal damage. As well as investigating microglial changes occurring to soma area and dendritic span (arbour), the number of cells within each image is also analysed to investigate movement of microglia towards affected regions.

6.3.1 Incubation Tests

Incubation tests, performed by heating rat retinal tissue in a heat bath, were used as control to determine the response of microglia to thermal insult without mechanically induced trauma (though implantation of a heating element). An example of microglial images from incubation trials with a low temperature heat bath ($<34.0°C$) and a high temperature heat bath ($43°C$) is shown in Figure 6.4, with inserts showing the arbour and soma areas of individual microglia.

Measurements of soma area, arbour area and the percentage ratio between the soma and arbour areas are listed in Table 6.2 from each of the incubation trials.

Table 6.2. Temperatures, soma and arbour areas and the ratio between the soma and arbour areas for all incubation tests, shown as an average for all microglia measured from each image, and each set of images performed at each temperature

Temperature (°C)	Number		Area (μm^2)		Ratio (%Soma/Arbour)
	Rats	Images	Soma	Arbour	
<31.0	2	10	25.68±6.9	1951±318	1.31±0.26
31.0 – 31.5	2	9	25.04±5.1	2042±257	1.26±0.39
31.5 – 32.0	3	13	24.07±4.1	1933±352	1.26±0.20
32.0 – 34.0	2	9	29.46±8.1	2104±246	1.43±0.47
34.0 – 37.0	4	22	30.83±3.1	1887±254	1.66±0.25
37.0 – 40.5	2	9	40.47±2.5	1651±140	2.47±0.26
>40.5	2	5	43.34±6.8	1410±199	3.12±0.64
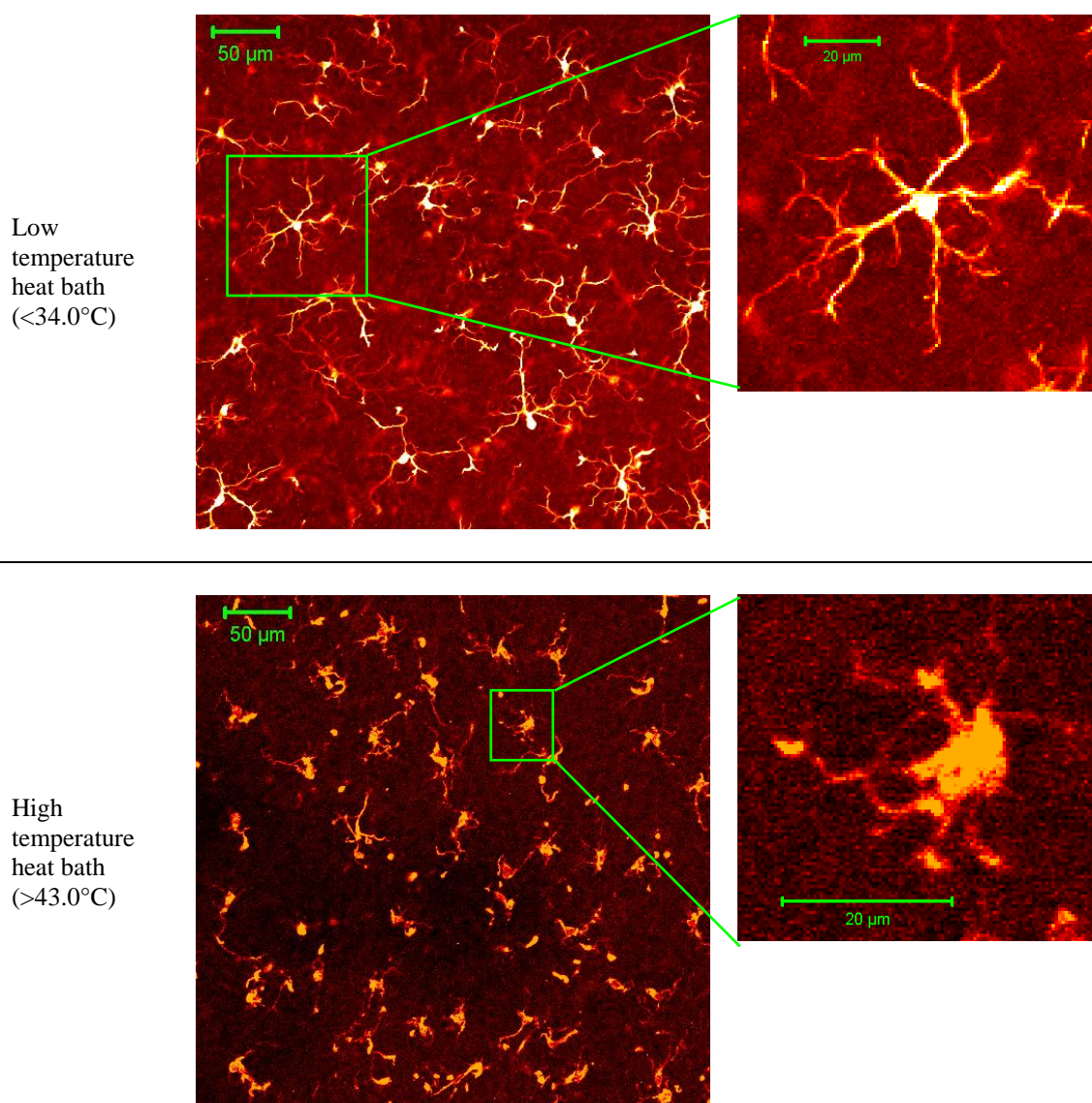
Figure 6.4. Confocal images of microglia from incubation tests performed with a low temperature heat bath (<34.0°C) and a high temperature heat bath (>40.5°C) with inserts displaying individual microglia. Scale bars for images are both 50 μm with scale bars for inserts both 20 μm

The average soma areas obtained from these trials, with heat bath temperatures ranging from 30.3°C to 43.1°C, are shown in Figure 6.4. Data points from experiments with heat bath temperatures below 35°C are indicative of the average soma area from at least three images taken per retina, with error bars indicating the total standard deviation between all measured microglia. At heat bath temperatures above 35°C, multiple rats were used at each temperature, with the average and error bars calculated as the average and standard deviations obtained from all measurements. A red dose response curve was fit to the data (with error margins indicative of 95% confidence intervals), showing microglia soma areas increasing from a basal soma area of 26.1±3.4 μm^2 to a maximum (upper plateau) soma area of 42.1±4.8 μm^2. The T_{50} threshold temperature (where the

soma area was 34.1 μm^2, half way between the basal and upper limits) was calculated at a heat bath temperature of 37.2±0.9°C. The R^2 value for the incubation soma area dose response curve was 0.9362, with an absolute sum of squares of 23.53. The standard error for the basal, upper and T_{50} values are 1.213 μm^2, 1.717 μm^2 and 0.33°C, respectively.
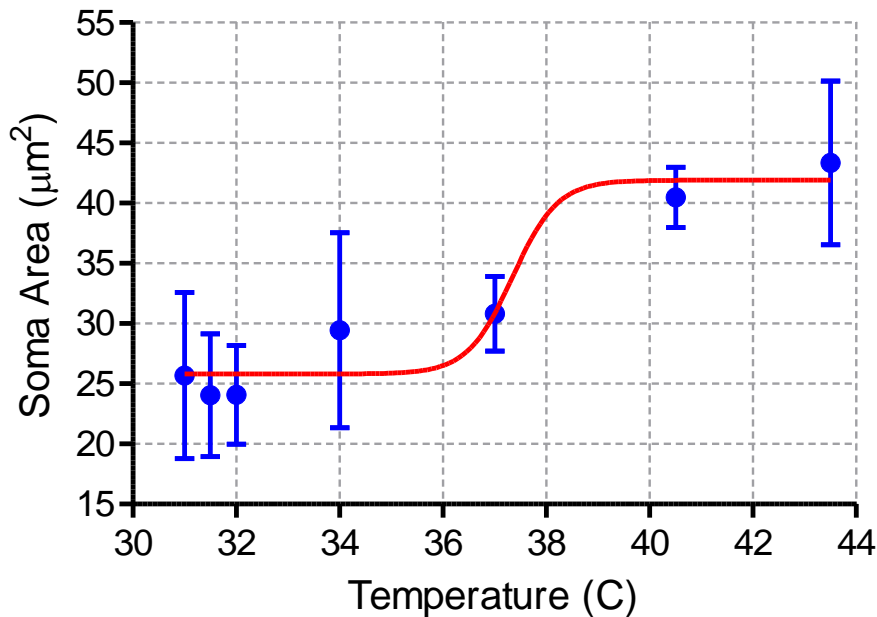
Figure 6.5. Soma area as a function of heat bath temperature with data points and error bars indicative of average microglia soma areas and standard deviations across all images. Red line represents the calculated dose response curve.

Results from incubation trials investigating the spread of dendritic branches (arbour area) is shown in Figure 6.5. The dose response curve (red line) shows a decrease in microglia area from a baseline plateau of 1973±152 μm^2, reaching a minimum size of 1410±216 μm^2 at temperatures greater than 42.5°C. The T_{50} temperature for microglia arbour area was calculated at 40.2±1.6°C, 3.0°C higher than that observed from the soma area response. The R^2 value calculated by GraphPad Prism was 0.8634, with an absolute sum of squares value of 48208. Standard errors for the basal, upper and T_{50} values are 54.91 μm^2, 77.71 μm^2 and 0.58°C, respectively.
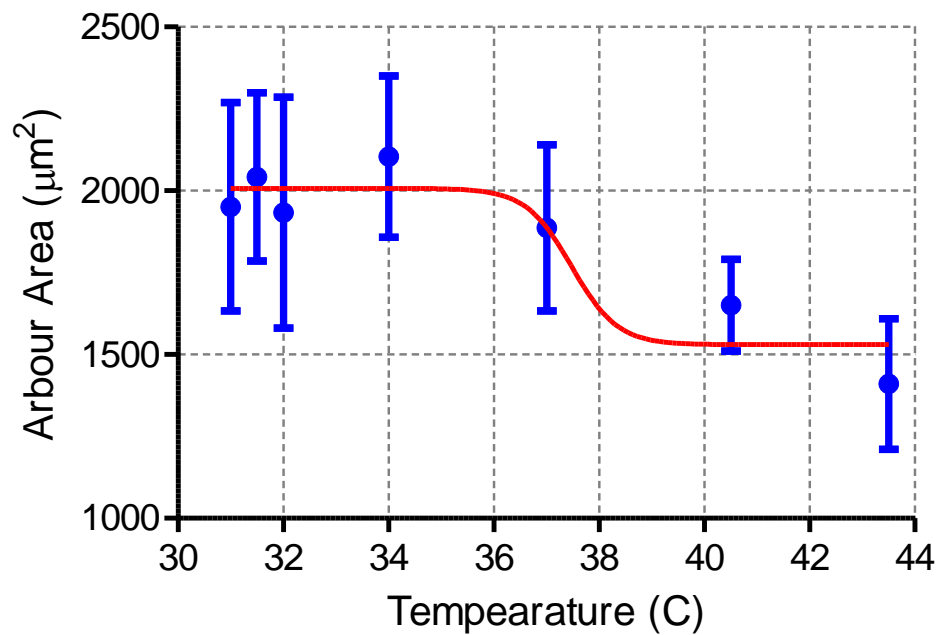
Figure 6.6. Arbour area as a function of heat bath temperature with data points and error bars indicative of average microglia arbour areas and standard deviations across all images. Red line represents the calculated dose response curve.

Results comparing the ratio between the soma and arbour areas indicate the soma area increases from a basal limit of 1.35±0.22% of the arbour area to an upper limit of 3.12±0.47%, with a T_{50} threshold occurring at 40.2±0.6°C. A graphical representation of all the averages is shown in Figure 6.7, with the thick red line indicative of the calculated dose response. Calculations of the R^2 and absolute sum of squares values are 0.964 and 0.114, with standard errors of 0.08%, 0.17% and 0.21°C for the basal, upper and T_{50} thresholds, respectively.

The values calculated for the T_{50} temperatures suggest that microglia response will initially be observable through increases in soma area (a T_{50} temperature of 37.2°C) and that this will occur earlier than alterations in arbour areas (a T_{50} temperature of 40.1°C). It is expected that this is due to the magnification used to analyse microglia, with many of the fine processes not visible. The retraction of the smaller dendritic protrusions (sprouting of the major branches) would have occurred at lower temperatures than those required to induce retractions of the larger branches, although the exact temperature at which this occurs is unknown.
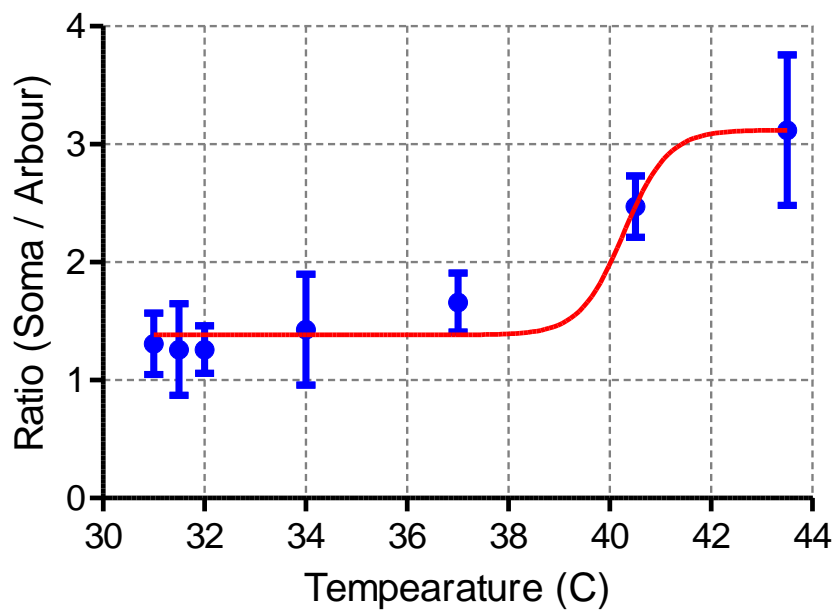
Figure 6.7. Arbour area as a function of heat bath temperature with data points and error bars indicative of average microglia arbour areas and standard deviations across all images. Red line represents the calculated dose response curve.

6.3.2 Thermal Heating Trials

The thermal heating trials investigated the effect of mechanical and thermal trauma on microglial response, aiming to determine thermal damage thresholds for implanted retinal tissue. These tests investigated and compared damage that occurred through power dissipation into neighbouring tissue with damage that occurred mechanically through the implantation of a 'switched off' heating element and under a 'pure' control situation, where no heating element was implanted. An example of control and mechanical control images taken from the central ganglion cell layer are shown in Figure 6.8.

In the control images, the microglial cells have large dendritic arbours, with the microglia able to observe a large region of the extracellular medium. These processes retract, and are shown to be smaller in the presence of mechanical pressure and further reduced in the presence of mechanical trauma and thermal stress (heating tests). The soma area is also relatively small in the control image, although can be seen to increase as mechanical pressure is applied and further as both mechanical and thermal trauma is inflicted upon the retina.
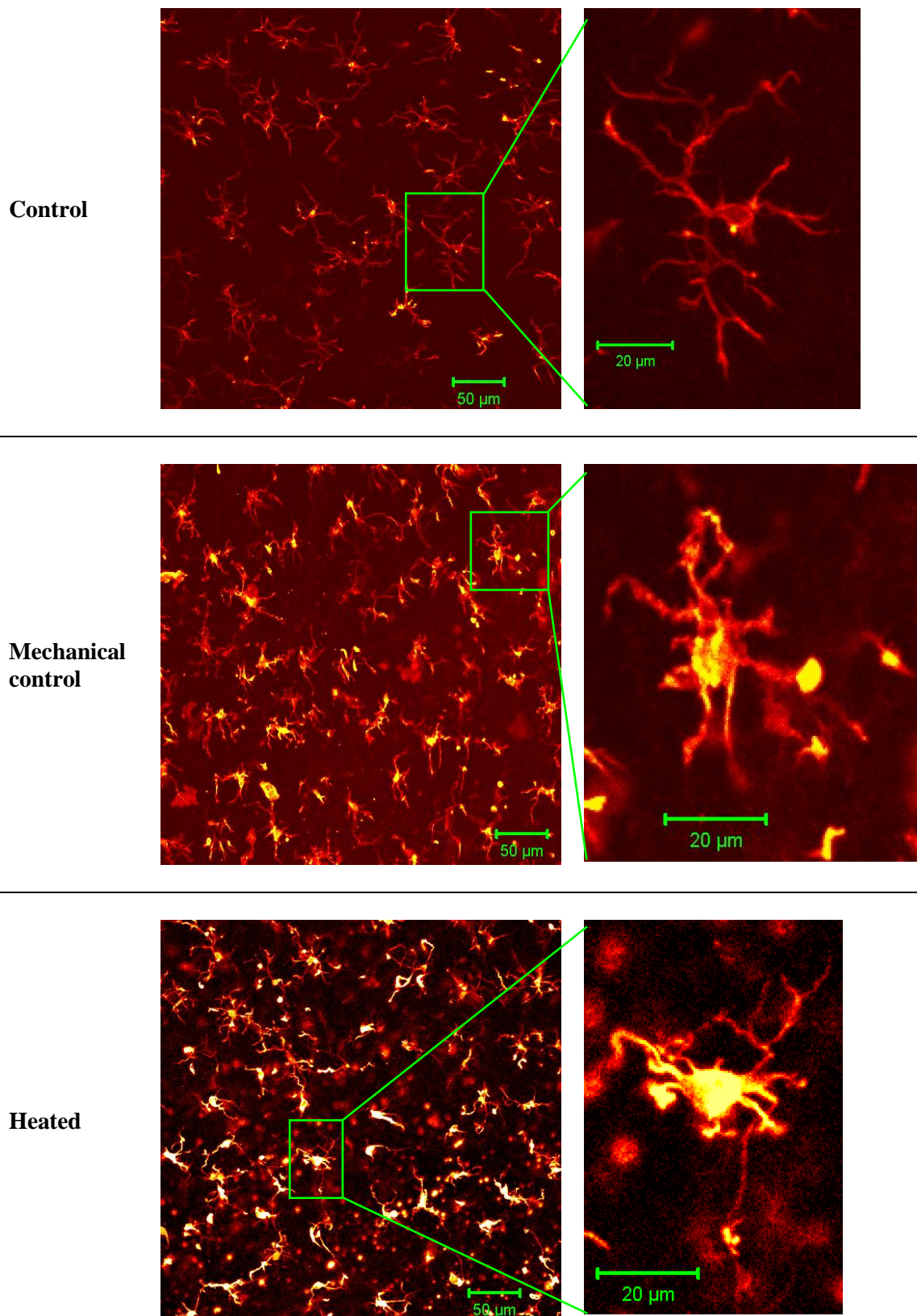
Figure 6.8. Microglial images from control, mechanically damaged and heated tests taken from the central ganglion cell layer (scale bars are 50 μm). Inserts magnify a single microglia from each of the images (Scale bars all represent a 20 μm distance).

6.3.2.1 Microglia Soma Area

The test number and the tissue temperature for the control tests (both pure and mechanical control) are listed in Table 6.3. The control tissue temperatures are taken as the average bath temperature in the case where multiple bath measurements were recorded. Bath temperatures ranged from 30.3°C to 36.4°C between tests, with a 0.37°C maximum temperature difference observed over the course of any hour long recording. Results from all tests are listed in Appendix 6.

Table 6.3. Test numbers and tissue temperatures for all control and mechanical control trials

Test Number	Bath Temperature (°C)		Tissue Temperature (°C)	
	Bath 1	Bath 2	Control	Mechanical
Test 1	31.00±0.29	-	31.00±0.29	-
Test 2	30.38±0.14	-	30.38±0.14	27.55±0.17
Test 3	33.58±0.34	-	33.58±0.34	-
Test 4	33.24±0.17	27.41±0.04	30.32+0.10	28.36±0.09
Test 5	31.19±0.21	31.77±0.23	31.48±0.22	-
Test 6	31.49±0.26	31.99±0.24	31.74±0.25	29.83±0.16
Test 9	32.19±0.19	31.70±0.18	31.95±0.19	30.90±0.11
Test 13	36.39±0.19	-	36.39±0.19	32.84±0.19
Test 14 A	36.76±0.31	-	36.76±0.31	-
Test 14 B	36.76±0.31	-	36.76±0.31	-
Test 16 A	36.31±0.24	-	-	34.64±0.27
Test 17 B	35.99±0.14	-	-	32.87±0.11

A graphical representation of all averaged microglia (from each image) for the control, mechanical control and heated tests (irrespective of induced temperature) for each of the four regions is shown in Figure 6.9.

There was no significant difference between soma areas in the central and peripheral ganglion cell layers (p=0.135) or central and peripheral outer plexiform layers (p=0.699) in the control images using two-sided t-tests. This was similar for the ganglion cell layer (GCL) and outer plexiform layer (OPL) microglia in the central region (p=0.294) and the GCL and OPL microglia measured in the periphery (p=0.723), indicating that in the control tissue, the soma areas are not dependant on location or layer. There was also no difference between the microglia soma areas in the OPL when comparing mechanical and control tissues at either the central (p=0.564) or peripheral regions (p=0.162), or between soma areas in the ganglion cell layer centrally (p=0.012) or peripherally (p=0.055).
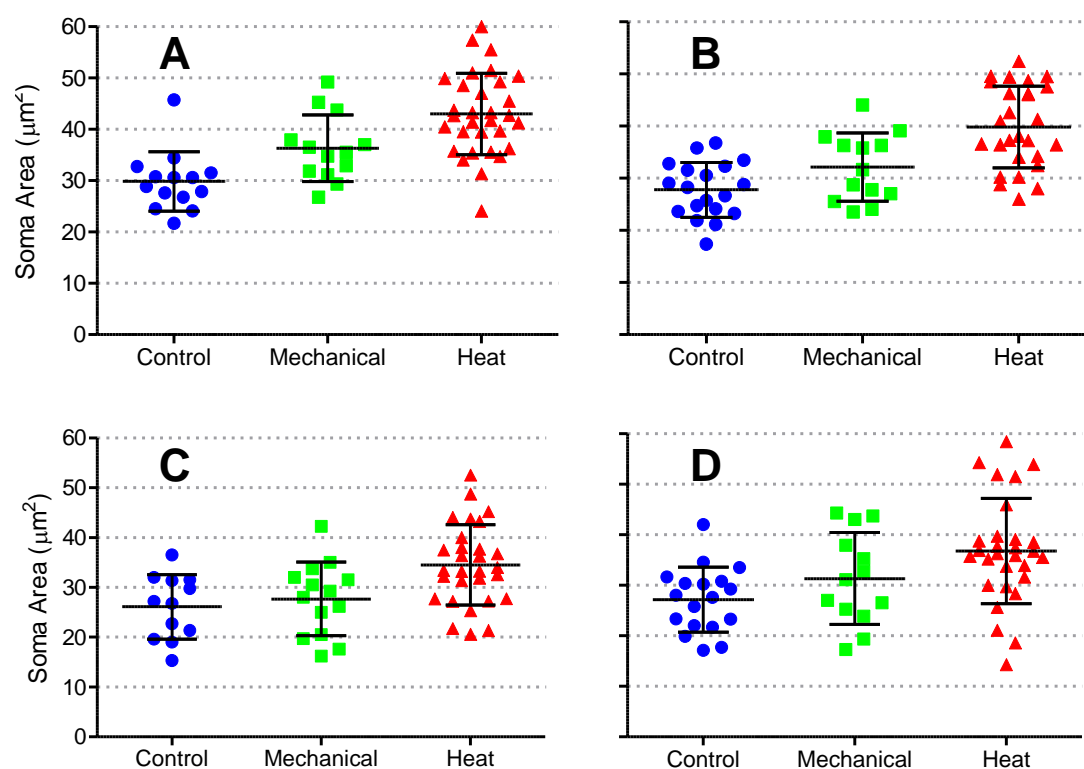
Figure 6.9. Soma areas for control, mechanical and heated test images taken from the **(A)** central ganglion cell layer, **(B)**, peripheral ganglion cell layer, **(C)** central outer plexiform layer and **(D)** peripheral outer plexiform layer for each test type irrespective of bath or induced temperature. Mean and standard deviations are shown in black.

The average microglia soma areas from all of the images taken in either the central or peripheral ganglion cell layers (GCL-C and GCL-P respectively) or in the central or peripheral outer plexiform layers (OPL-C and OPL-P respectively) are listed in Table 6.4. This table indicates the increase in soma area (from control) due to mechanical damage, increasing further when mechanical trauma is coupled with thermal insult. This occurred to the largest degree in the central ganglion cell region where cells were in direct contact with the implanted heating element. It is expected that due to the size of the heating element, the peripheral regions would also have been affected by mechanical trauma (although to a smaller degree) and this is shown as an increase above control for all mechanical soma areas in the peripheral regions. In each case, the microglia soma area is largest for the heated trials and smallest for the control tissues measured.

There was a statistically significant difference between the soma areas from the heated and control tests ($p < 0.005$) and the heated and mechanical tests ($p < 0.005$), but not between the mechanical and control tests ($p = 0.012$) in the central ganglion cell layer. This was also the case in the peripheral GCL (GCL-P), where the heated tests were

significantly different (p<0.005) when compared with the mechanical and control trials, although there was no significant difference (p=0.055) when comparing the two types of control (pure control and mechanical control).In the peripheral cell layer, there was only a significant difference between microglia soma areas between the control (pure) and heated, with no difference seen between the control and mechanical or mechanical and heat.

Table 6.4. Average microglia soma areas for control, mechanical control and heated *in vitro* experiments

Test	Average Soma Area (µm^2)			
	Ganglion Cell Layer		**Outer Plexiform Layer**	
	Central	Peripheral	Central	Peripheral
Control	29.8±5.8	27.8±5.3	26.1±6.5	27.1±6.6
Mechanical	36.3±6.5	32.3±6.7	27.7±7.4	31.3±9.1
Heat	43.3±8.4	39.8±7.8	34.5±8.4	36.8±10.4

Using a two-sided t-test to compare the control and heated trials indicated that there was a significant difference (p<0.005) for all regions (GCL-C, GCL-P, OPL-C and OPL-P). There was a statistically significant difference (p<0.005) between the mechanical trials and the heated trials in both the ganglion cell layers (GCL-C and GCL-P), although no significant difference within the microglia soma in the outer plexiform layers, in either the central (p=0.021) or peripheral (p=0.123) regions. This could be representative of a large amount of mechanical damage occurring in these layers, hiding any thermally induced damage. In each of the locations, there is a larger (than control) microglial response caused by mechanical damage, which is exacerbated when mechanical and thermal damages are combined in the heat trials.

6.3.2.1.1   Thermal Response

To investigate whether the microglia soma area size increase is related to the amount of thermal energy dissipated in the tissue (a temperature increase) or by the absolute temperature of the tissue, a temperature dependant soma area analysis was performed. Figure 6.10 indicates the average soma area at each induced temperature, with error bars relating to the standard deviation between the average image microglia areas measured. The control soma area (and standard deviation) is indicated by a blue dot (and blue error bars) with the green dot (and green error bars) indicative of the average soma area measured from the mechanical damage trials.
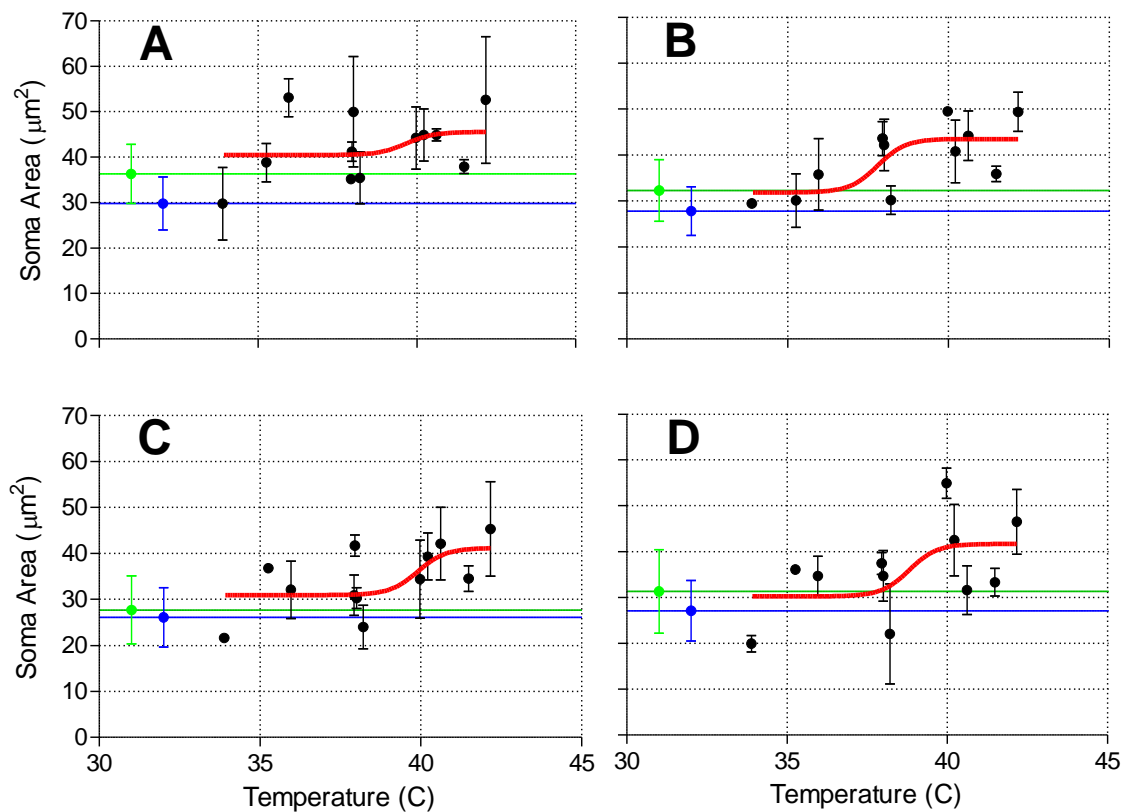
Figure 6.10. Average microglia soma area as a function of tissue temperature for **(A)** central ganglion cell layer, **(B)** peripheral ganglion cell layer, **(C)** central outer plexiform layer and **(D)** peripheral outer plexiform layer. Green and blue lines and error bars are indicative of mechanical control and control averages and standard deviations. Red line represents the calculated dose response.

The dose response curve upper, lower and T_{50} values are listed in Table 6.5 indicating that the soma areas will not increase indefinitely with increasing heat with all tests producing similar upper limits (between 41 and 46 μm^2). There is a reasonable amount of difference between the temperatures at which a 50% increase in microglia soma area occurs, with T_{50} values occurring between 37.80°C in the peripheral ganglion cell region and 39.67°C in the central ganglion cell layer. It should be kept in mind that these temperatures are relative to temperature measurements taken by the sensor at the optic disk and thus temperatures measured in the peripheral regions (GCL-P and OPL-P) are lower than those measured by their central counterparts. Figure 6.11 shows the response curves fit to each of the four regions with all curves (except for the GCL-C) having similar basal area and upper areas.
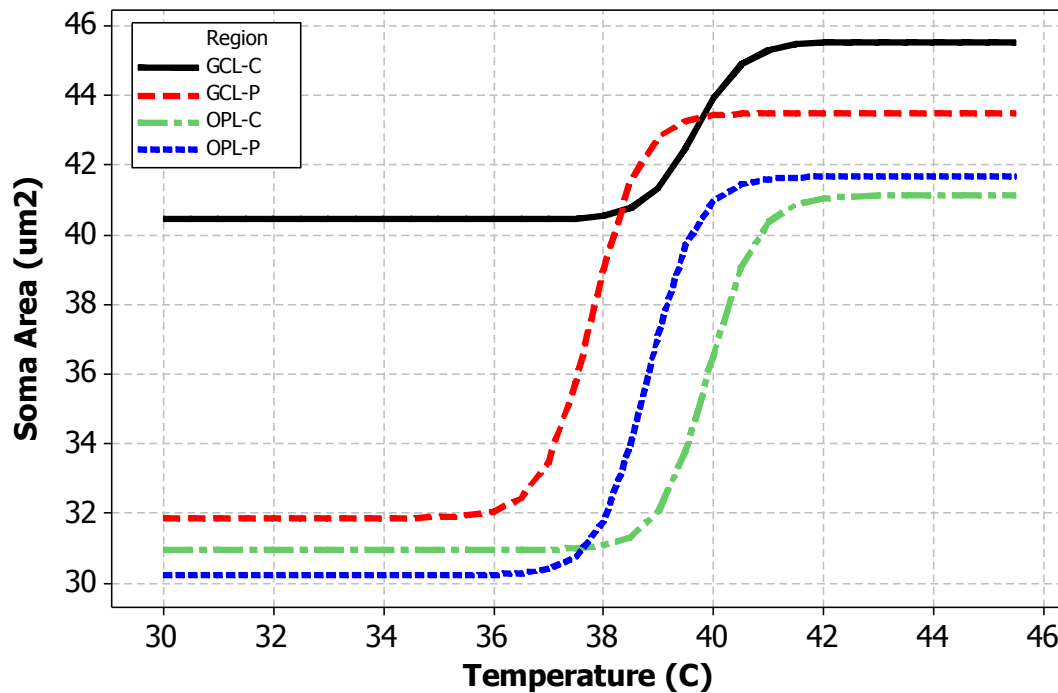
Figure 6.11. Response curves for heated *in vitro* microglia central ganglion cell (GCL-C), peripheral ganglion cell (GCL-P), central outer plexiform (OPL-C) and peripheral outer plexiform (OPL-P) soma areas.

The control threshold temperatures (temperature in which the soma size was greater than the average control size plus one standard deviation) are listed in Table 6.5. This data provides the first insight into temperatures which induce thermal damage, with temperatures very similar to the T_{50} temperatures obtained from the dose response curves. There was no threshold temperature for the GCL-C, with the equation predicting soma areas always greater than the control mean plus one standard deviation. This indicates that soma areas have already increased above the control threshold due to mechanical trauma caused by implant insertion.

The mechanical threshold temperatures where the soma areas were observed to be greater than one standard deviation above the average mechanical soma area are listed in Table 6.6. These areas suggest that the first temperatures at which a response that is not caused by mechanical trauma is observable is 39.96°C in the central ganglion cell layer. In cases with less mechanical damage (such as in the plexiform layers or peripherally), thermal damage requires an additional 0.13°C (GCL-P) to 1.38°C (OPL-C) to be observable (taken as the difference between the mechanical and control thresholds).

Table 6.5. *In vitro* microglia soma area dose response curve parameters and the temperature and area thresholds for heated test soma areas to increase above the control and mechanical averages plus one standard deviation

	Parameters	Region			
		Ganglion Cell Layer		Outer Plexiform Layer	
		Central	Peripheral	Central	Peripheral
Dose Response	Basal soma area (μm^2)	40.5	31.9±3.6	31.0±2.4	30.2±5.2
	Upper soma area (μm^2)	45.5	43.5±2.7	41.1±4.5	41.7±2.0
	T_{50} temperature (°C)	39.7	37.8±0.7	39.9±1.0	38.8±2.0
	R^2 Value	-	0.4549	0.3661	0.2964
Control	Threshold area (μm^2)	-	33.1	32.6	33.7
	Threshold temperature (°C)	-	37.9	39.2	38.5
Mechanical	Threshold area (μm^2)	42.8	39.0	35.1	40.4
	Threshold temperature (°C)	40.0	38.0	40.6	39.1

6.3.2.1.2   Thermal Increase Response

Analysis was also performed to determine whether the increase in microglia soma areas was related to energy dissipation (temperature increase) as opposed to an absolute temperature. These graphs, shown in Figure 6.12, indicate an increase of soma area with increasing temperature, with the largest response (steepest gradient) observed within the GCL-P region. All cases (with the exception of region GCL-C) also have a zero response soma area (temperature increase of 0°C) within the standard deviation of the control trials.

The threshold temperature increases above the control average (plus one standard deviation), listed in Table 6.6, were calculated using the linear fit equations. Again, there was no control threshold for the GCL-C region, with the linear interpolation predicting microglia soma areas greater than the control average plus one standard deviation for all positive temperature increases. The lowest threshold was observed for the peripheral ganglion cell region, increasing above control (plus one standard deviation) soma area at a temperature increase of 2.54°C.

The threshold temperature increases above mechanical damage averages (plus one standard deviation), also listed in Table 6.6, could be calculated for all the regions including the central ganglion cell layer. The lowest threshold was observed at 5.35°C for the peripheral ganglion cell layer.

Figure 6.12. Average microglia soma area as a function of temperature increase for **(A)** central ganglion cell layer, **(B)** peripheral ganglion cell layer, **(C)** central outer plexiform layer and **(D)** peripheral outer plexiform layer. Green and blue lines and error bars are indicative of mechanical control and control averages and standard deviations. Red line represents the linear fit.

Table 6.6. *In vitro* microglia soma area linear response curve parameters and the temperature and area thresholds for heated test soma areas to increase above the control and mechanical averages plus one standard deviation

		Region			
		Ganglion Cell Layer		**Outer Plexiform Layer**	
	Parameters	Central	Peripheral	Central	Peripheral
Linear Fit	Gradient (μm^2/°C)	0.40±1.08	1.93±0.92	0.85±1.04	1.59±1.41
	Zero response (μm^2)	40.1+6.4	28.7±5.3	29.8±6.1	27.2±8.3
	R^2 value	0.138	0.323	0.650	0.121
Control	Control threshold area (μm^2)	-	33.1	32.6	33.7
	Threshold temperature increase(°C)	-	2.54	3.30	4.10
Mechanical	Threshold area (μm^2)	42.8	39.0	35.1	40.4
	Threshold temperature increase (°C)	6.70	5.35	6.23	8.32

The steepest slope related to the GCL-P region, suggesting that microglial cell somas would increase the most in this region for a given temperature increase measured at the optic disk (where the heating element-sensor was implanted). The GCL-C had the lowest slope, although was predominantly above both the mechanical and control

average soma areas which suggests that damage had occurred prior to induction of thermal energy.

The effect of mechanical damage is reiterated in the control threshold temperatures, with smaller temperatures increases required to induce microglial responses in the peripheral regions when compared to control tissue Hence, damage done mechanically can obscure damage caused thermally, with smaller thermal damage required in regions absent of mechanical damage, and more required when mechanical damage is present to induce thermal damage that can be observed.

6.3.2.1.3 Response to Power Dissipation

A linear fit of the effect of power dissipation on the soma areas of microglial cells is shown in Figure 6.13 for all averaged data over each of the four regions investigated. With the exception of the central ganglion cell region, microglia respond to increasing power, observed as an increase in soma area.

The rate of increase for each of the four regions is 0.004, 0.21, 0.13 and 0.18 $\mu m^2/mW$ for the GCL-C, GCL-P, OPL-C and OPL-P regions respectively. This data complements previous data on the effect of thermal energy dissipation in retinal tissue and further reinforces the issue of mechanical trauma obscuring damage caused thermally.
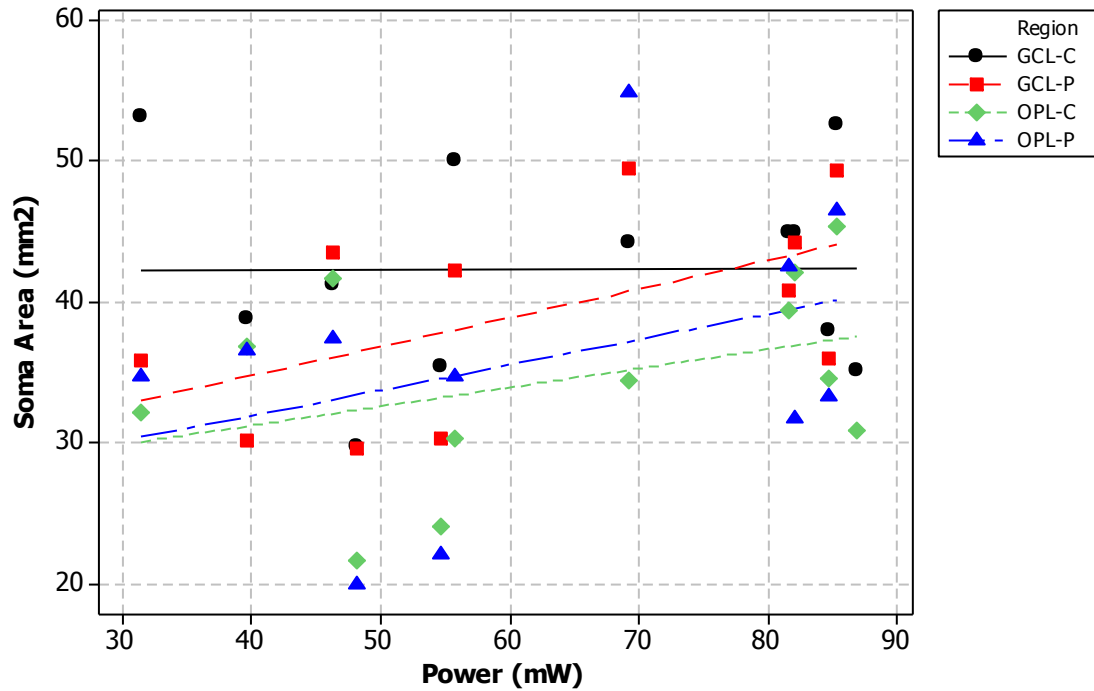
Figure 6.13. Microglia soma area increases as a function of power dissipated through the heating element for the central and peripheral, ganglion and outer plexiform layers (GCL-C, GCL-P, OPL-C, OPL-P) respectively

6.3.2.2 Microglia Arbour Area

While the soma size in activated microglia has been published to increase due to externally induced stress, the opposite has been reported to occur to the arbour area, with dendritic spans decreasing in effective area as processes retract (Kreutzberg 1996; Davalos, Grutzendler et al. 2005; Nimmerjahn, Kirchoff et al. 2005). These processes have also been published to re-orient themselves towards the direction of the insult, although this has not been seen in these experiments, and it is expected that due to the large amount of heat dissipated from a comparatively large heating element, the directionality of the thermal energy is obscure (Davalos, Grutzendler et al. 2005; Nimmerjahn, Kirchoff et al. 2005; Lee, Liang et al. 2008).

The microglia arbour areas for each of the control, mechanical control and heated trial images (irrespective of heat bath or induced temperature) are shown in Figure 6.14. There was no statistically significant difference between the arbour areas when comparing the central and peripheral ganglion cell layers (p=0.385), the central and peripheral outer plexiform layers (p=0.564), the two central regions (GCL-C and OPL-C, p=0.177) or the two peripheral regions (GCL-C and OPL-P, p=0.079) measured from the control tests. There was also no statistically significant difference using two-sided t-

tests between control and mechanical control microglia located in the central ganglion cell regions (p=0.139), peripheral ganglion cell regions (p=0.212) or peripheral outer plexiform regions (p=0.011), although a significant difference (p<0.005) was reported for arbour areas in the central outer plexiform layer.
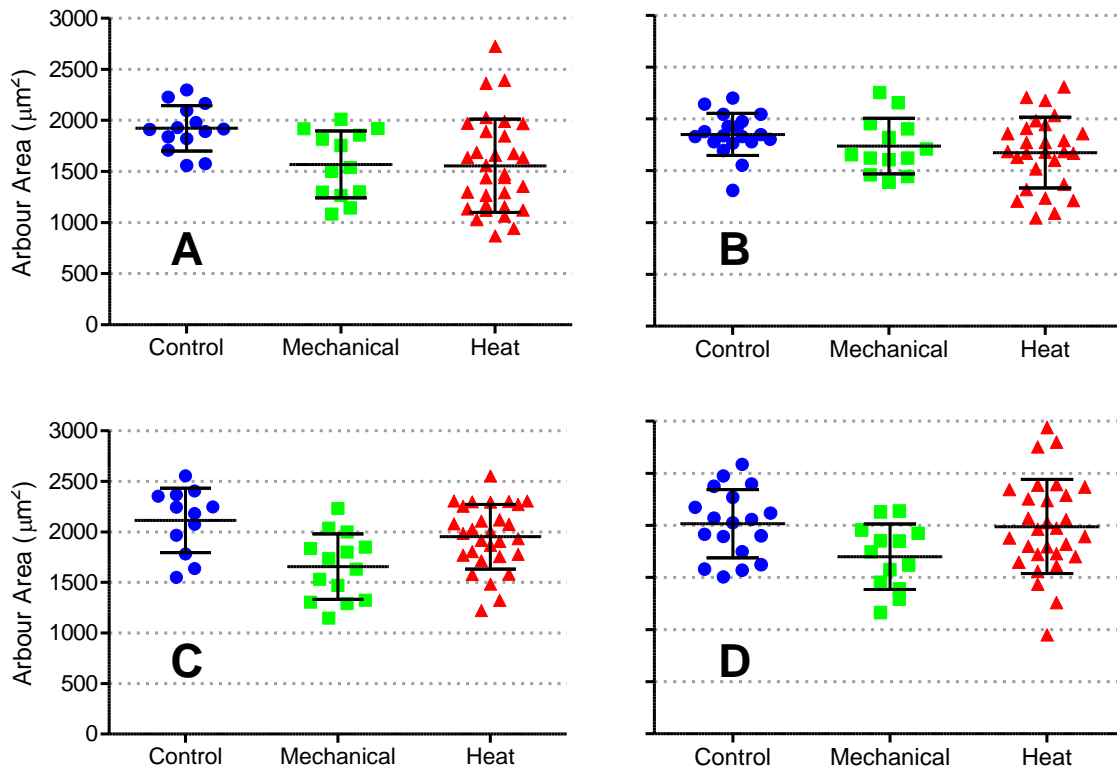
Figure 6.14. Results from measurements of arbour areas for control, mechanically damaged and heated trials taken from the **(A)** central ganglion cell layer, **(B)**, peripheral ganglion cell layer, **(C)** central outer plexiform layer and **(D)** peripheral outer plexiform layer for each test type irrespective of bath or induced temperature. Mean and standard deviations are shown in black.

The only significant difference (p<0.005) between the control trials and the heated trials was within the central ganglion cell layer (GCL-C) with the largest difference between the heat and mechanical control trials was between the two central, outer plexiform layer regions (p=0.006). These results suggest that while there is a poor correlation of difference (p=0.139) within the ganglion cell layer due to mechanical trauma (mechanical GCL-C versus control GCL-C), and a poor correlation (p=0.310) due to heat alone (mechanical GCL-C versus heat GCL-C), the combination of both mechanical trauma and heat exacerbates microglial arbour area changes with a significant difference (p<0.005) occurring between the control and heat tests. There was no clear indication in other layers of microglial activation by looking at arbour area size alone. The average soma areas for the control, mechanical and thermal heat dissipation tests are listed in Table 6.7.

TABLE 6.7. Average microglia arbour areas from control, mechanical control and heated *in vitro* experiments

Test	Average Arbour Area (mm^2)			
	Ganglion Cell Layer		Outer Plexiform Layer	
	Central	Peripheral	Central	Peripheral
Control	1922±222	1852±202	2091±162	2016±327
Mechanical	1646±492	1732±268	1657±324	1700±313
Heat	1556±456	1676±340	1953±320	1989±450

In the ganglion cell layer, the arbour areas are as expected, with microglial activation (in the form of dendritic retraction) occurring due to mechanical trauma and exacerbated by thermal heating. This was also the case in the peripheral ganglion cell layer (to a smaller extent) which could suggest either that the implant was positioned slightly peripherally or that thermal energy from the heating element induced microglial changes preferentially within the ganglion cell layer compared to the outer plexiform layer. With the mechanical damage trials in the outer plexiform regions having smaller average microglia soma areas than the heated trials within the outer plexiform layer, it is possible that the migration of healthy microglia was induced by heating. This would explain why the heated trial soma areas in the OPL regions are similar in area to measurements taken from control tests and larger than the mechanical control tests, although this has not been verified and it is expected that the large variance among tests is the primary reason for this observation.

6.3.2.2.1   Thermal Response

A graphical representation of the average arbour areas from each of the tests and locations is shown in Figure 6.15, to identify whether the area of observed extracellular space is relative to thermal energy dissipated within the tissue. In each of the four regions investigated, there appeared to be no clear dose response correlation or temperature dependence.

The affect of temperature is relatively independent to the arbour areas in the ganglion cell layer, with arbour areas below both control and mechanical ranges (average plus one standard deviation) for temperatures ranging between 34°C and 42°C. In the peripheral ganglion cell layer, a larger majority of tissue temperatures fell within the mechanically damaged range (lower bounds) over the same temperature range. In the outer plexiform layer, the arbour area is still within the mechanically damaged range (although within the upper bounds) and very similar to the control average, with all the data points in the outer plexiform layer within or above the mechanical damage range (and almost all within or above the control range). While this does not give an

indication of a temperature threshold response, it may suggest that microglia location is a factor in morphological change, with larger responses occurring to microglia closer to the source of trauma, initially affecting the ganglion cell layer (centrally greater than peripherally) before affecting the outer plexiform layer (centrally more than peripherally).
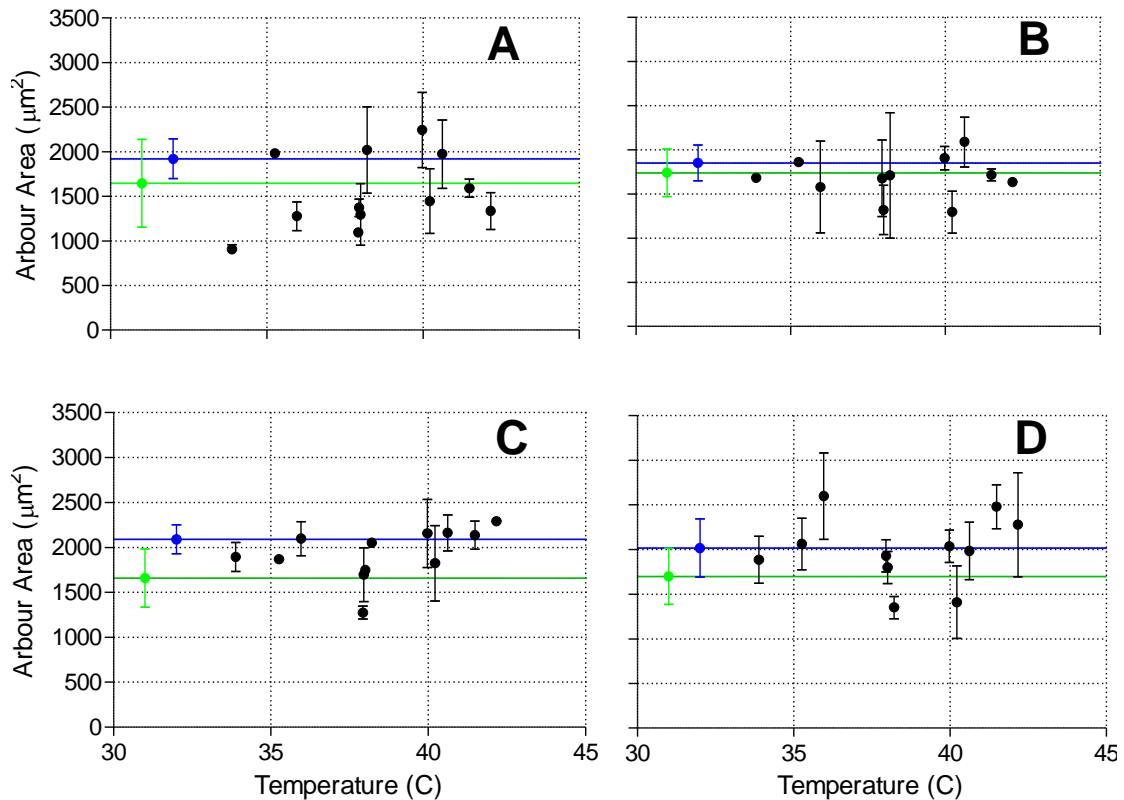
Figure 6.15. Microglia arbour areas as a function of tissue temperature for **(A)** central ganglion cell layer, **(B)** peripheral ganglion cell layer, **(C)** central outer plexiform layer and **(D)** peripheral outer plexiform layer. Green and blue lines and error bars are indicative of mechanical control and control averages and standard deviations.

6.3.2.2.2   Thermal Increase Response

To determine whether a decrease in arbour area seen between the GCL-C regions is dependant on the absolute temperature of the amount of thermal energy dissipated within the tissue, graphical representation of the arbour areas has been plotted against the measured temperature increase. These plots (Figure 6.16) compare the average temperature measured by the sensor implanted in the rat retina, with each point representing the average arbour area from all images measured at each temperature, with the error bars indicative of the standard deviation between images. The green and

blue lines (and error bars) indicate the average (and standard deviation) of the mechanical and pure control trials respectively.
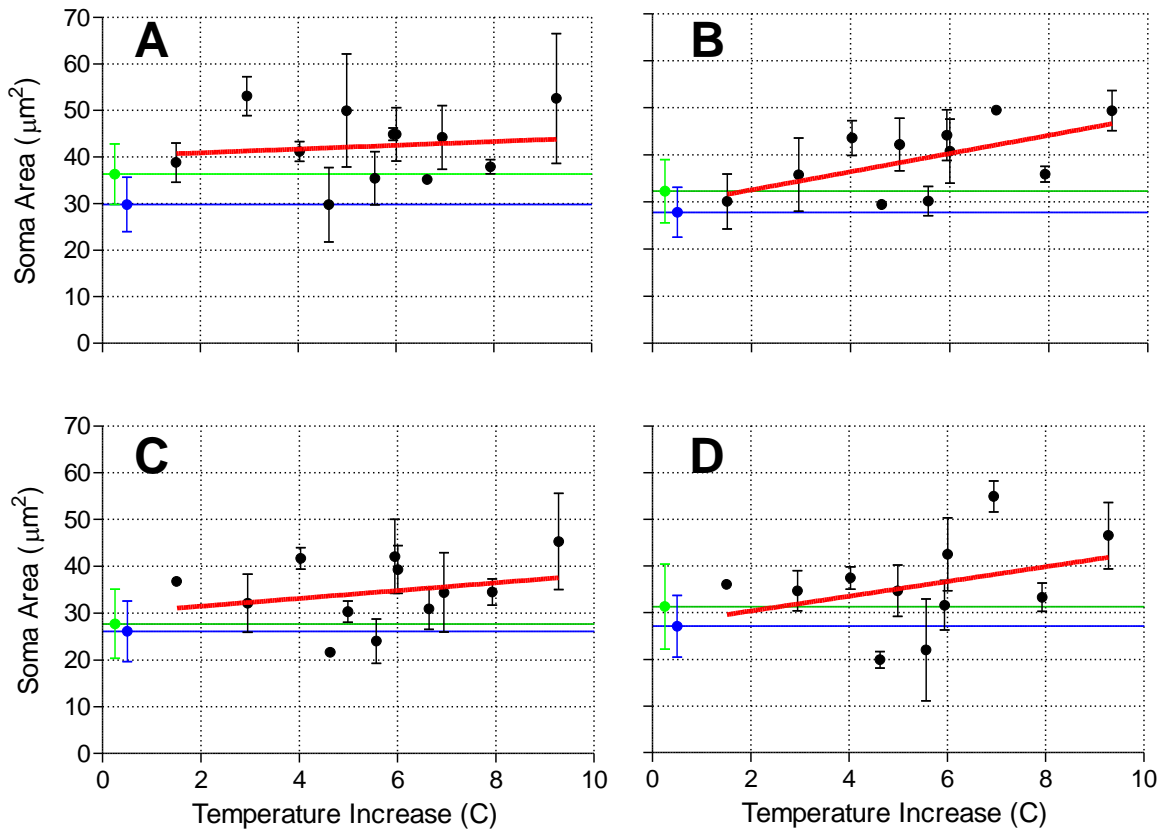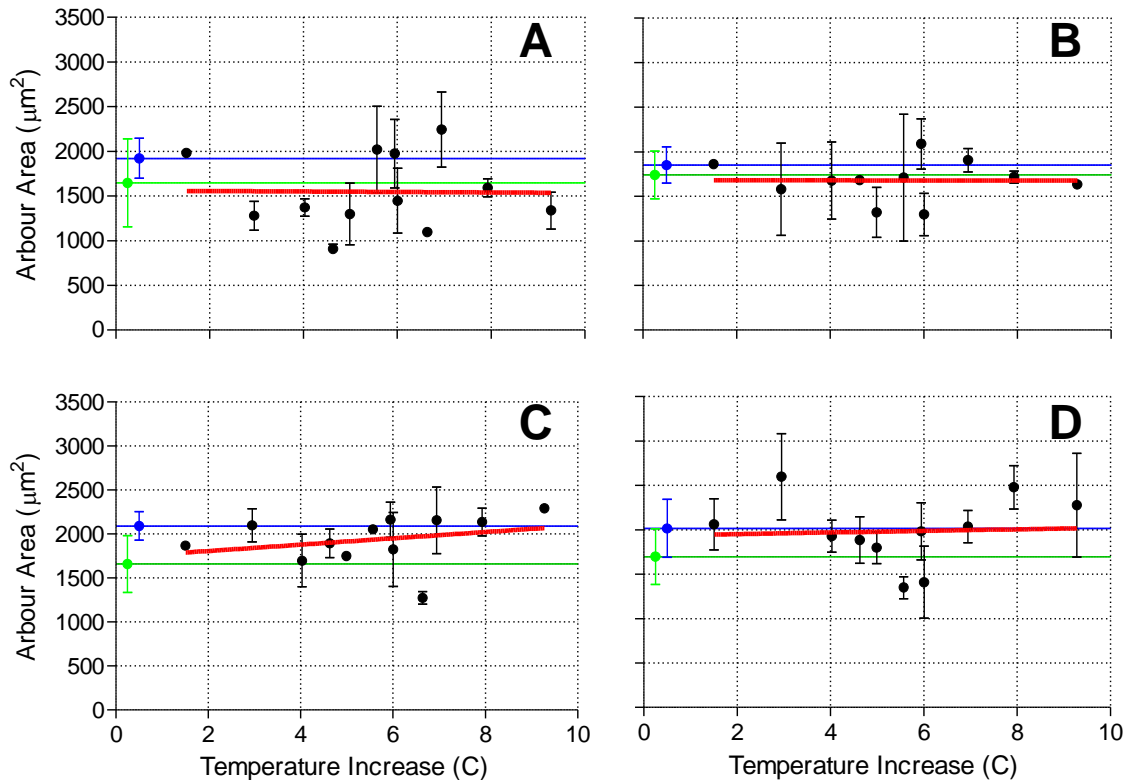

Figure 6.16. Average microglia arbour area as a function of temperature increase for **(A)** central ganglion cell layer, **(B)** peripheral ganglion cell layer, **(C)** central outer plexiform layer and **(D)** peripheral outer plexiform layer. Green and blue lines and error bars are indicative of mechanical control and control averages and standard deviations. Red line represents the linear fit.

In The GCL-C and GCL-P regions, majority of the points are below both the mechanical and control averages with measurements performed in the outer plexiform layer generally between the two (OPL-C) or even above the control (OPL-P).

The linear fits of the arbour areas as a function of temperature, are listed in Table 6.8. The thresholds at which the soma area increased above the mechanical and control ranges has not been shown with microglial arbour areas seemingly temperature independent. In the ganglion cell layer, the microglial soma areas decreased by 2.44 $\mu m^2/°C$ in the central and by 0.80 $\mu m^2/°C$ in the peripheral regions respectively. Both of these trend lines are within the mechanically damaged range (with temperature increases greater than 10°C), suggesting that the difference caused to the arbour areas due to thermal energy is negligible. There was a larger increase in arbour area as the temperature increased in the central outer plexiform layer (contrary to published data on

microglial dendritic areas decreasing due to stresses), increasing at a rate of 25.95 $\mu m^2/°C$.

Table 6.8. *In vitro* microglia arbour area linear fit parameters

Linear Fit Parameters	Region			
	Ganglion Cell Layer		Outer Plexiform Layer	
	Central	Peripheral	Central	Peripheral
Gradient ($\mu m^2/°C$)	-2.437±62.13	-0.799±35.31	25.95±39.86	9.036±58.59
Zero Response (μm^2)	1559+366	1684±207	1734±235	1935±341
R^2 Value	>0.0001	>0.0001	0.0752	0.0026

The ability to assess thermal damage based on morphological changes within microglial arbour areas does not seem viable from the data obtained, with large variability in the areas expected to have arisen through mechanical damage. It is possible that differences microglial arbour areas are the result of slight variations in the amount of mechanical trauma caused to the retinas on implantation rather than the thermal energy that was dissipated within the tissue and thus trials must be performed without implantation induced trauma.

6.3.2.3   Ratio of Soma and Arbour Areas

The ratio between the soma areas and the measured arbour areas was devised to determine whether some regions had inherently larger or smaller microglia. A comparison between all measured data under control, mechanical and heated situations is shown in Figure 6.17 for each of the four tested location irrespective of tissue temperature.

There was no statistically significant difference between ratios measured within the control regions, with two-sided t-tests indicating similarity between within the ganglion cell layer (GCL-C and GCL-P, p=0.500), the outer plexiform layer (OPL-C and OPL-P, p=0.518), the central regions (GCL-C and OPL-C, p=0.045) and the peripheral regions (GCL-P and OPL-P, p=0.219) in the control tissues. There was however, a statistically significant difference between control and mechanical control tests within the two central ganglion cell regions (p<0.005), and to a lesser degree between microglia within the two peripheral ganglion cell regions (p=0.012), and microglia in the outer plexiform region located centrally (p=0.020) and in the peripheral region (p=0.008).
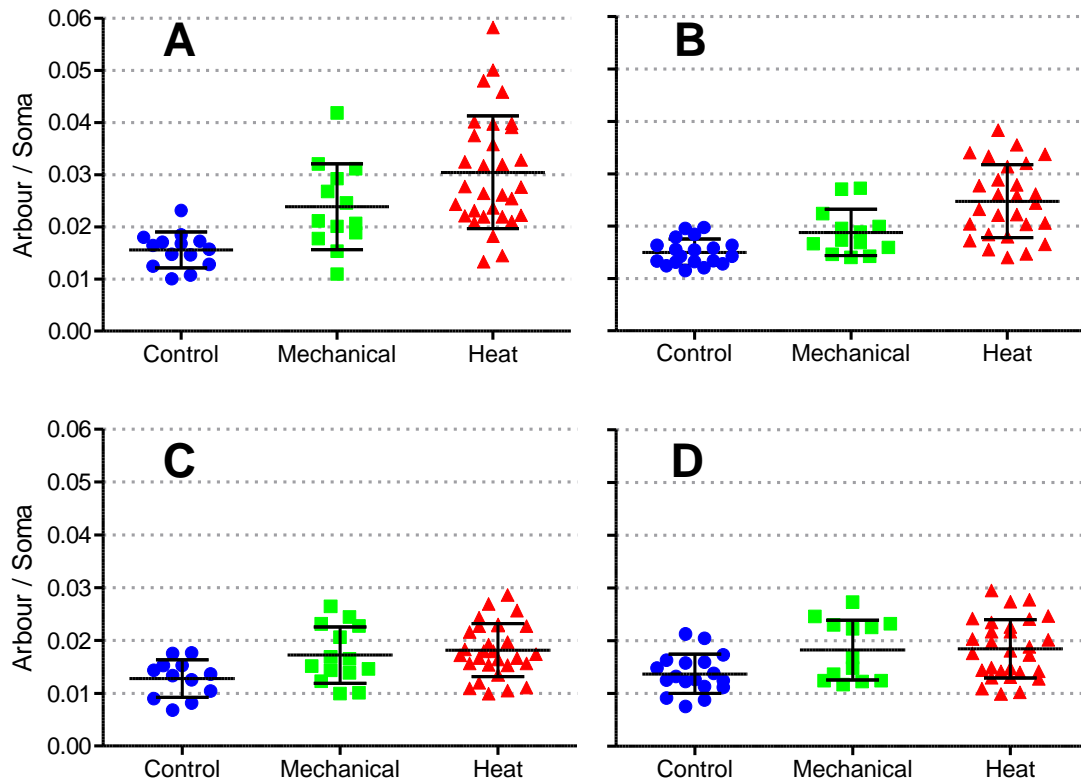
Figure 6.17. Soma areas divided by the arbour areas for **(A)** central ganglion cell layer, **(B)** peripheral ganglion cell layer, **(C)** central outer plexiform layer and **(D)** peripheral outer plexiform layer for each test type irrespective of bath or induced temperature. Mean and standard deviations are shown in black.

Comparing the average results from all tests (irrespective of thermal energy dissipation) shows statistically significant differences between the control tests and the heat tests in the GCL-C, GCL-P and OPL-C ($p<0.005$) and to a lesser extent within the OPL-P region ($p=0.007$). Statistical differences ($p<0.005$) also occur between the GCL-C and GCL-P between the mechanical and heated trials. There was no difference between the mechanical and heated outer plexiform layers, at either the OPL-C ($p=0.830$) or OPL-P ($p=0.674$). The averages for microglia ratios for each region and test are listed in Table 6.9.

Table 6.9. Average microglia ratios for control, mechanical control and heated *in vitro* experiments from the central and peripheral ganglion cell layers (GCL-C and GCL-P) and the central and peripheral outer plexiform layers (OPL-C and OPL-P)

Test	Average Ratio of Soma Area to Arbour Area (%)			
	Ganglion Cell Layer		**Outer Plexiform Layer**	
	Central	Peripheral	Central	Peripheral
Control	1.56±0.34	1.50±0.25	1.28±0.35	1.37±0.37
Mechanical	2.38±0.82	1.88±0.44	1.92±0.53	1.78±0.53
Heat	3.12±1.12	2.53±0.67	1.76±0.49	1.97±0.94

6.3.2.3.1 Thermal Response

To determine whether the increase in ratio was a product of the absolute temperature or the amount of thermal energy dissipated in the tissue, analysis was performed comparing ratio changes to temperature and temperature increase. The graphical representation of ratio with respect to tissue temperature is shown in Figure 6.21.

Similarly to the changes observed in microglia arbour area, a dose response curve could not be fit to the GCL-C, OPL-C or OPL-P regions, which indicates a lack of temperature dependence. In the GCL-C, almost all measures are above the control and mechanical regions, although this was observed to be irrespective of induced temperature change. This is similar to the OPL-C and OPL-P, although as the distance increases, an increase in data points within the control and mechanical ranges can be observed.

A dose response could be produced for the GCL-P region although the large error bars within the data do not provide a convincing fit. Data from the GCL-C region from comparisons between temperature increase and ratio changes reiterates the difficulty in isolating damage caused mechanically from thermally induced damage, with all temperature elevations within the mechanically damaged range. This is similar to all other regions, suggesting additional testing to determine thermally induced damage (in the absence of mechanical trauma) would greatly assist in the determination of a power budget.

6.3.2.3.2 Thermal Increase Response

To determine whether the soma area-arbour area ratio could be described as a function of temperature increase, linear trend lines were fit to the data. These trend lines, shown in Figure 6.19 indicated that the ratio would increase by 6.92×10^{-4} in the central ganglion cell layer and by 1.19×10^{-3}, 5.44×10^{-4} and by 9.84×10^{-4} in the peripheral ganglion cell layer and central and peripheral outer plexiform layers, respectively. Due to the poor correlation between the linear fits (due in part to the poor correlation between arbour area and increasing temperature), the ratios were not used in further analysis.
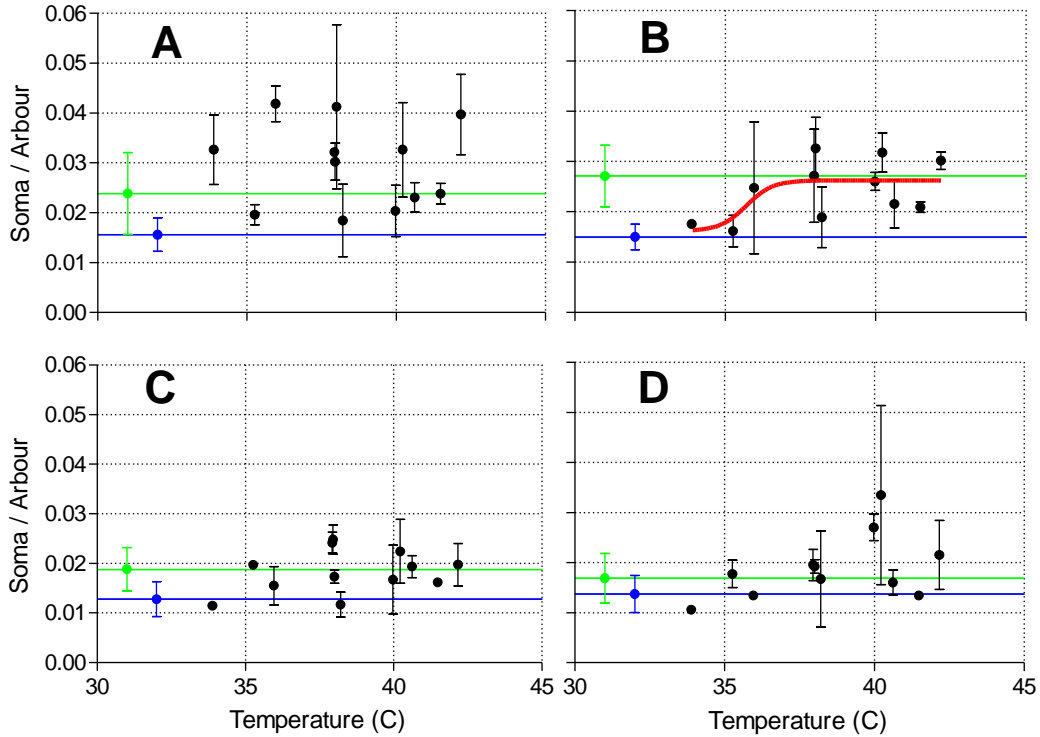
Figure 6.18. Average ratio of soma area to arbour area as a function of tissue temperature for **(A)** central ganglion cell layer, **(B)** peripheral ganglion cell layer, **(C)** central outer plexiform layer and **(D)** peripheral outer plexiform layer. Green and blue lines and error bars are indicative of mechanical control and control averages and standard deviations. Red line represents the calculated dose response
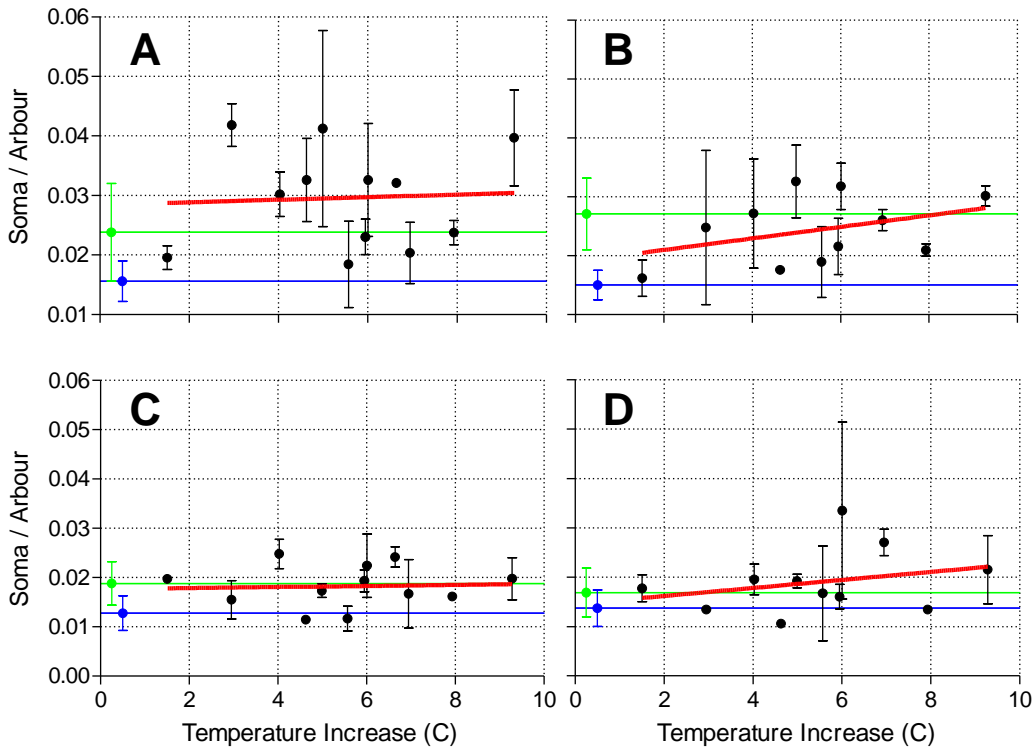
Figure 6.19. Average ratio of soma area to arbour area as a function of tissue temperature for **(A)** central ganglion cell layer, **(B)** peripheral ganglion cell layer, **(C)** central outer plexiform layer and **(D)** peripheral outer plexiform layer. Green and blue lines and error bars are indicative of mechanical control and control averages and standard deviations. Red line represents the calculated linear fit

232

6.3.3 Microglial Cell Counts

To investigate whether movement of microglia affected measurements of soma or arbour areas, cells were counted in each image. The number of cells recorded in the control and mechanical control trials, as well as within the images taken from heated tests is graphically represented in Figure 6.20.

There was no statistical significance between cell numbers in the ganglion cell layers (p=0.702) or in the outer plexiform layers (p=0.136) although there was a statistically significant difference (p<0.005) between cells located in the central and peripheral regions. There was also no statistical significance between mechanical and control trials over all areas using two-sided t-tests (GCL-C, p=0.822, GCL-P, p=0.815, OPL-C, p=0.062, OPL-P, p=0.449).
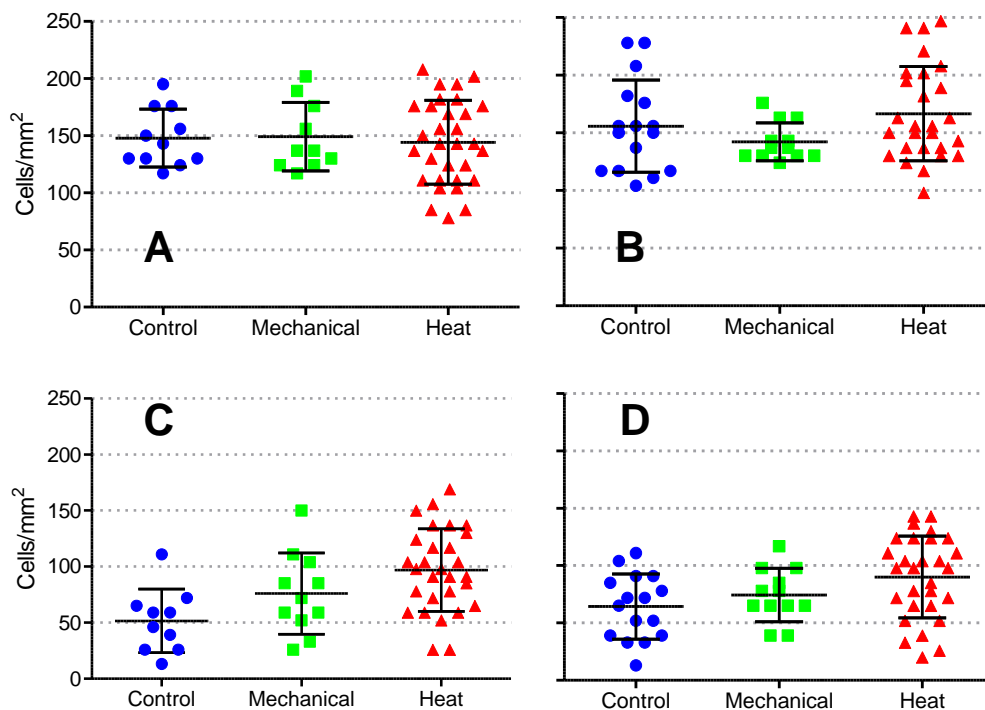
Figure 6.20. Soma areas for **(A)** central ganglion cell layer, **(B)** peripheral ganglion cell layer, **(C)** central outer plexiform layer and **(D)** peripheral outer plexiform layer for each test type irrespective of bath or induced temperature. Mean and standard deviations are shown in black.

Cell numbers, averaged across all of the control, mechanical and heat trials are listed in Table 6.10. While the control and mechanical tests can be averaged with confidence (all tests essentially identical), taking the average for the heat tests disregards differences in induced temperature increase and may not give a reliable indication of microglial

movement. In cases where the temperature is low, it would be expected that the results from these tests are similar to the mechanical control data. Tests with large amounts of dissipated heat would be expected to induce larger microglial changes than from tests with less thermal energy dissipated into the tissue although the average values can be useful in suggesting whether differences do occur.

Table 6.10. Average cell counts for control, mechanical control and heated *in vitro* experiments from the central and peripheral ganglion cell layers (GCL-C and GCL-P) and the central and peripheral outer plexiform layers (OPL-C and OPL-P)

Test	Average Cell Count (Cells/mm^2)			
	Ganglion Cell Layer		**Outer Plexiform Layer**	
	Central	Peripheral	Central	Peripheral
Control	149±25	153±37	50±26	65±28
Mechanical	153±50	140±17	72±33	73±23
Heat	144±37	166±41	97±37	90±36

The number of cells in the GCL-C and GCL-P are very similar regardless of the type of test, with averages of between 140 and 166 cells/mm^2 found in each of the six areas. The average number of cells measured in the outer plexiform layer is much smaller than the respective ganglion cell counterparts, with cell count averages ranging from 50±26 cells/mm^2 in the OPL-C control trials to 97±37 in the heated OPL-C trials. Results from the OPL-C test have the greatest difference, with OPL-P tests similar across all three modalities. The only average difference that occurred consistently was within the OPL regions, with an increase in cell number due to mechanical damage and a further increase when mechanical and heat stresses were applied.

There was no statistical difference between the average number of cells counted in the GCL-C ($p=0.758$, $p=0.888$) and GCL-P ($p=0.020$, $p=0.388$) between the heat and mechanical and heat and control trials, respectively. There was also no difference between heat and mechanical trials in the OPL-P ($p=0.041$) and OPL-C ($p=0.117$) regions. There was an increased significance ($p=0.028$) between the OPL-P regions in the control and heat tests with a significance between the OPL-C ($p<0.005$) observed. It is possible that this increase in cell numbers was due to a net influx of microglia towards the region of injury, although it is also possible that an increase in mechanical pressure as well as thermal energy reduced the ability to differentiate between microglia located within the ganglion cell layer and the outer plexiform layer, with cell dendrites often appearing to point downwards (towards the ganglion cell layer).

Combinations of two-sample t-tests were performed to investigate whether there was any statistically significant difference between the average microglial cell numbers in each of the four locations across the three trial parameters. The only significant

difference (p<0.005) was found between cells numbers in the ganglion cell layer and outer plexiform layer (within each test type) and between the heat and control tests in the central outer plexiform layer. There was no statistically significant difference observed between the control and mechanical tests (p=0.062) or between the control and heated trials (p=0.041) in the central outer plexiform later or between the control and heated tests in the peripheral outer plexiform layer (p=0.028). The large variance within the mechanical control trials for this layer reduces the difference between the number of cells measured in the mechanical control compared to the heat and pure control trials, with p values of 0.062 and 0.041, respectively.

With a finite number of cells, if there was a statistically significant increase in cells within the central outer plexiform layer, it would be expected that there would be a decrease in cell numbers peripheral to this region. A comparison of the number of cells measured within the heated trials as a function of temperature increase is shown in Figure 6.21. There was a small increase observed from the GCL-C, OPL-C and OPL-P regions, with cells increasing by 4.86, 7.38 and 3.13 cells/mm^2/°C. A net decrease was observed in the GCL-P region, although this decrease was negligible at 0.60 cells/mm^2/°C.
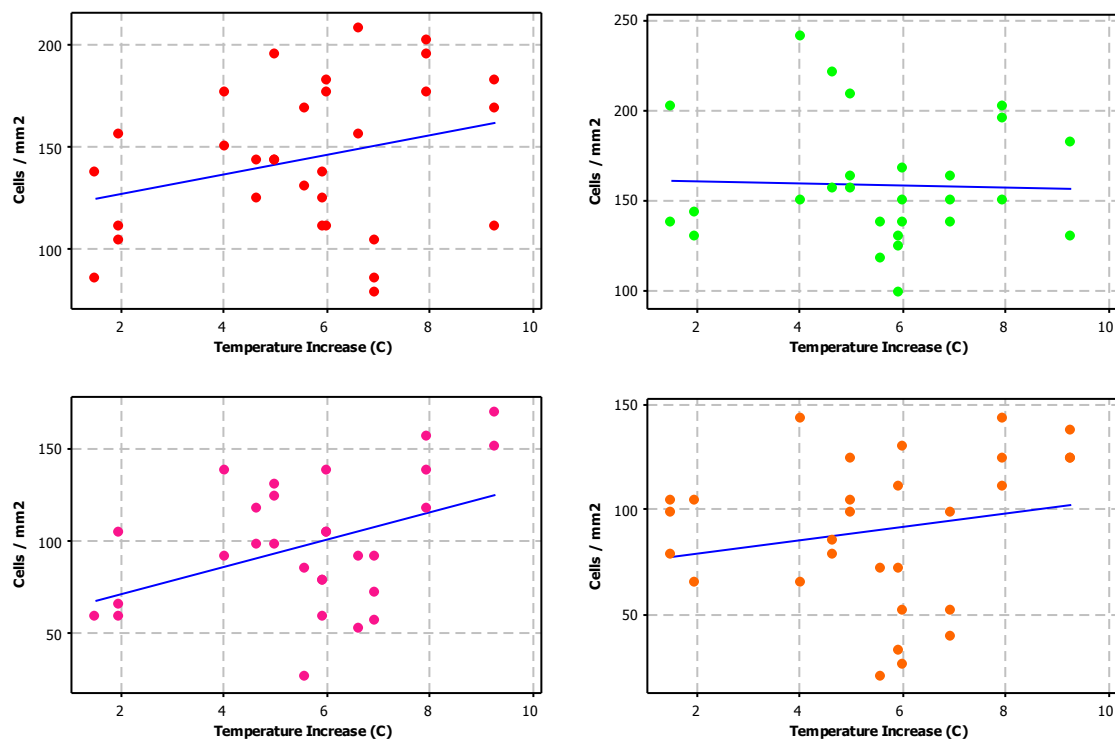
Figure 6.21. Average number of cells as a function of temperature increase for each region

From this data it is possible that there was some movement of microglial cells from the peripheral ganglion cell region towards the central ganglion cell region, although it is

expected that with the large heating element (relative to the size of the rat eye), the source of thermal damage would be difficult to locate.

6.3.4 Temperature–Power Analysis

To enable the determination of power dissipation levels that are likely to induce thermal damage, the temperature that causes damage must be related to the amount of power dissipated by the heating elements implanted in the rat retinas. Results from the thermal heating tests are listed in Table 6.11. These results indicate the temperature of the heat bath, the initial baseline and final baseline temperatures (where measured) and the temperature during the heating phase that resulted from a power (or current) dissipation through the implanted heating element. The difference in temperature between the initial baseline and the heating period temperature is also indicated.

Table 6.11. *In vitro* experiment power dissipations and thermal measurements

| Test Number | Temperature (°C) | | | | | Current (mA) | Power (mW) |
	Bath	Initial Baseline	Heating	Final Baseline	Difference		
1	31.00±0.29	29.67±0.07	42.94±0.50		13.27	93.17	173.6±6.49
3	33.58±0.34	32.26±0.33	40.36±1.10	29.43±0.26	8.10	66.24	87.76±0.97
5	31.48±0.37	29.26±0.03	33.89±0.28	-	4.63	49.09	48.20±1.69
7A	31.70±0.50	30.72±0.04	35.66±0.38	-	4.94	65.92	86.91±1.05
7B		31.29±0.04	37.93±0.39	-	6.64	64.35	82.81±0.60
8A	32.44±0.47	31.16±0.05	38.85±0.47	-	7.69	79.38	126.03±2.68
8B		31.87±0.06	42.51±0.47	-	10.6	79.28	125.70±0.76
10A	36.44±0.22	34.68±0.10	40.62±0.31	34.40±0.06	5.94	64.05	82.06±0.61
10B		33.03±0.20	39.98±0.42	32.90±0.15	6.95	58.82	69.20±1.91
11A	36.38±0.21	34.21±0.37	40.22±1.90	34.16±0.12	6.01	63.88	81.62±0.68
11B		32.64±0.31	38.21±1.78	32.85±0.19	5.57	52.28	54.66±0.57
12	36.51±0.21	33.01±0.25	38.00±0.22	-	4.99	52.78	55.71±0.50
14A	36.76±0.31	32.89±0.23	42.17±0.54	32.85±0.22	9.28	65.33	85.35±1.98
14B		33.56±0.27	41.49±0.50	33.84±0.21	7.93	65.12	84.80±2.60
15A	36.07±0.31	33.01±0.14	35.96±0.23	33.51±0.51	2.95	39.67	31.48±0.39
15B		33.92±0.14	37.95±0.25	34.36±0.51	4.03	48.15	46.37±0.46
16B	36.31±0.24	33.75±0.25	35.26±1.36	-	1.51	31.44	19.65±0.23
17A	35.99±0.14	34.95±0.13	38.06±0.30	-	3.11	46.90	43.99±0.22

The temperature of the heat bath was kept below 34°C for the initial seven trials, with the temperature increased to approximately 36°C (35.99°C to 36.76°C) for the subsequent eleven tests. The initial baseline temperatures ranged from between 29.67°C for a 31.00°C bath temperature to 34.95°C for a bath temperature of 35.99°C. Powers ranging from 31.48 mA to 173.60 mA were dissipated through the heating element,

increasing the tissue temperature by up to 13.27°C. In almost all of the cases, the baseline temperature before and after the period of heating was very closely matched.

A graphical representation of the amount of power required to increase the tissue temperature, both as an absolute temperature and as an increase above the baseline temperature, is shown in Figure 6.22. Red and black data points are indicative of heat bath temperatures below and above 33°C respectively. When the heat bath temperature is below 33°C, the power required to increase the measured absolute temperature is greater than for heat bath temperatures above 33°C. This is to be expected as larger thermal increases will require more power and this is indicated by plot of power versus temperature increase being very similar for both low and heat baths. The linear fits, plotted to match the power dissipation as a function of both the absolute temperature and the temperature difference have R-squared values of 0.482 and 0.812 for the absolute temperature and temperature difference values respectively, following:

$$\text{Tissue Temperature (°C)} = 35.1 + 0.0494 \times \text{Power (mW)} \qquad (6.2)$$
$$\text{Temperature Difference (°C)} = 0.0825 \times \text{Power (mW)} \qquad (6.3)$$

These results suggest that in order to ensure the surface of an implantable device is at no more than 2°C above the ambient body temperature (as defined in the international standards for implantable devices), power dissipated in retinal tissue should be kept below 24.24 mW. With the device surface area measuring 1.36 mm^2 (0.85 × 1.6 mm), the power budget for an implantable device to ensure operation below 2°C would be 18.48 mW/mm^2, although the smaller dimensions of the rat retinal tissue are likely to play a negative role in the ability of thermal energy to be dissipated to surrounding media such as vitreous fluid.
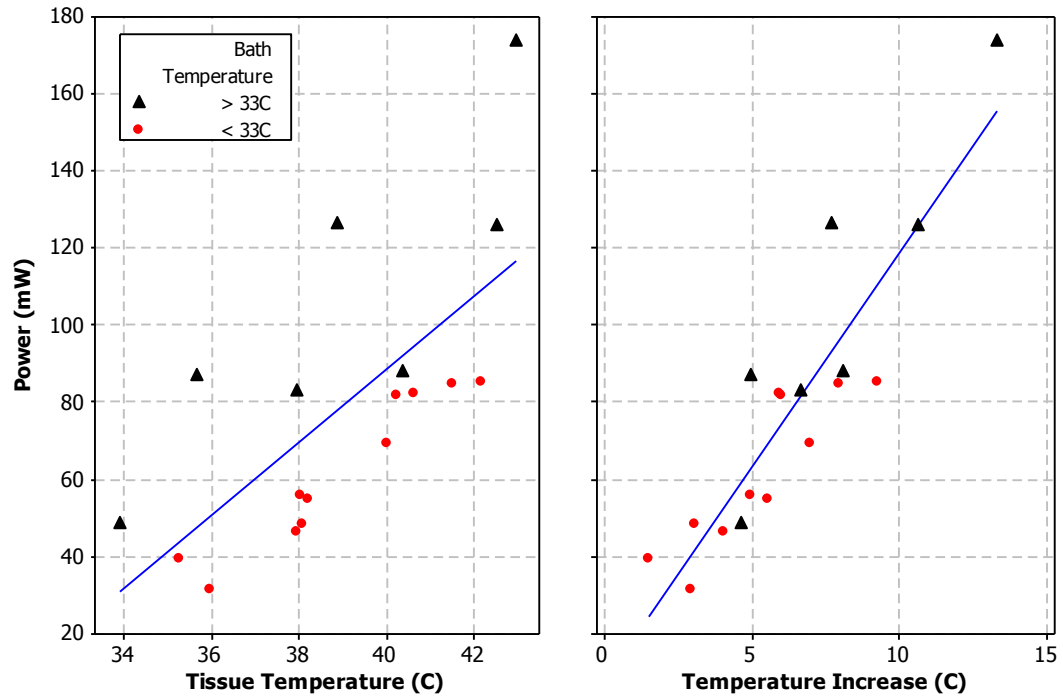
Figure 6.22. Tissue temperature and temperature increase as a function of power dissipated by the *in vitro* heating element. Black and red data points are for bath temperatures below and above 33°C respectively with blue line indicating a linear fit.

6.4   DISCUSSION

To determine thermal damage thresholds *in vitro*, tests investigated changes occurring to microglial morphology within rat retinae. Comparisons were made between microglial soma areas, the extracellular medium observed by the microglial branches and processes (arbour area) and the ratio between the two. Cell counts were also performed to investigate whether microglia had migrated towards damaged regions of the retina. Damage, caused by increasing the temperature of a heat bath (incubation trials), inserting a heating element (mechanical damage trials) or through both the insertion of a heating element and dissipation of power from the heating element into the neighbouring retinal tissue, were used as a means to investigate retinal response.

Through incubation trials, soma area increased with increasing temperature and the arbour area decreased with increasing temperature. The T_{50} threshold temperatures were greater for arbour areas and it is expected that many of the fine processes would have retracted prior to the observable retraction of the large dendritic arms. Whether the responses would have occurred at the same temperatures is unclear, although this is quite possible.

Due to mechanical trauma caused by the insertion of a heating element, the ability to investigate changes occurring to microglia arbour areas was not possible. No dose response curves could be fit to the measured data, although there was a statistically significant difference between microglia arbour areas measured in the central and peripheral ganglion cell regions. Large variations in the size of the arbour areas made threshold determination difficult and indicated that increased power would act to increase the size of microglia arbour areas, rather than decrease them. This may have been in part due to the movement of healthy microglia (with large dendritic branches) into regions of stress with cell counts shown to increase with increasing temperature. The earliest detection of thermal damage was observed through alterations in microglia soma.

6.4.1 Comparison between Tests in the Ganglion Cell Layer

In the incubation tests, microglia soma areas increased from a basal area of 26.1 μm^2 to greater than 42.0 μm^2 as the temperature was increased. In the thermal damage tests where temperature increase was induced through power dissipation from the implanted heating element, soma areas maintained a similar dose response curve to that observed without implantation. A comparison between the soma area increase as a function of temperature for the incubation tests and the heated tests is shown in Figure 6.24 for the central ganglion cell layer.

The effect of thermal damage exacerbating microglia response when subjected to both thermal and mechanical trauma was observed, with the soma areas in the heated tests larger than both the incubation average (26.1 μm^2)and the mechanical average (36.3 μm^2). This indicates that even at low temperatures (low power dissipation) soma areas will be affected by combinations of both mechanical and thermal damage, with the soma areas almost as large as the upper plateau for the incubation tests (40.5 μm^2 for the low temperature heat tests compared with 42.1 μm^2 observed at high temperatures during incubation tests). There was a 2.5°C increase in the T_{50} thresholds observed for the heated and incubation trials, which suggests that the extent of mechanical damage obscures the earliest microglia response to thermal trauma.

In the peripheral ganglion cell layer (Figure 6.25), the average soma area observed during the implantation of a passive heating element (mechanical average of 32.3 μm^2) was very similar (although slightly lower) to that observed at very low temperatures from the heated trials (31.9 μm^2). In the peripheral region, where mechanical trauma is not as severe (compared to the central regions), thermal trauma alone can be observed to follow a very similar curve to that observed during incubation trials, with similar T_{50} thresholds (37.2°C and 37.8°C) and maximum soma areas observed, although slightly higher values observed from heated trials in both cases. Microglial response in this region was shown to increase by 5.8 μm^2 due to mechanical trauma alone.
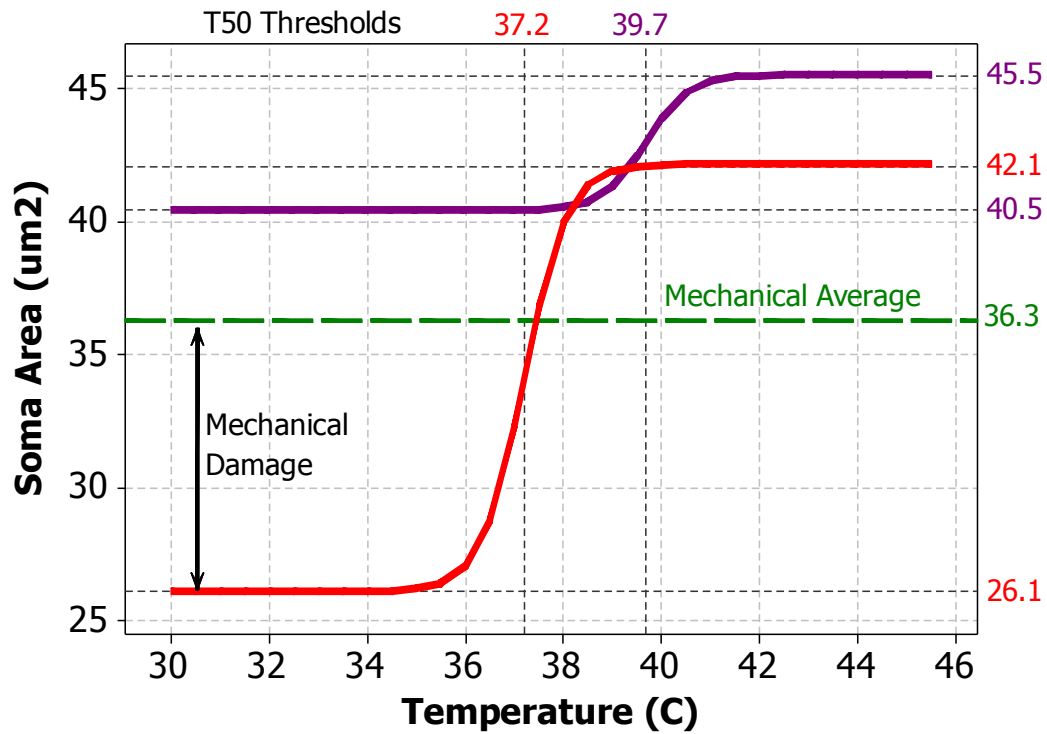
Figure 6.24. Central ganglion cell region soma area shown as a function of temperature, comparing incubation tests (red trace) with thermal heating trials (purple trace). The average soma area from the mechanical damage trials for the central ganglion cell layer is shown (green broken line), with indication of the amount of mechanical trauma (incubation baseline to the average mechanical damage).
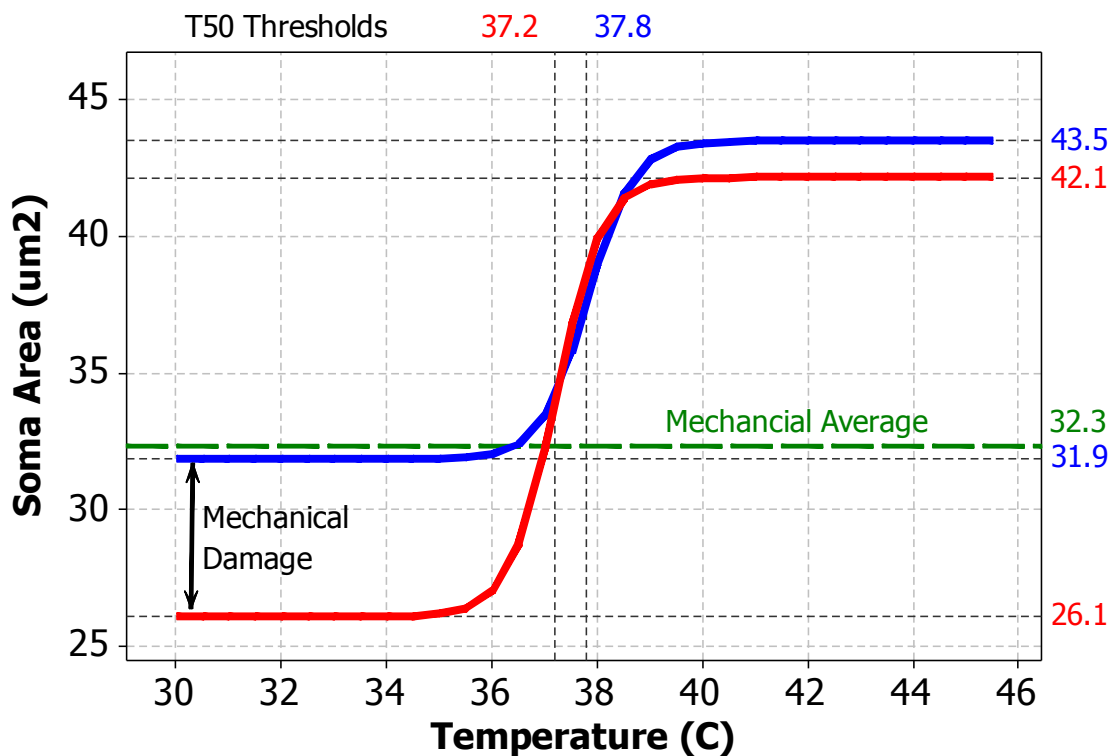
Figure 6.25. Peripheral ganglion cell region soma area shown as a function of temperature, comparing incubation tests (red trace) with thermal heating trials (blue trace). The average soma area from mechanical damage trials for the peripheral ganglion cell layer is shown (green broken line), with indication of the amount of mechanical trauma (incubation baseline to the average mechanical damage).

6.4.2   Comparison between Tests in the Outer Plexiform Layer

Figure 6.26 shows the response of microglia soma areas observed within the central outer plexiform layer from both the heated trials and the incubation trials. Similarly to the central ganglion cell region, soma areas at very low heat (in the presence of both mechanical and thermal stress) are greater than observations from incubation trials and greater than the average soma areas observed through mechanical trials. There is a large difference in the observed T_{50} thresholds, although this is expected to have arisen due to the location of the heating element (with temperatures measured in the central region not the peripheral region). The maximum soma areas are similar, although slightly smaller for the heated trials, contrary to observations in the ganglion cell regions.

Comparing the incubation trial averages to those obtained from the peripheral outer plexiform region (Figure 6.27) indicates a similar mechanical trauma threshold response to that observed within the peripheral ganglion cell layer. In this comparison, the low temperature heating trials are similar to mechanical averages (slightly lower) and increase to a soma area slightly less than the maximum observed in the incubation trials. Again, these graphs give strength to the hypothesis that mechanical damage is exacerbated by thermal trauma, with regions in the periphery not as affected by the combination of mechanical and thermal stress when compared to from data obtained from central regions.
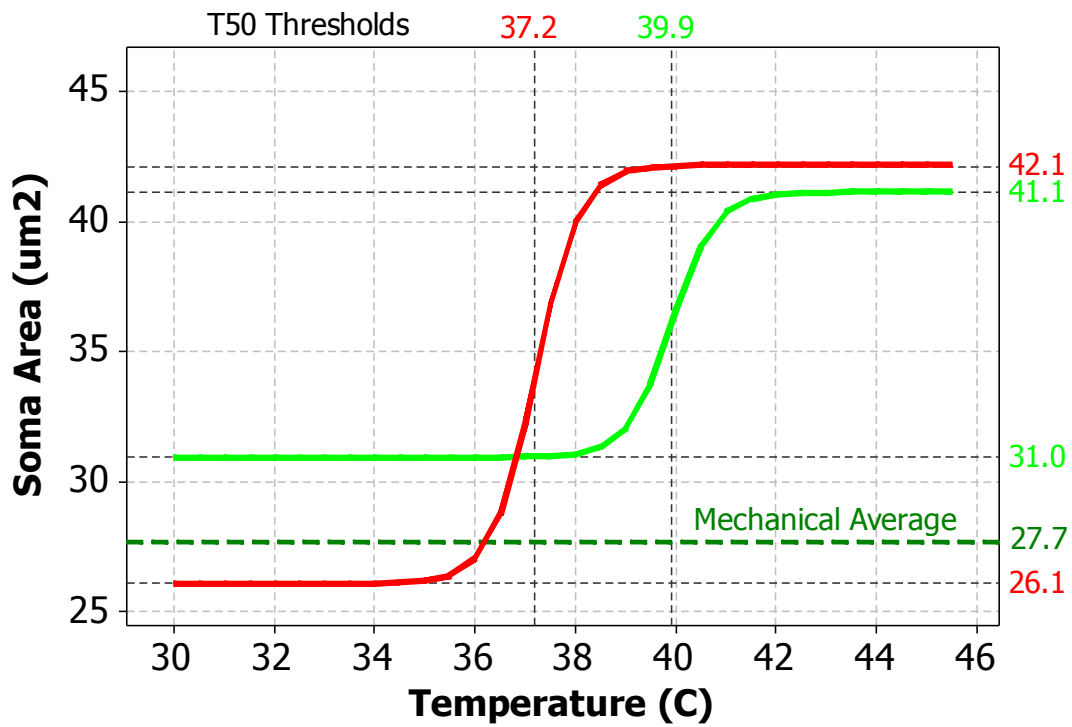
Figure 6.26. Central outer plexiform layer soma area shown as a function of temperature, comparing incubation tests (red trace) with thermal heating trials (green trace). The average soma area from mechanical damage trials for the peripheral ganglion cell layer is shown (green broken line), with indication of the amount of mechanical trauma (incubation baseline to the average mechanical damage).
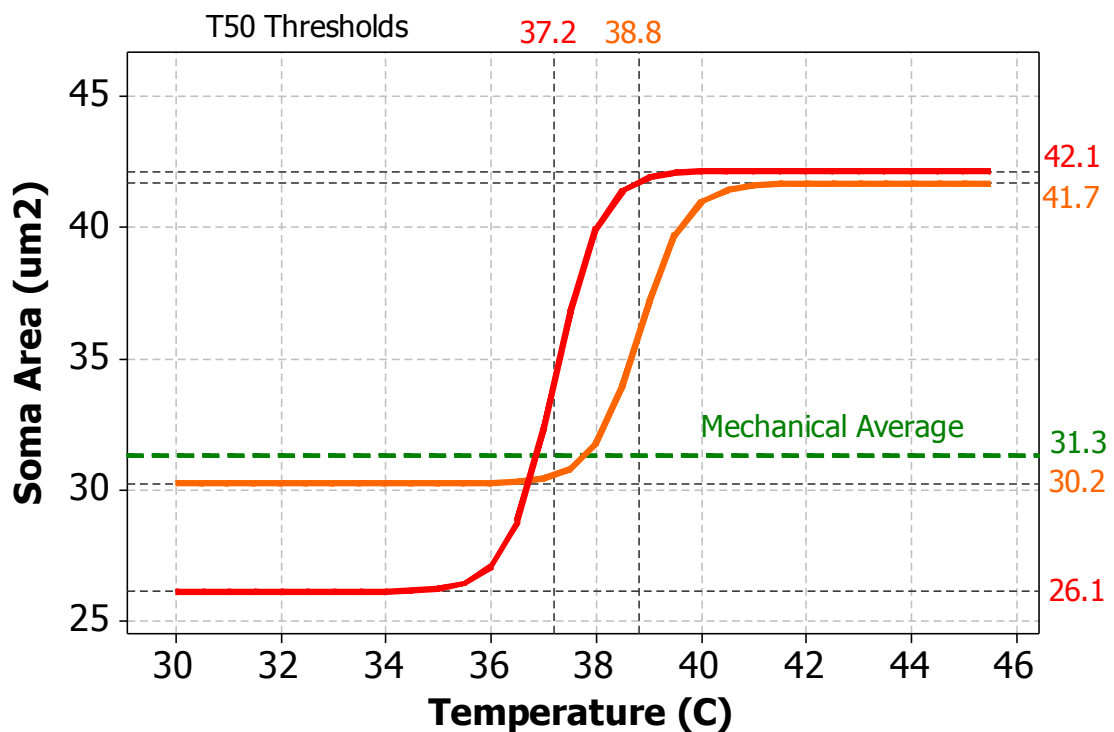
Figure 6.27. Peripheral outer plexiform layer soma area shown as a function of temperature, comparing incubation tests (red trace) with thermal heating trials (orange trace). The average soma area from mechanical damage trials for the peripheral ganglion cell layer is shown (green broken line), with indication of the amount of mechanical trauma (incubation baseline to the average mechanical damage).

6.4.3   Power Dissipation Thresholds

Thermal damage thresholds (where the soma area had increased above the control plus one standard deviation) were observed to occur at 37.87°C in the peripheral ganglion cell layer and at 39.20°C and 38.45°C in the central and peripheral outer plexiform regions respectively. No threshold could be determined from microglia within the central ganglion cell region, as the degree of mechanical trauma was too severe and obscured microglia morphological changes induced by thermal stress. Threshold values above soma areas (plus one standard deviation) taken from mechanically damaged control microglia indicated temperatures of 39.96°C, 38.00°C, 40.58°C and 39.05°C in the GCL-C, GCL-P, OPL-C and OPL-P regions, respectively.

Using equation (Eq. 6.2) the amount of power that would need to be dissipated in the retinal tissue to evoke a microglial response observable (greater than the control soma area plus one standard deviation) would be 58.35 mW, 84.48 mW and 69.75 mW, increasing the tissue temperature to above 37.87°C, 39.20°C and 38.45°C in the GCL-P, OPL-C and OPL-P regions, respectively. The amount of power delivered to the centrally located heating element to increase the microglial response above and beyond the areas observed from mechanical damage would be 99.41 mW, 60.90 mW, 111.59 mW and 81.53 mW for temperatures of 39.96°C, 38.00°C, 40.58°C and 39.05°C in the GCL-C, GCL-P, OPL-C and OPL-P regions respectively.

Using the temperature increase formula (Eq. 6.3), the amount of power required to increase the temperature above 2.54°C, 3.3°C and 4.1°C (relating to the temperature increase at which soma areas increased in size to greater than the control average plus one standard deviation) is 31.91 mW, 41.46 mW and 51.51 mW in the GCL-P, OPL-C and OPL-P regions, respectively. Temperature increases above the mechanical control regions would need to be 6.7°C, 5.35°C, 6.23°C and 8.32°C, equivalent to power dissipations of 84.18 mW, 67.22 mW, 78.27 mW and 104.54 mW, respectively. This is shown in Figure 6.28, where the threshold power is plotted as a function of location (central and peripheral ganglion cell and outer plexiform layers).

In each case, the power dissipations required to induce a microglial responses are lower when determined from thermal increase data (as opposed to absolute temperature data) due to the differences between the sigmoidal and linear interpolations used. To avoid a microglial response greater than control plus one standard deviation, the amount of power dissipated by the prosthesis should be less than the lowest threshold observed,

31.91 mW in the peripheral ganglion cell region. This excludes thermal damage caused to central ganglion cell regions, as the thermal threshold in this region is obscured by mechanical trauma.

31.91 mW is equivalent to a power density of 23.46 mW/mm^2 and would increase the tissue temperature by 2.54°C. While it is expected that a lower temperature would be observed to induce a microglial response greater than the control soma area (plus one standard deviation) in the central ganglion cell layer, this could not be confirmed.
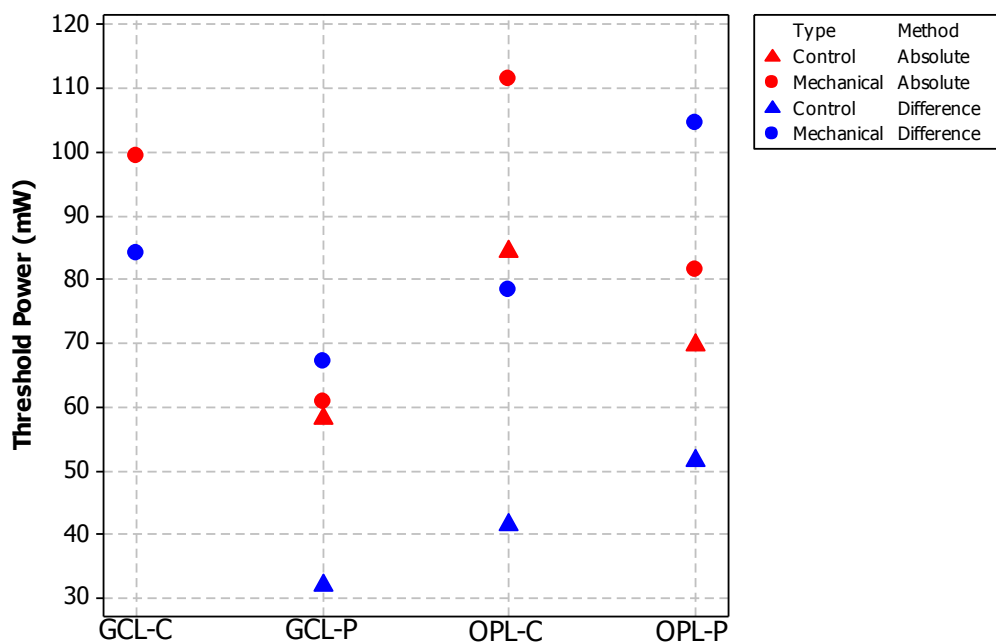
Figure 6.28. Power dissipation required to increase microglia soma areas above the control and mechanical averages (plus one standard deviation) both relating to tissue temperature (absolute) and temperature increase (difference) within the central ganglion cell layer (GCL-C), peripheral ganglion cell layer (GCL-P), central outer plexiform layer (OPL-C) and peripheral outer plexiform layer (OPL-P).

6.5 CONCLUSIONS

This chapter investigated the threshold temperatures and temperature increases that induced *in vitro* microglial responses in rat retinal tissue. Microglial response, one of the earliest detections of retinal stress, showed a marked increase in soma area due to dissipation of thermal energy through an implanted heating element.

Implants designed to be placed on the retinal surface (similar to epiretinal prostheses) were shown to cause damage, although the extent of the damage is expected to be much greater than damage and trauma caused in clinical trials. This is for two reasons. Firstly, the method in which the heating elements and sensors were implanted was done by using a micromanipulator to descend an implant into the eye cup of an enucleated rat retina. The ability to ensure that mechanical damage was consistent was difficult, with assurance of contact made by visual confirmation of retinal movement. This was not performed under a microscope, and the mechanical trauma caused by this method was required to be large enough to force the retinal tissue to move. This amount of trauma is not expected in epiretinal implantations performed delicately under microscopic control and by professional retinal surgeons. Secondly, the rat *in vitro* tissue did not have time to heal from any mechanical damage caused through implantation. In clinical trials, a permanently implanted prosthesis will have the ability to heal damaged neurons and reduce the impact of the mechanical trauma caused. These factors are expected to reduce to total amount of mechanical damage caused through implantation of a prosthesis device in acute and chronic trials.

A comparison between power dissipation and induced temperature increases was conducted to assist in the determination of a power budget to help retinal prostheses architects. This data suggested that a one degree increase in retinal tissue temperature would be caused by a power dissipation of 12.56 mW (9.24 mW/mm^2). A baseline temperature (at which no damage would have occurred) was observed to fall at a temperature of 34.9°C, which correlated well with trials performed to measure the temperature at the posterior margin of a rat orbit. While these temperatures measured were heavily dependent on the level of anaesthesia and the time the animal had been unconscious, the average orbital temperature was 34.35±1.56°C.

Experiments proposed to evaluate a temperature-damage correlation were undertaken, heating implanted devices up to temperatures beyond 43°C (an increase of up to 13°C, depending on the heat bath- baseline orbital temperature). Four methods of measurement were used to investigate damage involving measurements of microglial

response and morphological changes, including the number of cells observed per millimetre, the area of the microglia soma, the area of extracellular space observed by the microglia and the average between the microglia soma and arbour areas.

In each region, microglial arbour areas decreased due to mechanical damage, with further decreases observed in the ganglion cell layer when mechanical damage was coupled with thermal insult. In contrast, thermally damaged cells in the outer plexiform layer were more similar to control trials than their mechanical counterparts, which was presumably due to a microglial requirement to continue observing the extracellular space. Tests performed over longer time intervals would assist in determination of whether the arbour areas decreased in response to increased thermal energy or whether the lack of response was caused by a thermal elevation not surpassing threshold within this deeper layer. Implants were relatively large in comparison to the size of a rat retina and could have heated the peripheral ganglion cells preferentially to cells located within the inner plexiform layers, which is one explanation that would fit the experimental observations.

As there were contrasting responses to the soma and arbour areas, the ability to use the ratio as a method for thermal threshold determination could not be adequately achieved, with these results amplifying the differences observed within the different layers and testing protocols.

Cell counts within each of the locations and regions and between each of the tests were reasonably uniform throughout trials, with the one exception being a considerable increase in cells located in the plexiform layers in tissues induced with thermal stress, and in particular, the central outer plexiform region which was exposed to both thermal and mechanical insult. Cell numbers increased at a rate of 4.86, 7.38 and 3.13 cells/mm^2/°C in the GCL-C, OPL-C and OPL-P regions with a minor decrease in cell numbers located in the GCL-P region (0.60 cells/mm^2/°C). If the increase in cell number was caused by a net influx of microglia flocking to the damaged region, this could also explain why there was not a decrease in the average arbour size of the microglia measured. Additional healthy cells, with unaltered arbour areas could have moved into the damaged region in response to stress which would alter the average microglia soma and arbour areas.

To determine the extent of mechanical damage, an investigation on the increase in soma areas and decrease in arbour areas using tissue immersed in heat baths set to different temperatures was performed. No implantation was required in the incubation trials and retinal tissue was heated directly by the surrounding medium. Dose response curves for the heated control tests (without implantation), averaged over all regions and layers,

were similar to those obtained from tests in which a heating element was used to induce thermal damage. Comparison of this dose response curve to those obtained using a heating element indicated that mechanical damage, present in all regions, affected the cells through a microglial soma area increase of between 4.12 μm^2 (OPL-P) to 14.34 μm^2 (GCL-C). These differences in baseline soma areas did not affect the maximum microglia area which was observed to be similar throughout all trials. Mechanically traumatised cells were also observed to respond less to additional insult, with temperatures required to produce maximal responses greater than tests performed without mechanical damage. Whether this thermotolerance is due to a lack of microglial ability to respond once injured, the requirement of additional microglia to be involved or due to the ability of a heat bath to more uniformly heat tissue than an implanted heating element is unknown.

In the peripheral regions (both in the ganglion cell layer and outer plexiform layer) the soma areas observed at low temperatures were very similar to the average soma areas observed from mechanical trials within the same regions. This suggests that there was very little impact on dissipated thermal energy due to the additional distance between the heating element and the observed areas with the tissue able to dissipate the thermal energy effectively. In contrast, measurements taken from the central regions (both in the ganglion cell and outer plexiform layers) showed an increase significantly above the mechanical average soma area, even at very low temperatures (very low power dissipations). The impact of this is suggestive that mechanical damage will be exacerbated by thermal trauma.

These experiments analysed whether thermal damage could be assessed using alterations in microglial morphology and have shown that soma areas are larger when the absolute tissue temperature rises or when thermal energy is dissipated. Soma areas were also shown to increase due to mechanical stress, which was often larger than the thermal damage caused. The extent of mechanical damage could be removed by tests performed by whole tissue incubation (as opposed to implantation of a heating element), and suggested that the ability of cells to endure thermal insult is greater when smaller regions of tissue are affected. This was shown by an increase in temperature required to produce T_{50} responses when tissue was heated by an implanted device. While these tests were unable to use microglia arbour areas to examine the effect of thermal heating, the potential for this method remains, with higher magnification of microglial cells able to more accurately determine the area observed by the microglial dendritic branches and fine protrusions. Analysis of microglial movement and orientation towards source of trauma was reduced by the size of the implant relative to the size of the rat eye. The use of animals with larger eyes would allow the implantation of a heating element of similar size to that of a prosthesis chip and would allow for a better investigation into these

features. Tests performed over longer time periods would allow for the microglial response to be fully understood, allowing for a determination of whether the morphological microglial changes observed assist retinal neurons in surviving or act to enhance their demise.

As a tool to determine initial tissue responses to thermal energy dissipation and temperature increases, alterations in microglia morphology provided a useful and early measure of cellular change, with the earliest observable response occurring at a power of 31.91 mW (equivalent to a power density of 23.46 mW/mm^2), increasing the tissue temperature by 2.54°C.

To ensure that mechanical damage is not exacerbated by thermal trauma from the heating up of an implant or through power dissipation by a prosthesis, it is advised that any damage caused through implantation should be given a sufficient amount of time to stabilise (and hopefully repair and regenerate) prior to the induction of power dissipation from the implant. Thus, the implant should not be turned on until a time at which the eye and retinal tissue has been able to recover from the surgical trauma, as this may cause more severe damage than either thermal damage or mechanical damage alone.

7

CONCLUSIONS

This thesis has aimed at determining the limits of induced thermal damage potentially caused through implantation and function of retinal prostheses, thereby increasing patient safety.

At the time of writing, there were no publications that directly related thermal energy dissipation by an implanted retinal prosthesis to temperature elevations and thermal damage caused to retinal neurons. To ensure that permanently implanted visual prosthesis are functional and safe for the lifetime of the patient, the determination of retinal tissue thermal damage thresholds are required.

While many studies have investigated thermal damage thresholds using lasers and electromagnetic irradiation, these studies cannot be directly compared for a number of reasons. First, the manner in which thermal energy is supplied to the retinal tissue is not identical to the conductive heat transfer from the implanted electronics to the tissue. The potential for mechanical trauma caused through prosthesis implantation and the tissue reaction to the presence of foreign objects, exacerbated by additional thermal insult, is not included in these studies. Secondly, the durations of exposure cannot be correlated with a possible eighteen hours of daily visual prosthesis use, with many studies investigating the effects of thermal heating caused by sub-second insults. The temperatures used in these trials are also much greater than would be expected (and allowed) for an implanted device and therefore comparisons between many publications must be performed with caution.

Publications investigating alternative means of thermal heating can be of assistance to enhance the protocols used in experiments designed to investigate thermal damage thresholds. Publications have displayed noticeable differences between species, with

choice of animal model imperative for direct human comparison. Primates and cats have similar orbital sizes and structures, including analogous vasculature which is expected to play a major role in the homeostatic thermo-stability of the eye. Differences occurring between tissues are also mentioned, with tissues such as skin and bone being far more resilient to thermal stress than cortical tissue and retinal neurons.

The exacerbation of thermally induced damage has been reported to occur due to additional stressors such as ischemia, with increased body temperature (hyperthermia) being widely reported to reduce thermal damage thresholds. To ensure accuracy of experiments, body temperatures must be maintained at a normal level, and additional stress should not be applied. The exception is mechanical damage, which must be included to accurately replicate visual prosthesis use. Increased thermo-tolerance, through durations of sub-threshold pre-treatment, has been reported to increase the resistance of tissue to thermal damage, and experimental protocols should aim to avoid this to prevent over-estimation of power dissipation thresholds.

It is imperative that thermal damage is measured appropriately, with decisions made on the definition of thermal damage extremely influential in threshold determination. Whether thresholds are defined as visible alterations or functional modifications may grossly skew thermal or power dissipation limits. Similarly, different measurement techniques have different sensitivities and the potential for retinal trauma to go unnoticed using inadequate methods may have devastating consequences if they are used to define safety limits.

Bionic Vision Australia has proposed two types of visual implants to restore sight to profoundly blind patients suffering from retinitis pigmentosa and age related macular degeneration. The potential of the epiretinally implanted prosthesis to induce thermal damage is of greater concern than other current prosthesis devices, with the stimulating electronics directly attached to the electrodes. These electrodes, too, are novel in that they will penetrate into the retinal tissue. Thus, any thermal dissipation from the circuitry will have a direct impact on the retinal neurons being stimulated, and the potential to induce deleterious temperature increases within the tissue is of large concern. To ensure the generated thermal increases do not exceed temperatures that cause irreversible retinal trauma is the primary aim of this thesis, with obtained thresholds used to guide retinal prostheses power budgets.

To determine thermal damage thresholds, imitation implants have been created. These implants have been designed as a component of this thesis to be inserted in identical positions to current epiretinal and suprachoroidal prostheses using identical surgical techniques. The implants have been constructed of similar materials, with a flexibility,

thickness and width replicating current designs. To induce thermal increases within the eye, heating elements were constructed from combinations of surface mounted resistors or thin copper coils. The heating element size is similar to the proposed size of the prosthesis stimulating chip (5.0 × 5.0 mm), although implants have been deigned to accommodate for sizes between 0.5 and 9.5 mm^2. Current sources have been created to supply power to the heating elements (and thereby heat the neighbouring tissue), with an error of less than 8% for currents up to 250 mA. These implants have been tested in saline baths, cadavers and *in vivo* and have demonstrated the ability to locally heat retinal tissue and simultaneously measure and record the induced temperature change.

To measure temperatures within the retinal tissue, platinum resistance temperature detectors are soldered onto the implants, central to the heating elements and along the flexible polyimide shaft. Resistance changes in these components are measured using a high resolution temperature measurement system and are converted into temperatures, with saline bath trials indicating an average error margin of 0.002°C. Simultaneous, real time measurements of multiple retinal tissue temperatures, taken from the sensors lining the retinal tissue, are acquired and graphically displayed using LabView SignalExpress.

Thermal finite element models that can accurately determine temperature elevations that occur within an eye due to energy dissipation by suprachoroidal or epiretinally implanted visual prostheses were also designed and compared to cadaver and *in vivo* experiments. Various parameters, including location of the implanted heat-generating chip, alterations in body and room temperature, changes in thermal conductivities, choroidal blood perfusion, metabolically generated heat, and the magnitude of temperatures and powers dissipated by the heating elements have been investigated and validated by experimental results.

Retinal tissue temperatures, induced by suprachoroidally implanted heating elements, were observed to increase by 1°C per 67.6 mW during cadaver trials and by 1°C per 65.0 mW in FEM simulations. Epiretinal simulations have indicated that perfusion will enhance the removal of thermal energy, with thermal increase rates of between 1°C per 45.0 mW (no perfusion) and 1°C per 59.2 mW (37°C choroid) observed. Retinal temperatures influenced by bioheat perfusion were observed to reside within these limits, with thermal energy more effectively removed as the tissue temperature increased. The reduction in thermal influence observed when suprachoroidally implanted heating elements were modeled suggests that this region may be thermally safer for the placement of electrical devices. This region is, however, more distant from the retinal neurons at which stimulation is directed, and the increased distance is expected to require additional power from the implanted circuitry (and hence potentially a greater thermal increase).

Thermal model simulations have indicated that while power dissipation and perfusion will play large roles in implant-induced retinal tissue temperatures, metabolically generated heat and variations in body and room temperatures do not have a significant influence on retinal temperature. Alterations to retinal and choroidal thermal conductivities will influence the localization of thermal energy, although these effects are not expected to be observed in living (unfixed) tissue.

The FEMs were able to predict retinal tissue temperature increases induced by an epiretinally implanted heating element *in vivo* up to 2°C. At temperatures greater than 2°C, the effect of active perfusion enabled the tissue to significantly increase the rate of thermal energy removal. This suggests that damage thresholds obtained from acute cadaver experiments performed in the absence of perfusion will give an overestimation of the temperature rise and an underestimation of the maximum power that can be safely tolerated by retinal tissue. Hence, provided these overestimated thresholds are not surpassed, the additional ability of the eye to remove thermal energy will further act to mitigate deleterious cellular effects.

Predicted thermal damage thresholds, adhering to an upper surface temperature limit of 2°C, were derived from cadaver trials and FEM simulations. In order to stay within the Australian and international guidelines, the power dissipated by a 5 × 5 mm, suprachoroidally implanted heating element should not exceed 135 mW (5.4 mW/mm^2) when in direct contact with retinal tissue. Increasing the distance between the retinal tissue and the heat generating circuitry would allow the implant to dissipate more power without inducing deleterious thermal increases, with a 0.5 mm separation between the implant and the retina required to increase the safe power dissipation level to 250 mW (10.0 mW/mm^2). When a 5 × 5 mm epiretinally implanted heating element is in direct contact with retinal tissue, however, the power dissipation to avoid a 2°C increase is reduced to less than 36.6 mW (1.46 mW/mm^2).

The finite element models have been shown to be accurate representations of both *in vivo* and cadaver experiments, and can be used to analyze thermal alterations occurring due to prosthesis implantation in both suprachoroidal and epiretinal locations. The use of finite element models that have been validated against experimental data will allow a reduction in the number of animals required to investigate causes of tissue temperature increase and assist in determination of thermal damage thresholds. These models, in conjunction with the high resolution temperature measurement system, are effective in determining the ranges of temperatures that may cause thermal damage to retinal tissue and neuronal components in an acute and chronic setting. Future work investigating these detrimental thermal levels can be used to guide retinal prosthesis circuit design,

ensuring that cellular damage and patient safety is not compromised with the use of visual implants.

While these models give accurate temperature distributions within the cat eye when subjected to temperature increases occurring within the implants, determination of temperatures which induce thermal damage or cellular alterations are also required. *In vivo* cat experiments were conducted to analyse thermal trauma and to investigate the ability of choroidal circulation to regulate retinal tissue temperature. Three experiments were performed, and while of great assistance to the enhancement and optimisation of surgical methods and techniques, were unable to define the thermal damage threshold of retinal tissue.

To optimise damage analysis methods, *in vitro* rat retinal tissue studies were undertaken. Unlike the *in vivo* cat studies that used Fluoro-Jade C to analyse thermal damage (ineffective for both cat retinal tissue and positive control tissue), the rat studies looked at alterations in microglial morphology to determine retinal stress. Studies were conducted to analyse the affect of temperature elevations (in the absence of mechanical trauma) and indicated that microglial soma areas would increase and arbour areas would decrease with increasing temperature. A threshold temperature of 37.1°C was determined, defined as an increase in soma area half way between the minimal and maximal measurements (approximately 2.75°C above the average measured temperature of 34.35±1.6°C).

Experiments were performed using implanted heating elements to induce temperature increases within the retinal tissue (heated trials), and were compared to the incubation trials (thermal stress only) and mechanically damaged trials (implantation of a passive heating element) to determine the affect of combining both mechanical and thermal stress. In the peripheral regions (implant was positioned centrally), when the implant dissipated low amounts of power, there was no discernable difference between mechanical control trials and the heated trials, although these both induced a microglia soma area increase above that observed in the incubation trials. As the temperature of the heating element was increased, the dose response curve followed that obtained from the heated trials, indicating that while there was an initial change related to implant insertion, the threshold at which a 50% response was observed was very similar. In this region, the earliest observable indication of retinal alteration (defined as an increase in soma size above the average control soma size plus one standard deviation) was observed by increasing the tissue temperature by 2.54°C (above a 36°C heat bath temperature). This is equivalent to a power dissipation of 31.91 mW, comparable to Australian and international regulations enforcing surface temperatures limits of implantable devices.

In the central regions, even at very low power dissipations, the size of the measured microglia was greater than both the incubation and mechanical control sizes, and almost as large as the observed size for microglia subjected to high incubation temperatures. This suggests that that retinal response will be greatly exacerbated by the combination of mechanical and thermal stress and that this should be avoided. While no thermal threshold could be observed in this region (all measured soma areas were greater than the control average plus one standard deviation), it is expected the temperature required to induce a response would be significantly smaller than the 2.54°C threshold observed in the peripheral region.

While it is not clear that these changes in microglia are representative of thermal damage, it is clear that combining mechanical and thermal insults will stress the tissue to a much larger degree than thermal or mechanical stress alone. To ensure that thermal damage does not result, it is recommended that implanted prosthesis are not turned on (do not dissipate any thermal energy) until sufficient time such that the mechanical insults caused by implant insertion have been appropriately resolved.

As the global population continues to age and the number of people suffering from profound vision loss increases, the use of artificial visual aids will become increasingly beneficial. Advancement of technological ability and the desire to enhance the resolution of visual implants will increase the number of electrodes used to stimulate retinal tissue, which, in turn, will increase the power required and thus power dissipated by the implanted circuitry. This will also increase the risk of surpassing the thermal tolerance of retinal tissue and may compromise device functionality and patient safety if thermal limits are not resolved and enforced. This thesis is important preliminary research in ensuring patients requiring retinal prostheses can have restored vision without compromising their safety.

REFERENCES

Acland, G., G. Aguirre, et al. (2001). "Gene therapy restores vision in canine model of childhood blindness." Nat Genet **1**: 92-95.

Adair, E. and R. Rawson (1973). "Step-Wise Changes in Thermoregulatory Responses to Slowly changing Thermal Stimuli." Pflugers Arch. **339**: 241-250.

Ali, R., G. Sarra, et al. (2000). "Restoration of photoreceptor ultrastructure and function in retinal degeneration slow mice by gene therapy." Nat Genet **3**: 306-310.

Anderson, G., Valvano, JW., Santos, RR (1992). "Self heated thermistor measurements of perfusion." IEEE Transactions on Biomedical Engineering **39**(9): 877-885.

Anderson, K., K. Miller, et al. (2005). "Regional distribution of Fluoro-Jade B staining in the hippocampus following traumatic brain injury." Experimental Neurology **193**: 125-130.

AS-EN (2002). "Active implantable medical devices, general requirements for safety, marking and information to be provides by the manufacturer." AS EN 45502.1-2002.

AS-ISO (2003). "Implants for surgery - Active implantable medical devices - General requirements for safety, marking and information to be provided by the manufacturer." AS ISO 14708.1-2003.

AS-ISO (2003). "Implants for surgery - Active implantable medical devices - General requirements for safety, marking." AS ISO 14708.1-2003.

Bajzek, T. (2005). "Thermocouples: A sensor for measuring temperature " IEEE Instrumentation and Measurement Magazine: 35-40.

Balthhasar, C. d., S. Patel, et al. (2008). "Factors affecting perceptual thresholds in epiretinal prosthesis." Investigative Ophthalmology and Visual Science **49**(6): 2303-2314.

Barbe, M., M. Tytell, et al. (1988). "Hyperthermia protects against light damage in the rat retina." Science **241**(4874): 1817-1820.

Bashirullah, R., W. Liu, et al. (2003). "A smart bi-directional telemetry unit for retinal prosthetic device." IEEE: V5 - V8.

Ben-Shlomo, g., M. Belokopytov, et al. (2006). "Functional Deficits Resulting From Laser-Induced Damage in the rat Retina." Lasers in Surgery and Medicine **38**: 689-694.

Benedict, R. (1969). Fundamentals of temperature, pressure and flow measurements, . New York, John Wiley & Sons, Inc.

Bernardi, P., M. Cavagnaro, et al. (1996). "Specific absorption rate and temperature increases in the head of a mobile-phone user." IEEE Transactions on Microwave Theory and Techniques **48**(7): 1118-1126.

Bhatt, N., G. Peyman, et al. (1993). "Microwave-induced retinal destruction with sparing of sclera and choriocappillaris." Ophthalmic Surgery **24**: 125-128.

Bian, G., L. Wei, et al. (2007). "Fluoro-Jade C can specifically stain the degenerative neurons in the substantia nigra of the 1-methy-4-phenyl-1,2,3,6-tetrohydro pyrindine-treated C57BL/6 mice." Brain Research **1150**: 55-61.

Bignami, A. (1984). "Glial Fibrillary Acidic (GFA) Protein in Muller glia. Immunofluorescence study of the goldfish retina." Brain Research **300**: 175-178.

Bignami, A. and D. Dahl (1979). "The radial glia of Muller in the rat retina and their response to injury. An immunofluorescence study with antibodiues to glial fibrillary acidic (GFA) protein." Experimental Eye Research **28**: 63-69.

Birngruber, R., C. Puliafito, et al. (1987). "Femto-second laser tissue interactions: retinal injury studies." IEEE Journal of Quantum Electronics **QE-23**(10): 1836-1844.

Bollemeijer, J., J. Lagendijk, et al. (1989). "Effects of microwave-induced hyperthermia on the anterior segment of healthy rabbit eyes." Graefe's Archives of Clinical and Experimental Ophthalmology **227**: 271-276.

Braakman, R., P. V. D. Valk, et al. (1989). "The effects of Ultrasonically Induced Hyperthermia on Experimental Tumors in the Rabbit Eye." Investigative Ophthalmology and Visual Science **30**(5): 835-844.

Bresnick, G., G. Frisch, et al. (1970). "Ocular effects of argon laser radiation I. Retinal damage threshold studies." Investigative Ophthalmology **9**(11): 901-910.

Bronzino, J. (2000). The Biomedical Engineering Handbook CRC Press.

BS-EN (1998). "Active Implantable Devices - Part 1: General Requirements for Safety, Marketing and Information to be provided by the Manufacturor." European Standard BS EN 45502-1:1998.

Burgman, P., A. Nussenzweig, et al. (1995). Thermotolerance. Berlin, Springer-Verlag.

Burkitt, A. (2010). Retinal implants "down under" - the research program of Bionic Vision Australia. The Eye and The Chip World Congress on Artificial Human Vision, Detroit, MI, USA.

Butterwick, A., A. Vankov, et al. (2007). "Progress towards a high-resolution retinal prosthesis." Ophthalmic Technologies XVII 6426A.

Cai, W., F. Li, et al. (2001). "Development of Normal and Injury-Induced Gene expression of aFGF, bFGF, CNTF, GFAP and IGF-I in the rat retia." Experimental Eye Research 72: 591-604.

Cain, C. and A. Welch (1973). "measured and predicted laser-induced temperature rises in the rabbit fundus." Investigative Ophthalmology 13(1): 60-70.

Caprioli, J., S. Kitano, et al. (1996). "Hyperthermia and hypoxia increase tolerance of retinal ganglion cells to anoxia and excitotoxicity." Investigative Ophthalmology and Visual Science 37(12): 2376-2381.

Carroll, L. and T. Humphreys (2006). "Laser tissue interactions." Clinics in Dermatology 24: 2-7.

Caudras, A., Casas, O (2006). "Determination of heart rate using high resolution temperature measurement." IEEE Sensors Journal 6(3): 836-843.

Cha, K., K. Horch, et al. (2000). "Mobility performance with a pixelized visual prosthesis." Vision Research 32(7): 1367-1372.

Cha, K., W. Horch, et al. (1992). "Mobility performance with a pixelised vision system." Vision research 32(7): 1367-1372.

Cha, K., W. Horch, et al. (1992). "Reading speed with a pixelised vision system." J. optical Soc. America A: Optics, Image Science and Vision 9(5): 673-677.

Chauhan, B., B. Pan, et al. (2002). "Effect of intraocular pressure on optic disk topography, electroretinal and axonal loss in a chronic pressure induced rat model of optic nerve damage." Investigative Ophthalmology and Visual Science 43: 2969-2976.

Chen, B., S. Thomsen, et al. (2006). "Modeling thermal damage in skin from 2000nm laser irradiation." Journal of Biomedical Optics 11(6).

Chen, L., P. Yang, et al. (2002). "Distribution, markers and functions of retinal microglia." Occular Immunology and Inflammation 10(1): 27-39.

Chen, S., N. Lovell, et al. (2004). Effect on prosthetic visual acuity by filtering schemes, filter cut off frequency and phosphene matrix: a virtual reality simulation. Proceedings of the 26th International Conference of the IEEE EMBS. San Francisco, USA.

Cheong, A., G. Legge, et al. (2008). "Relationship between visual span and reading performance in age related macular degeneration." Vision Research 48: 577-588.

Chia, S. and K. Teo (2003). "Prognosis of adult men with heat exhaustion with regard to postural stability and neurobehavioral effects: a 6 month follow up study." Neurotoxicol. Teratol. 25: 503-508.

Chidlow, G., J. Wood, et al. (2009). "Evaluation of Fluoro-Jade C as a marker of degenerating neurons in the rat retina and optic nerve." Experimental Eye Research 88: 426-437.

Chow, A. and V. Chow (1998). "Subretinal electrical stimulation of the rabbit retina." Neuroscience Letters 225: 13-16.

Chow, A. and N. Peachey (1998). "The subretinal microphotodiode array retinal prosthesis." Ophthalmic Research 30: 195-198.

Chung, G., Kim, C (2008). "RTD characteristics for micro thermal sensors." Microelectronics Journal 39: 1560-1563.

Clarke, A., W. Ham, et al. (1969). "Laser Effects on Eye." Archives of Environmental Health 18(3): 424-428.

Colodetti, l., J. Weiland, et al. (2007). "Pathology of Damaging electrical Stimulation in the Retina." Experimental Eye Research 85: 23-33.

Colombo, J. and V. Puissant (2002). "Fluoro Jade stains early and reactive astroglia in the primate cerebral cortex." Journal of Histochemistry and Cytochemistry 50(8): 1135-1137.

Davalos, D., J. Grutzendler, et al. (2005). "ATP mediates rapid microglial response to local brain injury in vivo." Nature Neuroscience 8(6): 752-757.

DeJuan, E. and J. Crittenden (1994). Retina tacks. Retina. S. Ryan. St Louis, MO, Mosby-Year book, Inc. 3.

DeJuan, E. and J. Crittenden (1994). Retina tacks. Retina S. Ryan. St Louis, MO, Mosby-Year book, Inc. 3.

DeJuan, E., B. McCuen, et al. (1986). "The use of retina tacks in the repair of complicated retinal detachments." American Journal of Ophthalmology 102: 20-24.

DeJuan, E., B. McCuen, et al. (1986). "The use of retina tacks in the retpair of complicated retinal detachments." American Journal of Ophthalmology **102**: 20-24.

deLint, P., D. vanNorren, et al. (1992). "Effect of body temperature for threshold retinal light damage." Investigative Ophthalmology and Visual Science **33**(8): 2382-2387.

DeMarco, S., G. Lazzi, et al. (2003). "Computed SAR and thermal elevation in a 0.25-mm 2-D model of the human eye and head in response to an implanted stimulator - Part I: Models and methods." IEEE Transactions on Antennas and Propagation **51**(9): 2274-2285.

Desmettre, T., C. Maurage, et al. (2001). "heat Shock Protein Hyperexpression on Chorioretinal Layers after Transpupillary Thermotherapy." Investigative Ophthalmology and Visual Science **42**(12): 2976-2980.

Desmettre, T., C. Maurage, et al. (2003). "Transpupillary Thermotherapy (TTT) With Short Duration Laser Exposures Induce Heat shock Protein (HSP) Hyperexpression on Choroidoretinal Layers." Lasers in Surgery and Medicine **33**: 102-107.

Dewey, W. (1994). "Arrhenius relationships from the molecule and cell to the clinic." Int. J. Hyperthermia **10**(4): 457-483.

Dewhirst, M., J. Gross, et al. (1986). Effects of heating rate on normal and tumor microcirculation. New York, American Society of Mechanical Engineers.

Dewhirst, M., B. Vigilanti, et al. (2003). "Basic principles of thermal dosimetry and thermal thresholds for tissue damage from hyperthermia." International Journal Of Hyperthermia **19**(3): 267-294.

Dobelle, W. (2000). "Artificial vision for the blind by connecting a television camera to the visual cortex." ASAIO J **46**: 3-9.

Dobelle, W., M. Mladejovsky, et al. (1976). ""Braille" reading by a blind volunteer by visual cortex stimulation." Nature **259**: 111-112.

Dobelle, W., M. Mladejovsky, et al. (1974). "Artificial vision for the blind: Electrical stimulation of visual cortex offers hope for functional prosthesis." Science **183**: 440-444.

Donaldson, N. and T. Perkins (1983). "Analysis of resonant coupled coils in the design of radio frequency transcutaneous links." Medical and Biological Engineering and Computing **21**: 612-627.

Dong, B., P. Liang, et al. (1998). "Sonographically guided microwave coagulation treatment of liver cancer: an experimental and clinincal study." Americal Journal of Roentgenology **171**: 449-454.

Downie, L., M. Pianta, et al. (2007). "Neuronal and Glial Cell Changes are Determined by Retinal Vascularization in Retinopathy of Prematurity." Journal of Comparative Neurology **540**: 404-417.

Drake, R., W. Vogl, et al. (2005). Gray's Anatomy for Students, Churchill Livingstone.

Duckworth, E., T. Butler, et al. (2005). "Temporary focal ischemia in the mouse: Technical aspects and patterns of Fluoro-Jade evident neurodegeneration." Brain Research **1042**: 29-36.

Duret, F., M. Brelen, et al. (2006). "Object localisation, discrimination and grasping with the optic nerve visual prosthesis." Restorative Neurology and Neuroscience **24**: 31-40.

Dyer, M. and C. Cepko (2000). "Control of Muller glial cell proliferation and activation following retinal injury." Nature Neuroscience **3**(9): 873-880.

Eckhorn, R., M. Wilms, et al. (2006). "Visual resolution with retinal implants estimated from recordings in cat visual cortex." Vision Research **46**: 2675-2690.

Eisch, A., L. Schumed, et al. (1998). "characterizing cortical neuron injury with Fluoro-Jade labelling after a neurotoxic regimen of methampheramine." Synapse **30**(3): 329-333.

Eisenbarth, W., M. MacKeben, et al. (2008). "Characteristics of dynamic processing in the visual field of patients with age related maculopathy." Graefe's Archives of Clinical and Experimental Ophthalmology **246**: 27-37.

Eisenfeld, A., A. Bunt-Milam, et al. (1984). "Muller Cell Expression of Glial Fibrillary Acidic Protein after Genetic and Experimental Photoreceptor Degeneration in the Rat Retina." Investigative Ophthalmology and Visual Science **24**(11): 1321-1328.

Elwassif, M., Q. Kong, et al. (2006). "Bio-het transfer model of deep brain stimulation induced temperature changes." Journal of Neural Engineering **3**: 306-315.

Erickson, P., S. Fisher, et al. (1987). "Glial Fibrillary Acidic Protein Increases in Muller Cells after Retinal Detachment." Experimental Eye Research **44**: 37-48.

Eter, N., D. Engel, et al. (2008). "In vivo visualization of dendritic cells, macrophages and microglial cells responding to laser-induced damage in the fundus of the eye." Investigative Ophthalmology and Visual Science **49**(8): 3649-3658.

Fauci, A., J. Martin, et al. (1998). Harrison's Principles of Internal Medicine, 14th Edition, International Edition, McGraw Hill.

Fernandes, A., C. Maurer-Morelli, et al. (2004). "Fluoro-Jade, but not Fluoro-Jade B, stains non-degenerating cells in brain and retina of embryonic and neonatal rats." Brain Research **1029**: 24-33.

Flack, F., E. James, et al. (1971). "Mutual inductance of air-cored coils: effect on design of radio-frequency coupled implants." Medical and Biological Engineering and Computing **9**: 79-85.

Flyckt, V., B. Raamakers, et al. (2007). "Calculation of SAR temperature rise in a high resolution vascularised model of the human eye and orbit when exposed to a dipole antenna at 900, 1500 and 1800 megahertz." Physics in Medicine and Biology **52**: 2691-2701.

Flyckt, V., B. Raaymakers, et al. (2006). "Modelling the impact of blood flow on temperature distribution in the human eye and orbit: fixed heat transfer coefficients versus the Pennes bioheat model versus discrete blood vessels." Physics in Medicine and Biology **51**: 5007-5021.

Foran, S., J. Wang, et al. (2003). "Causes of visual impairment in two older population cross sections: the Blue Mountain Eye Study." Ophthalmic Epidemiology **10**: 215-225.

Framme, F., G. Schuele, et al. (2004). "Influence of Pulse Duration and Pulse Number in Selective RPE Treatment." Lasers in Surgery and Medicine **34**: 206-215.

Fujii, S., H. Sasaki, et al. (2002). "Temperature dependence of synaptic responses in guinea pig hippocampal CA1 neurons in vitro." Cellular and Molecular Neurobiology **22**(4).

Fujii, T. and Y. Ibata (1982). "Effects of heating on electrical activities of guinea pig olfactory cortical slices." European Journal of Physiology **392**: 257-260.

Garvey, D. (2007). "So, what is a platinum RTD." Retrieved June 11, 2008, from http://www.rdfcorp.com/anotes/pa-rtd/pa-rtd_01.shtml.

Geeraets, W., R. Williams, et al. (1962). "The relative absorption of thermal energy in the retina and choroid." Investigative Ophthalmology **1**(3): 340-347.

Gehrs, K., D. Anderson, et al. (2006). "Age-related macular degeneration - emerging pathogenetic and theraputic concepts." Annals of Medicine **38**: 450-471.

Gekeler, F., H. Schwahn, et al. (2001). "Subretinal microphotodiodes to replace photoreceptor function. A review of the current state." Les Seminaires Ophthalmologiques, d'ISPEN **12**: 77-95.

Gekeler, F., P. Szurman, et al. (2007). "Compound subretinal prosthesis with extra-ocular parts designed for human trials: successful long-term implantation in pigs." Graefe's Archives of Clinical and Experimental Ophthalmology **245**: 230-241.

Gekeler, F., P. Szurman, et al. (2007). "Compound subretinal prosthesis with extra-ocular parts designed for human trials: sucessful long-term implantation in pigs." Graefe's Arch Clin Exp Ophthalmol **245**: 230-241.

Gekler, F., P. Szurman, et al. (2007). "Compound subretinal prosthesis with extra-ocular parts designed for human trials: sucessful long-term implantation in pigs." Graefe's Arch Clin Exp Ophthalmol **245**: 230-241.

Gerding, H., S. Taneri, et al. (2001). "Successful long-term evaluation of intraocular titanium tacks for the mechanical stabilization of posterior segment ocular implants." Mat.-wiss. u. Werkstofftach. **32**: 903-912.

Gerweck, L. (1977). "Modification of cell lethality at elevated temperatures. The pH effect." Radiation Research **70**: 224-235.

Gibbons, W. and R. Allen (1977). "Retinal damage from long-term exposure to laser radiation." Invest. Ophthalmol. Vis. Sci. **16**(6): 521-529.

Glaze, M. and M. Turk (1986). "Effects of radiofrequency hyperthermia on the healthy canine cornea." American Journal of Vetinary Research **47**: 913-918.

Glickman, R. (2002). "Phototoxicity to the retina: Mechanisms of damage." International Journal of Toxicology **21**: 473-490.

Goldblatt, W. S., P. T. Finger, et al. (1989). "Hyperthermic treatment of rabbit corneas." Invest. Ophthalmol. Vis. Sci. **30**(8): 1778-1783.

Gorgels, T., L. Beek, et al. (1997). "Effect of Body Temperature on Retinal Damage by 488nm Light in Rats." Microscopy Research and Technique **36**: 89-95.

Gorgels, T., L. VanBeek, et al. (1997). "Effect of body temperature on retinal damage by 488nm light in rats." Microscopy Research and Technique **36**: 89-95.

Gosalia, K., J. Weiland, et al. (2004). "Thermal elevation in the human eye and head due to the operation of a retinal prosthesis." IEEE Transactions on Biomedical Engineering **51**(8): 1469-1477.

Greenberg, R. and B. Mech (2010). Argus II clinical trial update. The Eye and The Chip World Congress on Artificial Human Vision, Detroit, MI, USA.

Grunwald, J., S. Hariprasad, et al. (1998). "Foveolar choroidal blood flow in age-related macular degeneration." Investigative Ophthalmology and Visual Science **39**(2): 385-390.

Hallum, L., N. Lovell, et al. (2005). Retinal image and phosphene image: An analogy. Neural Engineering. M. Akay, Wiley Press.

Ham, W., J. Ruffolo, et al. (1978). "Histologic analysis of photochemical lesions produced in rhesus retina by short-wave-length light." Invest. Ophthalmol. Vis. Sci. **17**(10): 1029-1035.

Hanisch, U. and H. Kettenmann (2007). "Microglia: active sensor and versatile effector cells in the normal and pathologic brain." Nature Neuroscience **10**(11): 1387-1394.

Harmon, B., A. Corder, et al. (1990). "Cell death induced in a murine mastocytoma by 42-47 degrees C by heating in vitro: evidence that the form of death changes from apoptosis to necrosis above a critical heat load." Int. J. Radiat. Biol **58**: 845-858.

Hartnett, M. and T. Hirose (1998). "Cyanoacrylate glue in the retpair of retinal detachment associated with posterior retinal breaks in infants and children." Retina **18**: 125-129.

Hayes, J., J. Yin, et al. (2003). "Visually guided performance of simple tasks using simulated prosthetic vision." Artificial Organs **27**(11): 1016-1028.

Hazzard, W., E. Bierman, et al. (1994). Principles of Geriatric Medicine and Gerontology, 3rd Edition, McGraw Hill.

Hellmich, H., K. Eidson, et al. (2007). "Injured Fluoro-Jade positive hippocampal neurons contain high levels of zinc after traumatic brain injuryq." Brain Research **1127**: 119-126.

Herman, T., E. Gerner, et al. (1981). "Rate of Heating as a determinant of hyperthermic cytotoxicity." Cancer Research **41**: 3519-3523.

Hirata, A. (2005). "Temperature increase in human eyes due to near field and far field exposures at 900MHz, 1.5GHz and 1.9GHz." IEEE Transactions on Electromagnetic Compatibility **47**(1).

Hirata, A., M. Fujimoto, et al. (2006). "Correlation between maximum temperature increase and peak SAR with different average schemes and masses." IEEE Transactions on Electromagnetic Compatibility **48**(3).

Hirata, A., S. Matsuyama, et al. (2000). "Temperature rises in the human eye exposed to EM waves in the frequency range 0.6-6 GHz." IEEE Transactions on Electromagnetic Compatability **42**(4): 386-393.

Hirata, A., U. Ushio, et al. (1999). "Formation of hot spots in human eye for plane wave exposures." Asia Pacific Microwave Conference **2**: 477-480.

Hirata, A., S. Watanabe, et al. (2006). "Computational verification of anaesthesia effect on temperature variation in rabbit eyes exposed to 2.45GHz microwave energy." Bioelectromagnetics **27**: 602-612.

Hirsch, S., B. Appleton, et al. (1977). "Effects of microwave irradiations to the albino rabbit eye." Investigative Ophthalmology and Visual Science **16**(4): 315-318.

Hoffman, H. and V. Dionne (1983). "Temperature dependance of ion permeation at the endplate channel." Journal of General Physiology **81**: 687-703.

Hoopes, P., K. Wishnow, et al. (2000). "Evaluation and comparison of five experimental BPH/prostate cancer treatment modalities." SPIE Optical Engineering Press: 519-545.

Horsager, A., R. Greenberg, et al. (2010). "Spatiotemporal interactions in retinal prosthesis subjectsq." Investigative Ophthalmology and Visual Science **51**(2): 1223-1233.

Hughes, A. (1979). "A schematic eye for the rat." Vision Research **19**: 569-588.

Humayun, M. (2001). "Intraocular retinal prosthesis." transactions of the American Ophthalmological Society **99**: 271-300.

Humayun, M., E. DeJuan, et al. (1999). "Pattern electrical stimulation of the human retina." Vision Research **39**: 2569-2576.

Humayun, M., E. d. Juan, et al. (2000). "Human neural retinal transplantation." Investigative Ophthalmology and Visual Science **41**(10): 3100-3106.

Humayun, M., E. d. Juan, et al. (1996). "Visual perception elicited by electrical stimulation of the retina in blind humans." Archives of Ophthalmology **114**: 40-46.

Humayun, M., M. Prince, et al. (1999). "Morphometric analysis of the extramacular retina from postmortem eyes with retinitis pigmentosa." Journal of Investigative Ophthalmology and Visual Science **40**: 143-148.

Hume, S., J. Marigold, et al. (1979). "The effect of local hyperthermia on the small intestine of the mouse." British Journal of Radiology **52**: 657-662.

Hymen, L. (1987). "Epidemiology of eye diseases in the elderly." Eye **1**: 330-341.

Ibarra, M., J. Hsu, et al. (2004). "Retinal temperature increases during transpupillary thermotherapy: effects of pigmentation, subretinal blood and choroidal blood flow." Investigative Ophthalmology and Visual Science **45**(10): 3678-3682.

Imran, M., Bhattacharyya, A (2006). "Effect of thin film thicknesses and materials on the response of RTDs and microthermocouples." IEEE Sensors Journal **6**(6): 1459-1467.

Jain, A., M. Blumenkranz, et al. (2008). "Effect of pulse duration on size and character of the lesion in retinal photocoagulation." Archives of Ophthalmology **126**(1): 78-85.

Jiang, L., E. Ng, et al. (2005). "A perspective on medical infrared imaging." Journal of Medical Engineering and Technology **29**(6): 257-267.

Johnson, P., G. Lewis, et al. (2003). "Drusden-associated degeneration of the retina." Investigative Ophthalmology and Visual Science **44**(10): 4481-4488.

Jung, H. (1994). "A generalized concept for cell killing by heat." Radiation Research **139**: 280-289.

Kendir, G., W. Liu, et al. (2004). "An efficient power link design for retinal prosthesis." IEEE ISCAS **IV**(41-44).

Kendir, G., W. Liu, et al. (2005). "An optimal design methodology for inductive power link with class-E amplifier." IEEE Transactions on Circuits and Systems **52**(5): 857-866.

Kester, W. (2007). "Bridge circuits."   Retrieved June 11, 2008, from http://www.analog.com/UploadedFiles/Associated_Docs/49470200sscsect2.PDF.

Kim, J., Kim, J., shin, Y., Yoon, Y (2001). "A study on the fabrication of an RTD (resistance temperature detector) by using Pt thin film." Korean Journal of Chemical Engineering **18**(1): 61-66.

Kim, J., K. Park, et al. (2006). "Thermal injury induces heat shock protein in the optic nerve in vivo." Investigative Ophthalmology and Visual Science **47**(11): 4888-4894.

Kim, S., P. Tathireddy, et al. (2007). In vitro and in vivo study of temperature increases in the brain due to a neural implant. Preeedings of the 3rd International IEEE EMBS Conference on Neural Engineering, Kohala Coast, Hawaii, USA.

Kim, S., P. Tathireddy, et al. (2007). "Thermal impact of an active 3D microelectrode array implanted in the brain." IEEE Transactions on Neural Systems and Rehabilitation Engineering **15**(4): 493-501.

Kim, S., Z. Zoschke, et al. (2006). "Switchable polymer-based thin film coils as a power module for wireless neural interfaces." Sensors and Actuators A **136**: 467-474.

Kiyatkin, E. (2007). "Brain temperature fluctuations during physiological and pathological conditions." European Journal of Applied Physiology **101**: 3-17.

Klee, M., F. Pierau, et al. (1974). "Temperature effects on the resting potential and spike parameters of cat motorneurons." Experimental Brain Research **19**: 478-492.

Ko, W., S. Liang, et al. (1977). "Design of radio-frequency powered coils for implant instruments." Medical and Biological Engineering and Computing **15**: 634-640.

Krauss, J., C. Puliafito, et al. (1986). "Interferometric technique for investigation of laser thermal retinal damage." Investigative Ophthalmology and Visual Science **28**(8): 1290-1297.

Kremers, J. and D. v. Norren (1989). "Retinal Damage in Macaque after White Light Exposures Lasting Ten Minutes to Twelve Hours." Investigative Ophthalmology and Visual Science **30**(6): 1032-1040.

Kreutzberg, G. (1996). "Microglia: a sensor for pathological events in the CNS." Trends in Neuroscience **19**: 312-318.

Krinke, G., W. Classen, et al. (2001). "Detecting necrotic neurons with fluoro jade stain." Experimental Toxicology and Pathology **53**: 365-372.

Kurz, A., D. Sessler, et al. (1993). "Thermoregulatory response thresholds during spinal anaesthesia." Regional Anaesthesia and Pain Management **77**: 721-726.

L'Esperence, F. (1989). Ophthalmic Lasers, The CV Mosby Company.

Lagendijk, J. (1982). "A mathematical model to calculate temperature distributions in human and rabbit eyes during hyperthermic treatment." Physics in Medicine and Biology **27**(11): 1301-1311.

LaManna, J., K. McCracken, et al. (1989). "Stimulus-activated changes in brain tissue temeprature in the anesthetized rat." Metabolic Brain Disease **4**(4): 225-237.

Langmann, T. (2007). "Microglia activation in retinal degeneration." Journal of Leukocyte Biology **81**: 1345-1351.

Lappin, P. and P. Coogan (1970). "Histologic evaluation of ophthalmoscopically subvisible retinal laser exposures." Investigative Ophthalmology **9**(7): 537-542.

Lazzi, G. (2005). "Thermal effects of bioimplants." IEEE Engineering in Medicine and Biology Magazine: 75-81.

Lee, J., K. Liang, et al. (2008). "Ex vivo dynamic imaging of retinal microglia using time-lapse confocal microscopy." Investigative Ophthalmology and Visual Science **49**(9): 4169-4176.

Lee, J., K. Liang, et al. (2008). "Ex Vivo Dynamic Imaging of Retinal Microglia Using Time Lapse Photography." Investigative Ophthalmology and Visual Science **49**(9): 4169-4176.

Li, D., S. Qiu, et al. (1988). "Acute heat injury to normal swine rectum." International Journal Of Hyperthermia **4**: 191-201.

Li, D., S. Zhou, et al. (1987). "Thermodamage, thermosensitivity and thermotolerance of normal swine esophagus." International Journal Of Hyperthermia **3**(2): 143-151.

Linke, C., W. Lounsberry, et al. (1967). "Localised heating of tissue by electric and non-electric means." Investigative Urology **4**: 586-599.

Lint, P. d., D. v. Norren, et al. (1992). "Effect of Body Temperature for Threshold retinal Light Damage." Investigative Ophthalmology and Visual Science **33**(8): 2382-2387.

Lint, P. d., D. v. Norren, et al. (1992). "Effect of body temperature on threshold for retinal light damage." Investigative Ophthalmology and Visual Science **33**(8): 2382-2387.

Liou, H. and N. Brennan (1997). "Anatomicallu accurate, finite element model eye for optical modeling." Journal of the Optical Society of America **14**(8): 1684-1695.

Liou, H. and N. Brennan (1997). "Anatomically acurate, finite model eye for optical modeling." J. Optical Soc. America A: Optics, Image Science and Vision **14**(8): 1684-1695.

Liu, D., C. Smith, et al. (1999). "Astrocytic demise precedes delayed neuronal death in focal ischemic rat brain." Molecular Brain research **68**: 29-41.

Liu, E., G. Saidel, et al. (2003). "Model Analysis of Tissue Responses to Transient and Chronic Heating." Annuls of Biomedical Engineering **31**: 1007-1014.

Loudin, J., D. Simanovskii, et al. (2007). "Optoelectronic retinal prosthesis: system design and performance." Journal of Neural Engineering **4**: S72-S84.

Lovell, N., J. Morley, et al. (2010). "Biological-Machine stystems integration: Engineering the neural interface." Proceedings of the IEEE **98**(3): 418-431.

Lowenstein, D., P. Chan, et al. (1991). "The stress protein response in cultured neurons: characterization and evidence for a protective reole in excitotoxicity." Neuron **7**: 1053-1060.

Lowenstein, J., J. Rizzo, et al. (1999). "Novel retinal adhesive used to attach electrode array to retina." Investigative Ophthalmology and Visual Science **40**(4): S733.

Lund, B. (2006). "Laser retinal thermal damage threshold: impact of small scale ocular motion." Journal of Biomedical Optics **11**(6).

Lyons, B., W. Obana, et al. (1986). "Chronic histological effects of ultrasonic hyperthermia on normal feline brain tissue." Radiation Research **106**: 234-251.

Majii, A., M. Humayun, et al. (1999). "Long term histological and electrophysical results of an inactive epiretinal electrode array implantation in dogs." Investigative Ophthalmology and Visual Science **40**(9).

Margalit, E., M. Maia, et al. (2002). "Retinal prosthesis for the blind." Survey of Ophthalmology **47**(4): 335-356.

Marshall, J. (1969). "Thermal and mechanical mechanisms in laser damage to the retina." Investigative Ophthalmology **9**(2): 97-115.

Matweb (2010). Material Properties, http://www.matweb.com/.

MAXIM. (2008). "Resistive bridge basics: Part one."   Retrieved June 11, 2008, from http://www.maxim-ic.com/appnotes.cfm/an_pk/3426.

McDannold, N., R. King, et al. (2000). "Usefullness of MR Imaging-derived thermotherapy and dosimetry in determining the threshold for tissue damage induced by thermal surgery in rabbits." Radiology **216**: 517-523.

Merino, O., L. Peters, et al. (1978). "Effect of hyperthermia on the radiation response of the small jejunum." International Journal of Radiation, Oncology and Biological Physics **4**: 407-414.

Merrill, D., M. Bikson, et al. (2005). "Electrical stimulation of excitable tissue: design of efficacious and safe protocols." Journal of Neuroscience Methods **141**: 171-198.

Millard, R. and R. Shepherd (2007). "A fully implantable stimulator for use in small laboratory animals." Journal of Neuroscience Methods **166**: 168-177.

Milligan, A., J. MEtz, et al. (1984). "Effect of intersitial hyperthermia in the Chinese hamster." International Journal of Radiation, Oncology and Biological Physics **10**(295-263).

Minamisawa, H., M. Smith, et al. (1990). "The effect of mild hyperthermia and hypothermia on brain damage floowing 5, 10 and 15 minutes of forebrain ischemia." Annals of Neurology **28**(1): 26-33.

Ming, Y., P. Algvere, et al. (2004). "Subthreshold Transpupillary Thermotherapy Reduced Experimental Choroidal Neovascularization in the Mouse without Collateral Damage to the Neural Retina." Investigative Ophthalmology and Visual Science **45**(6): 1969-1974.

Miura, S., H. Nishiwaki, et al. (2003). "Non-invasive technique for monitoring chorioretinal temperature during transpupillary thermotherapy, with a thermosensitive liposome." Investigative Ophthalmology and Visual Science **44**(6): 2716-2721.

Mizutani, M., C. Gerhardinger, et al. (1998). "Muller cell changes in Human Diabetic Retinopathy." Diabetes **47**: 445-449.

Moore, K. and A. Agur (2002). Essential Clinical Anatomy, 2nd Edition, Lippencott, Williams & Wilkins.

Morimura, Y., A. Okada, et al. (2004). "Histological Effect and Protein Expression in Subthreshold Transpupillary Thermotherapy in Rabbit Eyes." Archives of Ophthalmology 122: 1510-1515.

Moriyama, E. (1990). "Cerebral blood flow changes during localized hyperthermia." Neurological Medicine Chir (Tokyo) 30: 923-929.

Moser, E., I. Mathieson, et al. (1993). "Association between brain temperature and dentate field potentials in exploring and swimming rats." Science 259.

Murphy, P., S. Patel, et al. (2001). "The minimum stimulus energy required to produce a cooling sensation in the human cornea." Journal of Ophthalmology, Physiology and Optometry 21(5): 407-410.

Nakauchi, K., T. Fujikado, et al. (2007). "Threshold suprachoroidal-transretinal stimulation current resulting in retinal damage in rabbits." Journal of Neural Engineering 4: S50-S57.

Nakazawa, T., M. Takeda, et al. (2007). "Attenuated Glial reactions and Photoreceptor Degeneratioon after Retinal Detachment in Mice Deficient in Glial Fibrillary Acidic Protein and Vimentin." Investigative Ophthalmology and Visual Science 48(6): 2760-2768.

Narasimhan, A., K. Jha, et al. (2010). "Transient simulations of heat transfer in human eye undergoing laser surgery." International Journal of Heat and Mass Transfer 53: 482-490.

Neumann, N., R. Kainer, et al. (1982). "reaction of normal equine eyes to radio-frequency current-induced hyperthermia " American Journal of Vetinary research 43: 1938-1944.

Newland, H., J. Hiller, et al. (1996). "Prevalence and causes of blindness in the South Australian population aged 50 and over." Ophthalmic Epidemiology 3: 97-107.

Ng, E. and E. Ooi (2006). "FEM stimulation of the eye structure with bioheat analysis." Computer Methods and Programs in Biomedicine 82: 268-276.

Ng, E. and E. Ooi (2007). "Bioheat transfer in the human eye: A boundary element approach." Engineering Analysis with Boundary Elements 31: 494-500.

Ng, E. and E. Ooi (2007). "Ocular surface temperature: A 3D FEM prediction using bioheat equation." Computers in Medicine and Biology 37: 829-835.

Ng, E. and E. Ooi (2008). "A comparative study between the two-dimensional and three-dimensional human eye models." Mathematical and Computer Modelling 48: 712-720.

Nimmerjahn, A., F. Kirchoff, et al. (2005). "Resting microglial cells are highly dynamic surveillants of brain parenchyma in vivo." Science 308: 1314-1318.

Nolte, C., M. Matyash, et al. (2001). "GFAP Promoter-Controlled EGFP-Expressing in Transgenic Mice: A tool to visualise astrocytes and astrogliosis in Living Brain Tissue." GLIA 33: 72-86.

Normann, R., E. Maynard, et al. (1996). "Cortical implants for the blind." IEEE Spectrum 33(5): 54-59.

Ohira, A., E. deJuan, et al. (1991). "Long-term histologic and electrophysiologic evaluation of the alloy retinal tack." Graefe's Archives of Clinical and Experimental Ophthalmology 229: 95-98.

Okada, M., M. Matsumura, et al. (1990). "Muller cells in detached human retina express glial fibrillary acidic protein and vimentin." Graefe's Archives of Clinical and Experimental Ophthalmology 228: 467-474.

Okuno, T. (1991). "Thermal effect of Infra-Red radiation on the eye: a study based on a model." Ann Occup Hyg 35(1): 1-12.

Olsen, E. and R. McKeon (2004). "Characterization of cellular and neurological damage following unilateral hypoxia/ischemia." Journal of Neurological Sciences 227: 7-19.

Ooi, E. and E. Ng (2007). "Ocular surface temperature: A 3D FEM prediction using bioheat equation." Computers in Medicine and Biology 37: 829-835.

Opie, N, L., Burkitt, A, N., Meffin, H., Grayden, D, B (In Press). "Heating of the eye by a retinal prosthesis: Modeling, cadaver and in vivo study" IEEE Transactions on Biomedical Engineering

Organisciak, D., R. Darrow, et al. (1995). "Hyperthermia accelerates retinal light damage in rats " Investigative Ophthalmology and Visual Science 36(6): 997-1008.

Oyster, C. (1999). The human eye: Structure and Function. Birmingham, Raven Press.

Oyster, C., Ed. (1999). The Human Eye: Structure and Function. Birmingham, Raven Press.

Palanker, D. (2010). Photovoltaic retinal prosthesis: System design and electrophysiological testing. The Eye and The Chip WOrld COngress on Artificial Human Vision, Detroit, MI, USA.

Palanker, D., A. Vankov, et al. (2005). "Design of a high-resolution optoelectronic retinal prosthesis." Journal of Neural Engineering 2: S105-S120.

Pardue, M., E. Stubbs, et al. (2001). "Immunohistochemical studies of the retina following long term implantation with subretina microphotodiode arrays." Experimental Eye Research 73: 333-343.

Paulus, Y., A. Jain, et al. (2008). "Healing of retinal photocoagulation lesions." Investigative Ophthalmology and Visual Science 49(12): 5540-5545.

PCB (2009). Properties of Polyimide Substrates, The PCB Company Pty. Ltd.

Peyman, G., A. Chow, et al. (1998). "Subretinal semiconductor microphotodiode array." Ophthalmic Surgery and Lasers **29**: 234-241.

Pezaris, J. (2010). Psychophysical Performance of Simulated Thalamic Visual Prosthesis. The Eye and The Chip World Congress on Artificial Human Vision, Detroit, MI, USA.

Pezaris, J. and E. Eskandar (2009). "Getting signals into the brain: visual prosthetics through thalamic microstimulation." Neurosurgery Focus **27**(1): 1-19.

Pezaris, J. and R. Reid (2009). "Simulations of Electrode Placement for a Thalamic Visual Prosthesis." IEEE Transactions on Biomedical Engineering **56**(1): 172-178.

Philip, J., Long, MC., Quinn, MD., Newbower, RS (1984). "Continuous themal measurement of cardiac output." IEEE Transactions on Biomedical Engineering **31**(5): 393-400.

Piyathaisere, D., E. Margalit, et al. (2003). "Heat effects on the retina." Ophthalmic Surgery, Lasers and Imaging **34**(2): 114-120.

Polhamus, G. and A. Welch (1975). "Effect of pre-exposure fundus temperature on threshold lesion temperatures in the laser irradiated rabbit retina." Investigative Ophthalmology **14**(7): 562-565.

Prince, J., C. Diesem, et al. (1960). Anatomy and Histology of the Eye and Orbit in Domestic Animals. Springfield, Illinois, USA, Thomas Books.

Prionas, S., M. Taylor, et al. (1985). "Thermal sensitivity to single and double heat treatments in normal canine liver." Cancer Research **45**: 4791-4797.

Qiu, G., M. Seiler, et al. (2005). "Photoreceptor differentiation and integration of retinal progenitor cells transplanted into transgenic rats." Experimental Eye Research **4**: 515-525.

Quraishi, H. and I. Brown (1995). "Expression of heat shock protein 90 (hsp90) in neural and non-neural tissues of the control and hyperthermic rabbit." Experimental Cell Research **219**: 358-363.

Radtke, N., R. Aramant, et al. (2004). "Vision change after sheet transplant of fetal retina with retinal pigment epithelium to a patient with retinitis pigmentosa." Arch Ophthalmology **8**: 1159-1165.

Ramirez, J., A. Ramirez, et al. (2001). "Changes in Astrocytes in Retinal Agina and Age-Relater Macular Degeneration." Experimental Eye Research **73**: 601-615.

Ransohoff, R. and V. Perry (2009). "Microglial physiology: unique stimuli, specialized responses." Annual Review of Immunology **27**: 119-1145.

Ransohoff, R. and V. Perry (2009). "Microglial Physiology: Unique Stimuli, Specialized Responses." Annual Review of Immunology **27**: 119-145.

Rasohoff, R. and V. Perry (2009). "Microglial Physiology: Unique Stimuli, Specialized Responses." Annual Review of Immunology **27**: 119-1145.

Rawson, R., J. Hardy, et al. (1967). "Visceral Tissue Vascularization: An Adaptive Response to High Temperature." Science **158**(3805): 1203-1204.

Rawson, R., K. Quick, et al. (1969). "Thermoregulatory Responses to Intra-Abdominal Heating of Sheep." Science **165**(3896): 919-920.

Ray, A., l. Colodetti, et al. (2009). "Immunocytochemical analysis of retinal neurons under electrical stimulation." Brain Research **1255**: 89-97.

Reitsamer, H., H. Groiss, et al. (2000). "Computer-controlled impalement of cells in retinal wholemounts visualized by infrared CCD imaging on an inverted microscope." Journal of Neuroscience Methods **95**: 47-53.

Rem, A., J. Oosterhuis, et al. (2003). "Transcleral thermotherapy." Arch Ophthalmology **121**: 510-516.

Resnikoff, S., D. Pascolini, et al. (2002). "Global data on visual impairment in the year 2002." Bulletin of the World Health Organisation **82**(11): 811-890.

Riva, C., J. Grunwald, et al. (1985). "Blood velocity and vollumetric flow rate in human retinal vessels." Investigative Ophthalmology and Visual Science **26**: 1124-1132.

Rizzo, J. (2010). The status of the Boston retinal implant project. The Eye and The Chip World Congress on Artificial Human Vision, Detroit, MI, USA.

Rizzo, J., M. Socha, et al. (1994). "Development of a silicone retinal implant: surgical methods and mechanical design." Investigative Ophthalmology and Visual Science **35**(4): 1380.

Rizzo, J. and J. Wyatt (1997). "Prospects for a visual prosthesis." Neuroscientist **3**: 251-262.

Roberts, D. (2002). Signals and Perception: The Fundamentals of Human Perception, Palgrave & MacMillan.

Rodrigues, B., D. Sigg, et al. (1998). " Voltage gating of shaker K+ channels." Journal of General Physiology **112**: 223-242.

Roider, J., R. Brinkmann, et al. (2000). "Subthreshold (retinal pigment epithelium) photocoagulation in macular diseases: a pilot study." British Journal of Ophthalmology **84**: 40-47.

Rosa, M. and R. Tweedale (2003). Maps of the visual field in the cerebral cortex of primates: functional organisation and significance, CRC Press.

Sachs, H., T. Schanze, et al. (2005). "Subretinal implantation and testing of polyimide film electrodes in cats." Graefe's Archives of Clinical and Experimental Ophthalmology **243**: 464-468.

Sailer, H., K. Shinoda, et al. (2007). "Investigation of thermal effects of infrared lasers on the rabbit retina: a study in the course of development of an active subretinal prosthesis." Graefe's Archives of Clinical and Experimental Ophthalmology **245**: 1169-1178.

Santos, A., D. Martin-Oliva, et al. (2009). "Microglial Response to Light-Induced Photoreceptor Degeneration in the Mouse Retina." The Journal of Comparative Neurology: 478-492.

Sapoff, M., Oppenheim, RM (1963). "Theory and application of self heated thermistors." Proceedings of the IEEE: 1292-1305.

Sauerland, E. (1999). Grant's Dissector, 12th Edition, Lippencott, Williams & Wilkins.

Schanze, T., H. Sachs, et al. (2006). "Implantation and testing of subretinal film electrodes in domestic pigs." Experimental Eye Research **82**: 332-340.

Schmued, L., C. Albertson, et al. (1996). "Fluoro-Jade: a novel fluorochrome for the sensitive and reliable histochemical localization of neuronal degeneration." Brain Research **751**: 37-46.

Schmued, L., C. Stowers, et al. (2005). "Fluoro-Jade C results in ultra high resolution and contrast labeling of degenerated neurons." Brain research **1035**: 24-31.

Schmued, L. C. and K. J. Hopkins (2000). "Fluouro-Jade B: A high affinity fluorescent marker for the localization of neuronal degeneration." Brain Research **874**: 123-130.

Schraermeyer, U., G. Thumann, et al. (2001). "Subretinally transplanted embryoinic stem cells rescue photoreceptor cells from degeneration in the RCS rats." Cell Transplant **8**: 673-680.

Schwan, H., F. Gekeler, et al. (2001). "Studies on the feasibility of a subretinal visual prosthesis: data from Yuctan micropig and rabbit." Graefe's Archives of Clinical and Experimental Ophthalmology **239**: 961-967.

Schwartz, B. and M. Feller (1962). "Temperature gradients in the rabbit eye." Investigative Ophthalmology **1**(4): 513-520.

Scott, J. (1988). "The computation of temperature rises in the human eye induced by infrared radiation." Physics in Medicine and Biology **33**(2): 243-257.

Scott, J. (1988). "A finite element model of heat transport in the human eye." Physics in Medicine and Biology **33**(2): 227-241.

Seese, T., H. Harasaki, et al. (1998). "Characterisation of the tissue morphology, angiogenesis and temperature in the adaptive response of muscle tissue to chronic heating." Laboratory Investigation **78**(12): 1553-1561.

Seiler, M. and R. Aramant (1998). "Intact sheets of fetal retina transplanted to restore damaged rat retinas." Investigative Ophthalmology and Visual Science **39**(11): 2121-2131.

Sekirnjak, C., P. Hottowy, et al. (2008). "High-resolution electrical stimulation of primate retina for epiretinal implant design." Journal of Neuroscience **28**(17): 4446-4456.

Seo, J., S. Paik, et al. (2006). "Silicon retinal tack for the epiretinal fixation of the polyimide electrode array." Current Applied Physics **6**: 649-653.

Sharma, H. and P. Hoopes (2003). "Hyperthermia induced pathophysiology and the central nervous system." International Journal Of Hyperthermia **19**(3): 325-354.

Sharma, H. and P. Hoopes (2003). "Hyperthermia induced pathophysiology of the central nervous system." Int. J. Hyperthermia **19**: 325-354.

She, H., X. Li, et al. (2006). "Subthreshold transpupillary thermotherapy of the retina and experimental choroidal neovascularization in a rat model." Graefe's Archives of Clinical and Experimental Ophthalmology **244**: 1143-1151.

Shen, Q., H. Cheng, et al. (2006). "Magnetic Resonance Imaging of Tissue and Vascular Layers in the Cat Retina." Journal of Magnetic Resonance Imaging **23**: 465-472.

Silverman, M. and S. Hughes (1989). "Transplantation of photoreceptors to light damaged retina." Investigative Ophthalmology and Visual Science **30**(8): 1684-1690.

Singh, V., C. Cela, et al. (2007). "Bioelectromagnetics for a retinal prosthesis to restore partial vision to the blind." International Conference on Electromagnetics in Advanced Applications: 1030-1033.

Singh, V., A. Roy, et al. (2008). "On the thermal Elevation of a 60-electrode epiretinal prosthesis for the blind." IEEE Transactions on Biomedical Circuits and Systems **2**(4): 289-300.

Sivaprakasam, M., W. Liu, et al. (2005). "A variable range bi-phasic current stimulus driver circuitry for an implantable retinal prosthetic device." IEEE Journal of Solid State Circuits **40**(3): 763-771.

Smith, G. and D. Atchison (1997). The Eye. Cambridge, Cambridge University Press.

Soltys, Z., M. Ziaja, et al. (2001). "Morphology of reactive microglia in the injured cerebral cortex. Fractal analysis and complementary quantitative methods." Journal of Neuroscience Research **63**: 90-97.

Soora, S., K. Gosalia, et al. (2008). "A comparison of two and three dimensional dipole antennas for an implantable retinal prosthesis." IEEE Transacions on Antennas and Propagation **56**(3): 622-629.

Stiles, J., I. Kovyanzina, et al. (1999). "Temperature Sensitivity of miniature endplate currents is mostly governed by channel gating: Evidence from optimized recordings and monte-carlo simulations." Biophysical Journal **77**: 1177-1187.

Streit, W., M. Graeber, et al. (1988). "Functional plasticity of Microglia: A Review." GLIA **1**: 301-307.

Suaning, G., W. Gill, et al. (2003). "Monitoring the electrical behavior of the electrode tissue interface." IFESS.

Suaning, G., L. Hallum, et al. (2004). An efficient multiplexing method for addressing large numbers of electrodes in a visual prosthesis. Proceedings of the 26th International IEEE EMBS, San Francisco, USA.

Suaning, G. and N. Lovell (2002). "CMOS stimulation system with 100 channels, scalable output and bi-directional radio frequency telemetry." IEEE Transactions on Biomedical Engineering **48**(2): 248-260.

Suanning, G. and N. Lovell (2010). Australian research into a visual prosthesis for the suprachoroidal space. The Eye and The Chip World Congress on Artificial Human Vision, Detroit, MI, USA.

Suzumura, A., T. Marunouchi, et al. (1991). "Morphological transformation of microglia in vitro." Brain Research **545**: 301-306.

Sykes, S., W. Robison, et al. (1981). "Damage to the monkey retina by broad-spectrum fluorescent light." Investigative Ophthalmology and Visual Science **20**(4): 425-434.

Tahvanainen, K., Nino, J., Halonen, P., Kuusela, T., Alanko, T., Laitinen, T., Lansimies, E., Hietanen, M., Lindholm, H (2007). "Effects of cellular phone use on ear canal temperature measured by NTC thermistors." Clinical Physiology and Functional Imaging **27**(3): 162-172.

Tallis, R. and H. Fillit (2003). Brocklehurst's Textbook of Geriatric Medicine and Gerontology, 6th Edition Churchill Livingstone.

Tasman, R. and B. Rover (2004). "Age related macular degeneration." Archives of Ophthalmology **122**(4).

Taylor, H., R. Guymer, et al. (2006). The impact of age-realted macular degeneration. Melbourne, Access Economics Pty. Ltd, University of Melbourne.

TC, M. C. (2008). TC Guide to thermocouple and resistance thermometry. Oakleigh, Victoria.

Terasawa, Y. (2010). Efficacy of Retinal Prosthesis Based on Suprachoroidal-transretinal Stimulation. The Eye and The Chip World Congress on Artificial Human Vision, Detroit, MI, USA.

Thanos, S., J. Mey, et al. (1993). "Treatment of the adult retina with microglia-supressing factors retards axotomy-induced neuronal degradation and enhances axonal regeneration in vivo and in vitro." Journal of Neuroscience **13**(2): 455-466.

Tokuda, K., T. Tsukamoto, et al. (2004). "Evaluation of toxicity due to vial stains in isolated rat retina." Acta Ophthalmologica Scandinavica **82**: 189-194.

Turano, K., S. Herdman, et al. (1993). "Visual stabilization of posture in retinitis pigmentosa and in artificially restricted visual fields." Investigative Ophthalmology and Visual Science **34**(10): 3004-3010.

Uney, J., J. Kew, et al. (1993). "Transfection-mediated expression of human Hsp70i protects rat dorsal root ganglion neurons and glia from severe heat stress." FEBS Lett. **334**: 313-316.

Valvano, J., Cochran, JR., Diller, KR (1985). "Thermal conductivity and diffusivity of biomaterials measured with self heating thermistors." International Journal of Thermophysics **6**(3): 301-311.

Vander, Sherman, et al. (2001). Human Physiology: The Mechanisms of Body Function, 8th Edition.

Vaughn, D., P. Erickson, et al. (1990). "Glial Fibrillary Acidic Protein (GFAP) Immunoreactivity in Rabbit Retina: Effect of Fixation." Experimental Eye Research **50**: 385-392.

Vincelette, R., B. rockwell, et al. (2009). "Trends in retinal damage thresholds from 100-millisecond near-infrared laser radiation exposures: a study at 1100, 1130, 1150 and 1319nm." Lasers in Surgery and Medicine **41**: 382-390.

Vingolo, E., M. Rocco, et al. (2008). "Slowing the degenerative process, long lasting effect of hyperbaric oxygen therapy in retinitis pigmentosa." Graefe's Archives of Clinical and Experimental Ophthalmology **246**: 93-98.

Vizi, E. (1998). "Different temperature dependence of carrier mediated (cytoplasmic) and stimulus evoked (exocytotic) release of transmitter: a simple method to separate the two types of release." Neurochemistry International **33**: 359-366.

Vogel, P., E. Dux, et al. (1997). "Evidence of apoptosis in primary neuronal cultures after heat shock." Brain Research **746**: 205-213.

Wainwright, P. (2007). "Computational modelling of tempearture rises in the eye in the near field of radiofrequency sources at 380, 900 and 1800 MHz." Physics in Medicine and Biology **52**: 3335-3350.

Wang, G., W. Liu, et al. (2004). "A closed loop transcutaneous power transfer system for implantable devices with enhanced stability." IEEE ISCAS **IV**: 17-20.

Wang, J. and O. Fujiwara (1999). "FDTD computation of temperature rise in the human head for portable telephones." IEEE Transactions on Microwave Theory and Techniques **47**(8): 1528-1534.

Ward, B. and R. Bruce (1971). "Role of body temperature in the definition of retinal burn threshold." Investigative Ophthalmology **10**(12): 955-958.

Wasowicz, M., C. Morice, et al. (2002). "Long term effects of light damage on the retina of albino and pigmented rats." Investigative Ophthalmology and Visual Science **43**(3): 813-820.

Weiland, J. (2010). Factors Affecting Thresholds in Epiretinal Stimulation. The Eye and The Chip World Congress on Artificial Human Vision, Detroit, MI, USA.

Weiland, J. and M. Humayun (2008). "visual Prosthesis." Proceedings of the IEEE **96**(7): 1076-1084.

Weiland, J., M. Humayun, et al. (1999). "Understanding the origin of visual precepts elicited by electrical stimulation of the human retina." IEEE Transacions on Antennas and Propagation **1**: 2274-2286.

Weiland, J., M. Humayun, et al. (1999). "Pattern electrical stimulation of the human retina." Vision Research **39**.

Welch, A. (1984). "The thermal response of laser irradiated tissue." IEEE Journal of Quantum Electronics **QE-20**(12): 1471-1481.

Welch, A. and G. Polhamus (1984). "Measurement and prediction of thermal injury in the retina of the rhesus monkey." IEEE Transactions on Biomedical Engineering **31**(10): 633-644.

White, M., L. Luca, et al. (2007). "Cellular mechanisms of neuronal damage from hyperthermia." Progress in Brain Research **162**: 347-371.

White, T., M. Mainster, et al. (1970). "Chorioretinal Thermal Behavior." Bulletin of Mathematical Biophysics **32**: 315-322.

WHO. (2004). "Fact Sheet No. 282 - Magnitude and causes of visual impairment." Retrieved June 12, 2008, from http://www.who.int/mediacentre/factsheets/fs282/en/.

Wong, Y., S. Chen, et al. (2009). "Focal activation of the feline retina via a suprachoroidal electrode array." Vision Research **49**(8): 825-833.

Wu, K., M. Madigan, et al. (2003). "Differential expression of GFAP in early v late AMD: a quantitative analysis." British Journal of Ophthalmology **87**: 1159-1166.

Wyatt, J. (1996). "Ocular implants for the blind." IEEE Spectrum: 49-53.

Yamauchi, Y., L. Franco, et al. (2005). "Comparison of electriclaly evoked cortical thresholds generated with subretinal or suprachoroidal placement of a microelectrode array in the rabbit." Journal of Neural Engineering **2**: S48-S56.

Yerushalmi, Z. Shpirer, et al. (1983). "Normal tissue response to localized deep microwave hyperthermia in the rabbit's prostate: a preclinical study." International Journal of Radiation, Oncology and Biological Physics **9**: 77-82.

Zhang, C., T. Lam, et al. (2005). "Hetrogeneous population of microglia/macrophages in the retina and their activation after retinal ischemia and reperfusion injury." Experimental Eye Research **81**: 700-709.

Zhou, M., W. Liu, et al. (2006). A transcutaneous data telemetry system tolerant to power telemetry interface. Proceedings of the 28th IEEE EMBS Annual International Conference, New York City, USA.

Zierhofer, C. and E. Hochmair (1997). "Coil design for improved power transfer efficieny in inductive links." International Conference of Engineering in Medicine and Biology **4**: 1538-1539.

Zimmerman, M., N. Chaimanonart, et al. (2006). In vivo RF powering for advanced biological research. Proceedings of the 28th IEEE EMBS Annual International Conference, New York City, USA.

Zrenner, E. (2010). Subretinal Implants Allow Blind RP Patients to Read Letters and Combine Them to Words At Once Without Training. The Eye and The Chip World Congress on Artificial Human Vision, Detroit, MI, USA.

Zrenner, E., A. Stett, et al. (1999). "Can subretinal microphotodiodes sucessfully replace degenerated photoreceptors?" Vision Research **39**: 2555-2567.

Zrenner, E., R. Wilke, et al. (2008). Visual sensations mediated by subretinal microelectrode arrays implanted into blind retinitis pigmentosa patients. Proceedings of the 13th Annual Conference of the IFESS, September 21-25, Freiburg, Germany.

Zurbuchen, J. (2000). "Precision thermistor thermometry." Measurement Specialities Application Note **TD002**.

APPENDIX 1 – THERMAL DAMAGE STUDIES

Table A1.1. Published data for thermal damage caused by laser irradiation.

Author	Model	Laser		Measurement		Test			Endpoint
		Type	Spot Size	Temperature	Analysis	Temperature (°C)	Power	Time	
(Clarke, Ham et al. 1969)	Primate	Argon, 5.145 nm	10 μm	-	-	+9 – 10	-	-	Thermal lesions
						-	2 mW	250 ms	Thermal Damage
(Marshall 1969)	Rabbit	Ruby, 694.3 nm	100-800 μm	Thermocouple	Histology (Toluene Blue), Electron Microscopy, Radioautography	-	0.65 J/cm^2	-	Threshold determined by depletion of pigment granules
(Bresnick, Frisch et al. 1970)	Rhesus Monkey	Argon, 5.145 nm	1.6 mm	-	Ophthalmoscopy, Histology	-	-	12	ED50 threshold 19.0mW (Ophthalmoscopic), 15.0 (Pathologic)
								125	ED50 threshold 15.5mW (Ophthalmoscopic), 11.5 (Pathologic)
(Lappin and Coogan 1970)	Rhesus Monkey (n=1)	He:Ne	-	-	Histology (Paragon Stain), 1 day post	-	6.4 mW	100 ms	Damage. Histological lesions, small retinal burn, pyknosis in outer nuclear layer, swollen hyperchromatic cone cell inner segment, interstitial oedema and slight swelling of endothelium of choriocapillaris
(Gibbons and Allen 1977)	Rhesus monkey	Argon, 514.5 nm	-	-	Histology and Ophthalmoscopy	-	9.4 mW	0.5 s	ED50 threshold 1 hour post
							9.0 mW	0.5 s	ED50 threshold 24 hours post
							6.4 mW	5.0 s	ED50 threshold 1 hour post
							5.6 mW	5.0 s	ED50 threshold 24 hours post
							5.4 mW	30.0 s	ED50 threshold 1 hour post
							2.5 mW	30.0 s	ED50 threshold 24 hours post
							4.4 mW	120.0 s	ED50 threshold 1 hour post
							0.54 mW	120.0 s	ED50 threshold 24 hours post
							1.8 mW	1000 s	ED50 threshold 1 hour post
							0.12 mW	1000 s	ED50 threshold 24 hours post
(Polhamus and Welch 1975)	Rabbit (n=20)	Argon, 488 nm	200 μm	Thermocouple, Vitreous	Ophthalmoscopically determined lesions	Fundus 30 - 44.5			Thresholds. Threshold Temperature Rise (Ophthalmoscopically visible lesions) = -1.15 x Fundus Temperature + 52.4

Table A1.1 (cont'd). Published data for thermal damage caused by laser irradiation.

Author	Model	Laser		Measurement		Test			Endpoint
		Type	Spot Size	Temperature	Analysis	Temperature (°C)	Power	Time	
(Ham, Ruffolo et al. 1978)	Rhesus Monkey (n=10)	441 nm Blue, 2500W Xenon Lamp	-	-	1 h – 1 d post	-	62 μW 30 J/cm²	1000 s	Fundoscopic photochemical lesion threshold
							30-90 J/cm²	1000 s	No Damage
					2 d post	-	30-90 J/cm²	1000 s	RPE disruption, choroidal damage, pigmentary change in lesion area and mild oedema
					5-6 d post	-	30-90 J/cm²	1000 s	Damage and disorientation of outer segments, debris-laded macrophages in subretinal space, disruption, proliferation and hypo-pigmentation of RPE
					10-11 d post	-	30-90 J/cm²	1000 s	Damage with recovery. Hypo-pigmentation of RPE cells, no cell proliferation, choroid and outer segments of rods and cones almost normal (slightly shorter)
					30 d post	-	30-90 J/cm²	1000 s	Damage with recovery. Retinal pigment epithelium, outer segment and choroid are normal with macrophages still present in subretinal space
					60 d post	-	30-90 J/cm²	1000 s	Only slight hypo-pigmentation of lesion
					90 d post	-	30-90 J/cm²	1000 s	No Damage
(Welch and Polhamus 1984)	Rhesus Monkey (n=60+)	488 nm Argon, 647nm Krypton	-	10-30μm Thin Film thermocouple, Vitreous (100-200u from retina)	5 m post	+9.5	7.5 mW	1000 s	Threshold with 21 μm lesion radius
						+13	11 mW	100 s	Threshold with 34 μm lesion radius
						+8.5	16 mW	100 s	Threshold with 145 μm lesion radius
						+15	22 mW	60 s	Threshold with 120 μm lesion radius
						+14	22 mW	30 s	Threshold with 100 μm lesion radius
						+14	12 mW	10 s	Threshold with 39 μm lesion radius
						+15	7.4 mW	10 s	Threshold with 29 μm lesion radius
						+21	16 mW	10 s	Threshold with 104 μm lesion radius
						+18.3	26.6 mW	1 s	Threshold
						+15.7	28.1 mW	1 s	Threshold
						+27.4	49 mW	0.1 s	Threshold
						+22.5	41.1 mW	0.1 s	Threshold
						+21	23 mW	0.03 s	Threshold with 34 μm lesion radius
						+41	34 mW	0.03 s	Threshold with 35 μm lesion radius
						+46	142 mW	0.03 s	Threshold with 25 μm lesion radius
						+37	57 mW	0.01 s	Threshold with 33 μm lesion radius
						+34	97 mW	0.01 s	Threshold with 37 μm lesion radius
						+21	7 mW	0.003 s	Threshold with 38 μm lesion radius
						+31	230 mW	0.003 s	Threshold with 65 μm lesion radius
						+33	310 mW	0.002 s	Threshold with 50 μm lesion radius

Table A1.1 (cont'd). Published data for thermal damage caused by laser irradiation.

Author	Model	Laser		Measurement		Test			Endpoint
		Type	Spot Size	Temperature	Analysis	Temperature (°C)	Power	Time	
(Birngruber, Puliafito et al. 1987)	Chinchilla Grey Rabbits	Argon, 625 nm, 80 fs pulses	80 µm	-	Fluorescein Angiography, 1 h post	-	0.75 µJ	-	E50 threshold for swollen photoreceptors, destruction of outer segments, mechanical damage to melanin granules
					Ophthalmoscopy, 1 h post	-	4.5 µJ	-	E50 threshold of damage to RPE, sub-cellular structure damage, melanin granule disruption, neural retina, outer segments of photoreceptor layers and nuclei
							70 µJ	-	No damage to unpigmented retinal tissue
(Krauss, Puliafito et al. 1986)	Chinchilla Rabbit (n=1)	Argon, 514.5 nm	800 µm	-	Fundoscopy, Histology (H&E), 1 h post	-	0.51 J/cm², 1W	10 ms	No ophthalmoscopically visible damage
							0.64 J/cm², 1.25W	10 ms	Damage characterised by retinal photocoagulation (whitish irradiated area)
							0.76 J/cm², 1.5W	10 ms	Damage characterised by hyper-stained photoreceptors (indicating thermal necrosis), mild compression of photoreceptor layer, mild oedema in inner retinal layers and mild nuclear pyknosis
							1.9 J/cm2, 0.375W	100 ms	Severe damage to neural retina, 300µm central lesion, lost GCL integrity, INL widely dispersed, ONL elevated and depressed with severe condensation within the photoreceptor layer
(Kremers and Norren 1989)	Macaque Monkey	Xenon Arc Lamp, 450 W	-	-	Fundoscopy	-	230 J/cm²	10 m – 12h	Fundoscopic threshold defined as a just visible change (a patch smaller than the irradiated spot and with fuzzy edges)
					Densitometry	-	5 mW/cm², 600 J/cm2	10 m – 12h	Densitometry long term damage threshold
(Gorgels, Beek et al. 1997)	Long-Evans Rats	Argon, 488 nm	-	Thermistor, Rectal	Histology Toluidine Blue, Fundoscopy, 3 d post	30-40.5	0.1-1.0 W/cm²	-	Damage threshold decreased by 0.026 log (J/cm²)/°C increase in rectal temperature

Table A1.1 (cont'd). Published data for thermal damage caused by laser irradiation.

Author	Model	Laser		Measurement		Test			Endpoint
		Type	Spot Size	Temperature	Analysis	Temperature (°C)	Power	Time	
(Roider, Brinkmann et al. 2000)	Human, diabetic maculopathy (n=12), soft drusen (n=10), central serous retinopathy (n=4)	Nd:YAG, 527 nm	160 μm, 100-500 500 Hz pulses,	-	Ophthalmoscopy	-	30-130 μJ per pulse	-	No Damage
					Fluorescein Angiography	-	30-130 μJ per pulse	-	White lesion caused by photocoagulation of photoreceptors
(Desmettre, Maurage et al. 2001)	Rabbit (n=6)	810 nm, 92-150 mW	1.3 mm	Estimation of maximum temperature reached for 60 seconds irradiation	Histology, Hsp70 immunoreactivity, HES staining	50	127 mW 532 J/cm^2	60 s	No Damage
							150 mW 629 J/cm^2	60 s	Photocoagulation threshold (faint retinal whitening)
							98 mA 411 J/cm^2	60 s	Hsp70 hyper-expression restricted to cytoplasm of choroidal cells
							92 mW 386 J/cm^2	60 s	No Damage
(Desmettre, Maurage et al. 2003)	Pigmented Rabbits (n=9)	810 nm diode	1.3 mm	-	Histology, Microscopy	-	90 mW	60 s	No Damage
							130 mW	60 s	Mild Damage. Low congestion on choroid: the lumen of capillaries dilated by erythrocytes. No haemorrhage, necrosis, atrophy or detachment observed with HES staining and no tissue architecture modification observed
							150 mW	60 s	
							150 mW	30 s	No Damage
							210 mW	30 s	Mild Damage. No observable damage although Hsp70 immunoreactivity was strong
							250 mW	30 s	Photocoagulation threshold
							180 mW	15 s	No Damage.
							250 mW	15 s	Mild Damage. Vascularisation of endothelial cells, strong Hsp70 immunoreactivity in choroidal, non-pigmented cells and choroidal capillary endothelial cells
							300 mW	15 s	

Table A1.1 (cont'd). Published data for thermal damage caused by laser irradiation.

Author	Model	Laser		Measurement		Test			Endpoint
		Type	Spot Size	Temperature	Analysis	Temperature (°C)	Power	Time	
(Framme, Schuele et al. 2004)	Chinchilla Rabbits (n=6)	Nd:YAG , 527 nm	116 μm	-	Fundus Photography, Histology, Angiography	-	1 pulse	200 ns	Damage threshold of 354 mJ/cm^2 (ophthalmoscopy, Oph) and 123 mJ/cm^2 (angiography, FA)
							10 pulses	200 ns	Damage threshold of 335 mJ/cm^2 (Oph), 89 mJ/cm^2 (FA)
							100 pulses	200 ns	Damage threshold of 249 mJ/cm^2 (Oph), 42 mJ/cm^2 (FA)
							1 pulse	1.7 ms	Damage threshold of 461 mJ/cm^2 (Oph), 282 mJ/cm^2 (FA)
							10 pulses	1.7 ms	Damage threshold of 312 mJ/cm^2 (Oph), 123 mJ/cm^2 (FA)
							100 pulses	1.7 ms	Damage threshold of 356 mJ/cm^2 (Oph), 131 mJ/cm^2 (FA)
							11 μJ (10 pulses)	200 ns	RPE damage including condensed cores, enhanced staining, debris on Bruch's membrane, relaxed photoreceptor distal ends
(Ibarra, Hsu et al. 2004)	Albino Rabbit (n=17), Pigmented Rabbit (n=14	810 nm	0.78 mm	36 Gauge Micro-thermocouple, posterior pole of inner limiting membrane	Visual determination of lesions	+11.8	950 mW	60 s	Threshold. Faint retinal greying (albino)
						+5.28	90 mW	60 s	Threshold. Faint retinal greying (pigmented)
(Ming, Algvere et al. 2004)	Mice (n=42)	810 nm Diode	1.2 mm	-	Electron Microscopy	-	50 mW	60 s	3 days post - No Damage.
							60 mW	60 s	3 days post – Damage, slight oedema of photoreceptor layer
							60 mW	60 s	14 days post - Damage, shortening of outer segments
							80 mW	60 s	1 day post – Damage, retinal whitening, pykonisis and vacuolization of cells in inner and outer retina
							80 mW	60 s	7 days post - Thickening of RPE, thrombus formation in choroidal capillaries, macrophage-like granules accumulation in inner nuclear layer and disintegration of outer nuclear layer

Table A1.1 (cont'd). Published data for thermal damage caused by laser irradiation.

Author	Model	Laser		Measurement		Test			Endpoint
		Type	Spot Size	Temperature	Analysis	Temperature (°C)	Power	Time	
(Morimura, Okada et al. 2004)	Rabbit	810 nm	1.2 mm	-	Histology (Toluidine Blue), Ophthalmoscopy	-	50 mW 286 J/cm^2	60 s	No Damage
					Electron Microscope	-	50 mW, 71 J/cm^2	60 s	Damage, photoreceptor layer thinning and disruption of outer and inner segments
(Ben-Shlomo, Belokopytov et al. 2006 (n=25)	Pigmented DA Rats (n=25)	Argon, 514 nm, 544 nm	200 μm	-	Histology (Toludine Blue), Flash ERG	-	0.1 W	0.05 s	3 d post - Loss of photoreceptor nuclei, debris in ONL, outer and inner segment disruption, proliferation of RPE, B-wave amplitude of 351±104 μV
									20 d post - Damage similar to 3 d post with more INL tissue. B-wave amplitude of 350±112 μV
									60 d post - Thinning of subretinal membrane, B-wave amplitude of 456±106 μV
(Kim, Park et al. 2006)	Norwegian Brown Rats (n=126)	810 nm diode	50 μm	-	Histology, Electron Microscopy, Ophthalmoscopy	-	120 mW	60 s	1-3 days post - No Damage
							140 mW	60 s	1-3 days post - Definite morphological changes and peripapillary whitening observed
							100 mW	60 s	7 days post - No Damage
							120 mW	60 s	7 days post - Membrane like attachment of vitreous observed on optic nerve head
							100 mW	>60 s	7 days post - Peripapillary whitening observed
(She, Li et al. 2006)	Rat (n=81)	810 nm	2 mm	-	Fundus Fluorescence Angiography, TUNEL, Histology (H&E)	-	50 mW	60 s	White histo-pathological changes and sparse RPE disarrangement
							70 mW	60 s	INL and ONL thinning, disruption and pigmentation, widespread retinal oedema, damage and GC swelling

Table A1.1 (cont'd). Published data for thermal damage caused by laser irradiation.

Author	Model	Laser		Measurement		Test		Endpoint
		Type	Spot Size	Temperature	Analysis	Power	Time	
(Sailer, Shinoda et al. 2007)	Rabbits (n=9)	IR, 826.4 nm	3 mm 0.23 cm^2 sensor	25μm Type-K thermocouple, subretinal implant	Histology (H&E)		-	No Damage
(Paulus, Jain et al. 2008)	Rabbit (n=18)	523 nm Nd:YAG	330 μm	-	Fundus Photography, Histology (toluidine blue), Fluorescein Angiography	175 mW	100 ms — 1h post	Sharp lesions encompassing all retinal layers, RPE and choroid, retina edema and disorganisation present
							100 ms — 1d post	Lesion size reduced to 76% with edema of inner and outer retina, photoreceptor inner segments shortened, outer segments in disarray, vacuoles present between RPE and Bruch's membrane, loss of choroidal structures
							100 ms — 1w post	Lesion size reduced to 54%, extracellular edema absent, pigment cell invasion, gliotic tissue in all retinal layers, choroidal thickness normal
							100 ms — 1m post	Lesion size reduced to 40%, gliosis and pigmented cells present in all layers, RPE
							100 ms — 2m post	Lesion size reduced to 37% similar to 1m post
							100 ms — 4m post	Lesion size reduced to 36%, intraretinal pigmented cells absent
							10-50 ms — 1h post	Strong edema in inner retina, damaged inner and outer nuclear layers, large vacuoles in inner segment layers
							10-50 ms — 1d post	Decreased retinal edema, inner and outer photoreceptor segments reduced, central defect in ONL and INL (present in intense lesions) absent
							10-50 ms — 1w post	ONL and INL replaced by gliotic tissue and pigmented cells, RPE hypopigmented
							10-50 ms — 1m post	Lesion contraction to 40%, larger towards inner retina and smaller towards RPE, INL thickened, photoreceptors within lesion
							10-50 ms — 2m post	Cellular accumulation remained, decreased number of hyperpigmented cells
							10-50 ms — 4m post	Lesion maintained at 40%, normal INL structure at periphery but displaced at centre, gap in photoreceptor layer remained filled with gliosis and displaced INL cells
							5-7 ms — 1h post	Inner retinal largely unaffected, ONL hyperchromatic, RPE collapsed, outer photoreceptor segments disorganised
							5-7 ms — 1d post	Slight inner retina edema, inner segments shortened, outer segments displaced, ONL displaced towards RPE
							5-7 ms — 1w post	Lesion recovery to 34-69%, glial cells in photoreceptor layer, mild edema localised to outer retina, RPE restored, normal choroid
							5-7 ms — 1m post	Lesion contraction to 10%, absent gliosis in INL
							5-7 ms — 2m post	Lesion similar to 1m post
							5-7 ms — 4m post	Lesion distinguished by increased ONL density and vacuoles in inner segments, Photoreceptor morphology same as untreated retina

Table A1.1 (cont'd). Published data for thermal damage caused by laser irradiation.

Author	Model	Laser		Measurement		Test		Endpoint
		Type	**Spot Size**	**Temperature**	**Analysis**	**Power**	**Time**	
(Jain, Blumenkranz et al. 2008)	Rabbit	532 nm Nd:YAG	66, 132, 330 μm	-	Fundus Photography, Histology (Toluidine blue)	50 mW	10 ms	No damage
							20 ms	Fundus lesion (FL) 98 μm
							50 ms	FL 143 μm, Histological damage zone (HDZ) 96 μm
							100 ms	FL 148 μm, HDZ 82 μm
						100 mW	10 ms	No damage
							20 ms	FL 143 μm, HDZ 101 μm
							50 ms	FL 226 μm, HDZ 120 μm
							100 ms	FL 270 μm, HDZ 168 μm
						150 mW	10 ms	FL 103 μm, HDZ 132 μm
							20 ms	FL 197 μm, HDZ 146 μm
							50 ms	FL 305 μm, HDZ 281 μm
							100 ms	FL 344 μm, HDZ 252 μm
						200 mW	10 ms	FL 128 μm, HDZ 144 μm
							20 ms	FL 236 μm, HDZ 180 μm
							50 ms	FL 359 μm, HDZ 288 μm
							100 ms	FL 428 μm, HDZ 341 μm
						250 mW	10 ms	FL 162 μm, HDZ 185 μm
							20 ms	FL 251 μm, HDZ 204 μm
							50 ms	FL 403 μm, HDZ 322 μm
							100 ms	FL 487 μm, HDZ 362 μm
(Vincelette, rockwell et al. 2009)	Rhesus Monkey (n=4)	1110 nm, 1130 nm, 1150 nm, 1319 nm	-	-	Fundoscopy, Fluorescein Angiography,1-24 h post	193 mW 270 mW 872 mW 13,713 mW	100 ms	Threshold for 50% damage probability

Table A1.2. Published data for thermal damage caused by electromagnetic irradiation

Author	Model	EM Type	Measurement		Test			Endpoint
			Temperature	**Analysis**	**Temperature (°C)**	**Power**	**Time**	
(Ward and Bruce 1971)	Rhesus Monkey (n=12)	Xenon arc lamp, 1.5° field Xenon arc lamp, 3 °field	Thermistor, Rectal	Ophthalmoscopy	34.5	6 cal/sec.cm^2	100 ms	Thresholds determined by a slight greying, fundus-ground texture change and a change in the retinal reflex of the irradiated area
					38.5	3 cal/sec.cm^2	100 ms	
					34.5	13 cal/sec.cm^2	500 ms	
					39.5	6 cal/sec.cm^2	500 ms	
(Hirsch, Appleton et al. 1977)	Albino New Zealand Rabbits (n=35)	Microwave, 3000MHz	-	Slit Lamp Examination, Electron Microscope	-	50-200 mW/cm^3	15 min/d	No damage after 30 days
						300 mW/cm^3	15 min/d, 17.5 d	Congestion of limbal vessels, pupillary constriction, iritis, posterior subcapsular iridescence, vacuoles in posterior cortex of lens and posterior cataractous changes
						400 mW/cm^3	15 min/ d, 10 d	
						500 mW/cm^3	15 min/d, 5d	
(Sykes, Robison et al. 1981)	Rhesus Monkey (n=5), Pigtail Monkey (n=5)	Fluorescent light chamber, 5900-24700 lux 195–839 μW/cm^2	-	Electron Microscopy	-	5900 lux 195 μW/cm^2	12 h	Minor damage to less than 5% of macular photoreceptors
						195-361 μW/cm^2	12 h	Cone cell damage threshold
						361-615 μW/cm^2	12 h	Rod cell damage threshold
(Lagendijk 1982)	Rabbit, Human	Microwave, 2450MHz,	-	-	46 (rabbit)	-	30 min	Cataract production
					44 (human)	-	60 min	No damage
(Neumann, Kainer et al. 1982)	Horse (n=13), Pony (n=8)	RF, 2MHz	-	Ophthalmoscopy, Fluorescein Staining	48.7	-	30 s	Immediate damage, dense opaque electrode imprint regions, ulcerative keratitis persisted from day 2–6 with anterior uvitis from day 2-7
					56	-	30 s	Necrosis of limbus
(Yerushalmi, Shpirer et al. 1983)	Rabbit	Microwave	-	-	43.2	-	30 min	No Damage, 1 day – 3 month post
(Prionas, Taylor et al. 1985)	Canine	RF, 0.5MHz	Thermocouple	Histology (H&E)	40.5	-	30 min	Fibrosis and parenchymal cell loss at 28 d post
(Glaze and Turk 1986)	Canine (n=10)	RF, 2MHz	-	Ophthalmoscopy	50	-	10 s	Immediate damage, corneal opacification and epithelial disruption at electrode site. Ulcerative keratitis and anterior uvitis persisted for 4-6 d with stromal thinning, oedema, vascularisation and inflammatory cell infiltration

Table A1.2 (cont'd). Published data for thermal damage caused by electromagnetic irradiation

Author	Model	EM Type	Measurement		Test			Endpoint
			Temperature	Analysis	Temperature (°C)	Power	Time	
(Li, Zhou et al. 1987; Li, Qiu et al. 1988)	Pig	Microwave	-	-	45	-	30 min	Damage as percent of control, taken 48 hours post – 2% damage (degenerative necrosis or thrombosis)
					46	-	30 min	17% damage
					47	-	30 min	40% damage
					48	-	30 min	50% damage
					49	-	30 min	67% damage
					45	-	30 min	Damage as percent of control, taken 30 days post – 12% damage (fibrosis)
					46	-	30 min	23% damage
					47	-	30 min	30% damage
					48	-	30 min	34% damage
					49	-	30 min	51% damage
(Bollemeijer, Lagendijk et al. 1989)	Dutch Rabbit (n=5)	Microwave 2450 MHz 2.5 ms on/off pulses	Thermocouple sensors, anterior segment of lens and anterior segment of cornea	Histology	41.8	-	30 min	No damage
					42.6	-	30 min	No damage to eyelids, sclera, iris, choroid or retina damage to conjunctiva with oedema, hyperaemia inflammation, thinning of cornea 12 d post
					42.9	-	30 min	Reddening of eyelids, damage to conjunctiva and ciliary body, oedema, hyperaemia and inflammation, sclera swelling, corneal oedema and neovascularisation 12 days post
					43.5	-	30 min	Additional damage associated with chorioretinal scar tissue formation
					44.5	-	30 min	Additional damage including hyperaemia of choroid, erosion, necrosis and malformation of choroid
					44.7	-	30 min	Additional damage, scar tissue formation in choroid
					44.9	-	30 min	Additional damage including haemorrhage, hyperaemia and disruption of iris pigment and local cataract formation in lens
					45.8	-	30 min	Additional damage, haemorrhage, hyperaemia and thickening of iris
					45.9	-	30 min	Additional damage of haemorrhage, hyperaemia, thickening of iris and cell necrosis
				Fluorescein Angiography	43.5	-	30 min	No damage
					44.7	30 m	30 min	Damage resulting in fluorescein leakage
(Moriyama 1990)	Japanese Monkey (n=15)	2450MHz Microwave	Thermocouples	Hydrogen clearance	43		60 min	Thermal damage caused by increase in blood flow, vascular stasis and endothelial damage (brain). Cerebral blood flow rate did not return to normal

Table A1.2 (cont'd). Published data for thermal damage caused by electromagnetic irradiation

Author	Model	EM Type	Measurement		Test			Endpoint
			Temperature	Analysis	Temperature (°C)	Power	Time	
(Lint, Norren et al. 1992)	Long-Evans Rats	EM: 450W Xenon arc lamp, 380nm	Thermometer, Rectal	Fundus Photography	30	6 J/cm^2	10 m	Thresholds as indicated by a just visible change just smaller than the irradiated area with fuzzy edges
					42	1 J/cm^2		
(Bhatt, Peyman et al. 1993)	Dutch Pigmented Rabbits (n=12)	EM: 2.45GHz Microwave	Thermocouple, Sclera	Histology (Toluidine Blue), Ophthalmoscopy	43	-	1 m	Retinal pigment epithelial and outer retina damage and pigment granule migration without glial reaction. Normal choroid and sclera
					45	-	1 m	Damage characterised by loss of retinal architecture, atrophy of all layers of retinal pigment epithelium and retina with gliosis and pigment migration
(Dong, Liang et al. 1998)	Canine	Microwave	-	-	62	-	3 m	Damage to periphery of coagulated zone taken 3-7 days post
(Hoopes, Wishnow et al. 2000)	Canine rectum	Microwave	-	-	38.8	-	60 m	5 days post - No damage
(Wasowicz, Morice et al. 2002)	Long Evans Rats (n=10)	EM: 500 lux white light	-	Histology (GABA, TUNEL)	-	Constant Illumination	168 hours	No damage

Table A1.3. Published data for thermal damage caused by incubation

Author	Model		Measurement		Test		Endpoint
	Animal	**Tissue**	**Temperature**	**Analysis**	**Temperature (°C)**	**Time**	
(Linke, Lounsberry et al. 1967)	Rabbit	Liver	-	-	46	3 m	Damage characterised by necrosis seen 36-38 hours post
					46	5 m	
					46	10 m	
					46.5	5.5 m	
					47	4.4 m	
					47.5	3.5 m	
					47.5	10 m	
					48	3 m	
					48.5	2.4 m	
					49	1.7 m	
					49.5	1.3 m	
					50	1 m	
(Gerweck 1977)	Chinese Hamster	Ovary	Heat Bath Thermometer	Trypanized and Counted	41	250 min	Survival. 50%
					42	300 min	Survival. 8%
					43	120 min	Survival. 0.1%
					44	55 min	Survival. 0.1%
(Merino, Peters et al. 1978)	Mouse	Small Intestine	-	-	43	30 m	Damage associated with a decrease in jejuna crypt cell number, 3 days post
					45	30 m	Damage associated with death due to gut necrosis, 3 days post
(Hume, Marigold et al. 1979)	Mouse	Small Intestine	-	-	42	90 m	No damage seen at 24 hours post treatment
					42	162 m	Damage characterised by 50% probability of crypt cell damage, 24 – 20 days post
					43.9	20 m	
					44.5	10 m	
(Fujii and Ibata 1982)	Guinea Pig	Cortical	Thermistor, 0.7 mm Glass Insulated	Recordings of Evoked Potentials	43	5 min	No Damage. N potential reversible
					47	5 min	Damage. N potential irreversibly blocked
(Milligan, MEtz et al. 1984)	Hamster	Small Intestine	-	-	42.5	55 m	50% damage and death due to gut necrosis, 7 days post
					43.5	30 m	
					44.5	17 m	
(Barbe, Tytell et al. 1988)	Rat (n=40)	Eye	-	Light Micrography, Histology (H&E), Fluorography	40	60 min	No Damage. No Hsp expression
					41	15 min	Damage. Hsp expression
					42	15 min	Damage. Hsp expression

Table A1.3 (cont'd). Published data for thermal damage caused by incubation

Author	Model		Measurement		Test		Endpoint
	Animal	**Tissue**	**Temperature**	**Analysis**	**Temperature (°C)**	**Time**	
(Minamisawa, Smith et al. 1990)	SPF-Wistar Rats (n=72)	Brain	Thermocouple, in Bregma and Aorta	Direct visual cell counting (Percent Damage in CA1 and Subiculum in Hippocampus)	35	Ischemia 5 min	1-5% Damaged
						Ischemia 10 min	25-30% Damaged
						Ischemia 15 min	30-40% Damaged
					37	Ischemia 5 min	15-20% Damaged
						Ischemia 10 min	45-55% Damaged
						Ischemia 15 min	80-90% Damaged
					39	Ischemia 5 min	30-45% Damaged
						Ischemia 10 min	80-95% Damaged
						Ischemia 15 min	90-95% Damaged
(Dewey 1994)	Pig	Muscle and Fat			46.0	30 min	Necrosis, fibrosis
	Man, Rat, Mouse	Skin			46.5	45 min	Epidermal necrosis
	Man, Rat, Mouse	Skin			44	60 min	Epilation
	Pig	Oesophagus			45	30 min	Fibrosis
	Rat, Mouse	Cartilage			44	60 min	Necrosis
	Dog, Rabbit	Bladder			46.5	8 min	Mucosal necrosis
	Rat, Mouse	Small Intestine			43	40 min	Crypt loss
	Pig, Rabbit	Colon			43	30 min	Hepatocyte loss, fibrosis
	Dog, Rabbit	Liver			43	30 min	Neuronal pyknosis
	Cat, Dog	Brain			42.5	50 min	Necrosis of glomeruli and tubules
	Mouse	Kidney			43	20 min	Necrosis of glomeruli and tubules
(Jung 1994)	Chinese Hamster	Ovary Cells		Histology (crystal violet), Cell counting (Percentage of Control)	43	15 min	80% of Control
						30 min	50% of Control
						45 min	35% of Control
						60 min	15% of Control
						75 min	6% of Control
						90 min	1.5% of Control
						105 min	0.3% of Control
						120 min	0.15% of Control
(Organisciak, Darrow et al. 1995)	Sprague-Dawley Rats	Eye		Rhodopsin measurements (Percentage Rhodopsin Loss)	36.9	2 – 4 h post dark adaptation	0% Rhodopsin Loss
					37.6	2 – 4 h	10% Rhodopsin Loss
					38.4	2 – 4 h	30% Rhodopsin Loss
					39.0	2 – 4 h	50 – 60% Rhodopsin Loss
					39.2	2 – 4 h	60 – 70% Rhodopsin Loss
					39.7	2 – 4 h	70 – 80% Rhodopsin Loss
(Caprioli et al. 1996)	Rat	Retina		Histology (Trypan Blue)	42	60 m	60 m post - 90% survival
							200 m post - 82% survival

Table A1.4. Published data for thermal damage caused by ultrasound and drug administration

Author	Model			Measurement		Test		Endpoint
	Animal	Tissue	Heater Parameters	Temperature	Analysis	Temperature (°C)	Time	
(Lyons, Obana et al. 1986)	Cat (n=75)	Brain	Ultrasound, lithium niobate US transducer, 2.06 MHz resonant frequency, 200-300 mW/cm^2	Thermocouple Probe, Occipital Lobe	Histology (H&E, GFAP, Biodian stain, reticulin stain, Masson Trichrome, haematoxylin van Gieson, hemosiderin and haemoglobin, cresyl violet-luxol fast blue)	41.6 - 48.5	50 min	Acute damage (1-3 d post trauma), extensive coagulation, necrosis, pyknosis of grey matter, oedema and vacuolation of white matter and polymorphonuclear leukocytes. Lesion size increased by 4.293 mm^2/C.min with intercept at 42.2°C
						41.6 - 48.5	50 min	Subacute damage (3-21 d post trauma), appearance of lipid-laden macrophages, liquefaction of the necrotic regions, fibroblastic proliferation, vascular proliferation and inflammatory infiltration (lymphocytes). Lesion size increased by 2.495 mm^2/°C.min with an intercept of 41.1°C
						41.6 – 48.5	50 min	Chronic damage (21-56 d post trauma), fibrosis (rectulin and collagen formation) and gliosis (reactive astrocytic proliferation) occurring around the fluid filled necrotic centre
(Braakman, Valk et al. 1989)	Dutch Rabbits (n=19)	Eye	Ultrasound	Thermocouple probe, Tumour	Histology	43	30 min	Damage representative of corneal local hemorrhagic keratitis and local oedema in retina and choroid, 10% cell necrosis
						44	30 min	Above damage plus haemorrhage and iritis in iris and local cataract with damaged lens epithelium in lens and choroidal hyperaemia, 22.5% cell necrosis
						45	30 min	Similar damage to above although a larger percentage necrotic cells, 42.5% necrosis
						46	30 min	Above plus retinal haemorrhage, 45% cell necrosis
						47	30 min	Above damage plus retina and choroid local necrosis and local exudative retinal detachment, 25% cell necrosis
						48	30 min	Above damage plus scleral perforation and 42.5% cell necrosis
						49	30 min	Above damages plus 47.5% cell necrosis
(Quraishi and Brown 1995)	Rabbit	Brain and Kidney	LSD Injection	Thermistor probe, rectal	Gel electrophoresis, Western Blot, Immunocytochemistry	42.5 ± 0.5	1 h	Damage. Hsp90 expression
(McDannold, King et al. 2000)	Rabbit (n=13)	Thigh Muscle	Ultrasound	Thermocouple, Rectal and Thigh		50.4		Tissue damage (31.2 CEM)
						47.2		No damage (4.3 CEM)
(Rem, Oosterhuis et al. 2003)	Rabbit (n=15)	Eye	TSTT: Transscleral conductive heating (disk heater, 6 × 3 mm)	Thermocouples, water inflow and outflow	Ophthalmoscopy, Fluorescein Angiography, Histology	50	60 s	No damage (from 2 days to 4 months post op.)
						55	60 s	Short Term Damage. Fundus lesions were light grey, vasculature occlusion in retina and choroid
						60	60 s	Short Term Damage. Scleral fibres developed minimal undulation
						65	60 s	Short Term Damage. Scleral fibres clearly undulated, no long term damage
						70	60 s	Damage. Persistent severe damage to sclera including retinal tears

Table A1.5. Publications, animals, tissues and damage causes using Fluoro-Jade as a damage analysis tool.

Author	Animal	Tissue	Damage Cause
(Schmued, Albertson et al. 1996)	Rat	Brain	Neurotoxic Injection (Kainic acid, Domoic acid, Ibogaine, Phencyclidine, 3-nitropropionic acid, 1-methyl-4-phenyl-1,2,3,6-tetrahydropridine (MPTP)
(Eisch, Schumed et al. 1998)	Rat	Brain	Neurotoxic Injection (Methamphetamine)
(Schmued and Hopkins 2000)	Rat	Brain	Neurotoxic Injection (Kinaic acid)
(Krinke, Classen et al. 2001)	Rat	Brain	Neurotoxic Injection (3-acetylpyridine, acrylamide)
(Colombo and Puissant 2002)	Primate	Brain	Mechanical Lesioning
(Colombo and Puissant 2002)	Human	Brain	Alzheimer's Disease
(Fernandes, Maurer-Morelli et al. 2004)	Rat	Retina	Non-degenerating Neurons
(Olsen and McKeon 2004)	Mouse	Brain	Ischemia
(Anderson, Miller et al. 2005)	Rat	Brain	Cortical Contusion
(Duckworth, Butler et al. 2005)	Mice	Brain	Ischemia
(Schmued, Stowers et al. 2005)	Rat	Brain	Neurotoxic Injection (Kiainic acid, 3-nitropropionic acid)
(Bian, Wei et al. 2007)	Mouse	Brain	Neurotoxic Injection (1-methyl-4-phenyl-1,2,3,6-tetrahydropridine (MPTP))
(Hellmich, Eidson et al. 2007)	Mice	Brain	Traumatic Brain Injury
(Chidlow, Wood et al. 2009)	Rat	Retina	Degenerated retinal tissue

Table A1.6. Publications, animals, tissues and damage causes using glial fibrillary acidic protein expression as a damage analysis tool.

Author	Animal	Tissue	Damage Cause
(Bignami and Dahl 1979)	Rat	Eye	Mechanical Damage (Optic Nerve Crush)
(Eisenfeld, Bunt-Milam et al. 1984)	Rat	Eye	Electromagnetic Irradiation
(Erickson, Fisher et al. 1987)	Cat	Eye	Retinal Detachment
(Okada, Matsumura et al. 1990)	Human	Eye	Retinal Detachment
(Vaughn, Erickson et al. 1990)	Rabbit	Eye	Laser Photocoagulation
(Caprioli, Kitano et al. 1996)	Rat	Eye	Hyperthermia (42C Oven)
(Mizutani, Gerhardinger et al. 1998)	Human	Eye	Diabetic Retinopathy
(Liu, Smith et al. 1999)	Rat	Brain	Ischemia
(Dyer and Cepko 2000)	Rat	Eye	Neurotoxic Insult
(Cai, Li et al. 2001)	Rat	Eye	Mechanical Damage (Stab Wound)
(Gerding, Taneri et al. 2001)	Rabbit	Eye	Mechanical Damage (Retinal Tack Insertion)
(Nolte, Matyash et al. 2001)	Mice	Brain	Mechanical Damage (Stab Wound)
(Pardue, Stubbs et al. 2001)	Cat	Eye	Mechanical Trauma (Prosthesis Implantation)
(Ramirez, Ramirez et al. 2001)	Human	Eye	AMD
(Wu, Madigan et al. 2003)	Human	Eye	AMD
(Olsen and McKeon 2004)	Mice	Brain	Hypoxia / Ischemia
(Tokuda, Tsukamoto et al. 2004)	Rat	Eye	Neurotoxic Insult
(Schmued, Stowers et al. 2005)	Rat	Brain	Neurotoxic Insult
(Colodetti, Weiland et al. 2007)	Rat	Eye	Electrical Stimulation
(Downie, Pianta et al. 2007)	Rat	Eye	Retinal Vascularisation
(Nakazawa, Takeda et al. 2007)	Mice	Eye	Retinal Detachment
(Chidlow, Wood et al. 2009)	Rat	Eye	Degeneration

Table A1.7. Publications, animals, tissues and damage causes using microglia morphological response as a damage analysis tool.

Author	Animal	Tissue	Damage Cause
(Suzumura, Marunouchi et al. 1991)	Mice		Cytokine stimulation
(Thanos, Mey et al. 1993)	Rat	Optic Nerve	Axotomy induced neuronal degeneration
(Soltys, Ziaja et al. 2001)		Brain	
(Chauhan, Pan et al. 2002)	Rat	Optic Nerve	Ischemia
(Davalos, Grutzendler et al. 2005)	Mice	Brain	Laser Injury, Mechanical trauma
(Nimmerjahn, Kirchoff et al. 2005)			Laser Injury
(Zhang, Lam et al. 2005)	Rat	Retina	Ischemia and reperfusion injury
(Langmann 2007)	Mice	Retina	Retinal Degeneration
(Eter, Engel et al. 2008)	Mice	Retina	Laser Injury
(Lee, Liang et al. 2008)	Mice	Retina	Laser Injury
(Santos, Martin-Oliva et al. 2009)	Mice	Retina	Photoreceptor Degeneration

APPENDIX 2 –

EQUIPMENT SPECIFICATIONS

A2.1 - Program Written to Perform Second Order Linearisation for Platinum Resistance Temperature Detectors

```
%ENTER VALUES GIVEN IN SPEC SHEET FOT PRTD, DIN EN 60751, 1000 OHM, bCLASS
%TOLERANCE
ts(1)  = 1003.91; ts(2) = 1007.81; ts(3)= 1011.72; ts(4)= 1015.62; ts(5)= 1019.53;
ts(6)  = 1023.43; ts(7)  = 1027.33; ts(8)= 1031.23; ts(9)= 1035.13; ts(10)= 1039.03;
ts(11)= 1042.92; ts(12)= 1046.82; ts(13)= 1050.71; ts(14)= 1054.60; ts(15)= 1058.49;
ts(16)= 1062.38; ts(17)= 1066.27; ts(18)= 1070.16; ts(19)= 1074.05; ts(20)= 1077.94;
ts(21)= 1081.82; ts(22)= 1085.70; ts(23)= 1089.59; ts(24)= 1093.47; ts(25)= 1097.35;
ts(26)= 1101.23; ts(27)= 1105.10; ts(28)= 1108.98; ts(29)= 1112.86; ts(30)= 1116.73;
ts(31)= 1120.60; ts(32)= 1124.47; ts(33)= 1128.35; ts(34)= 1132.21; ts(35)= 1136.08;
ts(36)= 1139.95; ts(37)= 1143.82; ts(38)= 1147.68; ts(39)= 1151.55; ts(40)= 1155.41;
ts(41)= 1159.27; ts(42)= 1163.13; ts(43)= 1166.99; ts(44)= 1170.85; ts(45)= 1174.70;
ts(46)= 1178.56; ts(47)= 1182.41; ts(48)= 1186.27; ts(49)= 1190.12; ts(50)= 1193.97;
ts(51)= 1197.82; ts(52)= 1201.67; ts(53)= 1205.52; ts(54)= 1209.36; ts(55)= 1213.21;
ts(56)= 1217.05; ts(57)= 1220.90; ts(58)= 1224.74; ts(59)= 1228.58; ts(60)= 1232.42;
% IMPORT DATA "data" AND GET SIZE
clear data2;
clear m;
clear n;
clear temp;
[m,n]=size(data);
 % CORRECT RESISTANCE TO ACCOUNT FOR LEADS OF 0.46 OHM IF REQUIRED
%data2=data(:,2)-0.46;
data2=data(:,1);
 % CONVERT TO TEMPERATURE - LINEARISE DATA
for i=1:m
   for j=1:60
     if (data2(i)<ts(j))
     end
   if (data2(i)>=ts(j))
     temp(i)=j+((data2(i)-ts(j))/(ts(j+1)-ts(j)));
   end
   end
end
temp2=temp';
temp=temp2;
```
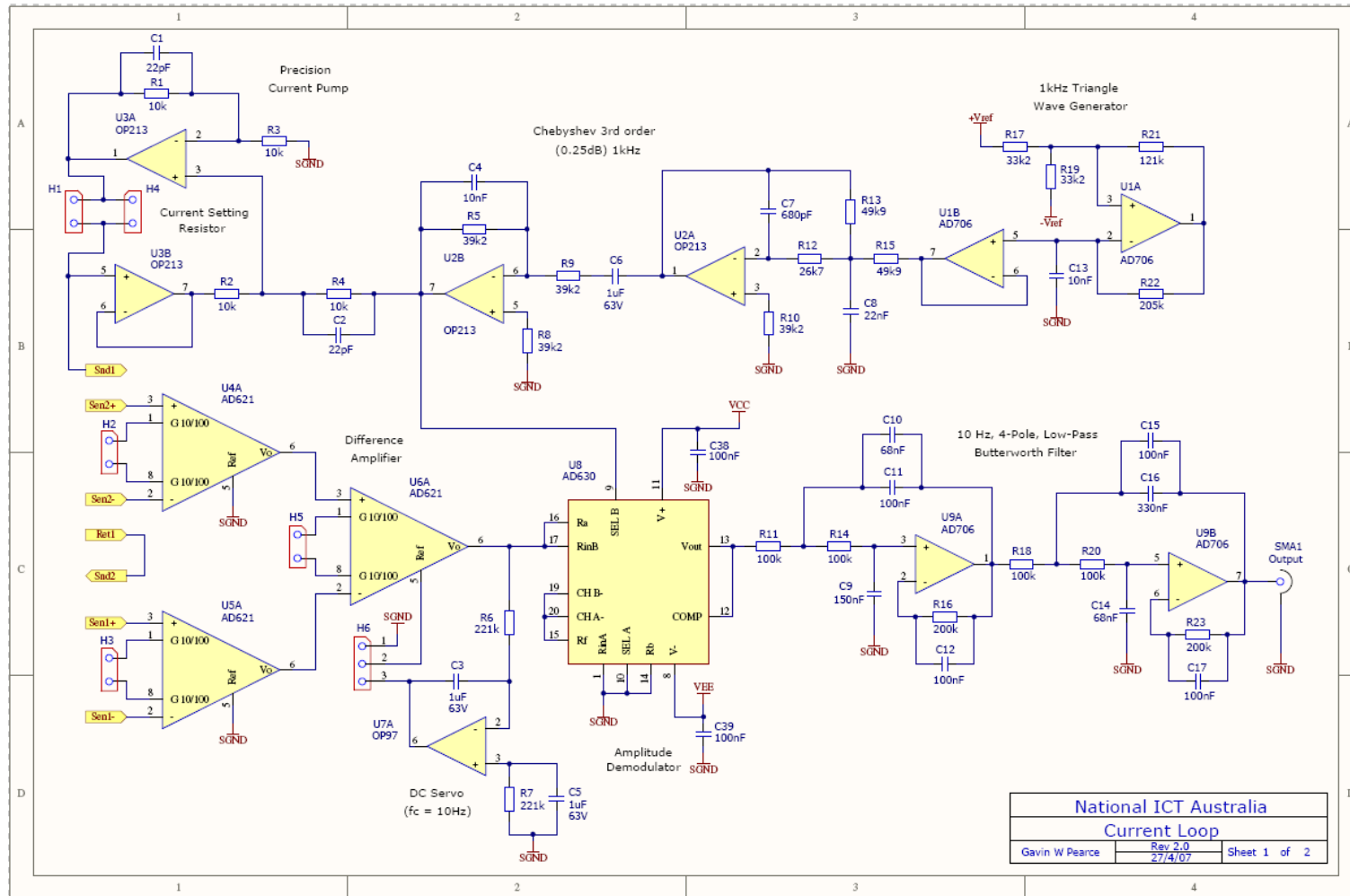
Figure A2.2. Circuit diagram of the high resolution temperature measurement system
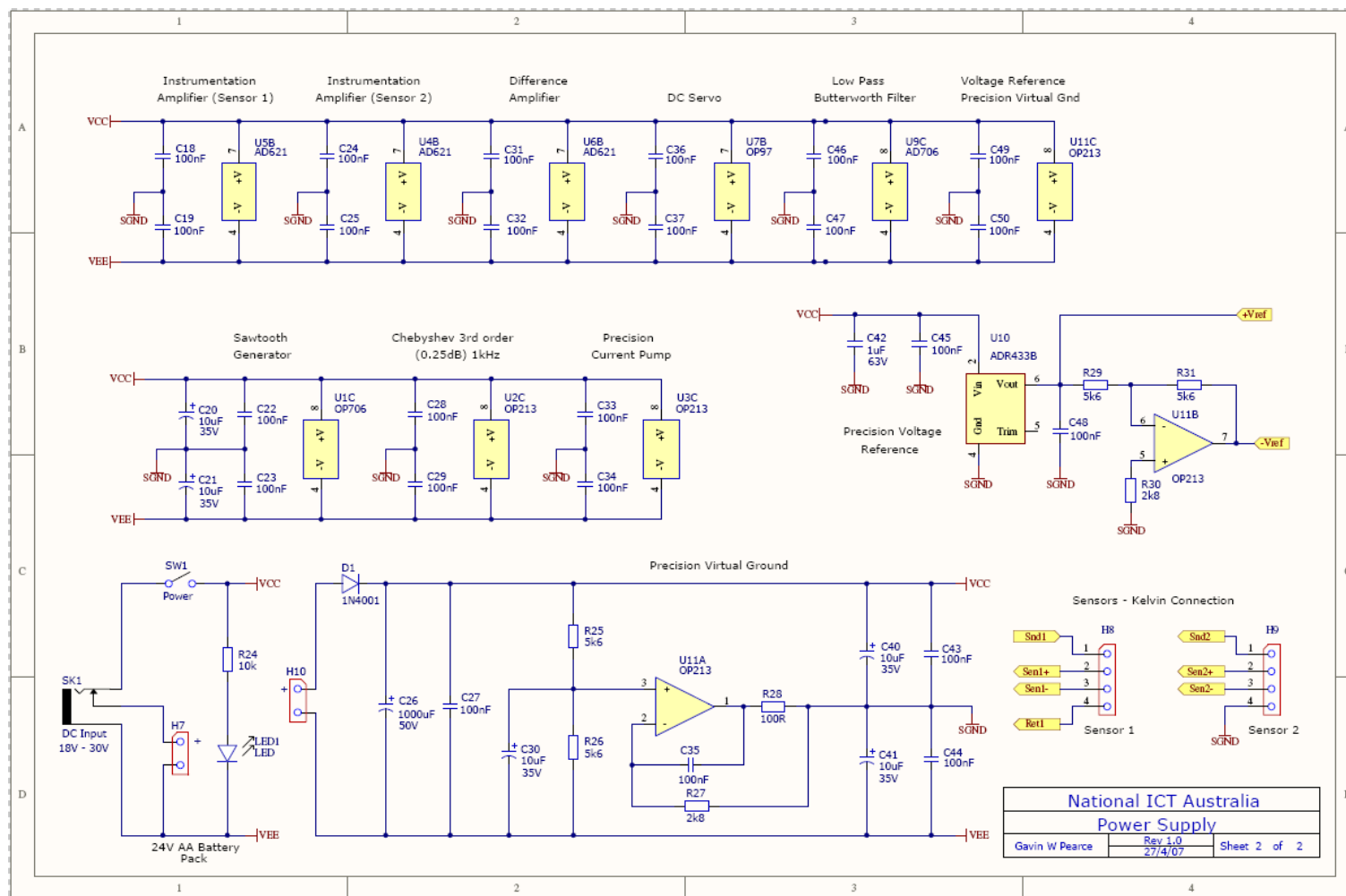
Figure A2.2 (cont). Circuit diagram of the high resolution temperature measurement system

APPENDIX 3 – ORBITAL THERMAL PROPERTIES

Table A3.1 Thermal and material properties of human tissue

Domain	Thermal Conductivity W/m·°C	R	Specific Heat J/kg·°C	R	Density kg/m3	R
FLUIDS						
Blood	0.530 0.530 0.490 0.530	2 4 5 6	3840 3600 3900 3840	2 4 5 6	1060 1050 1058	2 4 5
Humor	0.580 0.590 0.600	1 3 5	3997 4178 4000	1 3 5	996 1010 1009	1 3 5
Humor (Aqueous)	0.578 0.594	2 6	3997 3997	2 6	1003	2
Humor (Vitreous)	0.594 0.578	2 6	3997 3997	2 6	1009	2
MATERIALS						
Air	0.250 0.300	2 6	1300 1000 1300	2 4 6	1.16 1.00	2 4
Silicon	150.0 149.0	2 8	959.0	2	2330	2
Teflon	0.200	6	1172	6	-	
Copper	60.0	6	1025	6	-	
Nickel	90.90	8	26.07		8.908	
PCB	0.120	9	1.090	9	1.42 g/cc	9

Domain	Thermal Conductivity W/m·°C	R	Specific Heat J/kg°C	R	Density kg/m3	R
ORBITAL STRUCTURES						
Choroid	0.530 0.600	2 3	3840 4178	2 3	1060 1050	2 3
Cornea	0.580 0.580 0.600 0.580 0.580	1 2 3 5 6	4178 4178 4178 4200 4200	1 2 3 5 6	1050 1076 1050 1026	1 2 3 5
Iris	1.0042	1	3180	1	1100	1
Lens	0.400 0.400 0.400 0.400 0.400	1 2 3 5 6	3000 3000 3000 3000 3000	1 2 3 5 6	1050 1100 1050 1053	1 2 3 5
Lens zonules	0.498	2	3430	2	1040	2
Retina	0.565 0.600 0.565	2 3 6	3680 4178 3680	2 3 6	1039 1050	2 3
Sclera	0.580 0.600 0.580	2 3 5	3180 4178 4178 4200	1 2 3 5	1100 1170 1050 1026	1 2 3 5

References:

1: Ng and Ooi (2007), 2: DeMarco and Lazzi (2003), 3: Flyckt and Raamakers (2006), 4: Flyct and Raaymakers (2007), 5: Hirata and Ushio (1999), Hirata and Matsuyama (2000), Hirata (2005), Hirata and Fujimoto (2006), Hirata and Watanabe (2006), 6: Gosalia and Weiland (2004), 7: Liou and Brennan (1997), 8: Matweb (2010), 9: PCB Co. (2009), 10: Narasimhan and Jha (2010) 11: Oyster (1999)

APPENDIX 4 – CADAVER TESTS

Table A4.1. Cadaver 1, 2 and 3 power-temperature increase recordings from four sensors located 0.00 mm (S0, central), 2.80 mm (S1), 4.70 mm (S2) and 6.60 mm (S3) from the heating element edge using the variable size heating element implant with heating element dimensions of 4.65 x 4.65 mm.

Cadaver	Current (mA)	Power per Resistor (mW)	Temperature Increase (°C)			
			S0	S1	S2	S3
1	11	1.94	0.30	-	-	-
			0.34	-	-	-
			0.34	-	-	-
			0.31	-	-	-
			0.30	-	-	-
			0.32	-	-	-
			0.31	-	-	-
			0.34	-	-	-
			0.31	0.03	-	-
			0.31	0.06	-	-
			0.31	0.06	-	-
			0.40	0.05	-	-
	18	5.18	1.00	0.12	-	-
			0.93	0.18	-	-
			0.93	0.18	-	-
			1.10	0.19	-	-
	25	10.00	2.05	0.23	-	-
			1.93	0.32	-	-
			1.93	0.35	-	-
			2.49	0.47	0.10	-
	30	14.40	3.05	0.35	-	-
			2.99	0.41	-	-
			2.86	0.47	-	-
			2.86	0.64	-	-
			-	0.84	0.31	-
	35	19.60	3.80	0.53	-	-
			3.74	0.70	-	-
			3.80	0.82	0.61	-
	40	25.60	4.30	0.64	-	-
			4.17	0.82	-	-
			4.30	1.00	-	-
2	11	1.94	0.23	-	-	-
			0.27	-	-	-
			0.27	-	-	-
	18	5.18	0.77	-	-	-
			0.77	-	-	-
			0.69	-	-	-
	25	10.00	1.46	-	-	-
			1.61	-	-	-
			1.61	-	-	-
	30	14.40	2.23	-	-	-
			2.23	-	-	-
			2.75	-	-	-
	35	19.60	3.38	-	-	-
			3.67	-	-	-
			4.00	-	-	-
3	18	6.48	0.90	0.30	0.00	-
			0.80	0.20	0.00	-
	25	12.50	2.20	0.60	0.20	-
			2.30	0.60	0.10	-
	35	24.50	5.90	1.50	0.40	-
			5.70	1.30	0.30	-
	50	50.00	7.50	2.00	0.60	-
			8.10	2.30	0.60	-

Table A4.2. Cadaver 4,5,6 and 7 power-temperature increase recordings from four sensors located 0 mm (S0, central), 1.457 mm (S1), 3.457 mm (S2) and 5.457 mm (S3) from the heating element edge using the small heating element with heating element dimensions of 4.60 x 5.175 mm

Cadaver	Power (mA)	Power per Resistor (mW)	Temperature Increase (°C)			
			S0	S1	S2	S3
4	10	2.00	0.30	0.10	-	0.01
			0.28	0.07	-	-
			0.26	0.09	-	0.01
	20	8.22	1.30	0.38	0.08	0.00
			1.20	0.40	-	0.02
			1.25	0.38	0.09	-
	30	18.00	-	0.90	0.90	-
			3.20	1.00	0.44	0.28
			3.40	-	-	-
			3.20	1.00	-	0.34
	35	24.5	5.50	1.75	0.75	0.45
5	15	4.50	0.95	0.13	-	-
			0.90	0.15	-	-
			0.90	0.15	-	-
			0.83	0.11	-	-
			0.95	0.10	-	-
	30	18.00	3.70	0.53	-	-
			4.00	0.56	0.07	0.04
			3.90	0.56	0.08	-
	45	40.50	9.00	1.45	0.19	0.11
			8.75	1.45	0.23	0.10
			8.75	1.40	0.19	0.10
6	7	0.98	0.28	0.04	-	-
			0.30	0.04	-	-
			0.24	0.07	-	-
			0.22	0.08	-	-
			0.22	0.06	-	-
	14	3.92	0.90	0.32	0.18	0.08
			0.85	0.30	0.16	0.07
			0.90	0.34	-	0.07
	21	8.82	2.05	0.80	0.38	0.24
			2.00	0.73	0.36	0.17
			2.00	0.75	0.37	0.18
	28	15.68	3.50	1.40	0.78	0.44
			3.50	1.35	0.70	0.37
			3.50	1.35	0.70	0.40
	35	24.5	5.40	2.10	1.05	0.54
			5.40	1.60	0.95	0.42
7	2	0.20	0.04	-	-	-
	4	0.80	0.13	-	-	-
	5	1.25	0.20	-	-	-
			0.20	-	-	-
			0.21	-	-	-
	6	1.80	0.31	-	-	-
			0.30	-	-	-
			0.30	0.05	-	-
	7	2.45	0.42	0.10	-	-
			0.40	0.10	-	-
	8	3.20	0.53	0.19	-	-
			0.52	0.10	-	-
			0.53	0.12	-	-
	9	4.05	0.67	0.19	-	-
			0.67	0.16	-	-
	10	5.00	0.85	0.21	-	-
			0.85	0.21	-	-
			0.83	0.22	-	-
			0.90	0.22	-	-
	12	7.20	1.25	0.29	-	-

| 14 | **9.80** | 1.65 | 0.44 | - | - |

Table A4.3. Temperature measurements averaged from eight cadaver eyes (five cadaver trials measured with the high resolution temperature measurement system and three trials measured using a digital multimeter) for a heating element temperature 1°C above measured body temperature

Distance (mm)	Temperature Increase (°C)							
	HTRMS Measurements					DMM Measurements		
	1	2	3	4	5	1	2	3
0.000	1.00	1.00	1.00	1.00	1.00	1.00	1.00	1.00
1.125	0.31	0.14	0.37	0.40	0.36	0.36	0.39	0.41
2.250	0.10	0.20	0.19	0.15	0.19	0.31	0.35	0.09
3.375	0.07	0.01	0.10	0.08	0.08	0.23	0.26	0.21
4.500	-	-	-	-	-	0.18	0.21	0.06
5.625	-	-	-	-	-	0.18	0.19	0.16
9.750	-	-	-	-	-	0.08	0.08	0.04

APPENDIX 5 – SOP No. 12

STANDARD OPERATING PROCEDURE – No: 12

PROTOCOL FOR ACUTE EXPERIMENT PREPARATION AND ANAESTHETIC MAINTENANCE IN THE CAT

Date: 26/08/2008

1. Weigh cat and prepare drugs (Xylazil, Ketamine, Clavulox, Dexamethasone, Hartmann's solution and Sodium Pentobarbital in Hartmann's solution).
2. Inject Xylazil 2mg/kg (SC), wait 10-15 minutes until the animal is drowsy, inject Ketamine 20mg/kg (IM), place the cat in a basket for transport to experimental room.
3. Lubricate eyes with ocular lubricant, check general condition of animal, check ears with otoscope (for redness, swelling, light reflection of tympanic membrane).
4. Shave the base of the cat's tail, forearms, tracheal area, nape, head and any other areas required.
5. Prepare forearm for insertion of 22G catheter into cephalic vein in the forearm with alcohol swab, cut down superficially on the highest point of the forearm ridge to expose the cephalic vein. Insert a 22G catheter and ensure that the catheter is patent by injecting some sterile saline.
6. Attach a 3-way tap to the catheter and secure both catheter and tap with tape.
7. Administer Clavulox 10mg/kg (SC) and Dexamethasone 0.1mg/kg (IM). Repeat administration each 24 hours.
8. Insert endotracheal tube. Make a longitudinal incision along the tracheal region and blunt dissect to expose the trachea. Clear away muscle and other tissue from the trachea. Thread two pieces of silk suture in a horizontal direction underneath the trachea. Cut the trachea halfway horizontally and insert the endotracheal tube of appropriate size (approximately 3 – 4.5 mm ID, 70 mm length, tapered). Tie silk around the tube and trachea to secure the tube. Observe the cat freely respiring. Seal the incision using superglue, ensuring the end of the endotracheal tube is clear.
9. Place cat in the stereotaxic frame and continue to observe breathing during this period. Position thermostatically regulated heat blanket under the cat and insert probe to monitor core temperature. Core temperature should be 36 – 38 °C.
10. Attach capnograph to endotracheal tube and monitor respiration. End-tidal CO_2 should be 3 – 5 % and respiration rate 5-25 breaths/minute.
11. Attach heart rate monitoring equipment (e.g. recording electrodes for ECG monitoring). Heart rate should be 140 to 250 beats/minute.
12. Attach i.v. lines to deliver sodium pentobarbital for anaesthetic maintenance (1:6 dilution in Hartmann's solution:10ml of sodium pentobarbital (60mg/ml) + 50 ml of Hartmann's) and Hartmann's solution (2.5ml/kg/hr).
13. Record vital signs (heart rate, respiration rate, CO_2 levels, and body temperature) hourly throughout the experimental period and alter anaesthetic dose where required for anaesthetic maintenance (see anaesthetic dose chart attached).
14. Check for urine production every 24 hours. If no urine has been produced, check for a distended bladder and attempt manual evacuation with gentle pressure.
15. Perform additional surgery as required to expose area(s) of interest (eg. Auditory cortex) and perform experimental protocols as approved under individual projects.

16. At the completion of the experiment, overdose the cat with sodium pentobarbital (150 mg/kg, i.v.) and intracardially perfuse with 0.9% saline and formalin fixative.

Anaesthetic Dose Chart

The precise dose of anaesthetic required to maintain an appropriate level of anaesthesia is different for each animal. The following chart is a guide to be used in conjunction with SOP 10 (Cats monitoring anaesthesia and intraoperative support). The initial rate of delivery of 1:6 diluted sodium pentobarbital should be 0.1-0.2 ml/hr. The final rate of delivery will be higher (typically around 1.0 ml/hr) and will be reached by following these guidelines:

Vital Sign	Range	Action
Heat Rate	Stopped	Administer adrenaline (0.05-0.5mg of 1:10000 solution i/v). Dose may need to be repeated in 5 mins.
	< 140	Stop anaesthetic delivery, if the animal does not respond or other vital signs are poor give 0.15 ml antisedan (i.m.)
	140 – 170	Decrease anaesthetic rate
	170 – 220	None
	220 – 250	Increase anaesthetic rate
	> 250	Increase anaesthetic rate, if the animal does not respond or other vital signs indicate the animal is light, give up to 0.5 ml bolus of anaesthetic
Respiration Rate	< 5	Stop anaesthetic delivery, if the animal does not respond or other vital signs are poor give 0.15 ml antisedan (i.m.)
	5 – 10	Decrease anaesthetic rate
	10 – 20	None
	20 – 25	Increase anaesthetic rate
	> 25	Increase anaesthetic rate, if the animal does not respond or other vital signs indicate the animal is light, give up to 0.5 ml bolus of anaesthetic
CO_2	< 3	Increase anaesthetic rate, if the animal does not respond or other vital signs indicate the animal is light, give up to 0.5 ml bolus of anaesthetic
	3-5	None
	> 5	Stop anaesthetic delivery, if the animal does not respond or other vital signs are poor give 0.15 ml antisedan (i.m.)
Reflexes	Withdrawal or Palpebral	Increase anaesthetic rate, if the animal does not respond or other vital signs indicate the animal is light, give up to 0.5 ml bolus of anaesthetic

APPENDIX 6 – RAT RETINA TESTS

Table A6.1. Soma areas, arbour areas and ratio for all incubation test images performed at different heat bath temperatures

	Heat Bath Temperature (°C)									
	30.3	**30.4**	**31.0**	**31.5**	**31.7**	**32.0**	**33.6**	**36.8**	**40.3**	**43.1**
Soma Area	28.8 24.1 34.6 17.7	36.7 21.9 21.1 42.0 17.9 22.0	30.6 25.7 31.5 22.7 23.2 21.4 31.5 17.1 21.7	24.1 27.9 24.7 19.6 23.4	21.7 23.6 17.4 19.0	31.6 23.3 29.0 27.6	24.5 32.8 27.6 15.3 45.7 32.0 26.6 30.4 30.2	30.6 31.5 30.8 34.4 29.8 32.3 26.8 28.0 28.2 35.8 33.5 36.5 33.4 25.8 31.4 30.5 28.9 26.8 27.2 32.8 30.8 29.3	40.7 38.0 43.7 41.5 38.0 39.5 38.0 39.8 45.0	35.8 43.2 39.0 53.7 45.0
Soma Average	**26.3±7.2**	**26.9±7.7**	**25.0±5.1**	**23.9±3.0**	**22.8±5.0**	**28.3±1.0**	**29.5±8.1**	**30.7±3.0**	**40.5±2.5**	**43.9±6.1**
Arbour Area	2202 1554 2174 2027	2047 1765 1832 2582 1581 1748	1822 1804 1708 2184 1926 2367 1929 2271 2375	1890 1912 1839 1368 1893	2165 1848 1312 2353	2398 1901 1781 2476	2298 1780 2229 2248 1978 2555 1878 2059 1915	1577 2077 2096 1916 2245 2047 1559 1623 2143 1832 1571 2407 1696 2072 1782 1975 1838 1966 1551 1929 1507 2118	1713 1621 1505 1883 1689 1424 1563 1782 1685	1265 1544 1631 1465 1148
Arbour Average	**1989±300**	**1926±355**	**2043±258**	**1780+232**	**1996±404**	**2129±491**	**2104±247**	**1888±254**	**1652±141**	**1411±200**
Ratio	1.31 1.55 1.59 0.87	1.79 1.24 1.15 1.63 1.13 1.26	1.68 1.42 1.84 1.04 1.20 0.90 1.63 0.75 0.91	1.28 1.46 1.34 1.43 1.24	1.00 1.28 1.33 0.81	1.32 1.23 1.63 1.11	1.07 1.84 1.24 0.68 2.31 1.25 1.42 1.28 1.58	1.94 1.52 1.47 1.80 1.33 1.58 1.72 1.73 1.32 1.95 2.13 1.52 1.97 1.25 1.76 1.54 1.57 1.36 1.75 1.70 2.04 1.38	2.33 2.34 2.90 2.20 2.25 2.77 2.43 2.23 2.19	3.19 3.66 2.40 2.79 3.04
Ratio Average	**1.33±0.33**	**1.37±0.28**	**1.26±0.39**	**1.35±0.09**	**1.16±0.21**	**1.37±0.37**	**1.41±0.47**	**1.65±0.25**	**2.40±0.26**	**3.02±0.47**

Table A6.2. Retinal microglia average cell numbers and ratios for control trials

Test	Temperature (°C)	Cell Number (cells/mm^2)				Ratio			
		GCL		ONL		GCL		ONL	
		Central	Peripheral	Central	Peripheral	Central	Peripheral	Central	Peripheral
Control 1	31.00±0.29	176 117	150 156 150	59 46	65 91	1.68 1.84	1.20 1.63 1.42	1.04 0.90	0.75 0.91
Control 2	30.38±0.14	-	156 104 130	-	13 85 98	-	1.79 1.24 1.15	-	1.63 1.33 1.26
Control 3	33.58±0.34	124 130 189	176 137	26 13	72 39	1.07 1.24 2.31	1.42 1.84	0.68 1.25	1.48 1.58
Control 4	30.32±0.10	-	208 182	-	111 91	-	1.31 1.55	-	1.59 0.87
Control 5	31.48±0.22	195 176	228	65	78	1.28 1.46	1.34	1.43	1.24
Control 6	31.74±0.25	130	117 150	39	72 104	1.00	1.28 1.33	0.81	1.32 1.23
Control 9	31.95±0.19	85	117	-	33	-	1.63	-	1.11
Control 13	36.39±0.19	-	-	-	-	-	-	-	-
Control 14 A	36.76+0.31	150 156 137	111 117 143	59 26 33	33 52 52	1.94 1.80 1.72	1.95 1.97 1.54	1.75 1.52 1.33	1.73 2.13 1.25
Control 14 B	36.76±0.31	143 130 137	228 156	111 72 52	39 52	1.57 1.70 1.47	1.58 1.32	1.52 1.76 1.36	2.04 1.38
Control Average		**149±25**	**153±37**	**50±26**	**65±28**	**1.58±0.36**	**1.61±0.29**	**1.50±0.25**	**1.36±0.31**

Table A6.3. Retinal microglia average soma and arbour areas for control trials

Test	Temperature (°C)	Average Soma Area (mm²)				Average Arbour Area (mm²)			
		GCL		ONL		GCL		ONL	
		Central	Peripheral	Central	Peripheral	Central	Peripheral	Central	Peripheral
Control 1	31.00±0.29	30.6 31.5	23.2 31.5 25.7	22.7 21.4	17.1 21.7	1822 1708	1926 1929 1804	2184 2367	2271 2375
Control 2	30.38±0.14	-	36.7 21.9 21.1	-	42.0 17.9 22.0	-	1047 1765 1832	-	2582 1581 1748
Control 3	33.58±0.34	24.5 27.6 45.7	26.6 32.8	15.3 32.0	30.4 30.2	2298 2229 1978	1878 1780	2248 2555	2059 1915
Control 4	30.32±0.10	-	28.8 24.1	-	34.6 17.7	-	2202 1554	-	2174 2027
Control 5	31.48±0.22	24.1 27.9	24.7	19.6	23.4	1890 1912	1839	1368	1893
Control 6	31.74±0.25	21.7	23.6 17.4	19.0	31.6 23.3	2165	1848 1312	2353	2398 1901
Control 9	31.95±0.19	-	29.0	-	27.6	-	1781	-	2476
Control 13	36.39±0.19	-	-	-	-	-	-	-	-
Control 14 A	36.76+0.31	30.6 34.4 26.8	35.8 33.4 30.5	27.2 31.5 29.8	28.0 33.5 25.8	1577 1916 1559	1832 1696 1975	1551 2077 2245	1623 1571 2072
Control 14 B	36.76±0.31	28.9 32.8 30.8	32.3 28.2	36.5 31.4 26.8	30.8 29.3	1838 1929 2096	2047 2143	2407 1782 1966	1507 2118
Control Average		**29.8±5.8**	**30.3±6.5**	**27.8±5.3**	**24.2±6.5**	**1922+222**	**1852+202**	**2091+162**	**2016+327**

Table A6.4. Retinal microglia average cell numbers and ratios for mechanical control trials

Test	Temperature (°C)	Cell Number (cells/mm²)				Ratio (%)			
		GCL		ONL		GCL		ONL	
		Central	Peripheral	Central	Peripheral	Central	Peripheral	Central	Peripheral
Mechanical 2	27.55±0.17	198 137 286	137 143	85 104 59	117 65	2.06 2.01 2.46	1.73 1.66	0.99 1.39 1.59	1.68 1.23
Mechanical 4	28.36±0.09	156	130 143	26	65 85	1.53	1.69 1.99	2.44	2.30 2.25
Mechanical 6	29.83±0.16	176	163 130	111 59	98 39	3.20	1.40 1.59	1.01 2.43	1.48 1.24
Mechanical 15	30.90+0.11	130 202	163 176	72 150	98 78	2.11 2.92	2.72 1.95	1.65 2.31	2.23 2.46
Mechanical 15	30.90+0.11	130 202	163 176	72 150	98 78	2.11 2.92	2.72 1.95	1.65 2.31	2.23 2.46
Mechanical 16	32.84±0.18	117 124 111	124 130 117	59 33 72	78 39 52	1.88 1.09 1.77	1.88 1.46 1.42	1.46 1.23 1.69	1.77 1.36 1.24
Mechanical 17	34.64±0.27	137 124 98	130 137	85 52 52	65 65	4.18 2.68 3.11	2.24 2.70	2.27 2.06 2.64	2.73 2.32
Mechanical Average	**32.87±0.11**	**153±50**	**140±17**	**72±33**	**73±23**	**2.38±0.82**	**2.17±0.61**	**1.88±0.44**	**1.69±0.49**

Table A6.5. Retinal microglia average soma and arbour areas for mechanical control trials

Test	Temperature (°C)	Average Soma Area (mm^2)				Average Arbour Area (mm^2)			
		GCL		ONL		GCL		ONL	
		Central	Peripheral	Central	Peripheral	Central	Peripheral	Central	Peripheral
Mechanical 2	27.55±0.17	26.8 36.5 31.1	28.7 27.0	16.2 20.5 19.7	31.1 19.4	1298 1817 1266	1656 1623	1632 1470 1305	1852 1576
Mechanical 4	28.36±0.09	29.4	23.5 36.3	28.0	44.3 32.8	1919	1389 1822	1149	1926 1455
Mechanical 6	29.83±0.16	49.2	24.0 25.5	17.6 32.0	23.9 17.3	1538	1710 1607	1737 2231	1620 1391
Mechanical 9	30.90+0.11	-	-	-	-	-	-	-	-
Mechanical 15	32.84±0.18	37.0 43.8	39.7 44.0	30.5 42.3	43.7 43.0	1755 1502	1461 2256	1852 1853	1956 1746
Mechanical 16	34.64±0.27	37.9 31.9 32.9	35.8 31.6 27.8	26.2 25.0 22.8	37.9 25.3 26.5	2011 2922 1855	1903 2157 1957	1800 2038 2002	2139 1854 2132
Mechanical 17	32.87±0.11	45.3 34.8 35.5	36.3 39.1	29.3 31.5 35.0	35.3 27.0	1083 1300 1143	1624 1447	1292 1532 1327	1292 1164
Mechanical Average		**36.3±6.5**	**32.3±6.7**	**27.7±7.4**	**31.3±9.1**	**1646+492**	**1739+268**	**1657±324**	**1700±313**

Table A6.6. Retinal microglia average cell counts and ratios for heated trials

Test	Temperature (°C)	Temperature Increase (°C)	Cell Number (cells/mm²) GCL Central	GCL Peripheral	ONL Central	ONL Peripheral	Ratio (%) GCL Central	GCL Peripheral	ONL Central	ONL Peripheral
Heat 5	33.89±0.3	4.63	124 143	221 156	98 117	78 85	3.75 2.77	1.80 1.72	1.09 1.20	1.09 1.02
Heat 7	35.66±0.4	4.94	208 156	-	52 91	-	3.25 3.17	-	2.57 2.27	-
Heat 10A	40.62±0.3	5.94	137 111 124	98 130 124	78 78 59	111 33 72	2.64 2.19 2.08	2.22 1.65 2.60	1.72 1.92 2.16	1.44 1.48 1.89
Heat 10B	39.98±0.4	6.95	85 104 78	150 163 137	91 26 72	39 52 98	2.43 1.45 2.22	2.58 2.79 2.44	1.53 1.06 2.43	2.42 2.95 2.74
Heat 11A	40.22±1.9	6.01	182 176 111	150 163 137	104 137 104	130 52 26	2.19 3.58 4.01	3.55 3.21 2.77	1.57 2.86 2.30	2.47 2.17 5.41
Heat 11B	38.21+1.8	5.57	130 169	137 117	85 26	72 20	1.33 2.36	2.32 1.47	0.99 1.35	2.35 0.99
Heat 12	38.00±0.2	4.99	143 143 195	208 156 163	124 98 130	124 104 98	5.82 2.54 4.02	3.83 3.34 2.61	1.57 1.83 1.80	1.76 1.97 2.03
Heat 14A	42.17±0.5	9.28	111 169 182	182 130	150 169	137 124 124	3.91 3.19 4.80	2.89 3.14	1.67 2.28	2.78 1.42 2.26
Heat 14B	41.49±0.5	7.93	202 195 176	202 150 195	156 117 137	111 143 124	2.21 2.31 2.61	2.03 2.21 2.04	1.67 1.64 1.54	1.42 1.31 1.30
Heat 15A	35.96±0.2	2.95	156 111 104	143 130	59 104 65	104 65	3.98 4.59 3.97	3.40 1.55	1.74 1.80 1.11	1.40 1.28
Heat 15B	35.26±1.4	4.03	176 150	241 150	91 137	65 143	3.28 2.76	3.37 2.06	2.69 2.27	2.17 1.73
Heat 16	38.06±0.3	1.51	85 137	137 202	59	98 104 78	2.10	1.40 1.84	1.97	2.02 1.81 1.49

Table A6.7. Retinal microglia average soma and arbour areas for heated trials

Test	Temperature (°C)	Temperature Increase (°C)	Average Soma Area (mm²)				Average Arbour Area (mm²)			
			GCL		ONL		GCL		ONL	
			Central	Peripheral	Central	Peripheral	Central	Peripheral	Central	Peripheral
Heat 5	33.89±0.3	4.63	35.4	30.2	21.8	18.6	943	1682	2007	1700
			24.1	28.8	21.4	21.1	871	1678	1779	2071
Heat 7	35.66±0.4	4.94	34.7	-	34.0	-	1067	-	1325	-
			35.6		27.8		1124		1224	
Heat 10A	40.62±0.3	5.94	43.3	48.5	33.3	33.8	1639	2180	1933	2345
			41.4	38.1	44.1	25.6	1893	2312	2297	1731
			49.9	46.1	48.8	35.5	2394	1774	2256	1880
Heat 10B	39.98±0.4	6.95	49.3	49.4	32.2	54.3	2028	1912	2108	2242
			39.6	49.5	27.2	58.4	2727	1773	2556	1977
			43.8	49.6	43.8	51.9	1974	2036	1805	1896
Heat 11A	40.22±1.9	6.01	40.5	37.2	36.3	38.5	1848	1047	2309	1560
			48.6	48.7	45.2	37.4	1356	1521	1580	1723
			45.5	36.6	36.4	51.5	1136	1320	1584	1952
Heat 11B	38.21+1.8	5.57	31.4	28.0	20.6	29.7	2363	1208	2076	1262
			39.5	32.4	27.3	14.3	1677	2211	2025	1439
Heat 12	38.00±0.2	4.99	60.0	47.5	27.7	28.4	1031	1239	1759	1610
			42.8	36.4	31.4	38.8	1688	1091	1717	1967
			47.1	42.6	31.9	36.9	1173	1632	1772	1822
Heat 14A	42.17±0.5	9.28	61.0	46.3	38.0	45.9	1560	1600	2273	1649
			41.3	52.4	52.6	39.7	1294	1671	2308	2801
			55.5			53.9	1156			2388
Heat 14B	41.49±0.5	7.93	36.3	36.4	33.2	33.9	1639	1794	1986	2393
			34.1	37.3	37.7	30.0	1477	1686	2300	2292
			43.3	34.0	32.6	35.9	1661	1670	2121	2756
Heat 15A	35.96±0.2	2.95	57.4	41.3	33.4	31.6	1444	1213	1918	2256
			51.5	30.2	37.5	37.7	1121	1946	2080	2942
			50.4		25.4		1268		2298	
Heat 15B	35.26±1.4	4.03	42.7	46.2	40.0	39.1	1301	1370	1486	1801
			39.7	40.9	43.3	35.7	1441	1984	1908	2058
Heat 16	38.06±0.3	1.51	35.8	26.0	36.8	36.3	1972	1860	1868	1795
			41.8	34.2		36.8	1992	1862		2028
						35.2				2370